AN A.E.S STUDY OF S.E.E AND ELECTRON BEAM EFFECTS AT OXYGEN EXPOSED ALUMINIUM SURFACES

by

Ercan H. Adem B.Sc.

A thesis presented for the degree of
Doctor of Philosophy
at the University of Keele.

Physics Department
University of Keele
Staffordshire

October 1985

To my late Father

ACKNOWLEDGEMENTS

I would like to thank my supervisor Dr. E.B. Pattinson for his kindness, help and guidance during the course of this work, and Professor Watson Fuller, head of the Physics Department for the use of the research and laboratory facilities.

I would like to thank Dave Seymour my research colleague for many useful discussions and Arumugam Mahendrasingam for his friendship and useful general discussions and Dave Keeble, Richard Winski, Mike Mulheron, Steve McAdam and other fellow research students for their friendship.

My sincere thanks goes to Mike Wallace for his excellent technical assistance, friendship and devastating humour.

I would also like to thank Mr. F. Rowerth the Departmental laboratory superintendent for his invaluable help during my stay, and other members of the technical staff for their assistance and friendship.

I also acknowledge the financial assistance given to me by the department in the form of a Research Studentship for the period 1980 - 1983.

Finally my most sincere thanks goes to my Sister, Brother-in-Law and Şerif for being very supportive, loving and caring. (Ablam ve Enişteme, en zor durumlarda bile bana şimdiye kadar gösterdikleri ilgi, destek ve sevgileri için onlara ayrıca teşekkür etmeyi bir borç bilirim.)

CONTENTS

Appendix B

Paper submitted in support of theses

ABSTRACT

An AES technique has been used to investigate oxygen adsorption at clean polycrystalline aluminium surfaces. The adsorption process was found to consist of two stages: chemisorption, reached within the first 50L of oxygen exposure, is followed by an oxidation stage where a surface Al_2O_3 like oxide is formed. Saturation coverage is reached after 150L. From the adsorption profile, an initial sticking coefficient of ≈ 0.02 has been estimated.

In electron beam effect experiments the surface was exposed to oxygen (0 - 1000L) and the surface irradiated with electron beams of energy 1500 eV and current densities of 10^{-3} - 10^{-4} A/cm^2 for > 90 minutes. The predominant beam effect observed was decomposition of surface oxide, with subsequent desorption of oxygen via the **Coulomb explosion** mechanism proposed by Knotek and Feibelman. From the decay of AES peak-peak heights an effective total desorption cross-section of 5×10^{-20} cm^2 has been estimated.

In SEE as studied by the total yield σ versus E_p method, for the very early stages of oxygen coverage (< 15 L) a previously unreported small minima in the development of σ_{max} has been observed. This has been interpreted as mainly due to a reduction in the plasmon decay contribution to SEE via single electron excitations from the conduction band, and to the attenuation of plasmon loss peaks as revealed in ELS. Recent theories and calculations on SEE by Chung and Everhart, and Rosler and Brauer have indicated this contribution to be very important.

With increased oxygen coverages (> 15L), SEE from the surface is enhanced for all E_p. This has been interpreted as due to the presence of monolayer thickness Al_2O_3 like oxide which modifies the electronic band structure of

the surface resulting in increased effective escape depth of secondary electrons.

An extensive critical review of previous literature on Al surfaces covering adsorption, electron beam effects and SEE studies has also been given.

CHAPTER 1

General Introduction

Information on the electronic structure and hence physical and chemical properties of solid surfaces can be obtained by investigating the scattering of electrons by the surface. In this thesis, the techniques of Auger electron spectroscopy, electron energy loss spectroscopy and secondary electron emission yield spectroscopy has been used to study the following: adsorption of oxygen on clean polycrystalline aluminium surfaces; the study of electron beam interactions with clean and oxygen exposed surfaces leading to desorption-adsorption phenomena; and the study of quantitative changes in the emission of secondary electrons from these surfaces.

In addition to the reported experimental work, an extensive critical review of the previous relevant literature has also been given. In the surface analysis techniques employed in this work, low energy electron beams (up to 1500 eV) have been used to bombard the sample surface and energy analysis of the scattered electrons made.

In AES, energy analysis of the scattered electrons enables sensitive physical and chemical analysis of the surface elemental composition to be made and give an indication of the level of oxygen presence on the surface.

In SEE, electrons that originate from the occupied states and core levels of the solid, and their contribution to the total secondary electron yield are examined, in addition to the contribution by the backscattered primaries. Most of the secondary electrons created inside the solid, undergo multiple inelastic collisions before escaping over the potential

barrier. The secondary electron generation depth is of the order of 100 A for the low energy primary electrons, but due to a short inelastic mean free path of a secondary electron (10 A) on average it suffers many collisions and escapes with a very low kinetic energy. These electrons are formed as a result of the so called cascade process and contribute up to 80 % of the electrons to the total yield.

In ELS essentially, primary electrons lose discrete amounts of energy in setting up multiple collective or single particle excitations in the solid. These are thought to play a major role in SEE and this aspect has also been discussed.

In chapter 2 the surface analysis technique of Auger electron spectroscopy is introduced. Its physical principles, experimental basis, capabilities and limitations are also discussed. Other important and supplementary techniques have also been briefly described.

In chapter 3 electron beam effects induced at clean and gas adsorbed solid surfaces have been introduced. Physical and chemical changes arising from electronic processes that lead to desorption of ionic, neutral and excited neutral species have been described in terms of models devised by Redhead, Gomer and Menzel, and more recently by Knotek and Feibelman. Also indirect determination of ESD parameters by AES methods have also been described to serve as background to material reviewed in chapter 4 and experimental results of chapter 8.

In the first part of chapter 4 a critical review of the previous studies of adsorption of oxygen on to aluminium surfaces as studied by AES and other surface analysis techniques have been made. In the second part, literature on electron beam effects on clean and oxygen exposed aluminium surfaces

have also been reviewed along with CO_2 and CO exposed surfaces.

In chapter 5 the physics of SEE process is briefly described. The basic empirical theories and results of quantum treatments of SEE have also been presented though with the emphasis on the latter. Particular attention has been paid to the slow secondary electron distribution curve which has been described by Wolff's cascade theory and by more recent modifications of it by inclusion of the contribution by surface and bulk plasmons. This aspect is further discussed in chapter 9. The applications to aluminium of these theories have also been presented.

In chapter 6 a critical review of literature on SEE yield measurements from clean and oxidised surfaces of aluminium has been presented along with electron transmission and reflection characteristics of Al films as bombarded by keV electrons. The contribution to the total yield by the backscattered electrons have also been included. Also reviewed are the few experimental studies in which the evolution of the total yield with oxidation was undertaken. In this chapter the role of SEE in electron stimulated desorption and decomposition has also been highlighted since both effects are very surface sensitive.

In chapter 7 the experimental apparatus used throughout the course of this work is described. In addition, methods of sample preparation, mounting and manipulation and method of oxygen exposure has been described. The experimental procedures in recording of Auger spectra and SEE yield spectra have also been described. Possible sources of error in measurements associated with each technique has been discussed.

In chapter 8 the results of some prelimenary AES experiments have been given followed by the results of AES spectra of adsorption of oxygen on to

the clean polycrystalline aluminium surface from which the surface coverage could be determined. From the so formed adsorption profile initial sticking coefficients for the surface was estimated. In the second part, the results of electron beam irradiation experiments at various current densities of the monolayer oxygen exposed surfaces are also presented. The results have been interpreted and discussed in terms of the ESD theories presented in chapter 3.

Similarly, in chapter 9 the results of SEE yield measurements from the clean and oxygen exposed polycrystalline surface are presented. In particular the evolution of the total yield with initial oxygen exposure has been interpreted and discussed in terms of plasmon decay contribution to the slow secondary electrons, changes in the workfunction and backscattering yield.

Finally, in chapter 10 a summary and conclusion of the experimental results have been presented together with recommendations for further experiments and improvements to the apparatus.

CHAPTER TWO

AUGER ELECTRON SPECTROSCOPY AND OTHER SURFACE ANALYSIS TECHNIQUES

2.1 Introduction

The basic principle of surface analysis is that the surface of a solid which consists of the top few atomic layers, receives an external stimulus by a source and the response yields information about the nature of the surface. The external stimuli can be particles of low enough energy so that only the surface is probed. These particles can be either charged or neutral, ions or atoms. Ionising radiation e.g. x-rays and ultra-violet radiation are also widely used. Thermal radiation or direct resistive heating is also a useful stimulant.

The surface response is by ejection of electrons, ions, neutral atoms, photons etc. as illustrated in Fig. 2.1. These are energy analysed by a suitable detector. Each method has its particular merits and when used in conjunction in the same apparatus different and complementary information is gathered about an aspect of the surface. In this work, Auger electron spectroscopy (AES) has been used to monitor the surface cleanliness of the sample and to follow the adsorption of oxygen and subsequent oxidation of the surface. In addition electron beam effects have also been investigated using AES.

Because of its importance in this work, the purpose of this chapter is to describe the technique of AES, its physical principles, experimental basis, capabilities and limitations. Brief descriptions of other popular surface analysis techniques will also be described.

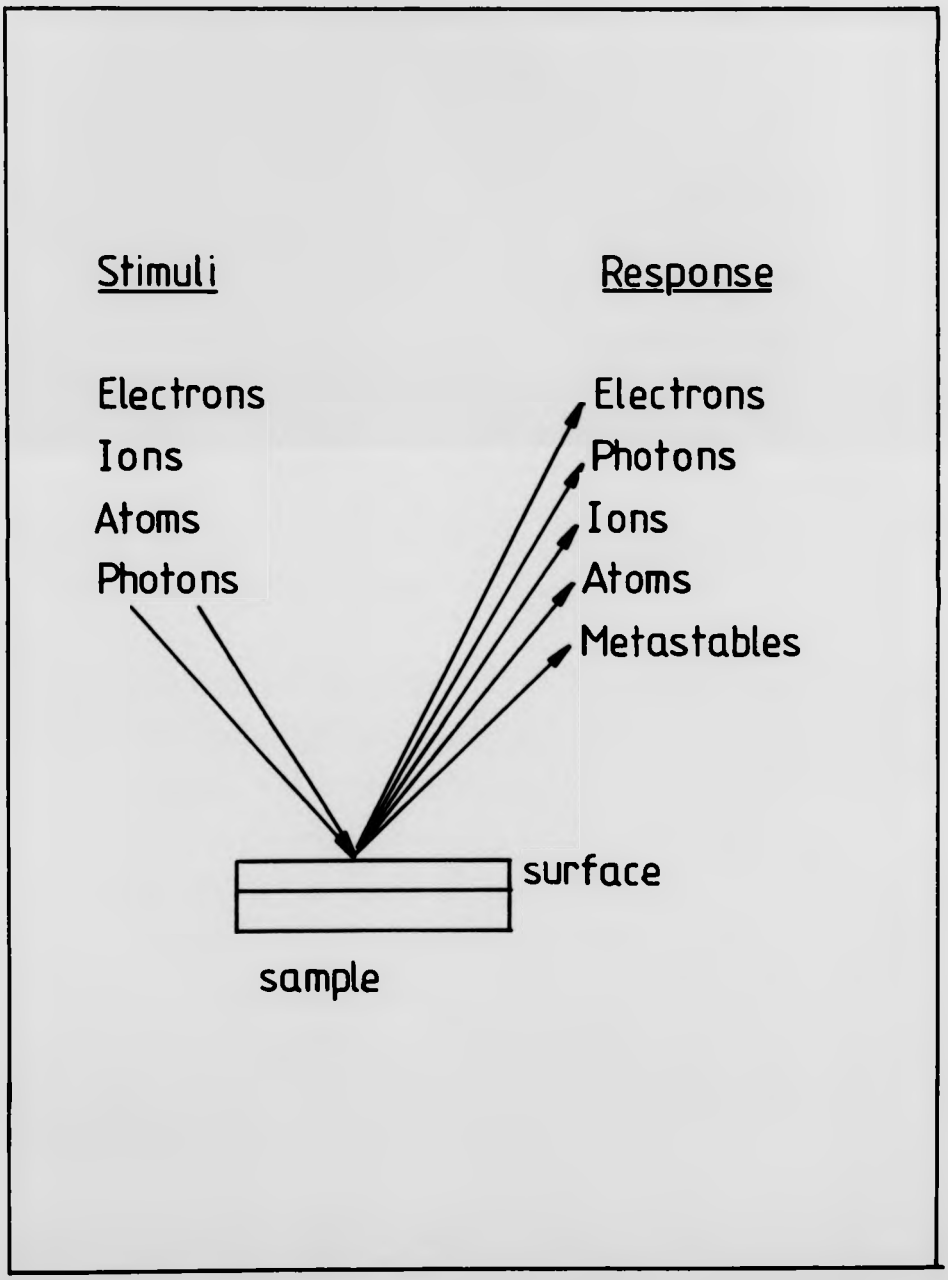

Fig. 2.1 Various means of surface excitation and responses.

2.2 Auger Electron Spectroscopy

Auger electron spectroscopy is a very powerful analytical technique where the incoming exciting radiation is normally a finely focussed primary beam of monochromatic electrons of kinetic energy 1-5 keV. Among the ejected electrons making up the energy distribution curve are the so called **Auger electrons** which have resulted due to **Auger processes** whereby the energy of a de-exciting atom is carried off by a second electron. Hence energy analysis of the ejected electrons by a suitable electron spectrometer helps identify the Auger electrons. But the energy distribution curve N(E) contains much more information other than just on Auger electrons.

A typical secondary electron distribution energy curve is distinguishable by three major features as shown in Fig. 2.2.

Region 1 consists of a sharp peak made up of elastically scattered primary electrons at energy E_p. The elastic peak contains information about the surface structure and is used in LEED and HREED (see section 2.3.3). In AES work the elastic peak is also used to align and optimise the electron spectrometer and used as zero-point energy for referencing the energy-loss peaks. These also occur in region 1 and normally accompany the elastic peak on the low energy shoulder and represent primary electrons which have lost a discrete amount in exciting plasmons which are collective oscillations of the valence electrons with respect to the ionic cores (see also section 2.3.2).

Region 2 is made up of a large number of slow electrons, the so called **true secondaries.** These are produced as a result of a cascade process whereby primaries in collision with atoms produce secondary electrons, these in turn create more secondaries with ever decreasing energy. The maximum of

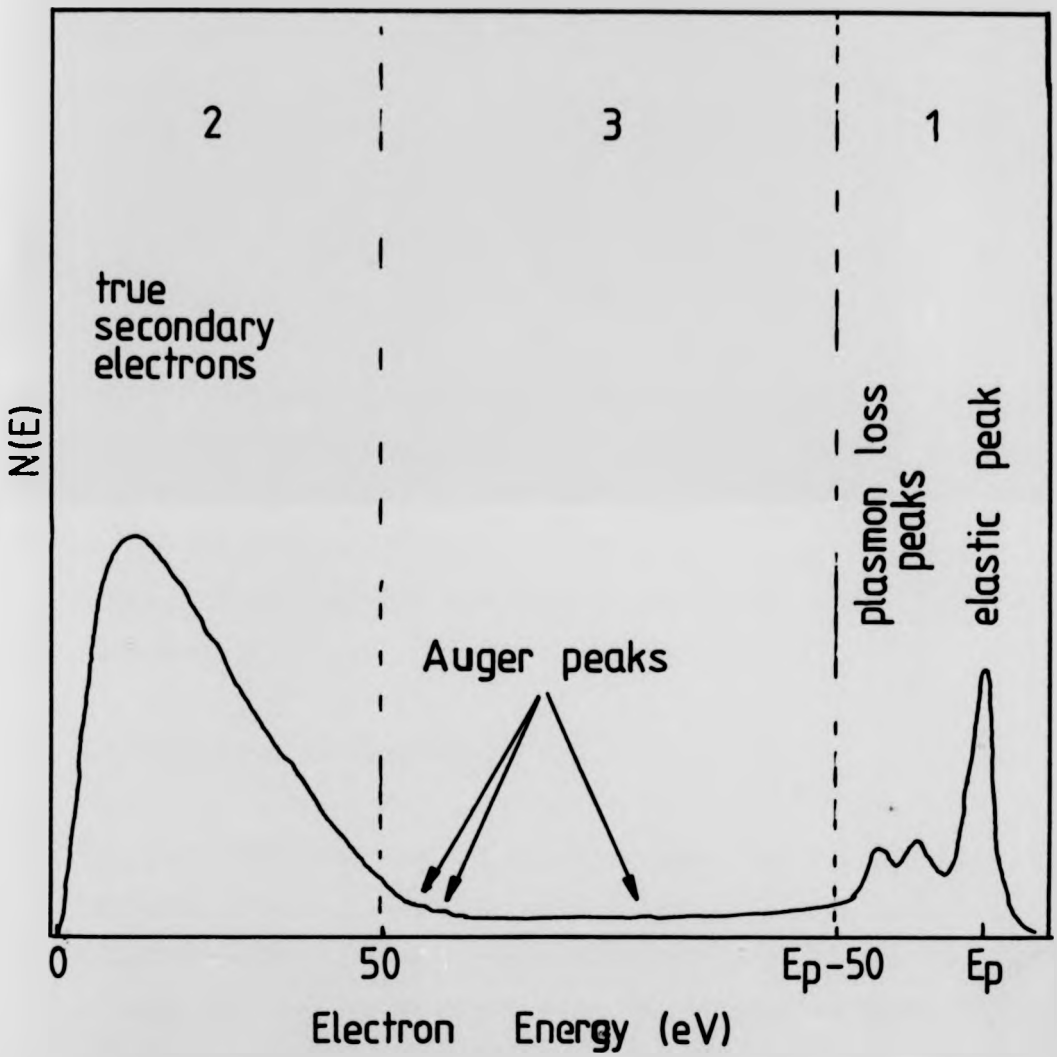

Fig. 2.2 Energy distribution of secondary electrons.

this broad peak occurs several electron volts above the vacuum level and has a full width at half maximum of less than 10 eV and is largely independent of the primary energy. Electron spectrometers with high resolution may show fine structure superimposed on the slow secondary peak which are thought to be largely due to single electron transitions via decay of plasmons or Auger processes from the valence bands (see section 5.2.4).

Region 3 consists of a relatively flat background due to inelastically backscattered primary electrons and Auger features. The position of the Auger features are independent of primary energy. Essentially AES is based on the detection and enhancement of these small discrete energy features relative to the inelastic background and consequently requires sensitive analysis.

2.2.1 Physics of the Auger Process

The Auger effect was first discovered and identified by Pierre Auger in 1925 while investigating the photo-electric effect of argon atoms using a Wilson Cloud chamber. Auger observed the simultaneous ejection of a pair of electrons from certain argon atoms. He correctly identified one of these electrons to be a photo-electron and the other to be due to a radiationless transition in an ionised atom in which the atom de-excites to a state of low energy and ejects an electron to carry off the energy difference leaving the atom doubly ionised. This phenomenon is known as the **Auger process** and is in direct competition with the x-ray fluorescence effect.

Inner shell ionisation in atoms can also be created by electron bombardment and Lander (1953) was one of the first to have observed Auger electrons

emitted by a solid under electron bombardment. The de-excitation events leading to an emission of an Auger electron is best described with the aid of a series of energy level diagrams as shown in Fig. 2.3.

Fig. 2.3(a) represents a simplified energy level diagram for a solid where the K and L sub-shells retain their atomic character. Incoming ionising radiation which can be an x-ray or an electron (even energetic ions) ejects an electron from the K shell thereby creating a vacancy. From this point the atom can de-excite in two ways, either through a fluorescence process or the Auger process. Fig. 2.3(b) illustrates the former. In the first step of the de-excitation an L_3 electron drops into the K-shell vacancy leaving a subsequent hole in the L_3 shell with a simultaneous emission of an x-ray quantum, its frequency corresponding to the difference in the energy levels of the K sub-shell and L_3 sub-shell. In this case the emitted x-ray radiation is Kα1. Typically the atom can de-excite in this way until the hole eventually travels to the outermost least negative energy level and is filled by an electron from the valence band or by the original K electron.

Fig. 2.3(c) illustrates the subsequent steps leading to the ejection of an Auger electron. The K-shell vacancy is filled by an L_2 electron and excess energy is removed by the ejection of an electron from the L_3 level. If this atom is near the surface, then the Auger electron can escape into the vacuum without loss of energy. This electron is labelled as a KL_2L_3 Auger electron and is characteristic of the energy levels of the de-exciting atom. If this electron can be detected and its energy determined, then the identity of the emitting atom can accurately be established. Hydrogen and helium cannot de-excite via the Auger process since their atomic numbers are less than 3. For lithium, Auger relaxation can only occur in the solid state.

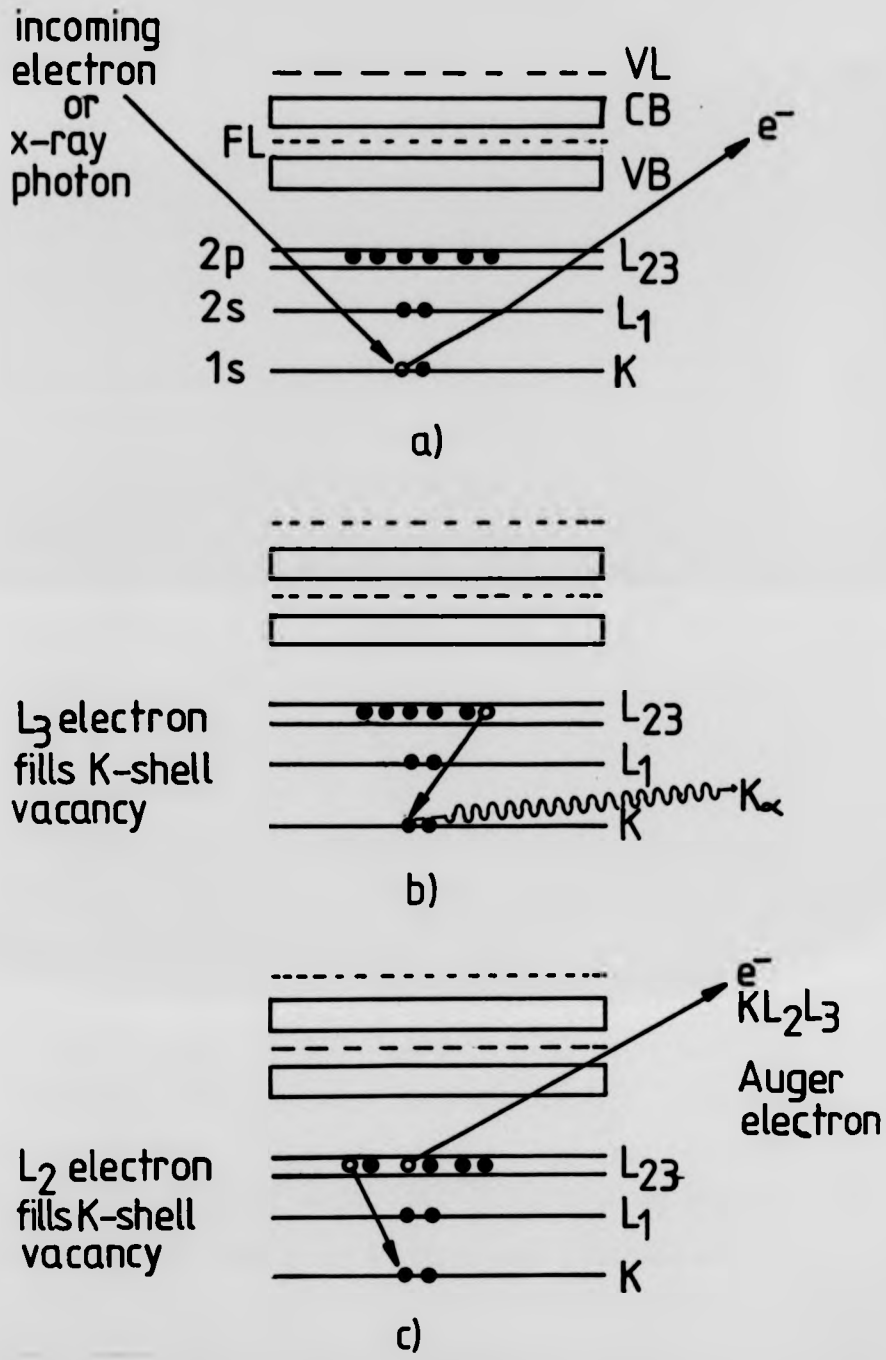

Fig. 2.3 Core-hole creation and de-excitation (a) Ionisation process, creation of K-shell vacancy. (b) De-excitation process, via x-ray fluorescence and emission of $K\alpha_1$ x-ray radiation. (c) De-excitation via the Auger process ejection of a KL_2L_3 Auger electron.

Another type of Auger de-excitation process is the Coster-Kronig transitions where the initially created hole is filled by an electron of the same shell and a super Coster-Kronig transition where all three electrons are from the same shell, though the probability of this process occuring is quite low.

2.2.1.1 Various Aspects of the Auger Process

Auger electron peak shapes and energy positions are determined by various inherent physical events, such as, doubly ionised initial states, multiplet splitting and multiple excitations, Coster-Kronig and cross-over or interatomic transitions and lifetime effects. For the work presented in this thesis the cross-over transitions are most important since the origin of some of the observed Auger peaks can only be explained by this concept and their appearance thus can confirm the existence of a specific molecule. In addition atoms in compounds which have been involved in such transitions, in their final state, lead to desorption effects as proposed by Knotek and Feibelman (1978).

Cross-over or interatomic Auger transitions may arise in neighbouring atoms of ionic metal oxides of Al_2O_3, BeO, MgO, TiO_2 etc. which all are maximal valence compounds. For example in Al_2O_3, core holes can be created either on the Al or O atoms. These holes may be filled by electrons from the modified valence band levels of O(2p) with subsequent emission of Auger electrons. These electrons are then approximately labelled as $L_{23}V_oV_o$, to indicate that the emitted Auger electrons have originated from the valence band of oxygen. This was demonstrated for Al_2O_3 by Quinto and Robertson (1971).

In this cross-over transition, a minimum of two electrons were removed from the oxygen atom. But in some, more complicated cases of Auger de-excitation, up to four or five electrons may be removed which can leave the atom singly, doubly or triply ionised. Knotek and Feibelman have proposed that this mechanism may lead to desorption or decomposition of the compound, via Coulomb repulsion of the neighbouring ionic cores. This desorption mechanism is further discussed in section 3.2.3.

2.2.1.2 Estimating the Energy of an Auger Electron

The kinetic energy of the E_{KL2L3} Auger electron illustrated in Fig. 2.3(c) can very simply be approximately estimated by use of the expression

$$E_{KL2L3} = E_K - E_{L2} - E_{L3} \qquad ...(2.1)$$

where E_K is the binding energy of the electron in the K sub-shell. E_{L2} and E_{L3} are the binding energies of the L_2 and L_3 sub-shells respectively. Reliable data on the binding energies of electrons are to be found in the results of Bearden and Burr (1967) and Seigbahn et.al. (1967) as carried out by the technique of Electron Spectroscopy for Chemical Analysis (ESCA) which is briefly described in section 2.3.1 of this chapter.

The expression 2.1 yields only a crude estimate of the kinetic energy and needs to be modified in order to account for the increase in the binding energy values due to the initial and subsequent creation of core holes. The expression used by Burhop (1952) partially allows for this effect and is reproduced below.

$$E_{WXY} = E_W(Z) - E_X(Z) - E_Y(Z+1) \qquad ...(2.2)$$

where E_{WXY} is the kinetic energy of the ejected electron. $E_W(Z)$ is the binding energy of W core of atom of atomic number Z. Similarly $E_X(Z)$ is the binding energy of X core of atom of atomic number Z. And $E_Y(Z+1)$ is the binding energy of the Y core level of atom of atomic number (Z+1).

A more accurate expression has been developed by Chung and Jenkins (1970) who modified expression 2.2 by taking the mean of the binding energies X, Y corresponding to atomic numbers Z and Z+1 i.e.

$$E_{WXY}(Z) = E_W(Z) - 0.5 [E_X(Z) + E_X(Z+1) + E_Y(Z) + E_Y(Z+1)] \quad ...(2.3)$$

Tabulated numerical results of elements using expression 2.3 have been prepared by Coghland and Clausing (1973). This expression is accurate to within several electron volts of observed Auger electron energies. Expressions dealing with Auger electrons emanating from the conduction and valence bands have been developed by Coad and Riviere (1971). And these are given below.

$$E_{WXV}(Z) = E_W(Z) - 0.5 [E_X(Z) + E_X(Z+1)] - E_V(Metal) \quad ...(2.4)$$

$$E_{WVV}(Z) = E_W(Z) - 2E_V(Metal) \quad ...(2.5)$$

where $E_V(metal)$ is the most prominent conduction band energy measured with respect to the vacuum level.

As mentioned earlier, when atoms are bombarded by an energetic (100 - 3000 eV) primary source of electrons the subsequent de-excitation can lead to the fluorescence process where photons, or the Auger process where electrons are emitted. For atoms with low atomic number Z ($\leq$ 14) where the initial vacancy has been created in the K shell the dominant

de-excitation is via the Auger process (Bishop and Riviere 1969), and the ejected Auger electrons are due to KLL transitions. Whereas in the high Z atoms, the major de-excitation is via the fluoroscence process and Auger electrons are mainly MNN transitions.

The cross-section for creation of Auger electrons of a particular transition is greater for electrons than for x-ray photons of comparable energy. This cross-section also depends on the energy of the impacting electron beam and increases linearly with electron energy until it levels off at about four times the energy of the core level, where the original ionisation is caused. The Auger electron yield is also maximised if the impacting electron beam is at grazing incidence with respect to the solid surface.

2.2.1.3 Escape Depth of Auger Electrons

The escape depth of Auger electrons depends on the mean free path λ (i.e. average distance an electron travels without suffering a collision and generally losing energy inside the solid) which in turn is kinetic energy dependent. Fig. 2.4 illustrates the kinetic energy dependence of the mean free path of Auger electrons for various materials as compiled by Seah and Dench (1979). As can be seen the mean free path of 50-100 eV electrons is around 5 A and rises to about 15 A for 1000 eV electrons. For very low energy electrons the MFP is of the order of 100 A.

Of the electrons that leave the surface ~ 95% originate from a depth of ~ 45 A. The kinetic energy of Auger electrons normally lie in the range 30 - 1000 eV and the overall sampling depth from which Auger electrons escape lies in this 45 A MFP range (~ 3λ). This indicates that Auger spectroscopy is very much a surface analytical technique.

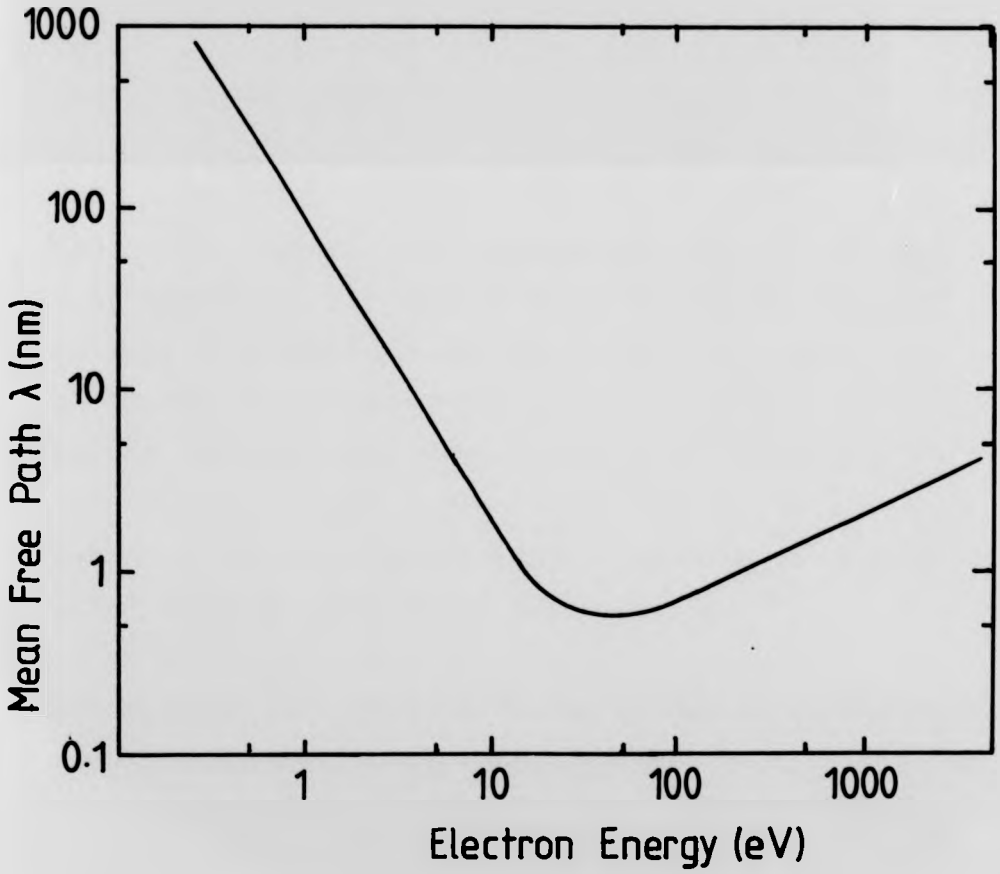

Fig. 2.4 Mean free path versus electron kinetic energy (Seah and Dench 1979).

2.2.2 Surface Analysis with Auger Electron Spectroscopy

From the foregoing it is clear that AES provides a means of probing surfaces. Elements present on a surface can be identified from very accurate spectra of electron energies and the prediction of Auger electron energies made by use of the semi-empirical expressions make the task of identification of unknown elements easier. Tables of Auger electron data have been published on virtually all the elements by Coghland and Clausing (1973), Davis et.al. (1976) and McGuire and Seah (1979) and more recently by Wagner (1983).

N(E) spectra of Auger electrons normally sit on a very high background of inelastically scattered slow secondary electrons (see Fig. 2.2). The exact location of the energy at the maximum of these peaks is rather difficult to determine with accuracy, because of the inherent width. One of the most popular ways of enhancing this maximum and at the same time removing the high background is to electronically differentiate the N(E) distribution with respect to energy so that dN(E)/dE of N(E) is formed. By convention, the Auger electron energy is measured at the negative going peak on the higher energy side of the energy scale.

One of the earliest applications of Auger electron spectroscopy was in the area of qualitative surface compositional analysis for the purpose of determining the extent of surface cleanliness. Surfaces previously thought to be free from contaminants were shown to contain traces of carbon, oxygen, sulphur and other contaminants. Thus experiments in which results depended very much on the cleanliness of the surface were proven to be unreliable and inaccurate.

AES also yields quantitative information on the relative concentration of elements if relative Auger sensitivity factors are known. The intensity of the differentiated Auger signal is measured in terms of the peak-peak height (PPH) and this has been shown to be directly proportional to the concentration of the element in the region of the escape depth.

Quartz crystal oscillator and optical ellipsometry techniques (Vrakking and Mayer 1971) which are widely used in the accurate measurement of thin film thickness, have been used to confirm the proportionality (Habraken et.al. 1977). Since the intensity of the differentiated Auger signal depends on the shape of the signal in the N(E) distribution, it is assumed this does not change during the experiment. Otherwise the area under the Auger peak on the N(E) distribution gives a better measure of the elemental concentration.

Specimens with a standard Auger signal have been successfully used in order to obtain a quantitative measure of adsorbed layers. However this technique has various shortcomings in that adsorbed layers form inhomogeneously and there are difficulties in producing reference standards (Gallon 1978).

One feature of the Auger process which can be used in quantitative analysis is the shift in the Auger electron energy that results when the emitting atoms have been chemically reacted with neighbouring foreign atoms. The Auger electron energy peak shifts arise in the following manner when for example a metal is reacted with oxygen to form an ionic bond. Since a transfer of electrons to the cation has occurred, the core levels of the anion will be shifted to greater binding energies. This effectively lowers the Auger electron energy. In metal oxides this shift can amount to as much as 13 eV as in aluminium oxide (see section 2.2.1.1 on Auger cross

transitions).

Auger peak changes in line shape and in energy can help to identify the chemical state of species present on the surface, but this process can be a little complex since Auger electron spectra energy shifts come about as a result of shifts in three electronic levels. This renders interpretation of spectra rather difficult. Haas, Grant and Dooley (1972) have shown that carbon exhibits distinct types of Auger spectra when in different chemical environments e.g. CO on W, metal carbide, graphite and diomond.

2.2.3 Experimental Aspects of AES

In order to record the Auger electron spectrum of a given sample an excitation source (electron gun), an appropriate sample analysis chamber, an electron energy analyser, an electron detection system and appropriate recording and control electronics are required. Fig. 2.5 shows a typical AES block diagram.

First of all ultra high vacuum (UHV) is necessary though not absolutely essential in a sample analysis chamber for carrying out AES. But in order to increase filament life, accelerate electrons from the source on to the sample and perform energy analysis without encountering residual gas atoms and maintaining a clean sample surface for long periods a chamber pressure less than 10^{-8} Pa is required and this pressure nowadays is routinely achieved with a variety of efficient pumps within several days.

First Auger electron spectra in the N(E) versus E mode was recorded by use of low energy electron diffraction (LEED) apparatus (see section 2.3.3). A slight modification of the LEED apparatus enabled energy analysis of the ejected electrons from the sample to be made. A diagram of this so called

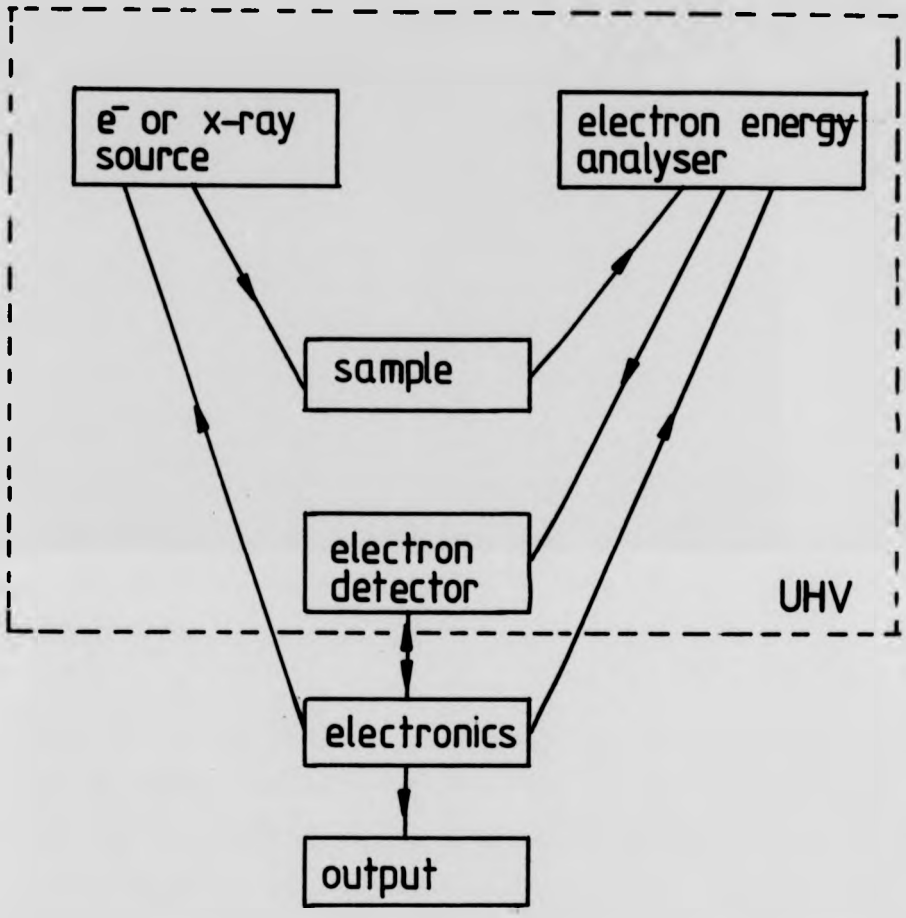

Fig. 2.5 Block diagram representation of an experimental AES system.

retarding grid analyser or **retarding field analyser** is shown in Fig. 2.6. It consists of 4 transparent hemispherical grids and a solid collector (for LEED applications this forms the screen, which is coated with a fluorescent material).

The sample together with the inner and outer grids are maintained at ground potential to provide a field free region and the inner two grids are connected to a retarding negative potential. Ejected electrons would have to surmount this in order to reach the collector, which is maintained at a positive potential to prevent creation of more secondary electrons by the returning secondaries. In this configuration the RFA acts as a high pass filter with a 180° acceptance angle and the collected current is directly proportional to the integral of the N(E) versus E curve.

With the RFA it was realised that the Auger signals could be easily enhanced by taking the differential of the energy distribution i.e. dN(E)/dE (see Fig. 2.7) by superimposing a small sinusoidal a.c. voltage on to the retarding grid and detecting the second harmonic with a lock-in-amplifier (see Fig. 2.6). Though this also improves the signal to background ratio, it tends to degrade the signal to noise figure of the analyser.

These two parameters are very important and the desire to improve the two have led to the use of different types of energy analysers. The most popular and widely used are the cylindrical mirror analyser (CMA) and the hemispherical sector analyser (HSA). In this work an RFA has been used and it is further described in chapter 7. The RFA has inherent advantages when used to record secondary electron yield plots.

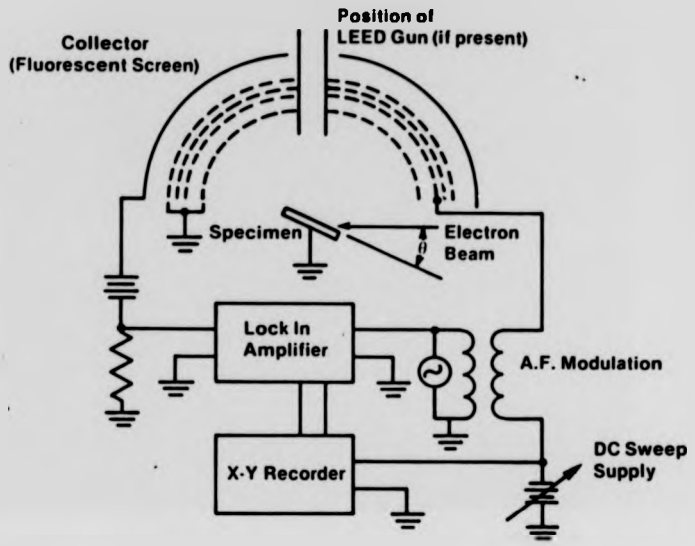

Fig. 2.6 Diagram of a 4-grid retarding field analyser.

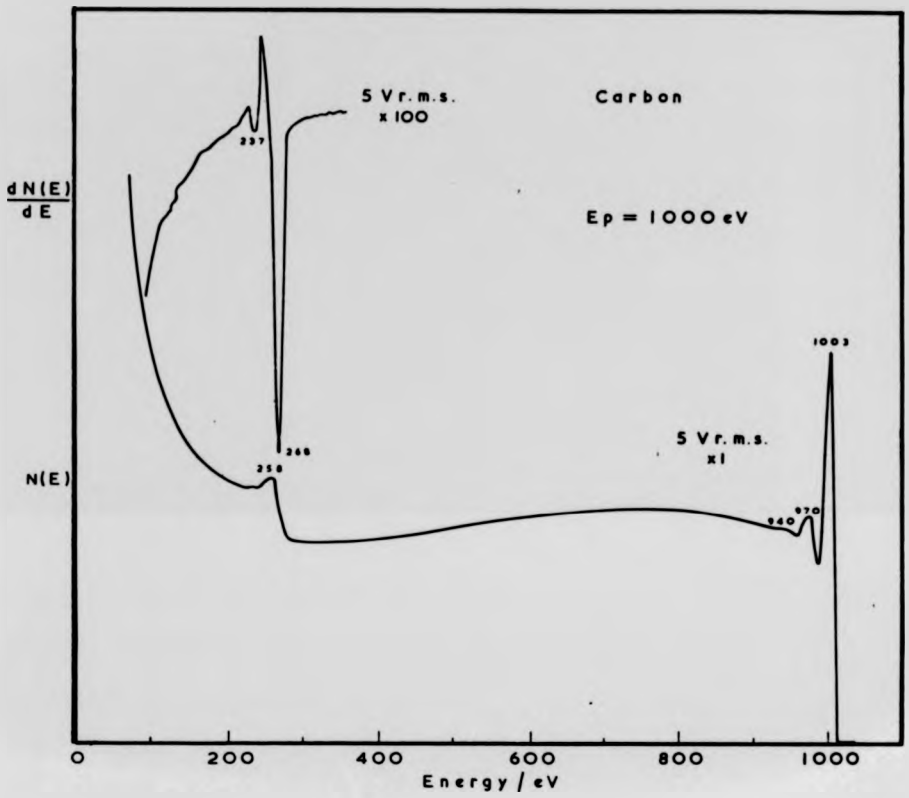

Fig. 2.7 N(E) of the C_{KLL} Auger peak and its derivative i.e. dN(E)/dE. (Riviere 1983).

In Fig. 2.8 is shown a schematic diagram of a CMA with its associated instrumentation. Ejected electrons enter the analyser at an angle of 42° and the applied voltage ramp between the inner and outer cylinders cause the electrons to reverse their radial momenta. Electrons with the correct energy arrive at the electron detector which is an electron multiplier with the result that the signal is further amplified. The CMA is a band pass analyser and the output of the detector is directly proportional to the EN(E). In order to obtain the derivative of this, only the fist harmonic of the a.c. signal need be detected with the lock-in-amplifier.

2.2.3.1 Scanning Auger Microprobe

An extention of the technique of AES which is now widely available with all commercial instruments is the scanning Auger microprobe (SAM), with which Auger images of the sample surface can be obtained (as well as secondary electron images with a suitable secondary electron detector). SAM is really a scanning electron microscope combined with an electron energy analyser, normally a CMA or an HSA. An element map of the surface is obtained by tuning to the element's particular Auger peak energy and scanning the surface with a high energy (5-15keV), low current (μA - nA) primary electron beam focussed into a 100 nm spot. Bright areas on the television image normally correspond to a large concentration of the element. Also by use of the secondary electron image SAM can be operated in the static mode by placing the electron spot on to any point of interest on the surface and perform AES. Best spatial resolution that can be obtained with SAM is of the order of 0.2 μm one of the limiting factors being the signal to noise ratio.

2.2.3.2 Depth Profiling with AES

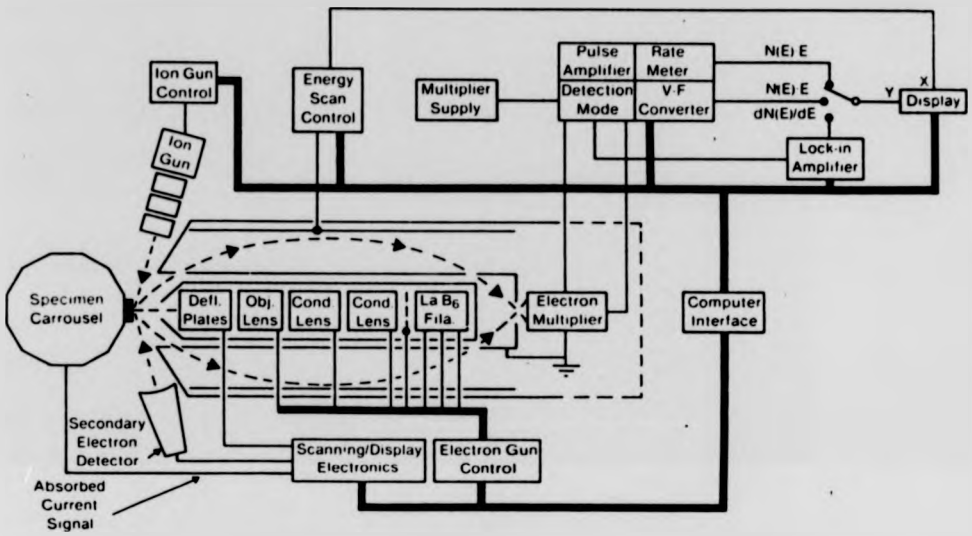

Fig. 2.8 Schematic diagram of a CMA based AES system (Seah and Briggs 1983).

It is also possible to carry out compositional analysis of thin films while sputtering with noble gas atoms. A finely focussed argon ion beam is scanned across the sample surface for pre-determined periods and Auger spectra recorded. A knowledge of sputtering rate, gives a concentration versus depth graph otherwise known as a depth profile.

2.3 Some Other Important Surface Analysis Techniques

AES has proven to be a very popular surface analysis technique but there are a number of other relevant techniques based on similar surface analysis principles i.e. electron, photon and ion stimulation sources, as introduced at the beginning of this chapter. In this section these will be introduced with emphasis on more relevant techniques to this work.

2.3.1 Photo-electron Spectroscopy

In photo-electron spectroscopy, the stimulating excitation consists of soft x-ray radiation and ultra-violet photons which cause the emission of photo-electrons via absorption and elastic scattering processes in the atoms. The photo-electron energies (the kinetic energy of the photo-electron is approximately equal to the energy of the incident photon minus the binding energy of the electron in the atom) when analysed by a suitable energy analyser normally a CMA or an HSA, yield accurate information on the core level binding energies and their chemical shifts, which help identify the emitting atoms as well as their chemical environment or state.

This technique is known as x-ray photo-electron spectroscopy (XPS) but is also commonly known by the acronym ESCA (electron spectroscopy for chemical analysis) which was coined by Kai Seigbahn who originally pioneered the

technique. Ultra-violet photo-electron spectroscopy is another aspect of the technique where the photon energies in the range 20 - 40 eV are used to study the valence band structure of materials.

More recently synchrotron radiation source (radiation emitted by accelerated electrons in a storage ring) have provided by use of appropriate monochromators, a continuously variable photon energy source for photo-electron spectroscopy. One ideal application of this source is in the study of local structure and short range order from the fine structure observed on the high energy side of x-ray absorption edges of materials. This technique is known as extended x-ray absorption fine structure spectroscopy (EXAFS). It has also been used successfully to study adsorption geometries of gases on metal surfaces and hence estimate bond lengths, where the technique is known as surface EXAFS or S-EXAFS (Bianconi 1980).

The mean free path λ versus kinetic energy shown in Fig. 2.4 equally applies to photo-electrons generated by XPS, indicating that the technique indeed is also a surface analytical tool in the same league as AES. In fact successful Auger electron spectra was obtained for the first time by Seigbahn (1967) directly on XPS spectra where the Auger signals appeared as extra features. XPS and AES, are the two most widely employed surface analytical techniques in surface studies and the two techniques give complementary information about the surfaces under investigation. Almost all commercial surface analysis systems nowadays have both techniques as standard.

2.3.2 Electron Energy Loss Spectroscopy (EELS)

Electron energy loss spectroscopy is based on the energy analysis of **quasi-elastically** reflected electrons in the energy range 2 - 50 eV from electron or photon excited solid surfaces. Elastically scattered electrons emerging from the surface can lose specific amounts of energy after interactions with the **electron gas** which is capable of being excited into quantised oscillations called **plasmons.** Plasmon losses which are one of the main loss features in ELS move along the energy scale as the primary electron energy E_p is varied and hence are measured a specific distance from the elastic peak as described in section 2.2 and shown in Fig. 2.2.

Bulk plasmons are due to three dimensional characteristic collective oscillations ω_B, of the electron gas density, and therefore require a characteristic amount of kinetic energy to be excited. From a consideration of classical dielectric theory it can be shown that the characteristic bulk plasmon frequency is given by $\omega_B = (n\, e^2/\varepsilon\, m)^{1/2}$ where n is the electron gas density, e is the electronic unit of charge, ε is the static dielectric constant and m is the electron rest mass. Hence the quantised bulk plasmon energy is $\hbar\omega_B$ (for Al $\hbar\omega_B$ = 15 eV).

Surface plasmons are due to 2 dimensional characteristic oscillations ω_S, localised to the surface and shown to be equal to $\omega_B/(1+\varepsilon)^{1/2}$ where ε = 1 so that ω_S is $\omega_B/\sqrt{2}$. Hence the surface plasmon loss energy for aluminium is equal to ~ 10 eV. A thorough theoretical treatment of the plasmon theory has been given by Pines (1963) and experimental work developed mainly by Raether (1980). Emergent primary electrons can create multiples of surface and bulk plasmons. Their relative intensities depend on the primary electron energy and angle of incidence. For low primary electron energies the surface plasmon intensity is dominant and is very sensitive to the presence of adsorbates on the surface.

Plasmons are thought to play a very important role in the phenomenon of secondary electron emission in the nearly free electron metals such as Al and Mg. A major contribution to slow secondary electron emission arises from the decay of these plasmons into single particle excitations via direct interband transitions from the conduction band. This aspect of the property of plasmons will be discussed further in sections 4.2.3, 5.2.4 and 6.2.3.

EELS has become quite popular, because it can be performed on existing ordinary spectrometers. EL spectra can be plotted directly in the N(E) or dN(E)/dE modes depending on the application and type of energy analyser used. In this work ELS spectra have been recorded using the latter mode of recording. To date the main research studies have concentrated on the identification of various loss events by measurement of the loss energy and subsequent building of theoretical models of the surface. Recently quantitative analysis work with ELS has also been carried out (Margoninski 1982).

2.3.3 Low Energy Electron Diffraction (LEED)

This technique employs the diffraction effect of electrons as discovered by Davisson and Germer (1927). Since the penetration depth of low energy electrons (10 - 800 eV) is of the order of several atomic layers, diffraction patterns that arise give information about the geometrical structure of single crystal surfaces. LEED has been widely used in the study of adsorption of various gases on clean single crystal surfaces. The framework for evaluating the surface structure is very similar to three dimensional bulk structure determination by x-rays.

Several notation schemes have been adopted to describe adsorption geometries based on the substrate unit cell. A typical notation example is Ni(110)c(2×2)-O where the substrate is a single crystal of nickel of orientation (110) normal to the incident electron beam with an oxygen overlayer and centered mesh, 2x2 being the ratio of surface to substrate mesh.

In LEED it is the elastically scattered electrons (region 1 of the N(E) distribution as discussed in section 2.2 and shown in Fig. 2.2) that give rise to the diffraction spot patterns. A negative potential placed just below the elastic peak energy prevents the inelastically reflected electrons from reaching the phosphor coated screen. Infact a standard LEED instrumentation after slight modification was first used to obtain differentiated Auger spectra by Weber and Peria (1967). This will be discussed in greater depth in section 7.2.1.

2.3.4 Secondary Ion Mass Spectrometry (SIMS)

Secondary ion mass spectroscopy (SIMS) is based on the fast ion bombardment of solid surfaces and subsequent mass analysis of ejected particles. Noble gases such as Ar, Ne, He and even reactive gases O_2 and N_2 are ionised and focussed into a very fine beam (typically 4 keV, 160 nA into 100 μm) by an ion gun and is incident on a sample. Substrate atoms as well as adsorbed species after ejection (neutrals and ions) are detected by a very sensitive quadrupole mass spectrometer and electron multiplier. Surface sensitivity is of the order of 10^{-6} of a monolayer i.e. 10^{8} atoms/cm^2 (Benninghoven and Loebach 1971 and McHugh 1975).

A new ion source is the liquid metal ion gun where a low melting point metal is allowed to wet the tip of a very fine needle from which metal ions

are pulled away by field emission and focussed into a very small spot. This allows SIMS imaging with spatial resolution surpassing that of SAM (Riviere 1983).

2.3.5 Ion Scattering Spectroscopy (ISS)

In this technique the surface is bombarded by energetic light ions of H^+ and He^+ and subsequent change in their kinetic energy after inelastic scattering is measured by an energy analyser. CMA or HSA operated with positive scanning potentials accomplishes this task. The amount of energy change gives information about the identity and atomic mass of the scattering substrate atoms as well as adsorbed species (Smith 1971 and Buck 1975).

2.3.6 Changes in the Work Function ($\Delta\phi$)

The work function ϕ of a solid is normally defined in terms of a surface potential barrier preventing the electrons from spilling out into vacuum (in a metal the work function is measured from top of the Fermi level to the vacuum level). As the definition implies, the work function plays an important role in thermionic emission of electrons, contact potential between solids, emission of electrons in the presence of very high electric potentials and bonding of adsorbates to a surface.

The work function of metals is normally of the order of several electron volts and is a function of crystal face orientation. When an electronegative element (affinity for electrons) is adsorbed on to a metal surface the work function of the metal is increased because of the attraction of electrons from the metal to the adatom. On the other hand adsorption of an electropositive element causes a decrease in the work

function. Variation of work function with different types of adsorbed gases has been discussed by Somorjai (1972). Adams and Germer (1971) have demonstrated that there is a direct correlation between work function change $\Delta\Phi$ of a metal and quantity of adsorbed species.

Measurement of the absolute work function is rather difficult, but monitoring $\Delta\Phi$ is a lot easier by using a constant potential difference CPD, or vibrating reed capacitance methods described by Prutton (1975).

2.3.7 Electron Stimulated Desorption

This surface analysis technique is based on the fact that when an adsorbate covered solid surface is subjected to low energy electron bombardment, ionic, neutral and excited neutral species are caused to desorb from the surface. The desorbed species are directly monitored by use of sensitive mass spectrometers and energy analysers. The method is ideal for the investigation of bonding of gases on to metal surfaces. Some aspects of this method has been discussed in the next chapter.

2.4 Conclusions

Auger electron spectroscopy is a well established and widely employed surface analysis technique. In this chapter its basic principles has been introduced and shown how it could be used to characterise and investigate the surfaces of solids. In this work AES was used to follow the oxygen coverage and subsequent oxidation of aluminium surfaces. Other important surface analysis techniques have also been briefly described and shown to complement AES and each other in applications.

In the next chapter the physical and chemical effects of electron beam bombardment of solid surfaces will be described.

CHAPTER THREE

ELECTRON BEAM EFFECTS

3.1 Introduction

A clean or gas adsorbed solid surface when subjected to electron beam bombardment can give rise to physical and chemical changes on the surface and bulk layers of the solid. These changes arise, due to various electronic excitation processes which cause dissociation or desorption of ionic and neutral surface species. In some cases, residual gases present in the analysis chamber can be induced to adsorb on the sample surface.

With more energetic electron beams, electronic excitation of the deep lying bulk atoms will cause ionisation, defect production and colour centre formation and diffusion. In insulators electron beam bombardment will induce charge accumulations which will lead to field enhanced migration of ions. In the case of very intense beams, thermal effects will also arise, leading to the desorption of weakly adsorbed surface species, annealing and segregation of impurities. A general review of the above type of beam effects has been given by Pantano and Madey (1981).

For metals the electronic excitation processes of electron stimulated desorption (ESD), electron beam induced decomposition (EBID) and electron stimulated adsorption (ESA) are most important and are in direct competition with Auger processes. A schematic illustration of the physical and chemical effects of electron beam irradiation of solid surfaces is shown in Fig. 3.1.

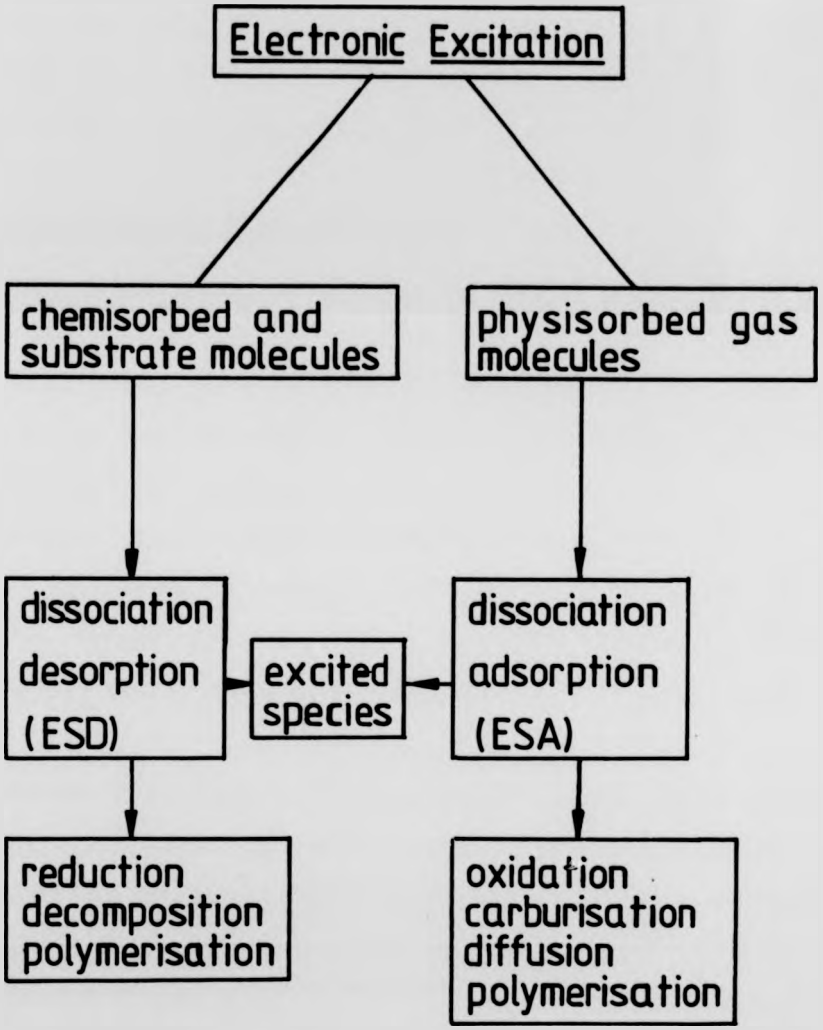

Fig. 3.1 Physical and chemical changes induced at a solid surface by electron impact via electronic processes.

In this chapter, these electron beam induced processes will be discussed. In particular the mechanism of ESD and a brief introduction of its theory as developed by Redhead, Menzel and Gomer. Also the methods of evaluation of experimental ESD data will be introduced so that ESD parameters can be determined by AES. Since some of these beam effects may be undesirable in quantitative AES measurements, expressions in terms of beam parameters will be given to define various threshold and critical electron beam doses, in order to minimise beam damage to the surface under investigation.

3.2 Electron Stimulated Desorption (ESD)

Electron stimulated desorption processes in general are viewed as a two step process whereby the surface adsorbate, suffers electronic transitions induced by the impacting electrons, followed by either the escape of ions or de-excitation and recapture by the surface. Electrons with energy 10 - 40 eV can cause valence electron excitations and ionisation of shallow core levels. Desorption of particles will occur if there is repulsive interaction between the excited particles and the surface. In addition ionic species, neutral and metastables are also emitted.

With electron energies approaching core levels of atoms, enhanced emission of adsorbate fragments is observed. Here for example the mechanism of emission is that of **Coulomb repulsion**, whereby creation of a core hole on the oxygen atom, leads via Auger decay to a two hole final state C^+ O^+ for CO on W. The Coulomb repulsion desorption mechanism is operable in both ionically and covalently bonded systems as proposed by Knotek and Feibelman (1978).

3.2.1 Measurement of ESD Parameters

ESD products, can be monitored either by direct or indirect methods. The direct methods, involve the measurement of particle current, mass and charge state and angular dependence using sensitive mass spectrometers or use of energy analysers.

The indirect methods involve the monitoring of a surface parameter that depends on the surface composition, such as AES peak-peak heights and work function change $\Delta\phi$ measurements as a function of surface coverage. Both the direct and indirect methods give an indication of the type of desorption mechanisms taking place on the surface. Desorption mechanisms have been observed to occur in isolation and can be described by first order relations where the rate of desorption of a particular adsorbate is proportional to the number of incident electrons per unit area, and time or electron flux. This relationship is given as follows:

$$-dN_i/dt = Q_i\ (J/\varepsilon)\ N_i \qquad \ldots(3.1)$$

where N_i is the desorbed adsorbate in state i, Q_i is the constant of proportionality defined as the total cross section for desorption of species i (this can further be split into contributions of different desorbing species and other processes) J is the electron current density (I_e/A) per unit time incident on the sample. Further I_e, is the incident electron current, A is the irradiated area and ε is the electronic charge.

Solution of eq. 3.1 gives

$$N_i(t) = N_i(0)\ \exp -[\ (J/\varepsilon)\ Q_i t\ ] \qquad \ldots(3.2)$$

or

$$N_i(t) = N_i(0) \exp -[(I_e/A\varepsilon) Q_i t] \quad \ldots(3.3)$$

where $N_i(0)$ is the initial coverage of adsorbate in state i. $N_i(t)$ is the coverage at time t of electron bombardment.

Experimentally, J would be made large enough to change $N_i(0)$ significantly so that the time constant (ε/JQ_i) can be measured to calculate the total desorption cross-section. In any experiment direct measurement of $N_i(t)$ is not strictly necessary, any quantity that is directly proportional to it e.g. AES peak-peak heights will do as indeed has been done in this work. Therefore equation 3.3 has been rewritten as

$$X(t)/X(0) = \exp -[(I_e/A\varepsilon) Q_i t] \quad \ldots(3.4)$$

where X(t) is the AES peak-peak height at time t, after irradiation has been switched on and X(0) is the AES peak-peak height just before irradiation commences.

A plot of the natural logarithm of X(t)/X(0) i.e. ln [X(t)/X(0)] as a function of irradiation time t, should yield a straight line, if the desorption process is of the first order type. Deviation from a straight line relationship may indicate that other secondary effects or desorption mechanisms may be occuring.

Experimental ESD total desorption cross-sections for ionic, and neutral species have been measured by direct or indirect methods just described for various gas adsorbate-metal systems, and these have been reviewed by Menzel (1975), and by Drinkwine and Lichtman (1977). A general summary of these experimental results will be given below.

3.2.2 Summary of General ESD Experimental Results

1. Threshold electron impact energy to stimulate desorption of ionic, neutral and excited neutral species is ~ 10 eV. The contribution to the total desorption by the ionic species is only a few percent.

2. ESD total and partial desorption cross-sections lie between 10^{-17} and 10^{-22} cm^2 for 100 eV impacting electrons. While that for free molecules are typically between 10^{-16} and 10^{-15} cm^2.

3. Desorption cross-sections in general tend to be large for weakly adsorbed states and smaller for strongly adsorbed states of the same species.

4. In addition to desorption, electron beam irradiation may cause break-up of molecular adsorbates and can also convert one adsorbate state to another. An example is the splitting of adsorbed CO molecules and deposition of C and O on the substrate.

5. The kinetic energy of ions created by ESD vary in the range 0 - 10 eV. Multiple peak structures are due to co-existing adsorption states. For example in the case of CO on W, the low energy peak was attributed to CO^+ and the high energy peak to O^+.

6. The ESD cross-section values i.e. Q_{ik} show strong isotope effects. High mass isotopes display small Q_i compared with low mass isotopes which show large Q_i.

7. Angular resolved work of emitted ESD products, show preferred angles of desorption. This may indicate direction of surface bonding.

8. Threshold energies for ESD, seem to be lower for neutral rather than ionic desorption. And ESD cross-sections appear to rise with primary energy and level off at around 300 eV. For free molecules dissociation cross-sections show a maximum at around 100 eV. This has been attributed to the role of the secondary electrons returning through the surface. This aspect will further be discussed in sections 3.5 and 6.3.

The foregone summary of the findings of ESD experiments, generally carried out on gas adsorbed surfaces can adequately be described in terms of mechanisms developed by Redhead (1964), and Menzel and Gomer (1964a,b).

3.2.3 Mechanisms of ESD

In order for desorption to occur energy must be supplied in excess of the binding energy between the adsorbate and metal substrate. Direct energy transfer from the impacting electron to the adsorbate is negligible compared with the binding energy and this desorption mechanism is only important for very energetic electrons. Thus for strongly bound species and low energy incident electrons direct momentum transfer must be ruled out. Then the cause of ESD must be due to electronic excitations of the surface bond. From an extension of the electron impact with free molecules, Redhead, Menzel and Gomer have suggested a two step mechanism for ESD.

1) Electron collision with the adsorbate-substrate complex will cause a Frank-Condon transition from the ground state to an excited state, either repulsive anti-bonding state or ionic state. The internuclear separation between the adsorbate and substrate atoms can be represented by a series of potential energy diagrams as illustrated in Fig. 3.2. Frank-Condon transitions, are vertical transitions from the ground state to a higher

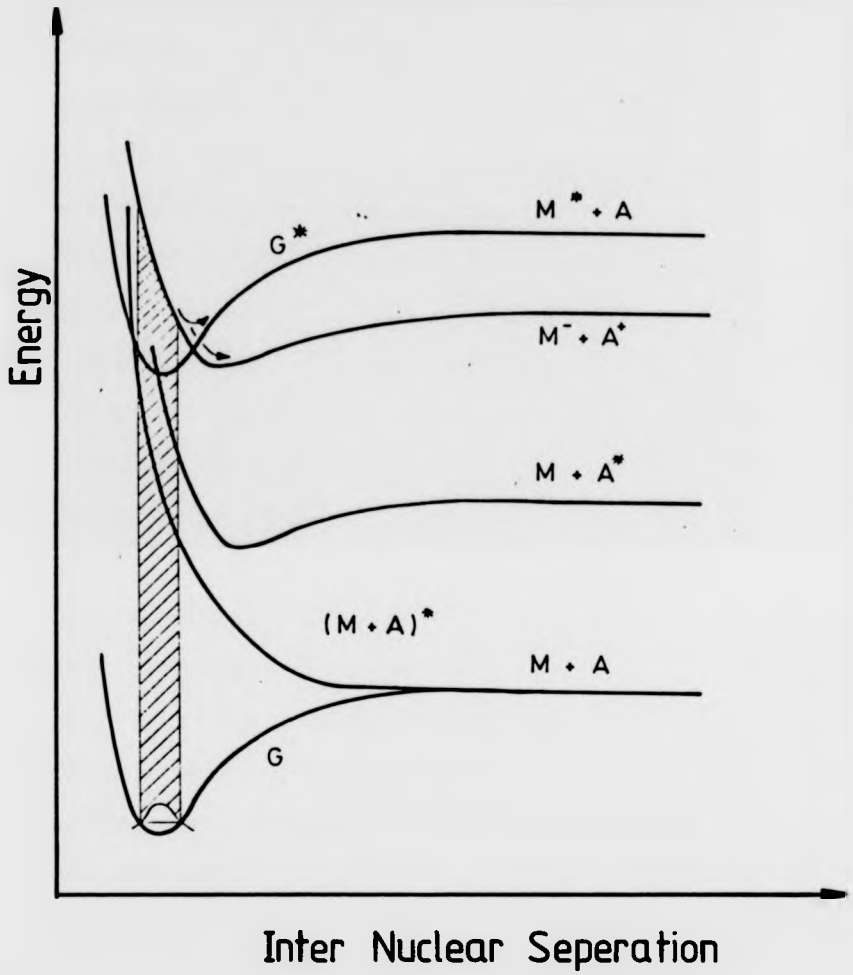

Fig. 3.2 Potential energy diagrams for an adsorbate system. Also illustrating the Frank-Condon principle (G=ground state; M+A= metal and adsorbate at ground state; $(M+A)^*$= antibonding state; $M+A^*$= adsorbate excited state; M^*+A= ground state metal excited only; M^-+A^+= excited ionic state, Menzel 1975).

excited state, during which no change in the position of the nucleus takes place. After this transition, the ion or neutral particle begins to move away from the surface.

2) As the particle moves away from the surface, a recapture process can occur whereby the excitation energy is transferred back into the solid and the particle is re-adsorbed into the ground state or another higher ground state. Ionic desorption will occur, if the particle has gained sufficient kinetic energy to surmount the surface binding energy. A neutral particle will be emitted if at this point, electrons from the substrate tunnel through to neutralise the holes created in the adsorbate.

The above ESD model, qualitatively explains all the experimental observations summarised in section 3.2.2. In the first stage of the ESD mechanism, dissociation cross-sections are comparable to gas phase cross-sections ($\sim 10^{-16}$ cm^2). The observation of smaller total desorption cross-sections may indicate that at the surfaces recapture and neutralisation processes are important. Dominant contributions of neutrals to the desorbed species also shows that, neutralisation without recapture may be important. The energy distribution of the desorbed ions can be understood as a reflection of the vibrational probability density distribution of the ground state at the ionic curve distorted by the recapture process. Different ground state curves will then lead to different peak energies.

In very simple quantitative terms the cross-section for desorption is given by

$$Q = Q_e P \qquad \ldots(3.5)$$

where Q_e is the gas phase dissociation cross-section and P is the escape probability.

The probability of escape P, is of the form $\exp(-\beta \tau_c)$ where τ_c is the critical time for desorption and in β is the mean stay time of the desorbing particle. But in practice the escape probability P is given by

$$P \simeq \exp (-c/M) \qquad ...(3.6)$$

where c is a constant for a given adsorbate environment and it includes the tunnelling probability, particle velocity and the repulsion potential. M is the mass of the desorbing particle.

Expression 3.6 effectively describes the isotope effect. A heavier isotope will have a smaller probability of desorption because it spends a longer period in the vicinity of the bonding region where it can be recaptured and re-neutralised. Hence the smaller desorption cross-section compared with a lighter isotope. This has been observed for O^{16} and O^{18} by Madey et. al. (1970).

An important part of the desorption mechanism is its competition with electronic de-excitation after the adsorbate complex has been excited. Desorption is favoured by very long life times of the order of 10^{-14} seconds. This compares with typical one electron excitation life times of 10^{-16} - 10^{-17} seconds. Therefore, it seems that states must have substantially long life times for desorption to proceed. Thus the Redhead, Menzel and Gomer model for ESD desorption appears to be quite satisfactory since it also successfully predicts the isotope effect. Brenig (1976) has developed a quantum mechanical treatment of the ionic ESD desorption problem which appears to predict some of the observations of the ESD

experiments including the isotope effect.

Knotek and Feibelman (1978, 1984) have put forward, quite a different desorption mechanism, involving creation of core holes and de-excitation via inter-atomic Auger transitions (see section 2.2.1.1). In a study of ESD from titanium dioxide they observed enhanced O^+ desorption when the electron energy approached the Ti(3p) and O(2s) core levels, which are not involved in the TiO_2 bonding. They postulated a mechanism whereby in a maximal valence ionic solid, such as TiO_2, (where the cation has ionic charge Ti^{4+} and the anion O^{2-}) a core hole can be created on either the anion or the cation, in the ensuing Auger cascade, O^{2-} will lose an electron into the hole, and in some cases two electrons will be emitted (double Auger process) transforming an O^{2-} ion to an O^+. The neighbouring unscreened positive Ti core and O^+ strongly repel due to Coulomb repulsion, leading to desorption of O^+. This sequence of events is illustrated in Fig. 3.3.

This ESD mechanism appears to be very important for all maximal valence compounds such as TiO_2, SiO_2, WO_3 and particularly Al_2O_3 which will be further discussed in sections 4.5 and 8.7.2. These compounds have been shown to be very unstable under electron beam bombardment and consequently display very high desorption yields. This desorption mechanism is also quite effective in the covalently bonded systems. Bellard (1980) has given a thorough review of ESD theories and experimental results of oxygen on tungsten surfaces.

3.3 Electron Stimulated Adsorption (ESA)

Electron stimulated adsorption is normally caused by gas phase dissociation or excitation of molecules in the vicinity of a surface. Interaction of

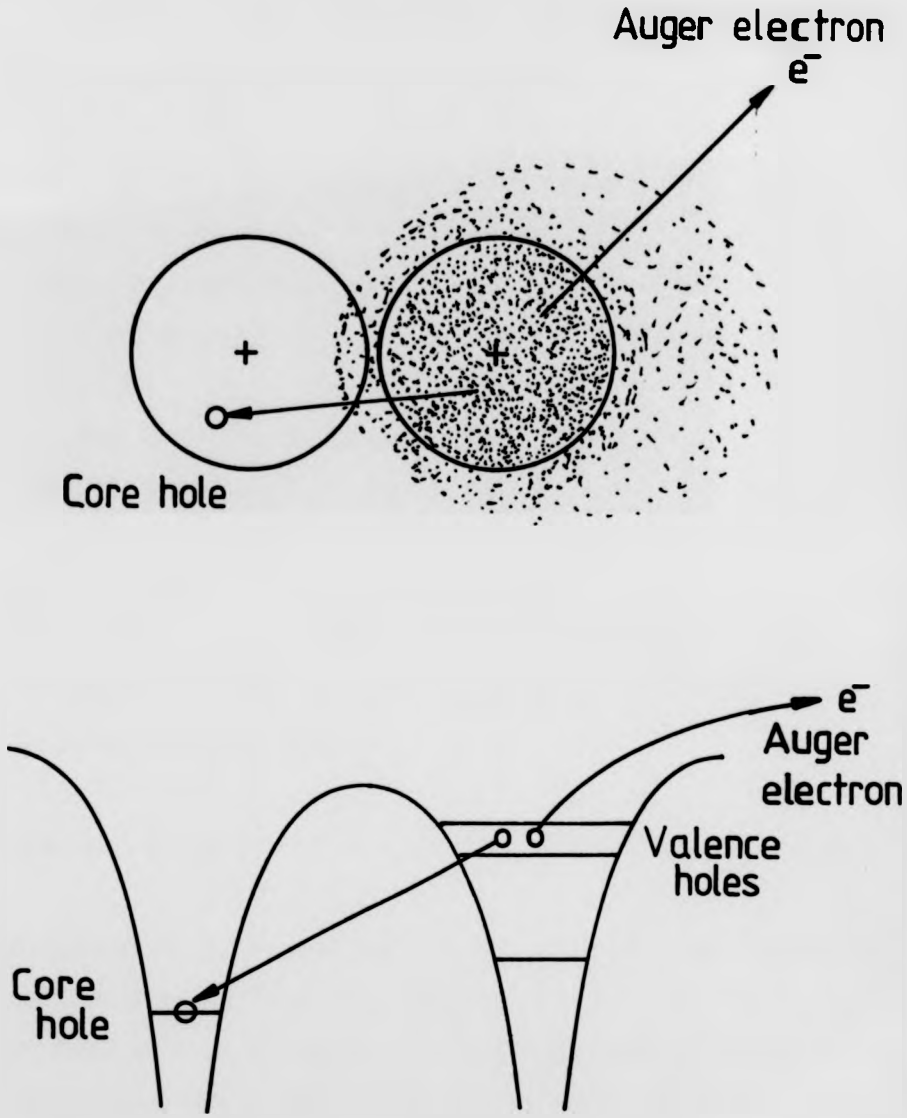

Fig. 3.3 Illustration of the inter-atomic Auger process in a maximal valence ionic solid leading to Coulomb repulsion.

the excited species with surface atoms may lead to adsorption via a chemical reaction. This process is particularly enhanced when the surface is exposed to simultaneous electron and gas exposure.

Clean metal surfaces almost always become contaminated by adsorption of residual gases. In the absence of irradiation this process may be absent or very slow. But when the surface is irradiated with electrons, enhanced adsorption of oxygen may be noticed. This has been interpreted as arising from residual CO. In oil pumped vacuum systems, C deposition with irradiation has been attributed entirely to hydrocarbons. Kirby and Lichtman (1974) have suggested a model for the ESA mechanism associated with CO and O_2 on Si system. The molecular species that have adsorbed under the electron beam will dissociate, one of the species desorbs while the other may diffuse or chemically react with the substrate atoms. For example O from CO, O_2 or CO_2. Further discussion of ESD and ESA from O on Al will be given in chapters 4 and 8.

3.4 Electron Beam Damage Thresholds for ESD of Monolayer Covered Surfaces

From the foregoing, it is clear that ESD and ESA result from electronic excitations of atomic and molecular species at the surfaces. For a metal surface with monolayer or sub-monolayer coverage of adsorbate, reduction in the concentration with irradiation time has been shown to be governed by equation 3.4 which is reproduced below.

$$X(t)/X(0) = \exp -[\ (I_e/A\varepsilon)\ Q\ t\ ] \qquad \ldots(3.7)$$

where X(t) is the Auger peak-peak height proportional to the concentration of atomic or molecular species on the surface at time t, X(0) is the Auger peak-peak height proportional to the initial undamaged concentration of

same species, I_e is the irradiation current, A is the irradiated area, Q is an effective cross-section for the electron stimulated decrease in the ratio of X(t)/X(0) and ε is the electronic charge.

Since in the case of AES, a 10% change in the monolayer concentration of an adsorbant can easily be detected a critical or threshold dose D_c can be estimated to cause such a change. Electron dose D is the product of electron current density and irradiation time i.e.

$$D = J\ t \qquad \ldots(3.8)$$

Thus from equation 3.7 D_c can be estimated to cause a 10% detectable change in the concentration of some species is given by

$$D_c = J\ t = (I_e/A)\ t = 0.11\ \varepsilon/Q \qquad \ldots(3.9)$$

The critical dose D_c is therefore inversely proportional to the effective desorption cross-section Q.

Since dissociative ionisation cross-sections of adsorbed species lie in the range 10^{-16} to 10^{-23} cm^2, the D_c is then 10^{-4} to 10^{3} C/cm^2. For typical electron beam parameters of current 5 μA and beam diameter of 0.05 cm will yield detectable damage to the monolayer adsorbate within $4x10^{-2}$ to $4x10^{5}$ seconds if all excitations lead to desorption. Typical cross-section for O_2 on a metal would be ~ 10^{-19} cm^2 which would give a critical time of 40 seconds for same beam parameters.

3.4.1 Electron Beam Damage Threshold for ESD and EBID of Multi-molecular Layers and Thin Films

In the case of samples where the surface is made up of multi-adsorbate layers, say for example oxide layers the effective ESD cross-section must be normalised by the number of mono-atomic or molecular layers. The over all information depth in AES, is approximately three times the mean free path length λ_e for the kinetic energy of the Auger electrons employed in the AES analysis (see section 2.2.1.3 on the escape depth of Auger electrons). The number of layers n is given by $3\lambda_e/a$ where a is the molecular dimension. Thus the effective cross-section in equations 3.7 and 3.9 is replaced by $Q' = Q/n$. Therefore the electron dose necessary to produce detectable damage is given by

$$D' = 0.11\ n\varepsilon/Q \qquad \ldots(3.10)$$

In the derivation of the threshold expressions the following assumptions were made:

i) That the intensity of the electron beam is uniform throughout the irradiated area.

ii) The cross-sections to be used in equations 3.9 and 3.10 are different for different materials and same adsorbates in different states.

iii) The cross-sections are also primary electron energy dependent. This is further complicated by the incident and backscattered primary electrons. The role of the secondary electrons in ESD will be discussed next.

3.5 Role of Secondary Electron Emission in ESD

The effect of secondary electrons, liberated by the impacting mono-energetic primary electrons, on ESD of monolayer or multilayer

3.5 Role of Secondary Electron Emission in ESD

The effect of secondary electrons, liberated by the impacting mono-energetic primary electrons, on ESD of monolayer or multilayer adsorbate covered surfaces, is expected to be in some cases as important as the primary beam itself. the general energy distribution of secondary electrons, was shown and briefly discussed in section 2.2 and will be further discussed in chapter 5. The ratio of the total number of electrons making up the this distribution, divided by the number of incident primaries defines the total secondary electron yield σ.

The true secondary electrons, making up the slow energy distribution curve EDC, contribute up to 60-70% of the secondary electrons to σ. The energy of these slow secondaries fall in the range 0-50 eV. The general shape of the EDC is independent of the primary electron energy and its maximum occurs at several electron volts above the vacuum level with a half width of $<$ 10 eV. Since the ESD threshold energies occur around 10 eV, a substantial number of slow secondary electrons will cause electronic excitations which may lead to desorption or decomposition. Another fact is that slow secondary electrons originate from the top surface layers of materials and the intensity of emission is a property of the surface. Inelastically backscattered primaries also are very efficient in the production of slow secondaries. For metals, oxidation of the clean surfaces generally leads to an enhancement of slow secondary electron emission particularly from fully oxidised metal surfaces.

In addition the secondary electron yield varies with angle of incidence of the primary beam (yield increases for glancing incidence), nature of the surface and type of material. It is not surprising that when comparison of energy dependence of gas phase dissociation cross-sections and ESD

3.6 Summary and Conclusions

Electron bombardment of gas adsorbed or clean metal surfaces, induces changes in the physical and chemical nature of the surface. The most common effects are electron stimulated desorption and decomposition of neutral ionic and excited neutral species. The most satisfactory qualitative explanation for the ESD processes was proposed by Redhead, Menzel and Gomer. As a result of direct interaction between the impacting electron and adsorbed atom or molecule, the system is raised to an anti-bonding state through a Frank-Condon transition with ensuing dissociation process giving rise to desorption of species.

An alternative mechanism particularly applicable to maximal valence ionic compounds proposed by Knotek and Feibelman, begins with ionisation of the core levels. In the resulting interatomic and intra-atomic Auger processes, the two neighbouring positive cores strongly repel leading to desorption of ionic or neutral adsorbates. Quantitatively, Redhead, Menzel and Gomer theory predicts the experimentally observed isotope effect and desorption cross-sections which vary in the range 10^{-16} and 10^{-22} cm^2. A knowledge of ESD cross-sections enables estimates of electron beam doses to be made, so that undesirable beam effects in AES can be reduced by use of appropriate beam parameters. The energy dependence of the ESD cross-sections is complicated by secondary electron emission.

In the next chapter a review of experimental AES and beam effect studies on clean and oxygen adsorbed aluminium surfaces will be given.

CHAPTER FOUR

(PART I)

Adsorption of Oxygen on Aluminium and Electron Beam Effects: A Review of Experimental Work

4.1 Introduction

There have been a large number of studies of initial oxygen adsorption at polycrystalline and low index crystal surfaces of aluminium by AES, LEED, XPS, Work Function, ELS, and ESD. In the first part of this chapter, these experimental studies will be reviewed to serve as a background to the work presented in chapters 8 and 9.

The second part of this chapter has been devoted to the review of electron beam effects at oxygen exposed aluminium surfaces studied by AES and ESD. Clean and oxygen covered aluminium surfaces, have received little attention in this area. Most of the work has concentrated on highlighting the apparent damage sustained by the surface under electron beam bombardment during acquisition of Auger electron spectra.

Electron stimulated adsorption of CO_2 and CO on aluminium surfaces will also be reviewed.

4.2 Adsorption Studies

4.2.1 Oxygen on Al(111), Al(110), and Al(100) Studied by AES, XPS, LEED and other Surface Analysis Techniques

Almost all the papers reviewed, dealing with experimental results, of adsorption on clean aluminium surfaces reveal undesirable inconsistencies. This largely arises from the differing experimental conditions and techniques used. In particular, sample preparation methods tend to change the surface to such an extent, that no two experiments will yield the same result. The method and pressure of oxygen exposure and scheme of UHV pumping in the analysis chamber, seem to influence the results and consequently lead to misinterpretation and widely differing conclusions.

One of the most common surface cleaning method employed in these experiments was by mechanical polishing with a series of progressively smaller alumina particles or fine grade diomond pastes, followed by chemical electrolytic etching. Once in the UHV system, the sample would be subjected to a series of argon ion sputtering and annealing cycles. In the case of single crystals, surface order would be confirmed by LEED and contaminants detected by AES or ELS.

There have been numerous investigations of low pressure, initial oxidation of **clean** aluminium surfaces at room temperatures involving various surface analysis techniques. The earliest experiments, were carried out by Jona (1967), Bedair, Hofmann, and Smith (1968), and Bedair and Smith (1971), who had used LEED to investigate the interaction of oxygen with the three low index faces of Al. They reported similar findings in that, the well defined LEED patterns gradually disappeared without formation of any new patterns upon exposure to oxygen. From these results they suggested that all three faces of aluminium behave in a similar fashion and immediately form amorphous oxide layers.

However preliminary AES and UPS measurements by Martinson, Petersson, Flodstrom and Hagstrom (1976), of oxygen interaction with Al(100), (110),

and (111) faces, was shown significant differences between the faces. Shortly after, an independent study by Gartland (1977) took advantage of the work function dependence on the crystal orientation, to measure the variation in the work function by a photo-electric method, with oxygen exposure of the three faces of Al. From the subsequent variations in Φ and additional AES measurements, Gartland also reported differences in the initial oxidation of the three faces and suggested that oxygen chemisorbed randomly on Al(111) but formed Al_2O_3 islands on the (100) face.

Photo-emission studies (with a tunable photon source from a synchrotron radiation source) of the Al(2p) core level and valence band region of the oxygen exposed three low index faces of aluminium by Flodstrom and Bachrach et al (1977), confirmed the anisotropies observed by Martinson et al and Gartland. Flodstrom and Bachrach et al have further concluded amorphous oxide forms directly on the (100) and (110) faces while there is a two stage process, one of chemisorption, followed by bulk-like oxide formation on the (111) face. The oxidation of the (111) face was also studied by Bradshaw, Hofmann and Wyrobisch (1977), this time employing XPS, AES, $\Delta\Phi$ (work function change measured by a contact potential method), ellipsometry and ELS techniques.

These authors have reported results supporting the two stage process of oxygen interaction at the Al(111) face. (The reported work function measurements of Gartland, and Bradshaw et al for the Al(111) surface are contradictory and these will further be reviewed in section 4.2.4). Eberhardt and Kunz (1978) have used synchrotron radiation to follow the changes in the Al(2p) and the valence band region of the (100) and (110) faces and interpreted their results, in terms of the oxygen penetrating the surface.

In an attempt to get a further insight into the mechanics of oxygen interaction with single crystal surfaces of Al, Martinson and Flodstrom (1979), have carried out further investigations, employing, LEED, AES and XPS techniques. They have used high purity Al single crystals of (100), (110) and (111) orientation. AES and LEED measurements were made by a 4-grid commercial LEED system and the XPS measurements by a commercial ESCA photo-electron spectrometer equipped with an Al K_α x-ray source (energy $\simeq$ 1486.5 eV). Martinson and Flodstrom kept the primary electron beam current to 2 μA at 2 keV and rastered over the analysis area, in order to minimise the electron beam effects.

The LEED measurements were made manually by varying the energy of the normally incident electron beam in the range 45 - 300 eV. A spot photo-meter of angular resolution $\sim 0.5^\circ$, was used to measure the intensity of the LEED patterns. The AES and XPS results of Martinson and Flodstrom have been reproduced in Fig. 4.1. Fig. 4.1(a) shows the normalised variation of the O_{KLL} (508 eV) Auger peak-peak height (PPH) with oxygen exposure for the three faces of Al. Fig. 4.1(b) shows the normalised variation in the O(1s) photoelectron peak (BE $\simeq$ 531 eV) intensity with oxygen exposure up to 600 L (1 L = 10^{-6} torr second).

In addition to the O_{KLL} Auger peak, Martinson and Flodstrom also identified the Al_{KLL} (1396 eV) and Al_{LVV} (67 eV) Auger transitions in the AES spectra, but preferred to use the O_{KLL} Auger PPH to represent the changes, because they did not observe any shift in energy or change in peak shape during the adsorption. A monolayer coverage was assumed to form when the Auger PPH of the O_{KLL} transition reached 90 % of its maximum amplitude corresponding to oxygen exposures $>$ 500 L.

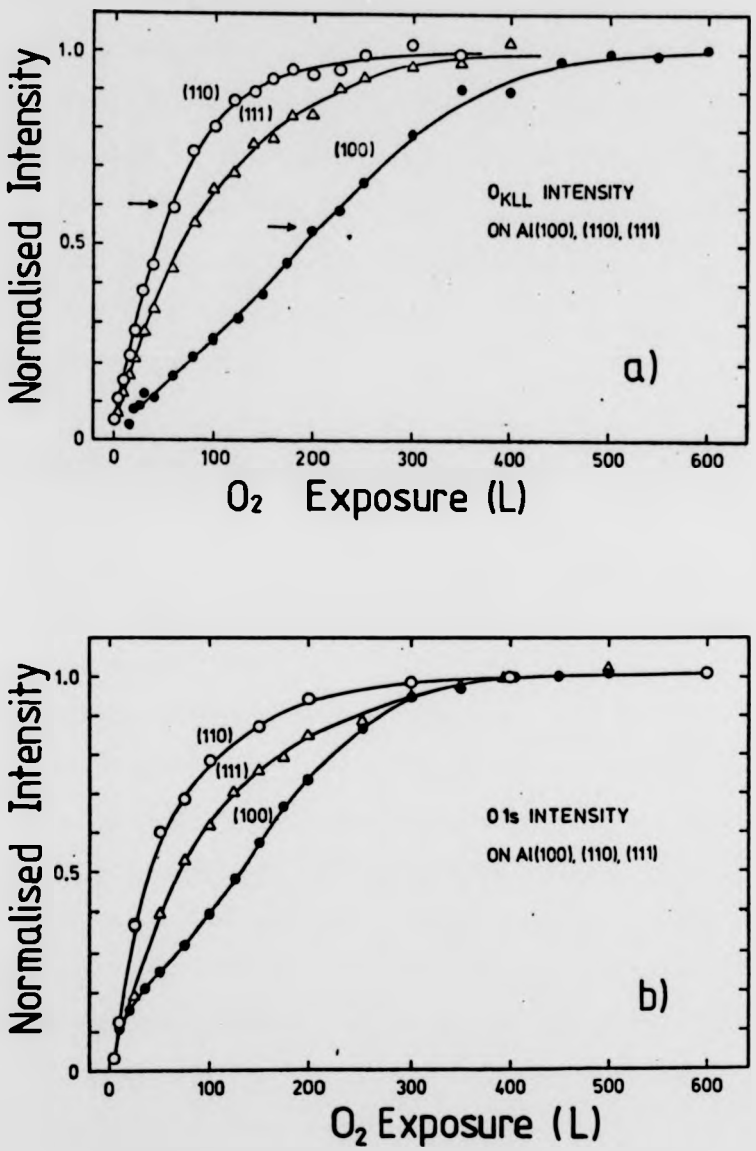

Fig. 4.1 Adsorption profile of the Al(100), (110) and (111) crystal faces.
(a) O_{KLL} Auger intensity versus oxygen exposure.
(b) O(1s) photo-electron peak intensity versus oxygen exposure.
(reproduced from Martinson and Flodstrom 1979)

It is apparent from Figs. 4.1(a,b) that the adsorption profiles for the (110 and (111) faces are similar, with the (100) face displaying striking differences in the oxidation rates. The oxygen uptake of by the (110) and (111) surfaces is quite fast with a sharp rise in the O_{KLL} intensity reaching monolayer (ML) coverage at 180 L and 270 L of oxygen exposure respectively. In contrast, for the (100) face the O_{KLL} peak increases linearly with oxygen exposure up to 0.75 monolayer coverage, there after gradually saturating after 400 L of exposure which corresponds to 1 ML coverage for this surface.

The adsorption profiles, obtained using the Al_{LVV} Auger PPH and XPS photoelectron peak heights are more or less identical to AES O_{KLL} profiles. This according to Martinson and Flodstrom, indicated that electron beam effects were negligible and did not introduce any noticeable errors. (Samples irradiated with soft x-rays show desorption effects to a lesser extent than electron beam irradiated samples.)

Simultaneous LEED observations by Martinson and Flodstrom of the (100) and (110) faces with oxygen exposure, showed that the distinct LEED patterns corresponding to clean surfaces, gradually faded, up to 0.5 and 0.6 ML coverage, and disappeared thereafter. For further exposures exceeding 1000 L, no LEED patterns developed. The (111) face on the other hand preserved the original LEED pattern until almost ML coverage. After 1000 L of oxygen exposure, the ML LEED pattern completely faded.

Martinson and Flodstrom also add that by heating the substrate at 250 $^{\bullet}C$ for 8 hours, **monolayer** LEED pattern transforms to that of the clean (111) crystal face without any loss in the Auger O_{KLL} PPH intensity.

From the above description of results reported by the previous authors, Martinson and Flodstrom conclude that the oxidation of the Al(111) face proceeds in two stages. First, chemisorption is in three fold hollow sites, forming an ordered overlayer with (1X1) symmetry at approximately monolayer coverage. This conclusion was reached with reference to the relatively high surface packing density of the Al(111) face (1.42×10^{19} atoms m^{-2}) which will effectively prevent the penetration of the adsorbed oxygen atoms into the sub-surface layers. Sticking coefficient measurements also confirm this.

Photoemission spectra of the Al(2p) photoelectron peak was observed by Flodstrom and Bachrach et al, and Flodstrom and Martinson et al (1978), to shift to a higher binding energy by 1.4 eV which corresponded to a precursor state and upon further oxygen exposure, the Al(2p) photoelectron peak position shifted to an even higher binding energy by 2.6 eV which marked the completion of the second stage of the adsorption process by formation of an amorphous aluminium oxide layer.

For the (110) crystal face, Martinson and Flodstrom suggested a similar two-stage process as proposed for the Al(111) face. This suggestion is a reasonable one since the Al(110) face has a low packing density, and the first two aluminium layers make up the surface which is very much like the (111) face. Another possible mechanism for the oxidation of the (110) face suggested by Martinson and Flodstrom, is by immediate formation of an oxide layer by a process in which oxygen atoms adsorb randomly on the (110) surface forming Al_2O_3 molecules. In the photoemission results reported by Flodstrom and Bachrach et al and Eberhardt and Kunz, the precursor state is absent showing a direct chemical shift by 2.6 eV to the higher binding energy oxidation peak. But Eberhardt and Kunz in the same study do detect a slight 1.4 eV shift of the Al(2p) photoelectron peak. Use of a higher

resolution spectrometer possibly employing monochromation may show that some chemisorption does take place.

For the Al(100) face, Martinson and Flodstrom suggested two possible mechanisms to explain the interaction of oxygen with this surface. The first is by a diffusion process, where an appreciable number of oxygen atoms diffuse into the bulk via the loosely packed (100) surface leaving a clean surface until diffusion slows down or stops. This mechanism is supported by the almost constant sticking coefficient, which indicates the creation of new adsorption sites that continue until 0.75 ML coverage.

The second mechanism is by island oxidation, based on the ideas of Blakely (1973). Here a site on the surface acts as a nucleation centre, and for further oxidation, the sites around the circumference of the oxide island act as active sites. As growth of the islands proceed, new sites for oxidation are produced.

More recent LEED experiments performed by Payling and Ramsey (1980), and Yu, Munoz and Soria (1980), confirm the observation by Martinson and Flodstrom (1979), that oxygen atoms chemisorb on the Al(111) surface at low exposures and form a p(1×1) overlayer on the metal surface. From these LEED experiments the chemisorbed oxygen overlayer-substrate distances have been estimated and compared with the theoretical calculations and simulations of Lang and Williams (1975, 1978), who used an adatom-jellium model, molecular cluster calculations of Salahub, Roche and Messner (1978), and Wang, Freeman and Krakuer (1981) who have used a recently developed selfconsistent linearised augmented plane wave (LAPW) electronic band structure calculations, have shown reasonable agreement. On the other hand, measurements and calculations based on recent experiments done with photoemission and surface-EXAFS (extended x-ray absorption and fine

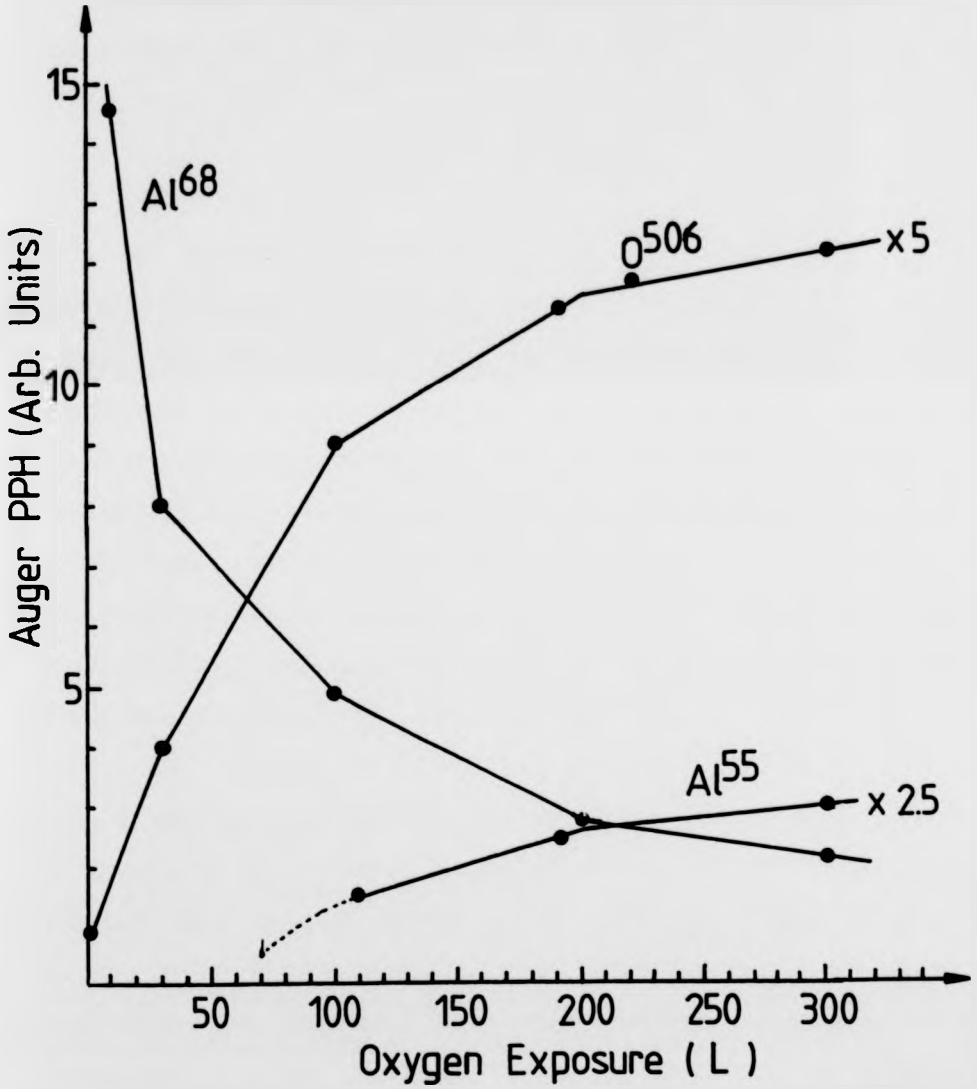

Fig. 4.2 Al^{68}, Al-O^{55} and O^{506} PPH intensities versus oxygen exposure for the Al(111) face (reproduced from Soria et al 1981).

structure) on the Al(111) face do not agree with LEED measurements.

EXAFS results reported by Johanson and Stohr (1979), Stohr and Johanson et al (1979, 1980) and Norman and Brennan et al (1980) give an oxygen chemisorption bond length of half that obtained by the LEED workers cited above.

Soria and Martinez et al (1981), reported results of AES, ELS and LEED experiments on the initial stages of oxidation of Al(111) surfaces and claimed to have resolved the discrepancy between LEED and EXAFS measurements of the interplanar separation between the chemisorbed oxygen overlayer and aluminium substrate. Soria et al have attributed some of the experimental inconsistencies to the preparation of the samples prior to analysis and preferred to use vapour deposited Al(111) on air cleaved mica in an UHV environment. This way they have produced a clean sample surface which gave an O_{KLL} PPH equivalent to .05 - .07 ML coverage which was rather better than that of Martinson and Flodstrom.

Soria et al, monitored the interaction of oxygen with the Al(111) surface by recording Al $L_{23}V_0V_0$ (55 eV) cross transition, Al $L_{23}VV$ (67 eV) and O_{KLL} (506 eV) Auger PPH and ELS spectra for E_p = 72 eV. A plot of the PPH intensities of the Auger signals versus oxygen exposure is reproduced in Fig. 4.2. This indicates a four stage adsorption process with clearly distinguishable breaks in the adsorption profiles. The four adsorption stages can be identified as 0 - 30 L, 30 - 100 L, 100 - 200 L and 200 - 1000 L.

During the 0-30 L exposure stage 0.3 ML coverage forms. The elemental Al_{LVV} 67 eV Auger PPH intensity is very sensitive to oxygen exposure and is

strongly attenuated. According to Soria et al, this reflects variations in the surface structure of the valence band and is not explainable by quantitative AES. Soria et al, arrived at the same conclusions about the oxidation processes occuring on the surface of the Al(111) face. His experimental data and calculations of self deconvoluted $L_{2,3}VV$ Auger transition density of states (TDOS) and theoretically calculated DOS for this stage of the adsorption, point to oxygen atoms occupying a threefold fcc hollows in underlayer configuration. This occurs before the onset of the chemisorption p(1x1) overlayer observed by LEED, which occurs during next stage of the adsorption i.e. 30 - 100 L.

In the 100 to 200 L adsorption stage the Al $L_{2,3}V_0V_0$ 55 eV Auger cross transition PPH grows in intensity and the oxygen (1x1) overlayer interplanar separation slightly increases. In the 200 to 1000 L stage, the Al $L_{2,3}VV$ 67 eV peak disappears and the O_{KLL} and Al $L_{2,3}V_0V_0$ 55 eV peaks, reach saturation indicating the formation of bulk like (Al_2O_3) amorphous oxide.

4.2.2 Oxygen Adsorption at Polycrystalline Aluminium Surfaces Studied by AES and Other Techniques

Polycrystalline aluminium samples have been used to a smaller extent than single crystals in the study of oxygen adsorption with these surfaces. This partly follows from the fact that apparatus employing the LEED technique could not be used to perform LEED on these samples. Also any explanation of observed phenomena would be complicated by the nature of the surface which would have been assumed to have a random distribution of the three low index faceted grains in the area of investigation.

Clean polycrystalline samples of aluminium can easily be prepared by evaporation in UHV environments, and these have been widely used in ELS studies of oxygen interaction with thin films of aluminium reviewed in the next section.

Kobayashi, Shiraki and Katayama, (1978) studied the initial oxidation of freshly evaporated polycrystalline films on silicon substrates by AES. They recorded AES window spectra of O_{KLL} and Al_{LVV} Auger transitions and particularly they monitored the appearence of interatomic cross transitions of Al $L_{2,3}V_0V_0$. These were recorded in the $dN(E)/dE$ and $-d^2N(E)/dE^2$ modes using a CMA the latter mode enhanced the sensitivity of the less prominent structures appearing on or near the main LVV Auger peak. Their AES adsorption profiles, are similar to those of Gartland, Martinson and Flodstrom (1979) corresponding to Al (111) face as already reviewed. Kobayashi et al checked the surface with reflection electron diffraction and confirmed that the polycrystalline grains normal to the surface were oriented along the [111] direction. These authors also proposed the two stage process for the oxidation of the surface, consisting of chemisorption, followed by oxidation.

Bujor, Larson and Poppa (1982) also investigated the initial oxidation of thin films of aluminium using AES, ELS and ESD. In their AES measurements they monitored the O_{KLL}, Al $L_{2,3}VV$ Auger and Al $L_{2,3}V_0V_0$ cross transition peaks with oxygen exposure. The plot of these peaks versus exposure is again very similar to the results of Kobayashi et al. The chemisorption stage appears to be completed after 50 L of oxygen exposure, followed by rapid growth of the oxidised aluminium cross transition signal marking the formation of Al_2O_3. After 3000 L of oxygen exposure, some elemental Al signal could still be detected.

Fontaine and Lee-Deacon et al had used a scanning electron microscope to identify (111) and (100) oriented facets of polycrystalline grains. The electron beam was then aimed on to these for recording AES spectra. According to Fontaine and Lee-Deacon et al, the adsorption profiles for the two faces of Al were similar to the findings of Martinson and Flodstrom.

4.2.3 Oxygen Adsorption at Aluminium Surfaces by ELS Studies

Electron loss features of clean and oxidised polycrystalline aluminium surfaces had been thoroughly investigated by Powell and Swan, (1959, 1960). They interpreted the loss features, as being due to the collective excitation of the conduction electrons and assigned the 15.3 eV and 10.3 eV loss peaks to the excitation of bulk and surface plasmons respectively. Upon exposure of the surface to oxygen, Powell and Swan observed the diminishing of the 10.3 and 15.3 eV surface and bulk plasmon peaks and appearence of two new peaks at 7.1 and 22.2 eV. The 7.1 eV peak was interpreted by them to be a modified surface plasmon of aluminium due to its surface oxide and the more prominent 22.2 eV peak as due to a modification of the bulk plasmon peak for similar reasons.

Similar results had been reported by a number of authors among them Suleman and Pattinson (1971), Pattinson and Harris (1972), and Wright and Pattinson (1974).

The tentative explanation of Powell and Swan for the 7.1 eV peak was deemed unsatisfactory in the light of the well known fact that ELS also provides information about single electron transitions from their ground states to some empty states or bands above the Fermi level. Careful study of the initial density of states just below the Fermi level for oxygen adsorption on silicon surfaces had been carried out by Ibach and Rowe (1974a, b) using

UPS and ELS. Newly observed energy losses were interpreted by them as due to transitions from occupied energy levels of oxygen to unoccupied energy levels below the conduction band.

By application of the dielectric theory Ibach and Rowe have predicted a shift or a split in the clean surface plasmon loss peak, when the theoretical, one electron transition energy is nearly the same as the surface plasmon energy. Photoemission and UPS studies by Yue et al (1976) and Flodstrom and Petersson et al (1976) of the valence band structure of aluminium have reported a maximum in the density of states at 7.1 eV after adsorption of 100 L of oxygen onto a clean polycrystalline aluminium surface. They assigned this peak to an O(2p) resonance level of chemisorbed oxygen. Subsequently the 7.1 eV loss peak observed by Powell and Swan has been attributed to a single electron excitation from the O(2p) level of oxygen to an empty state near the Fermi level of aluminium.

Benndorf and Keller et al, (1977) have carried out ELS investigations of oxygen interaction with freshly evaporated aluminium films. They recorded ELS spectra directly in the N(E) and dN(E)/dE modes with excitation energies above 250 eV. Oxygen uptake by the fresh films was monitored by a quartz crystal micro balance with a monolayer sensitivity of 10^{-2}. For the clean surface, Benndorf et al have observed an ELS spectrum dominated by the surface and bulk plasmon loss peaks.

Like Powell and Swan the loss peak energies for the surface and bulk plasmons, occured at 10.3 and 15.4 eV respectively. Less intense losses with peak positions further from the elastically scattered primary electron peak, were attributed to multiple and combinations of the SP and BP losses.

For very low oxygen exposure levels of 0-2 L, the surface plasmon intensity decreased and appeared to be very sensitive to adsorbed oxygen. In fact this apparent sensitivity of the aluminium surface plasmon to low levels of oxygen exposure, led Le Gressus, (1981) to suggest that the ratio of the peak intensities of the surface to bulk plasmons for excitation by 250 eV electrons at normal incidence should be greater than one. This provides a better check for the absence of oxygen, from a supposedly clean surface than just measurement of the oxygen Auger PPH. Also at this early stage of oxygen exposure, Benndorf et al, have observed the emergence of the 7.3 eV loss peak, initially reported by Powell and Swan.

For further exposures up to 13 L, the intensity of the 7.3 eV loss peak grew while the 10.3 SP loss peak disappeared. A new loss peak at 19.2 eV was also observed with some overlap with the 15.4 eV BP loss peak. The progressive changes of the aluminium loss peaks with oxygen exposure of Benndorf et al has been reproduced in Fig. 4.3. For maximum oxygen exposures of 3800 L the 7.3 eV loss peak had almost disappeared and no SP or BP losses corresponding to the clean aluminium surface were discernable.

From the above results, Benndorf et al have interpreted the ELS spectrum of clean and slightly oxygen adsorbed Al surface, by the classical dielectric and plasmon loss theory, mainly developed by Pines (1963), Bohm and Pines (1953), Ferrel (1957), Watanabe (1962), and Ritchie (1957), and experimentally by Raether (1965, 1980).

The SP and BP losses are described by the imaginary components of the dielectric constant i.e. $-\mathrm{Im}(1/\varepsilon)$ and $-\mathrm{Im}(1/1+\varepsilon)$ respectively. The 7.3 eV loss feature, which increased in intensity with initial oxygen exposure but decreased for large exposures, has been attributed to a single electron transition from the O(2p) resonance level to an empty conduction band of

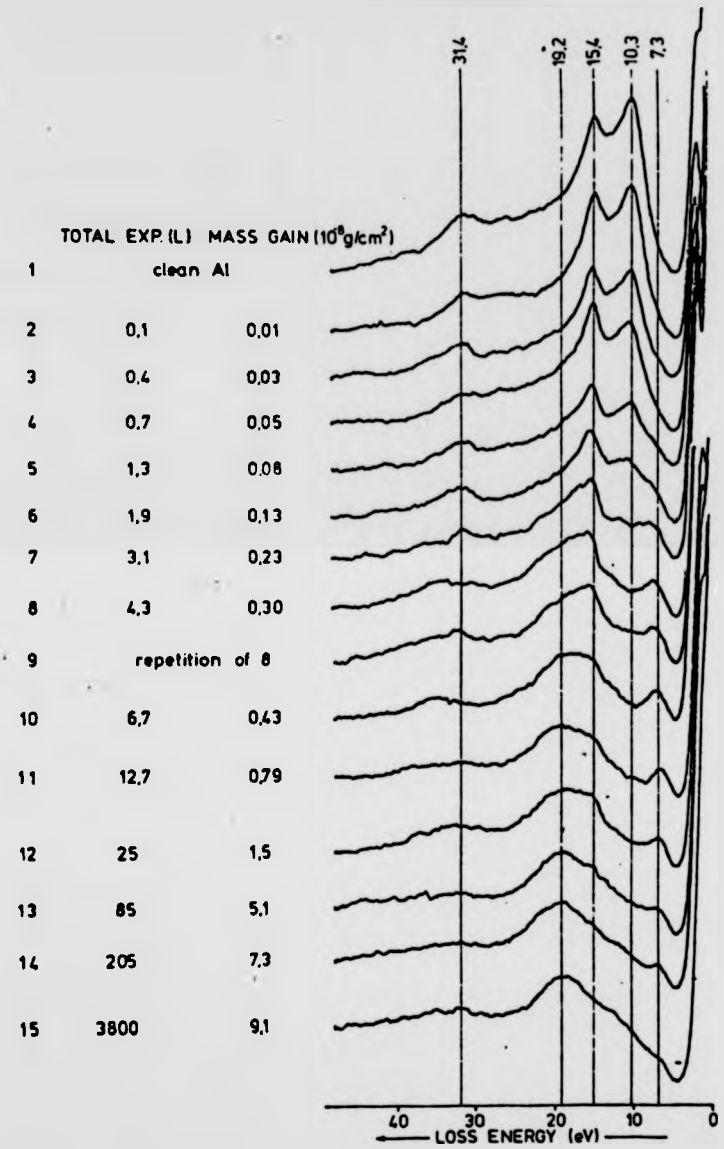

Fig. 4.3 Electron loss spectra N(E) of polycrystalline Al for different oxygen exposures. E_p = 250 eV (reproduced from Benndorf et al 1977).

aluminium from a consideration of results of Ibach and Rowe and Flodstrom and Petersson et al and Yue et al.

The 19.2 eV broad loss structure, which resulted from high oxygen exposure levels, was interpreted rather tentatively as due to interband transitions of amorphous Al_2O_3, as deduced from the electronic energy level schemes of Al_2O_3 devised by Balzarotti and Bianconi, (1976).

Bujor et al, (1982) have also studied the oxidation of in situ prepared aluminium films with ELS (E_p = 250 eV) in addition to ESD and AES and reported similar experimental results to Benndorf et al, except that the aluminium films of Bujor et al appeared to be less reactive to oxygen. Consequently the 7.0 eV loss peak attributed to an O(2p) transition to the empty Al conduction band was still detectable after 3000 L of oxygen exposure and similarly the 19 eV loss peak attributed to interband transition of Al_2O_3 was less intense.

The apparent reduction in sensitivity in the loss spectra, of the in situ prepared Al films, were most probably due to differences in the surface properties and residual gas contaminants in the UHV chamber.

Pellerin, Le Gressus and Massignon (1981a), used a mechanically polished polycrystalline aluminium sample, which was subjected to, cycles of sputter cleaning and annealing. In order to reduce the dominance of the loss spectra by the SP and BP peaks, they used primary electrons of energy in the range $30 < E_p < 250$ eV, to excite the surface and record ELS and SES (secondary electron spectroscopy) spectra in the EN(E) mode as a function of oxygen exposure as well as energy. Use of low primary electron energies below the plasmon excitation threshold turned out to be a fresh approach, which led Pellerin et al to report two previously unreported peaks in the

loss spectrum of clean and oxygen adsorbed Al surface. For the clean Al surface, this loss peak occured at 4.0 eV below the elastically scattered primary electron peak and did not shift in energy when the primary electron energy was varied. Also the intensity of the peak decreased and was extinguished after 100 L of exposure to oxygen.

Bachrach, Chadi and Bianconi (1978) have reported a 4.3 eV resonance above the Fermi level of clean (100) face of Al, from their UPS studies of the DOS of the valence band, and Surface-EXAFS studies of the DOS of the empty states above the Fermi level of Al. Pellerin et al had assumed that the surface of their original polycrystalline sample, due to cyclic ion bombardment and annealing treatments, had become primarily (100) oriented, and assigned the 4.0 eV loss peak as due to a transition between a surface state close to the Fermi level and the 4.3 eV resonance observed by Bachrach et al.

The other newly observed 12 eV loss peak by Pellerin et al for the oxygen exposed (3000-8000 L) Al surface, have been interpreted as due to a transition between the top of the valence band O(2p) photoemission peak 7.1 eV below the Fermi level, and the bottom of the conduction band (4.2 and 6.3 eV above the Fermi level of the oxide). Fig. 4.4 represents a schematic of the different loss peaks for clean and oxygen covered aluminium surface which has been reproduced from Pellerin et al (1981a). The 19.2 eV loss peak observed by Benndorf et al, and attributed to a bulk oxide (Al_2O_3) interband transition, was located to be at 21 eV by Pellerin et al, whose polycrystalline sample turned out to be less reactive compared to that of Benndorf et al.

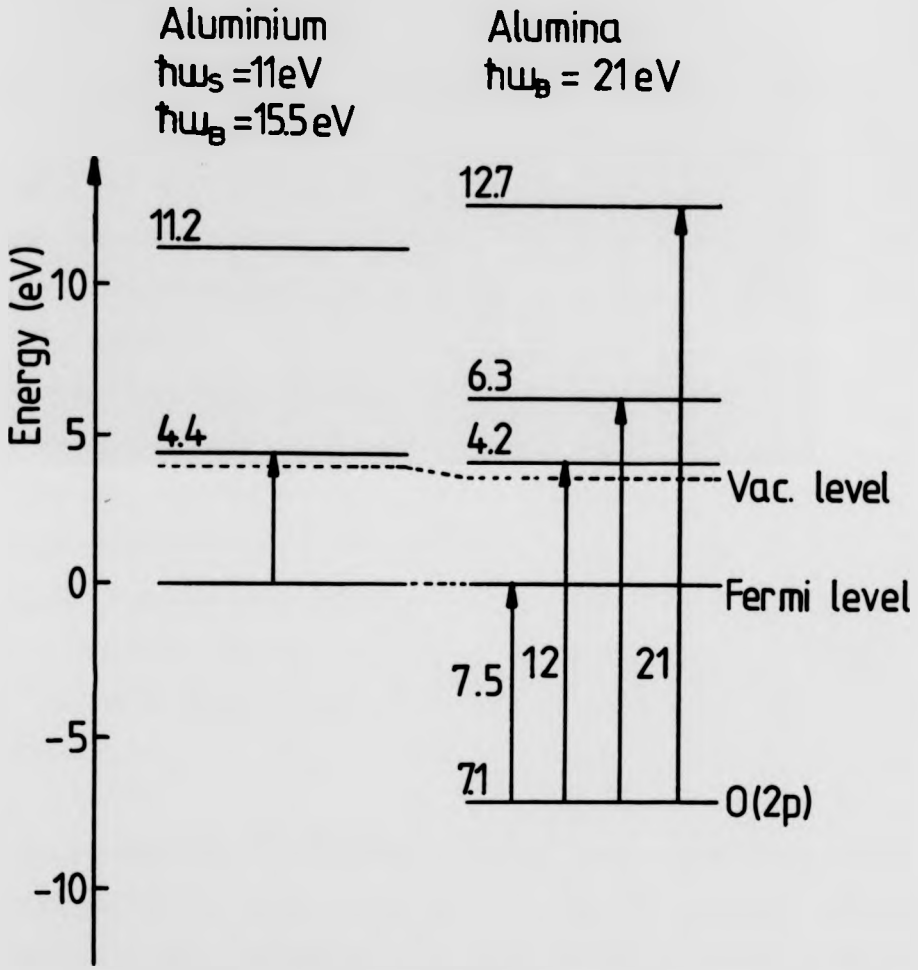

Fig. 4.4 Schematic diagram of the allocation of loss peaks observed on clean and oxygen covered aluminium surfaces (reproduced from Pellerin et al. 1981).

In the corrected i.e. N(E), spectra of clean aluminium, Pellerin et al observed some fine structure superimposed on a broad peak. These were located 6 eV and 11 eV with respect to the vacuum level (ϕ = 4.0 eV). Pillon and Ganachaud et al, (1977) and Everhart and Saeki et al (1976) who have used a 4-grid LEED, RFA to record their SES spectra and ELS spectra directly in the N(E) mode, and have reported, 6 and 11 eV structures in their slow SES spectra and have attributed them to plasmon decay into single electron excitation via inter band transitions. Therefore Pellerin et al, attributed their 6 and 11 ev peaks to a similar excitation mechanism. Upon full oxidation the 6 eV peak disappeared.

On the other hand for the uncorrected EN(E) SES spectra (for low electron energies transmission of the CMA gives a less intense slow secondary electron distribution), Pellerin et al observed two peaks at 8 and 20 eV which they have explained as being due to the scattering of electrons on the 2p and 2s oxygen induced orbitals i.e. at 23.6 and 7.1 eV below the Fermi level.

Of great importance to this work, are the results and interpretations thereof, of Pellerin et al on ELS and particularly SES spectra of aluminium in relation to the contribution of plasmons to secondary electron emission. This aspect will be further discussed in chapter 5.

In an attempt to shed further light on the true origin of the 4 eV loss peak, reported by Pellerin et al, Nall, Jette and Bargeron, (1981) have investigated the interaction of oxygen with a clean (111) oriented crystal of aluminium by ELS. Nall et al, under similar experimental conditions to as used by Pellerin et al recorded ELS spectra, using a CMA in the EN(E) mode, for primary electron energies in the range 20-50 eV.

The results of Nall et al, largely confirmed those of Pellerin et al and in addition they also reported , locating a 4 eV loss peak on the ELS spectrum of clean aluminium with one major difference. The 4 eV loss feature, was found to shift to higher energies by as much as 3 eV as a function of primary energy. Further surface-EXAFS experiments of Bachrach et al on the clean Al(111) face revealed no 4 eV surface resonance above the Fermi level but at 12 eV.

In light of this, the assignment by Pellerin et al, that the 4 eV loss peak was due to a transition between surface states, largely from the assumption that his polycrystalline Al sample, was predominantly (100) oriented, was shown by Nall et al to be false. Hence they have re-assigned the 4 eV peak as due to non-vertical direct inter and intra-band transitions of the bulk aluminium.

From the above review on ELS of Al surfaces it is clear that some of the processes leading to the observed loss peaks and features are far from clear and little understood. Further experiments in which analysers with higher absolute resolution with use of theoretical and computational techniques will be required to reduce the plasmon loss peak dominance of the ELS spectra.

Presented in Table 4.1 is a summary of the, observed loss peaks, and their assignment to date for clean and oxygen exposed aluminium surfaces.

4.2.4 Oxidation Studies by Mass Uptake and Work Function Measurements

Initial investigations of the oxidation processes on aluminium surfaces in the late sixties and early seventies, mainly consisted of mass uptake by quartz microbalance techniques and measurement of the changes in the work

Table 4.1 Summary of observed loss peaks and their allocation, on clean and oxygen exposed Al surfaces.

Primary energy (eV)	Nature of Al surface	Observed loss peak energies (eV)							Author
		4.0	7.0	10.0	12.0	15.1	19.4	22.0	
250<E<2000	clean poly film			SP		BP			1,2,3
250<E<2000	oxidised poly film		SP due oxide					BP due oxide	1,2,3
250<E<1000	clean poly film			SP		BP			4,5
250<E<1000	oxygen exp poly film		O(2p) reson				oxide inter band		4,5
30<E<250	clean poly sheet	surf state		SP		BP			6
30<E<250	oxygen exp poly sheet		O(2p) reson		O(2p) to CB			oxide inter band	6
20<E<50	clean(111) crystal	inter band		SP		BP			7
20<E<50	oxygen exp (111) crystal		O(2p) reson		O(2p) to CB			oxide inter band	7

1) Powell and Swan (1959,1960)
2) Suleman and Pattinson (1971)
3) Pattinson and Harris (1972)
4) Benndorf et al (1977)
5) Bujor et al (1982)
6) Pellerin et al (1981)
7) Nall et al (1981)

function or contact potentials.

Huber and Kirk, (1966, 1968), Roberts and Wells, (1969) and Dorey (1971) have all studied the initial stages of oxidation of evaporated polycrystalline films of aluminium at room temperatures using one or both of the above techniques with broadly similar results and interpretations.

Huber and Kirk reported a fast weight gain for initial interaction of oxygen with Al surface, until monolayer coverage after which no significant change in the weight gain occured. Simultaneously they measured contact potentials for the aluminium surface which indicated a sharp decrease of 0.05 ±.02 eV after which $\Delta\Phi$ increased, reaching a maximum for very long oxygen exposures. This have led Huber and Kirk to correctly suggest an adsorption process whereby a layer of chemisorbed oxygen atoms, is followed by oxidation and formation of alternating layers of aluminium-oxygen dipoles. The above interpretation appears to have been an accurate one, since more recent experiments, involving AES, XPS, LEED, EXAFS etc. appear to confirm this (see preceding section). The polycrystalline Al films were probably (111) or (110) oriented.

From the mass uptake versus exposure curve, they reported an initial sticking coefficient of 0.09 for the room temperature oxidation. Roberts and Wells (1969), have reported data which they believed to be at variance with Huber and Kirk's interpretation of the oxidation process. Roberts and Wells found the CPD changes on the Al surface to be reproducible at room temperatures except during the initial stages of oxygen interaction with the Al surface for which they observed a decrease of 0.05 eV in $\Delta\Phi$. For subsequent oxygen exposures the WF was observed to increase at times by 0.1 eV and then 0.6 eV. From these results Roberts and Wells have suggested that oxygen chemisorption was unstable and incorporation of chemisorbed

atoms into the substrate layers occur at a submonolayer coverage leaving sites for further chemisorption of oxygen.

This mechanism appears to be consistent with Martinson and Flodstrom's (1979) interpretation of their oxygen on Al(100) results obtained with AES, XPS and LEED. It is possible therefore that the films prepared by Roberts and Wells were predominantly (100) faceted.

Kruger and Pollack (1972) exclusively followed oxygen-aluminium reaction at room temperature, by the quartz crystal microbalance technique and examined the Al-Al_2O_3 surface by electron microscopy and scanning electron microscopy for surface roughness. Kruger and Pollack reported a two stage mass uptake by the surface. The weight of oxygen uptake, varied linearly with pressure (across the range $5x10^{-6}$ to $5x10^{-7}$ torr) and time and that over the above pressure range an abrupt change in the rate of uptake occurred. This they interpreted as a completion of a stable layer with an initial sticking coefficient of 0.03. Kruger and Pollack suggested an incorporation-chemisorption mechanism whereby initial incorporation by oxygen onto the second layer occured very quickly at 0.75 ML coverage, and in the second stage normal chemisorption occurs up to 1.5 ML coverage. There after the surface becomes non-reactive to further exposure and marks the formation of a stable oxide layer.

Dorey (1971), in a similar investigation to Huber and Kirk reported sticking coefficient values (10^{-1} - 10^{-3}) for clean, 0.5 ML and 1.0 ML covered Al surfaces at various temperatures in the range 110 K to 473 K and concluded that the initial adsorption of oxygen on aluminium at higher temperatures is thermally activated as confirmed by the high values of measured sticking coefficients.

More recent measurements of work function changes on Al surfaces characterised by AES, LEED and ELS was briefly mentioned in section 4.2.1. The change in the work function with oxygen exposure for the Al(111) surface reported by Bradshaw et al appears to be in variance with the photoelectric work function measurements of Gartland for the same surface Gartland reported no change until 20-30 L, and a rise of only 0.1 eV reaching saturation after 130 L of O_2 exposure as illustrated in Figs. 4.5(a,b).

Bradshaw et al reported a smooth fast decrease in $\Delta\Phi$ after 50 L of O_2 exposure. They have attributed the variance, to the sample preparation conditions and Φ measuring techniques. In order to reconcile these paradoxical Φ results, Hayden, Hachicha and Bradshaw (1980) repeated the $\Delta\Phi$ measurements for oxygen on Al(111), using both the Kelvin method and photoelectric method in the same apparatus and on the same crystal subjected to identical preparation conditions. For room temperature measurements, both methods yielded similar results; with $\Delta\Phi$ decreasing initially by 0.2 eV, and reaching a minimum at 30 L.

Between 30 L and 70 L $\Delta\Phi$ increased by 0.05 eV thereafter saturating. With the photoelectric method, the overall decrease was much smaller. But at other temperatures the two methods gave different results which tended to reflect the validity and definition of each measurement technique. Therefore it seems that work function measurements of O_2 on Al remains unresolved with the results depending on the method of measurement and preparation history of the sample.

4.2.5 Interaction of Carbon Monoxide and Hydrogen with Aluminium Surfaces at Room Temperatures

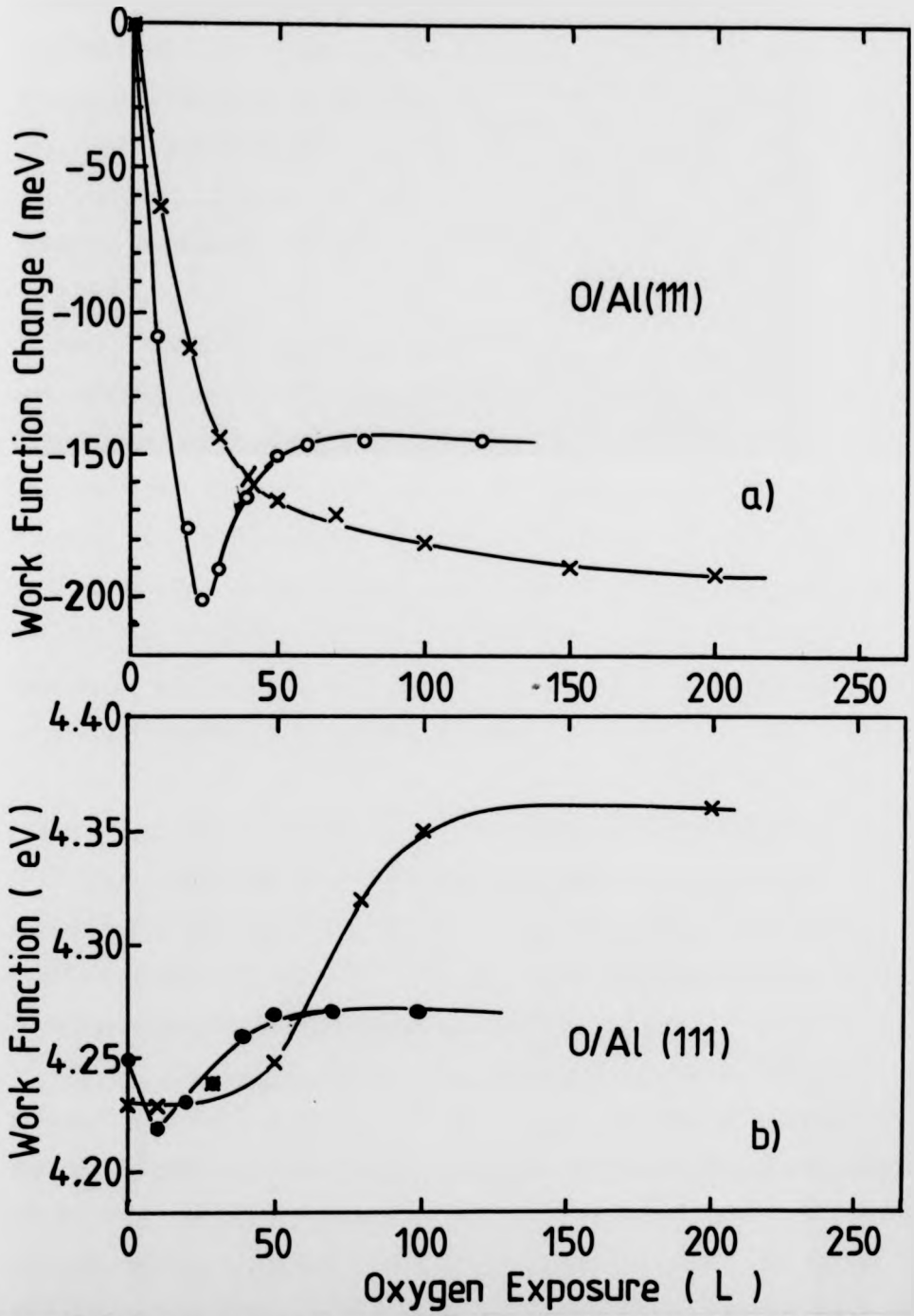

Fig. 4.5 (a) $\Delta\Phi$ versus oxygen exposure for the Al(111) surface. Crosses from Bradshaw et al 1977, circles from Hayden et al 1977.
(b) Φ versus oxygen exposure for the Al(111) surface. Crosses from Gartland 1977, full circles from Hayden et al 1980.

In comparison with oxidation studies there have been few studies of carbon monoxide and hydrogen on aluminium surfaces. These studies have been carried out at room temperatures on single crystal surfaces, polycrystalline, and on surfaces of evaporated films of Al using AES, ELS, XPS, LEED and WF techniques as in similar experiments to oxygen studies. The reported results have been rather conflicting but generally carbon monoxide and hydrogen appear not to adsorb on clean aluminium surfaces.

Shiraki, Kobayashi and Katayama (1978), Katayama et al (1979) and Pireaux and Ghisjen et al (1979), have all used AES with XPS to investigate the interaction of CO on in-situ evaporated films of aluminium. Shiraki et al and Kobayashi et al after only 720 L of CO exposure reported, significant changes in the interatomic cross transition signal of Al, O and C. For very high exposure (10^4 L) they showed that CO bonds stoichiometrically to Al and that Al_2O_3 type Al-O bonding precedes Al-C bonding. Shiraki et al, have ruled out residual oxygen adsorption or electron stimulated adsorption of O via dissociation of the CO molecules.

Pireaux and Ghisjen et al using XPS, observed CO adsorption after only 35 L. They showed the C(1s) photoelectron peak (of BE = 285 eV) to contain considerable loss structure but reported no such structure shifts in the O(1s) photoelectron peak (BE = 531 eV). These observations have led them to suggest that the C atoms are closer to the Al atoms.

Khonde, Darville and Gilles, (1981a) recorded AES and ELS spectra of CO exposed Al(100) surface. Their results indicated changes in the spectra after only 20 L of CO exposure. But their supposedly clean Al surface already contained, oxygen and carbon as revealed by AES. The changes in the intensity of the of the O_{KLL} and Al_{LVV} Auger PPHs remained small and after 100 L of CO exposure the Al_{LVV} PPH was still the dominant peak. In a

similar experiment but using a different Al(100) oriented sample, and use of additional techniques of LEED and WF measurements, Khonde et al (1981b) obtained different results. Compared with their previous study a 5 stage adsorption process was identified, along the course of exposure up to 10^5 L of CO. This time only carbon contamination was identified for the clean surface and the oxygen signal did not appear until 100 L of CO exposure.

Through the stages 2 and 3 ($\simeq 10^4$ L), the O_{KLL} and C_{KLL} Auger signals steadily increased while the Al_{LVV} signal decreased. By stage 5 (10^5 L) the C_{KLL} signal saturated and even began to decrease while the O_{KLL} signal continued to grow. The Al_{LVV} signal had completely disappeared. In addition Khonde et al mentioned the appearence of structures in the low energy Auger spectrum, corresponding to interatomic transitions and plasmon loss features of the Al $L_{2,3}VV$ Auger transition corroborating the work of Kobayashi et al.

ELS measurements for the clean surface, was similar to the previous results of authors described in section 4.2.2. For the first stage, the intensity of the surface and bulk plasmons were not modified. But the SP intensity decreased through stages 2 and 3 after which both the SP and BP loss peaks decreased drastically.

Khonde et al reported no particular LEED patterns and that the loss of contrast in the brightness was complete by 10^4 L of CO exposure. Work function changes determined by contact potential difference method as a function of CO exposure revealed no change in $\Delta\Phi$ until stage 2, where $\Delta\Phi$ decreased to a minimum of -0.120 eV, by stage 3, it was back at 0 and thereafter increased very rapidly with further exposure.

From the above results Khonde et al have suggested that the dissociation of CO, gave a progressive incorporation of oxygen and carbon with Al_2O_3 and Al-C (carbide) formation with reservations about the previous history of the samples.

More recently Bargeron and Nall, (1982) have recorded ELS spectra of CO exposed low index surfaces (100), (110), and (111) of Al and report essentially no changes in the ELS spectra for these faces. Bargeron and Nall using primary electron energies in the range $30<E_p<140$ eV, have shown that there is a very small decrease in the intensity of the SP after more than 10^4 L of CO exposure. They have attributed this small decrease to the sensitivity of this loss peak to adsorption of residual oxygen. Bargeron and Nall have repeated the experiments on polycrystalline and non-in-situ evaporated films of Al, with similar results and conclude that, no adsorption of CO on Al surfaces at room temperatures result.

The results of Bargeron and Nall appears to be in total contrast to the work of previous authors. But it seems likely that the CO adsorption observed by previous authors could have been due to electron beam effects (electron stimulated adsorption). Oxygen deposition could also have arisen from water vapour in the main chamber or CO gas admission manifolds. Electron beam effects at Al surfaces will be reviewed in the next section.

As far as adsorption of hydrogen on aluminium is concerned, no studies have been reported where extensive surface analysis techniques have been used except for Pellerin, Le Gressus and Massignon (1981b) who carried out ELS investigations on clean polycrystalline Al surfaces down to exposure pressures of 10^{-4} torr at room temperatures but report no modifications of the SP loss peaks. But alumina surfaces, did show some adsorption, only at 10^{-4} torr H_2. But upon pumping of the system chamber to UHV, the original

clean alumina ELS spectra was regained, indicating that hydrogen physisorbes only onto alumina surfaces.

4.3 Summary and Conclusions

The process of oxygen adsorption and oxidation of aluminium surfaces as gleaned from the results of AES, XPS, ELS, LEED and $\Delta\phi$ experiments appear to be rather complex and contradictory, largely due to experimental parameters and sample non-uniformities. On the (111) surfaces of Al, oxygen initially chemisorbs and forms a p(1×1) overlayer LEED pattern up to monolayer coverage (0-300 L). Upon heating to 550 °C the original LEED pattern is regained with no change in the oxygen concentration.

For further exposures, an amorphous oxide layer begins to form with oxygen being incorporated at a very slow rate. On the (100) and (110) surfaces of aluminium, oxygen incorporation is immediate, with formation of oxide islands. On the (100) face, oxygen penetrates the first couple layers of aluminium, resulting in new surface adsorption sites. No particular LEED patterns have been observed for these faces. With further oxygen exposure, an amorphous Al_2O_3 like oxide layer begins to grow on the surface.

Carbon monoxide and hydrogen have been observed not to adsorb on aluminium surfaces. Where adsorption has been observed, it may have been due to electron beam effects and the way the samples had been prepared. In the next section electron beam effects on clean and oxygen exposed aluminium surfaces will be reviewed.

CHAPTER FOUR

(PART II)

Electron Beam Effects on Clean and Oxygen Adsorbed Aluminium Surfaces: A Review of Literature

4.4 Introduction

A great deal of experimental work has been done on electron stimulated desorption (ESD) from many adsorbate-metal systems, in order to improve the understanding of adsorption-desorption phenomena caused by electron beam irradiation.

Clean and oxygen covered aluminium surfaces have received little attention in this area. Most of the work has concentrated on highlighting the apparent damage sustained by the surface under electron beam bombardment, during acquisition of Auger electron spectra.

In this section, adsorption, desorption decomposition and other electron beam induced phenomena at clean and oxygen exposed aluminium as well as alumina surfaces will be reviewed. This section will not be divided into subsections or the material reviewed in strict chronological order. Work dealing with electron beam enhanced adsorption of CO_2 and CO on aluminium surfaces will also be reviewed.

4.5 Electron Beam Effects Studied by AES

A number of workers have investigated a range of adsorbate-metal surfaces specifically to determine ESD yields and desorption cross-sections. Also

the extent of surface damage caused by the electron beam, during AES analysis. Drinkwine and Lichtman (1977) have reviewed this aspect and the area of ESD thoroughly. In these studies experimenters have noted the drastic changes in the peak position, shape and intensity of Auger signals, which indicated chemical and physical changes on the surface, directly induced by the electron beam. Studies were initiated to investigate the detrimental effects of electron bombardment, during qualitative and quantitative Auger electron spectroscopy.

Pantano and Madey (1981) have thoroughly reviewed the area of electron beam damage effects in AES and conclude that in general the electron beam, will induce adsorption (ESA), of carbon and oxygen on clean surfaces from the residual gases of O_2, H_2O, CO, and CO_2 present in the UHV chamber or desorbed from the chamber walls. The electronic processes leading to these phenomena have already been dealt with in chapter 3.

It will be seen later, that some of these (ESA) effects may be absent from clean aluminium surfaces. In the case of oxygen exposed metal surfaces, desorption of oxygen and decomposition of the oxide may result. Particularly prone to decomposition are the stable compounds of SiO_2, Al_2O_3, W_2O_3, TiO_2, V_2O_5 and other maximal valence ionic compounds. In particular the alkali-halides display very high desorption cross-sections and yields. Pantano and Madey report desorption cross sections of 10^{-16} cm^2 for weakly adsorbed species and halides, while 10^{-18} - 10^{-19} cm^2 for strongly bound species and stable compounds. The desorption mechanisms prevalent in these compounds have been described in chapter 3 together with experimental methods of analysing data and electron beam thresholds.

4.5.1 Decomposition from Aluminium Oxide Surfaces

In a specific investigation designed to verify the validity of some of the underlying assumptions in the interpretation of quantitative AES, Smith (1976) studied the decomposition of thin aluminium oxide films on aluminium substrates, by electron and ion beam bombardment using AES.

Smith used a coaxially mounted electron gun contained in a commercial CMA, to excite the oxide films with electron beams of energy 2-3 keV, at 63° to the sample normal, with sample to ground currents of 0.5 to 10 μA and beam diameter of 0.5 mm. The electron and ion beams were coincident on the same spot and a series of depth profiles were obtained with both beams maintained on, and in some cases with the ion beam off only. Smith recorded the O_{KLL}, Al_{KLL}, Al_{LVV} and C_{KLL} Auger transitions and Al $L_{2,3}V_0V_0$ cross transition

Smith reported a uniform removal of the oxide layer but after only a few minutes of etching and electron beam irradiation, well before the oxide-metal interface was reached, elemental $Al_{L2,3}VV$ 67 eV Auger signal grew in intensity and the O_{KLL} 515 eV had decreased, indicating that the sputtering and electron irradiation had decomposed the anodised Al film.

In order to confirm his suspicions Smith, recorded a series of spectra during which, the oxide film was first sputtered without electron bombardment and then electron beam switched on and time dependent Auger electron window spectra recorded overnight. Smith found that the O_{KLL} and Al LV_0V_0 Auger PPHs had decreased exponentially while the elemental aluminium PPH had increased to saturation. He obtained similar results from irradiation experiments on single crystal of aluminium oxide (sapphire).

Smith had rightly concluded that electron beams seriously changes the relative concentration of surface elements and cause reduction and decomposition of Al_2O_3 and desorption of oxygen. In order to reduce the decomposition effects, Smith varied the electron beam parameters and kept the beam on the sample, only during the recording of Auger spectra. This time metallic aluminium peaks increased only slightly above that caused by the initial ion beam sputtering. He had used a primary beam of 3 keV, energy and sample to ground current of 0.9 μA and beam diameter of 0.05 cm. Hence Smith recommended that the overall electron dose delivered to a surface must be minimised and when interpreting sputter depth profiles of multilayer specimens the deleterious effects of the electron beam must be taken into account, though he suggested no specific minimum dose.

Figs. 4.6 and 4.7 have been reproduced from Smith (1976), and show the subsequent changes in the Auger PPH intensities of Al (55 eV), Al (67 eV) O (515 eV) and Al (1390 eV) of sapphire as a function of electron beam irradiation time. By replotting, the normalised natural logarithm of oxygen PPH against irradiation time an estimate of the effective cross-section for the electron stimulated decrease in oxygen can be calculated as shown in section 3.2.1.

Fig. 4.8 shows this plot and it can be seen that the effective cross-section for the stimulated decrease in the O_{KLL} peak is not constant. Initial and final values of 1.1×10^{-19} and 2.7×10^{-20} cm^2 has been estimated (the electron beam parameters were as follows: E_p = 3 keV, I_{sg} = 7.1 μA estimated from a knowledge of the SEE yield of Al_2O_3 at this E_p and angle of incidence, and d_{beam} = 0.5 mm).

The decomposition of Al_2O_3 and subsequent desorption of oxygen under electron bombardment, has also been studied by van Oostrom (1979) who

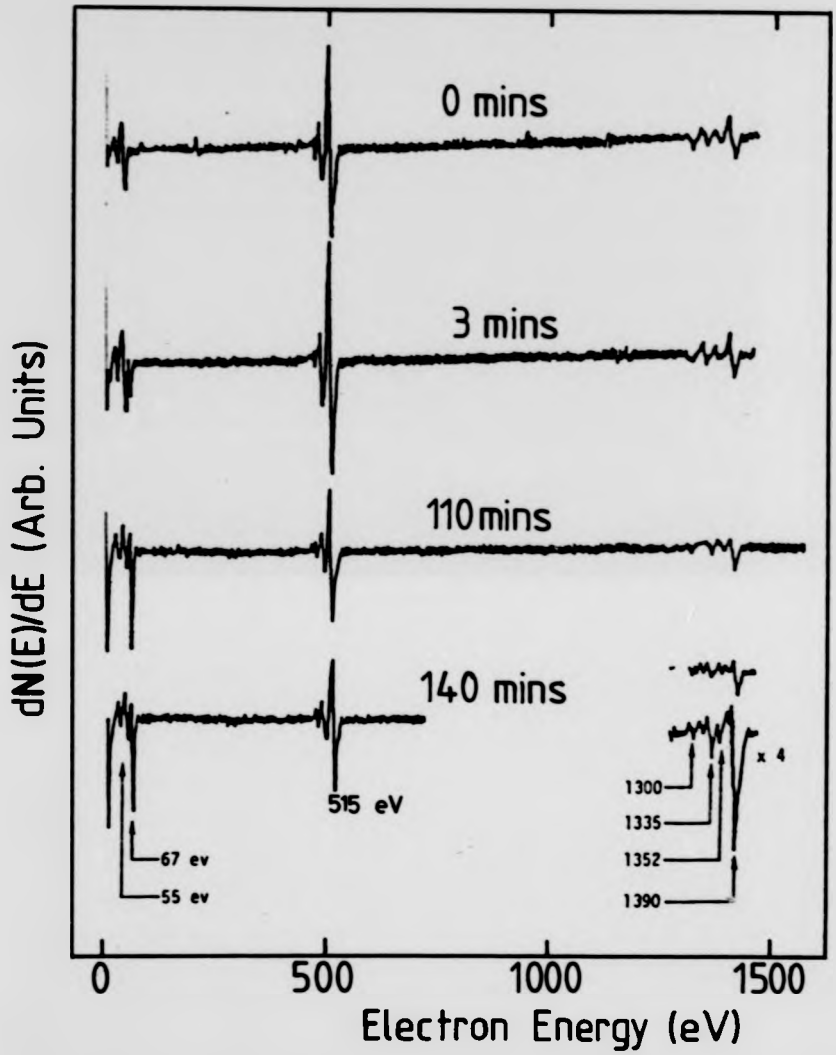

Fig. 4.6 Survey Auger spectra of alumina (sapphire) as a function of electron beam irradiation time. E_p = 3 keV, I_a = 7.1 μA beam dia. 0.5 mm (reproduced from Smith 1976)

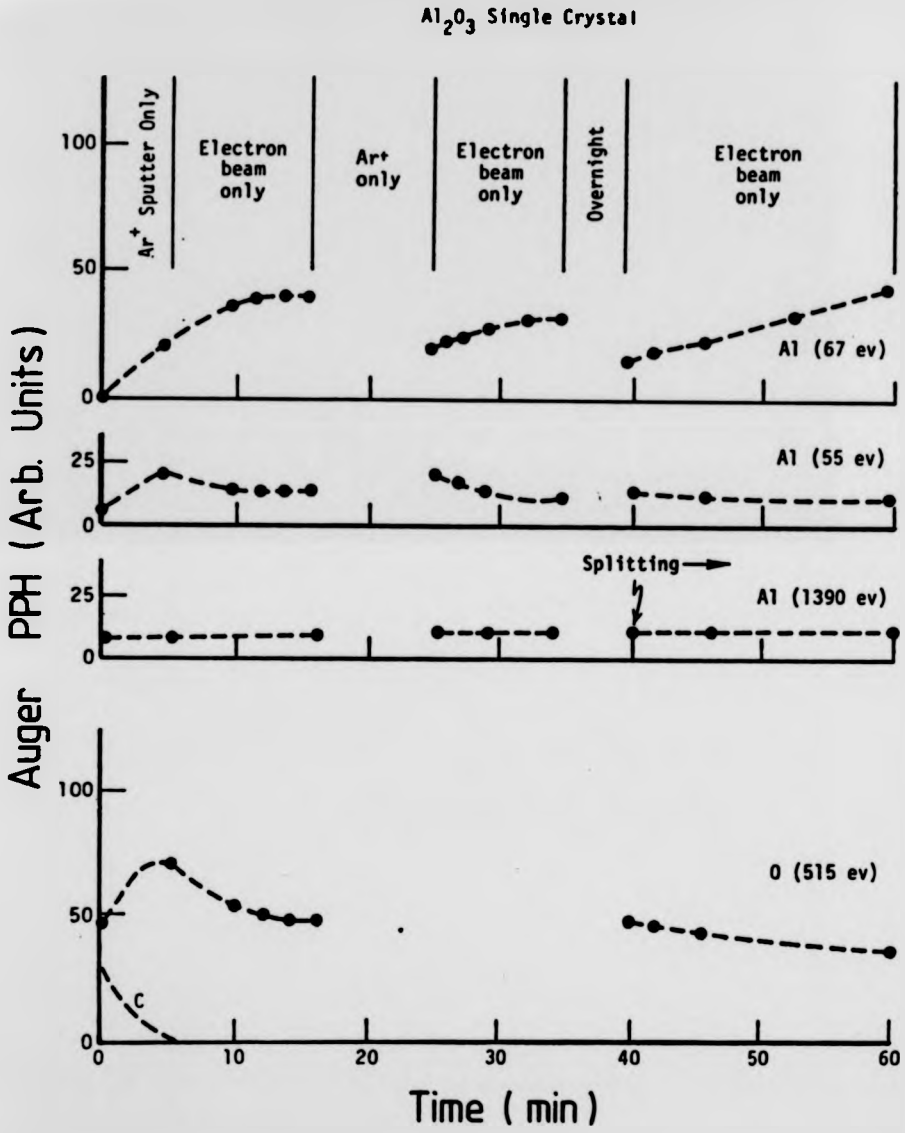

Fig. 4.7 Al^{67} and O^{515} Auger PPH intensities versus electron beam irradiation for the alumina surface (reproduced from Smith 1976).

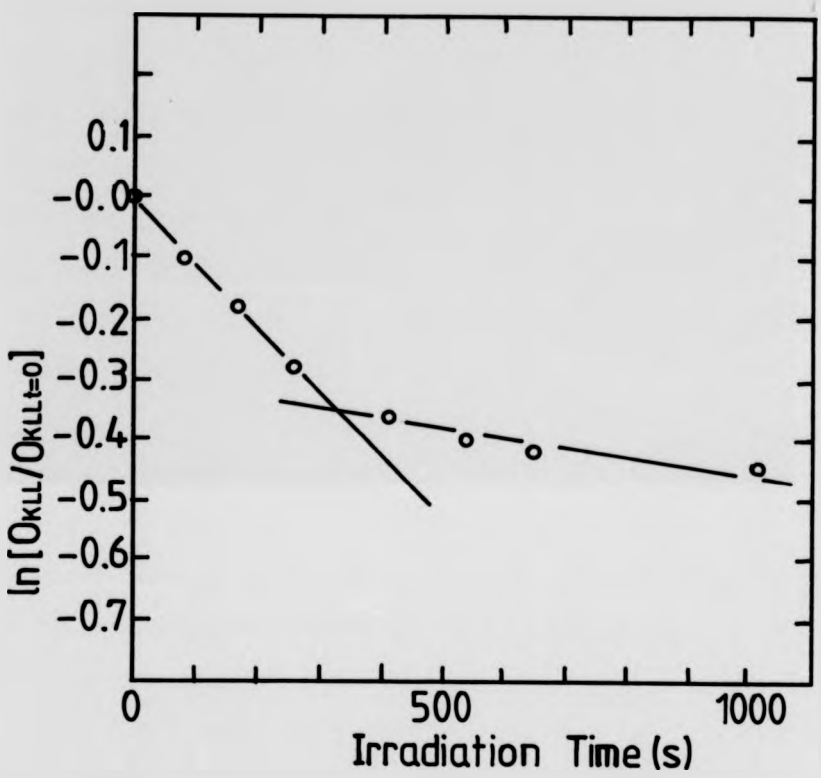

Fig. 4.8 The natural logarithim of [$0^{515}/0^{515}_{t=0}$] versus irradiation time (data from Fig. 4.7).

reported similar changes in the Auger PPHs to those observed by Smith. van Oostrom monitored the low and high energy Auger PPHs of metallic and oxidised aluminium and the O_{KLL} PPH of oxygen as a function of electron irradiation time, for an oxidised film of aluminium . He had used a 5 keV electron beam from a coaxially mounted electron gun, contained in a commercial CMA. Fig. 4.9(a) shows the variation of O_{KLL}, Al $L_{2,3}VV$ and Al $L_{2,3}V_0V_0$ Auger PPHs as a function of the logarithm of the electron beam dose D (I_p/A t). From this plot, he suggested a threshold for decomposition at an electron dose of 10 C/cm^2.

Fig. 4.9(a) has been replotted as in Fig. 4.9(b) so that the natural logarithm of the normalised O_{KLL} and Al^{54} peaks are on the vertical and electron beam dose D on the horizontal axis. The Al^{54} plot yields a straight line indicating a constant effective cross-section of $\simeq 10^{-22}$ cm^2. The effective cross-section for the decrease in the O_{KLL} signal is high at first ($\sim 3 \times 10^{-22}$ cm^2) decreasing to $\sim 5 \times 10^{-23}$ cm^2 with increasing dose. However using the critical dose D_c equation (3.9) an effective cross-section in the O_{KLL} signal of 1.8×10^{-20} cm^2 is obtained.

4.5.2 Oxygen Adsorption by ESD

Literature on the direct observation of initial stages of oxidation of clean aluminium surfaces by ESD is very scarce. The only reference at hand is that of Bujor, Larson and Poppa (1982), who have used additional techniques of AES and ELS as already reviewed in sections 4.1 and 4.3. The aluminium thin films were prepared in-situ, on molybdenum substrates and the surface was excited by low current density, 1 keV, 0.5 μA electron beam incident at 45° to the sample normal and rastered over an area of 10 mm^2. ESD of O^+ ions were detected using a quadrupole mass spectrometer with a high ion angle of acceptance.

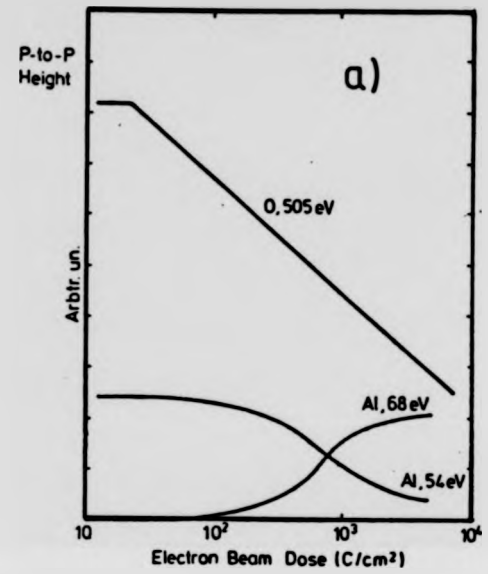

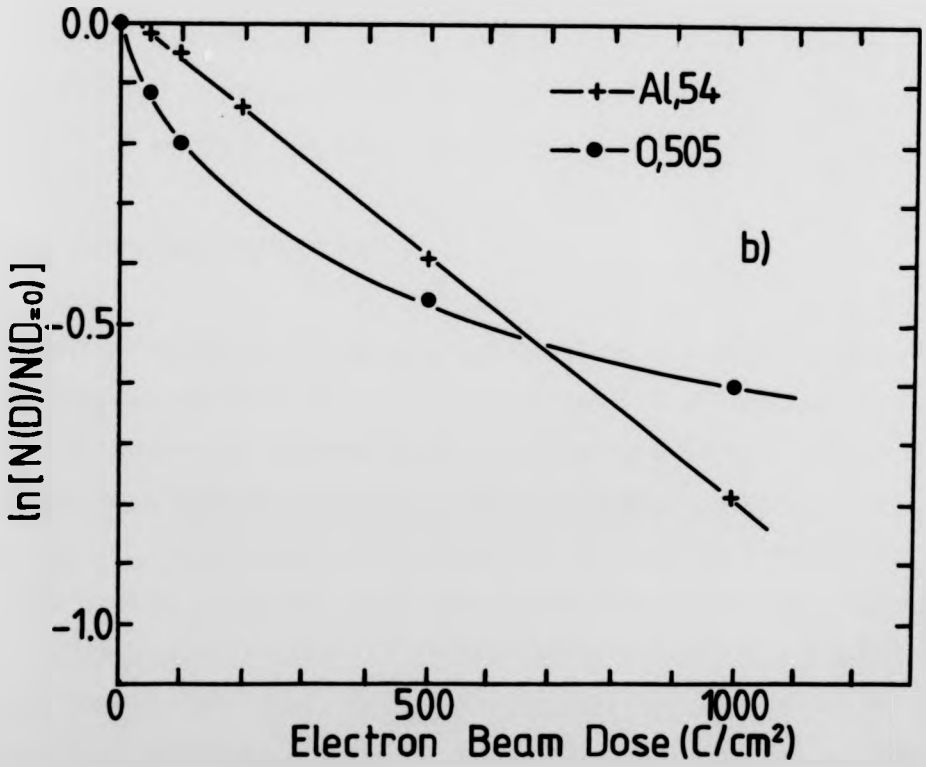

Fig. 4.9 (a) O^{505}, Al^{68} and Al^{54} Auger PPH intensities versus electron beam dose. E_p = 5.0 keV (reproduced from van Oostrom 1979). (b) The natural log of $[\ O^{505}/O^{505}_{D=0}\ ]$ and $[\ Al^{54}/Al^{54}_{D=0}\ ]$ versus electron beam dose.

For the clean aluminium surface, ESD signals of H^+, F^+ and O^+ were detected. No oxygen or fluorine contamination was detected when the surface was monitored using AES, indicating the true surface sensitivity of ESD. The F^+ ions were thought to be due to fluorocarbons from the ioniser grid of the quadrupole mass spectrometer. No mention of carbon contamination was made by them. ESD measurements had shown the clean films of Al to contain oxygen which was probably incorporated throughout the bulk of the film due to the evaporation process.

The evolution of the O^+ ESD signal as a function of oxygen exposure, was very similar to the AES obtained adsorption profiles as reviewed in section 4.2. A two stage adsorption process is suggested by the growth of the O^+ signal. In the 0-50 L oxygen exposure range a fast increase in the O^+ signal is observed, with subsequent reduction in the rate of increase of the O^+ signal as the exposure is increased. Fig. 4.10 is reproduced from Bujor et al and shows the evolution of O^+ ESD signal with oxygen exposure.

4.5.3 CO and CO_2 Exposed Aluminium Surfaces

In section 4.2.5 carbon monoxide adsorption on aluminium surfaces was reviewed, as studied by AES and ELS techniques. It was concluded that CO did not adsorb on aluminium surfaces at room temperatures, and in the absence of electron beam irradiation (Bargeron and Nall 1982).

Carbon dioxide adsorption in the presence of electron beams on clean films of polycrystalline aluminium has been studied by Falconer, Bischke and Hanna (1983), who have used AES to investigate the enhancement of CO_2 adsorption on thin surfaces of thin aluminium deposited on quartz substrates in a separate vacuum apparatus. The samples were cleaned by argon ion sputtering and Auger spectra recorded with a commercial coaxial

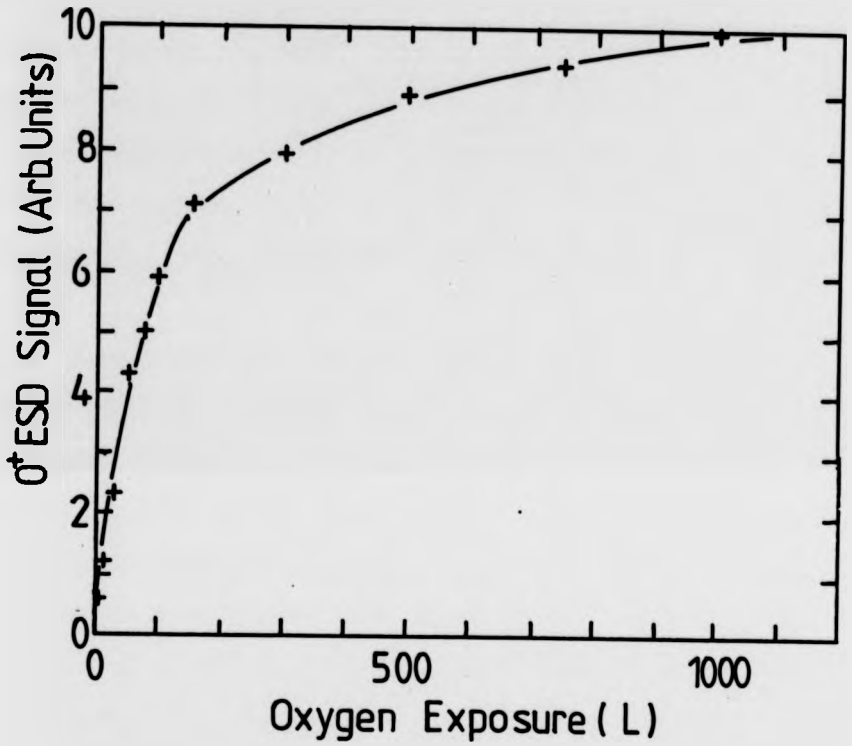

Fig. 4.10 Variation of the O^+ ESD peak with oxygen exposure. E_p = 1 keV, I_p = 0.5 μA, A = 10 mm^2 (reproduced from Bujor et al 1982).

electron gun. The sample was excited at normal incidence by a 2 keV, 5 μA beam of 0.24 mm (FWHM) diameter. By use of a high resolution specimen transfer device, Falconer et al were able to obtain spatially resolved spectra across the irradiated spot by reproducible linear movements of the specimen manipulation device. CO_2 adsorption pressure was in the range 2.4 x 10^{-6} torr and the adsorption was monitored by recording window spectra of the O_{KLL}, C_{KLL} Al_{LVV} Auger transitions and Al LV_0V_0 cross transition.

Auger survey spectra from the clean surface indicated the presence of oxygen which the ion sputtering had failed to remove, pointing to presence of oxygen through the bulk, incorporated during the evaporation process. Initial exposure of the clean surface to 4000 L of CO_2 in the absence of the electron beam, monolayer coverage was not reached. In the presence of the electron beam however, the rate of adsorption had increased drastically and for the equivalent exposure, more than a monolayer coverage of oxygen was present in the beam area. Falconer et al reported only slight build up in the carbon KLL Auger signal indicating CO_2 did not adsorb wholly.

A typical oxygen and aluminium concentration profile across the irradiated spot is shown in Fig. 4.11 which has been reproduced from Falconer et al (1983). The O_{KLL} PPH profile is bell shaped which points to an electron beam intensity of Gaussian distribution. In the areas outside the irradiated spot the O_{KLL} PPH was only slightly above the background recorded for the CO_2 exposed surface in the absence of the electron beam. Falconer et al report that in the absence of the electron beam and gas phase CO_2 exposure, the build up of the oxide in the beam area disappears which is confirmed by the enhancement of the Al $L_{2,3}VV$, matallic Auger signal. If however, only gas phase CO_2 was removed, in the continued presence of the electron beam, the oxide was stabilised permanently.

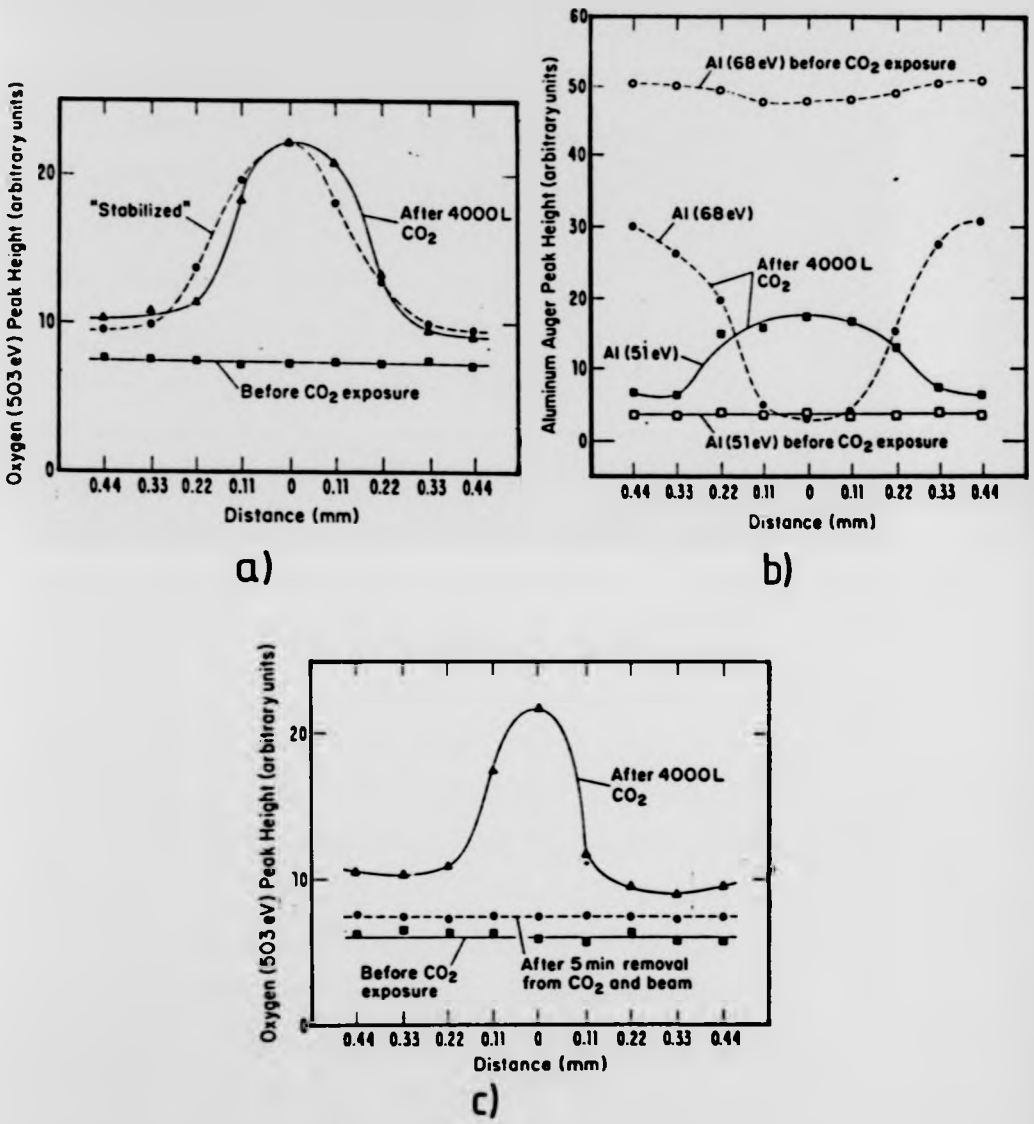

Fig. 4.11 Elemental concentration profiles across the electron beam irradiated spot. E_p = 2 keV, I_p = 5 μA and beam dia. 0.24 mm.
(a) O^{503} versus distance.
(b) Al^{68} and Al^{51} AES PPHs versus distance.
(c) O^{503} AES PPH versus distance (reproduced from Falconer et al 1983).

Similarly after electron beam enhanced oxidation of the spot, if the electron beam alone was removed, the O_{KLL} PPH decreased. Hence, Falconer et al have concluded that the rate of CO_2 adsorption and oxidation on evaporated thin films of Al was significantly enhanced by an electron beam. They proposed a mechanism whereby the adsorbed CO_2 molecule, dissociates under the electron beam, into O and CO, with the oxygen becoming adsorbed and subsequently reacting with the surface to form and oxide and CO desorbing into the vacuum. The instability of this oxide in the absence of gas phase CO_2 and electron beam was accounted by the subsequent diffusion of the oxygen into the bulk.

The above ESA mechanism was first suggested by Kirby and Lichtman (1974), from their LEED-AES studies of O_2 and CO adsorption on silicon surfaces.

As a continuation of the above work Pitts, Bischke, Falconer and Czanderna,(1984) have sought to identify the origin of the adsorbed oxygen on the oxidised Al surface (gas phase CO_2, residual O_2 or from the bulk). In the original work of Falconer et al, evaporated thin films of Al contained oxygen impurities in the bulk directly as a result of preparation which may have enhanced the initial rates of CO_2 adsorption. Pitts et al, have repeated the experiments of Falconer et al using polycrystalline sheets of aluminium of high purity (5N) and lesser bulk oxygen contamination, as well as freshly in situ prepared thin films.

Exposures were done with ^{18}O labelled CO_2 and surface analysis carried out with AES, XPS, ISS (ion scattering spectroscopy, see section 2.3.5) and SIMS (secondary ion mass spectroscopy, see section 2.3.4) all part of a commercial multitechnique instrument. Pre- C $^{18}O_2$ exposure AES measurements on the evaporated thin film surfaces, corroborated the results of Falconer et al. For the clean Al surface after ion etching still

contained some residual oxygen, and in the subsequent simultaneous C $^{18}O_2$, electron beam (J = 7 A/cm^2, which was approximately 1000 times the J used by Falconer et al) exposure, oxide islands were grown on the irradiated spot, very similar to the ones grown by Falconer et al. Positive and negative SIMS i.e. O^+, CO^+ and O^-, CO^-. analysis of the oxide island showed no enhancement of ^{18}O or fragments incorporating ^{18}O. Pitts et al concluded that the source of ^{18}O was below detection capability of their SIMS.

Similar experiments on the polycrystalline sheets, yielded identical results to above. Except this time no residual oxygen was detected on the clean aluminium surface, which ruled out oxygen diffusion from the bulk and saturation in the growth of the oxygen peak was observed after 5000 L of C $^{18}O_2$ exposure.

Pitts et al, have further investigated the C $^{18}O_2$ adsorption by exposing the surface to 42 kL, and electron densities of 0.8 mA/cm^2 rastered over the whole of the sample area for beam energies in the range 0.5 - 2 keV. For the argon ion sputter cleaned surface, XPS (photon source Mg K_α, 1257 eV), survey spectra revealed residual oxygen, O(1s) (BE = 531 eV), implanted argon, Ar(2p) (BE = 245 eV), copper Cu(2p) (BE = 931 eV, Cu_{LMM} = 920 eV) and a very small peak of carbon C(1s) (BE = 285 eV).

The O(1s) and Cu(2p) photoelectron peaks were due to, non-sputtered areas on the sample, seen by the broad Mg Kα photon flux. XPS window spectra of the O(1s) and Al(2p) regions taken after exposure of the surface to 42 kL of C $^{18}O_2$ in the absence of the electron beam showed a prominent Al(2p) photoelectron peak due to elemental aluminium with a slight shoulder 2.25 eV to the higher binding energy side of due to aluminium oxide. The oxygen O(1s) peak was also quite small.

XPS window spectra recorded in the presence of both $C^{18}O_2$ and electron beam exposure, showed enhancement of the O(1s) and substantial growth in the Al(2p), 2.25 eV shifted peak and decrease of the Al(2p) photoelectron peak due to elemental Al. The carbon C(1s) did not show any change in intensity, indicating that the surface is substantially oxidised by the electron beam. The XPS spectra for the above experiments are shown in Figs. 4.12(a-c) and have been reproduced from Pitts et al.

Positive SIMS results obtained from 217 kL of $C^{18}O_2$ and 500 eV, $0.8/cm^2$ exposed surfaces showed little indication of ^{18}O but negative SIMS gave ^{18}O and Al-^{18}O fragments. The presence of ^{16}O and $C^{18}O^{16}O$ and $C^{16}O_2$ fragments were attributed to residuals in the $C^{18}O_2$ gas and from the residual gases in the UHV chamber.

$^3He^+$, ISS analysis gave a more convincing result of the origin of the oxygen in the surface oxide with no detectable ^{16}O indicating clearly that the source of oxygen for oxide growth had come from $C^{18}O_2$. Hence, Pitts et al, have concluded that the most likely mechanism to account for the observed growth of the oxide is the initial dissociation of CO_2 into CO and O by the electron beam. The oxygen reacts with the Al surface and CO desorbs. Another possible mechanism is the gas phase excitation of CO_2 or ionisation in the area of the beam, upon impact with surface atoms dissociates with subsequent reaction of O with Al and desorption of CO which seems to support the findings of Bargeron and Nall (1982) who have also concluded that CO_2 did not adsorb on to clean surfaces of polycrystalline or monocrystalline aluminium as discussed in section 4.4.

Pitts et al also add that, they were unable to directly observe an increase in CO partial pressure with their SIMS apparatus operating in the RGA mode because the quantity of the CO desorbed may be below the detection limit of

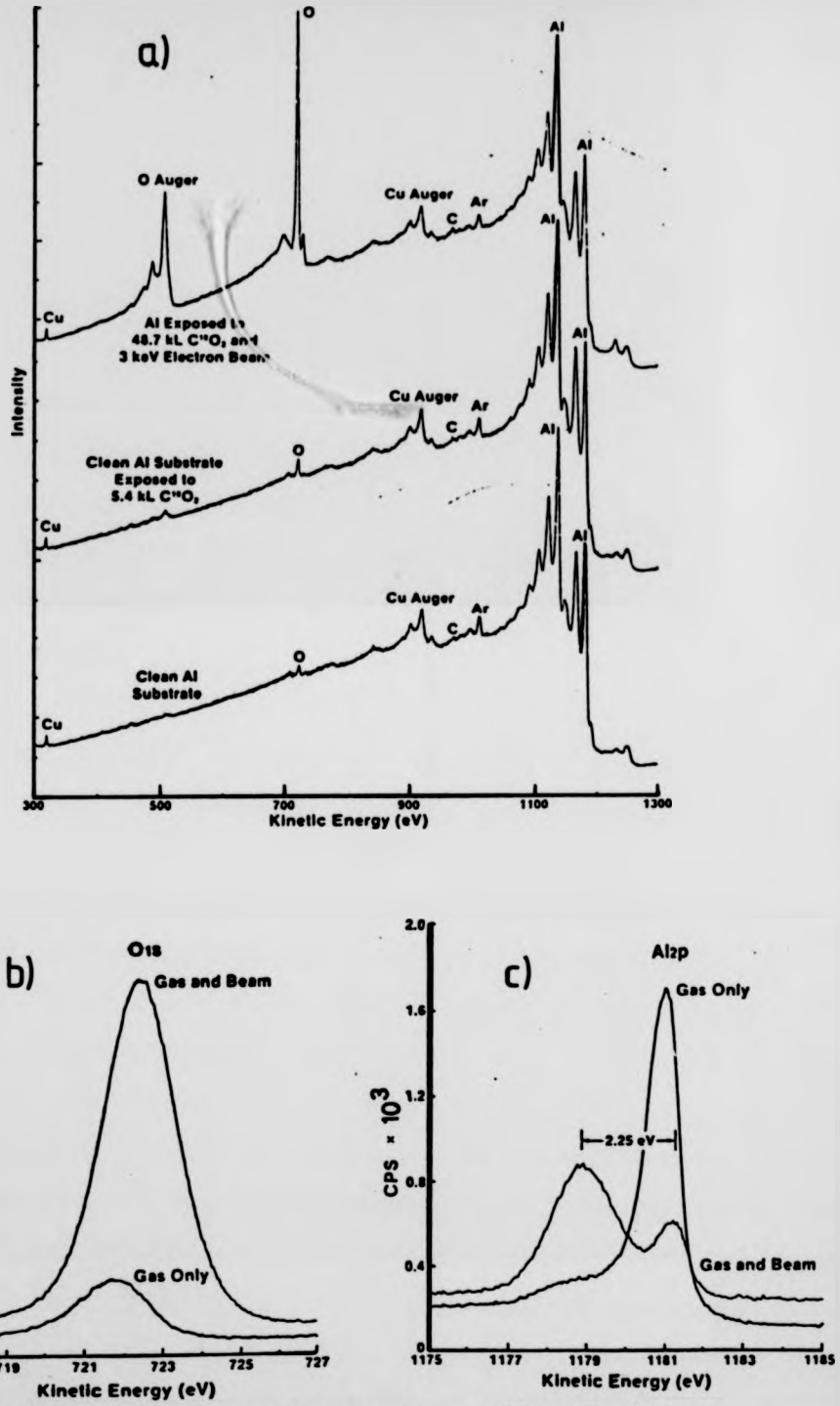

Fig. 4.12 (a) XPS survey spectra of clean, CO_2 and CO_2 with electron beam exposed Al sheet. E_p = 3 keV, I_p = 3 μA beam dia. 4 μm and J = 0.8 mA/cm^2.

(b) and (c) XPS window spectra of O(1s) and Al(2p) photo electron peaks from Al sheet exposed to CO_2 and C $^{18}O_2$ and electron beam

the RGA.

4.5.4 Oxygen Adsorbed Aluminium Surfaces

Of major importance to the work described in this thesis and possible implications for the conclusions reached by Falconer et al and Pitts et al are the reported findings of Fontaine and Lee-Deacon et al, (1982), on the electron beam effects at oxygen exposed polycrystalline and single crystal surfaces of aluminium. Fontaine and Lee-Deacon et al had set out to discover the physical and chemical processes leading to the observed artifacts in the absence of deliberate beam heating, charging and residual gas contamination.

Fontaine and Lee-Deacon et al used a commercial SAM/SEM/AES combined surface analysis system pumped by a combination of turbo, ion and titanium sublimation pumps with a cryogenic panel. A 5 keV electron beam with current density of 10^{-4} A/cm^2 was used to excite Auger electrons from clean and oxygen exposed polycrystalline aluminium surface, which turned out to consist of (111) faceted grains. Also the surface of (100) oriented, Al crystal was also investigated.

After acquisition of oxygen adsorption profiles for both surfaces, which they claim were similar to that of Martinson and Flodstrom, (1979) as reviewed in section 4.1.1. Fontaine and Lee-Deacon et al, exposed each surface to 100, 250 and 1000 L oxygen which corresponds to sub-monolayer and monolayer coverages, and irradiated a particular spot continuously for an hour. Auger window spectra of elemental Al $L_{2,3}VV$ (67 eV), oxidised Al $L_{2,3}V_OV_O$ (54 eV) inter atomic Auger transition and oxygen KLL (508 eV) transitions were recorded as a function of irradiation time. They were also able to record further Auger window

spectra from pre-determined non-irradiated spots by use of the SEM facility and high resolution, translational motion sample manipulation device. They reported drastic increases in the oxygen and oxide levels within the irradiated spot, compared with the non-irradiated spots on the (111) surface for all levels of oxygen exposures. No increase was observed on the (100) face. Fontaine and Lee-Deacon et al assumed the O_{KLL} PPH to be a measure of all the oxygen on the surface and the normalised ratio of Al (54 ev) PPH to sum of Al (54 eV) PPH and Al(67 eV) PPH to represent the over all oxide level.

For the (111) face the O_{KLL} PPH had increased by 20-25% after 70 minutes of electron beam irradiation where as the B ratio had increased up to 40% over the non-irradiated spot. Fontaine and Lee-Deacon et al ruled out ESA from the residual gases in the UHV chamber which were effectively removed by operation of the cryogenic and titanium sublimation pumps. Figs. 4.13(a,b) which have been reproduced from Fontaine and Lee-Deacon et al, show the O_{KLL} PPH and B value as functions of irradiation time for the Al(111) and (100) faces.

In order to account for these observations, other than by ESA, they proposed a mechanism whereby oxygen atoms, in a chemisorbed state on the (111) face, are transformed into an oxide state through near elastic collisions (estimated cross-section 2×10^{-19} cm^2 to impart 0.100 eV of energy) with the primary electrons. Chemisorbed oxygen atoms outside the beam area become ionised by low energy electrons scattered from the analyser walls. These excited species return to their ground states via Franck-Condon type transitions, during which sufficient energy is gained to enable them to diffuse into the primary beam area to become oxidised.

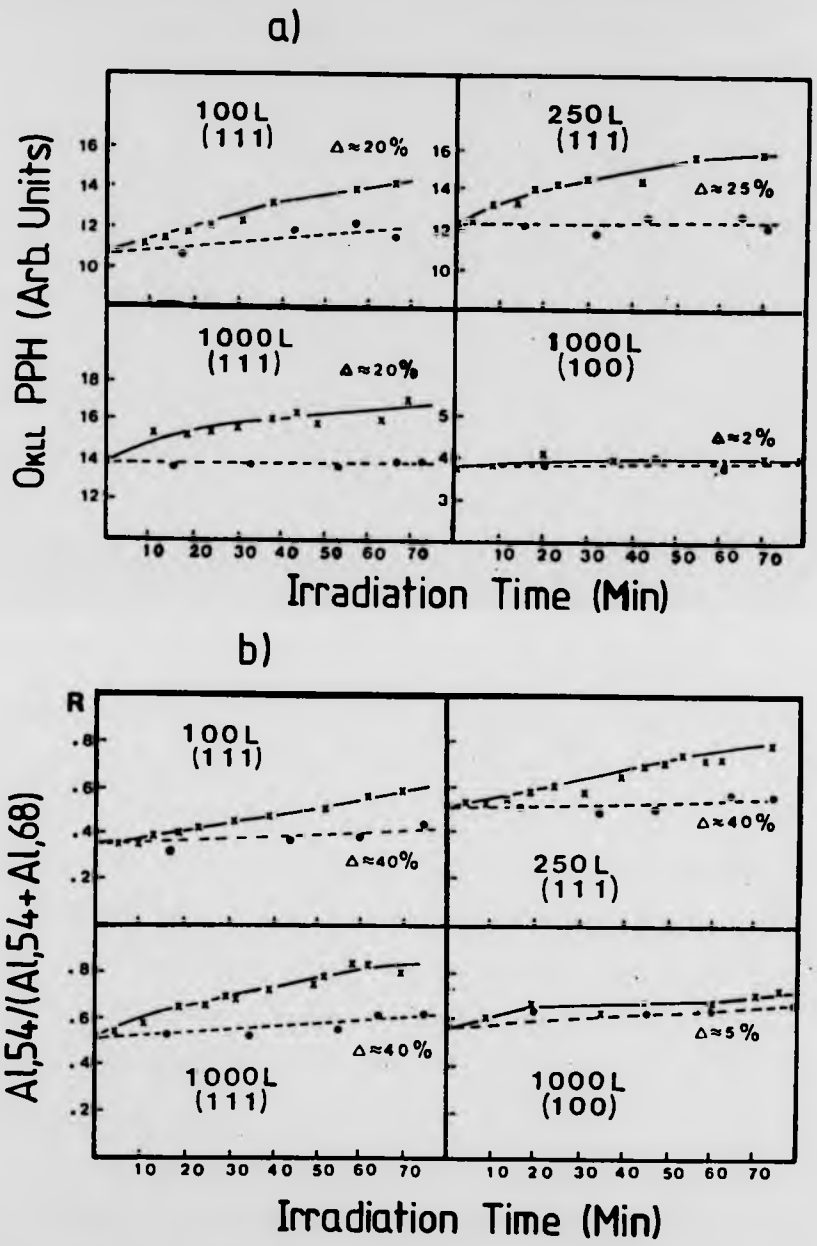

Fig. 4.13 (a) O_{KLL} PPH as a function of electron irradiation time. (b) Ratio B [$Al\text{-}O^{54}/(Al\text{-}O^{54} + Al^{67})$] versus irradiation time. E_p = 5 keV, J = 9 x 10^{-5} A/cm^2 (reproduced from Fontaine et al 1982)

Absence of oxide growth on the Al(100) face in the presence of the an electron beam, was explained by the fact that the initial oxygen adsorption dynamics on this face lacks the chemisorption phase and oxygen is directly incorporated into the sub surface layers (Martinson and Flodstrom (1979)), hence the proposed mechanism will not work for the Al (111) face.

This mechanism, will be further discussed in chapter 8 when interpreting the results of similar experiments performed in this work.

4.6 Summary and Conclusions

To summarise this section on electron beam effects observed on clean and oxidised aluminium surfaces, the situation appears to be far from clear. In general, electron beam effects cannot entirely be eliminated from electron spectroscopy techniques. On the heavily oxidised aluminium surfaces the predominant, beam effects observed were electron stimulated decomposition and desorption with estimated effective cross-section of 10^{-18} - 10^{-22} cm^2 for primary electron energies in the range 0.5 - 5 keV. Which agrees with cross-section values derived from ESD experiments at lower kinetic energies.

Carbon dioxide was observed not to adsorb on aluminium surfaces except in the presence of electron beams with a wide range of energy and current density in which case the irradiated spot becomes predominantly oxidised with the oxygen from the dissociated CO_2 and desorbed CO fraction.

On sub-monolayer and monolayer oxygen covered Al(111) surfaces, growth in the oxygen and oxide level was observed under electron beam bombardment. Though this was absent from the Al(100) face. No predominant decomposition or desorption has been reported from these surfaces. But again, results

Table 4.2 Summary of some electron beam effect experiments at oxygen and CO_2 exposed Al surfaces.

Substrate	Adsorbate	State	Method	Electron energy keV	Current density A/cm^2	Beam effects	Cross section	Author
Al(poly) sheet	O_2	oxide film	AES	3.0	10^{-4}-10^{-3}	EBID ESD	10^{-19} 10^{-20}	Smith (1976)
Al (poly) sheet	O_2	oxide	AES	5.0	10^{-4}-10^{-3} estm.	EBID ESA	10^{-22}	van Oostrom (1979)
Al (poly) film	O_2	chemi-sorbed	AES ESD	1.0	$5x10^{-6}$	ESD of O^+		Bujor et al (1982)
Al (poly) film	CO_2		AES	2.0	10^{-2}	ESA of O		Falconer et al (1983)
Al (poly) film	CO_2		AES,XPS SIMS,ISS	0.5-10	10^{-3}-10	ESA of O + therm		Pitts et al (1984)
Al (111) crystal	O_2	chemi-sorbed	AES	5.0	10^{-4}-10^{-3}	ESA of O + oxide		Fontaine et al (1982)
Al (100) crystal	O_2	chemi-sorbed	AES	5.0	10^{-4}-10^{-3}	no change		Fontaine et al (1982)

Key: EBID = Electron Beam Induced Decomposition
ESD = Electron Stimulated Desorption
ESA = Electron Stimulated Adsorption

and observations tend to vary to a greater extent from experimenter to experimenter, sample to sample. Table 4.2 is a summary of the response of oxygen and carbon dioxide exposed Al surfaces to electron beam irradiation for various energies and current densities where appropriate cross-section values have also been indicated.

CHAPTER FIVE

SECONDARY ELECTRON EMISSION

5.1 Introduction

The phenomenon of secondary electron emission (SEE), was first discovered by Austin and Starke in 1902, when they were investigating the interaction of electron beams with metal surfaces. Since then numerous experimental and theoretical studies of the effect has been made in terms of the secondary electron yield, i.e. ratio of the number of back-emitted electrons to the number of incident primaries.

Later, SEE was further investigated in terms of the secondary electron energy distribution, by use of electron energy and momentum analysers. Such a typical secondary electron energy distribution is shown in Fig. 5.1; its form has already been discussed in section 2.2 but will briefly be summarised here. The secondary electron energy distribution curve has been arbitrarily divided into three regions according to the main type of collision processes occuring inside the solid.

Region 1, consists of elastically scattered electrons and those that have suffered phonon losses (meVs). In addition, on to the low energy side of the elastic peak, are the primary electrons that have lost quanta of energy in exciting single or multiples of plasmons in the valence or conduction band or single particle excitations.

Region 2, consists of the true secondary electrons in the kinetic energy range of 0 - 50 eV, which have escaped across the potential barrier into

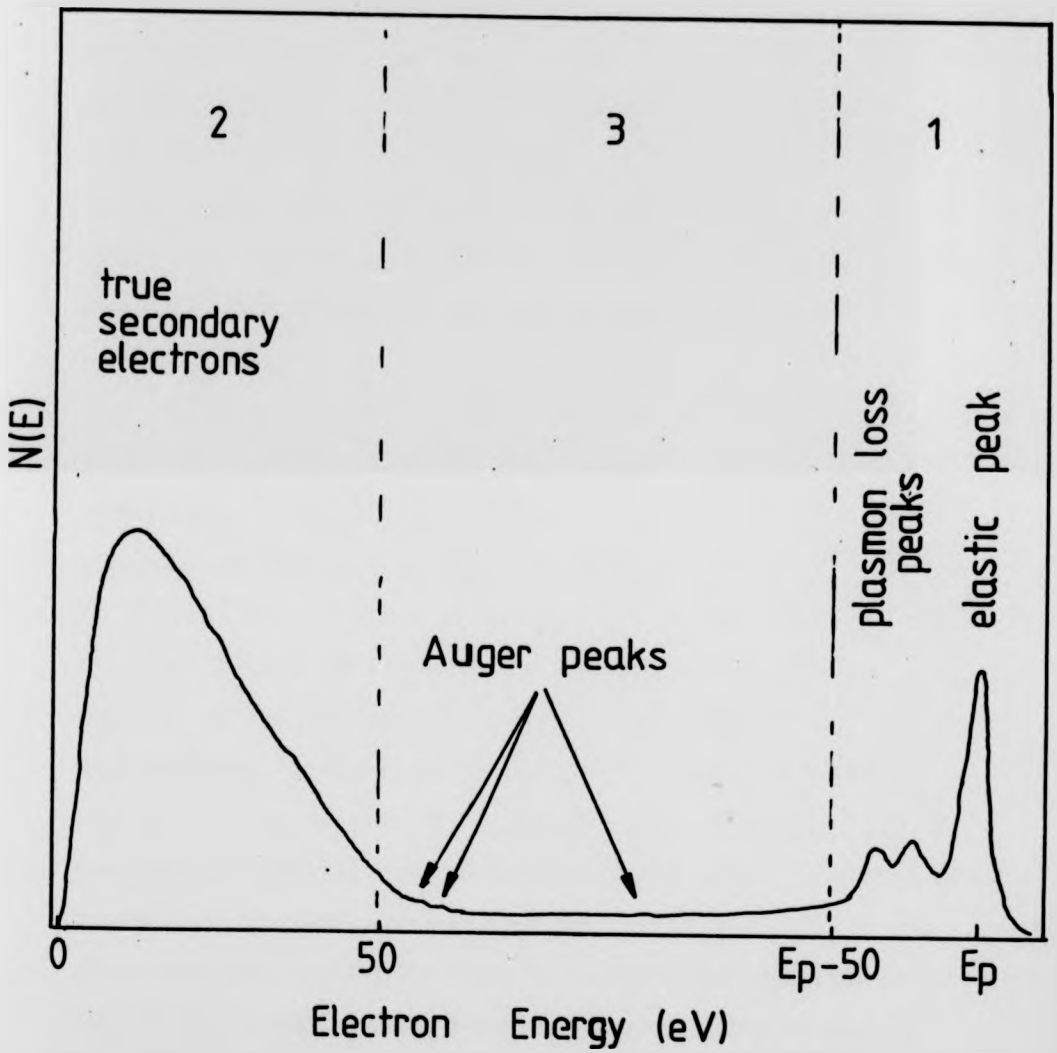

Fig. 5.1 Energy distribution of secondary electrons.

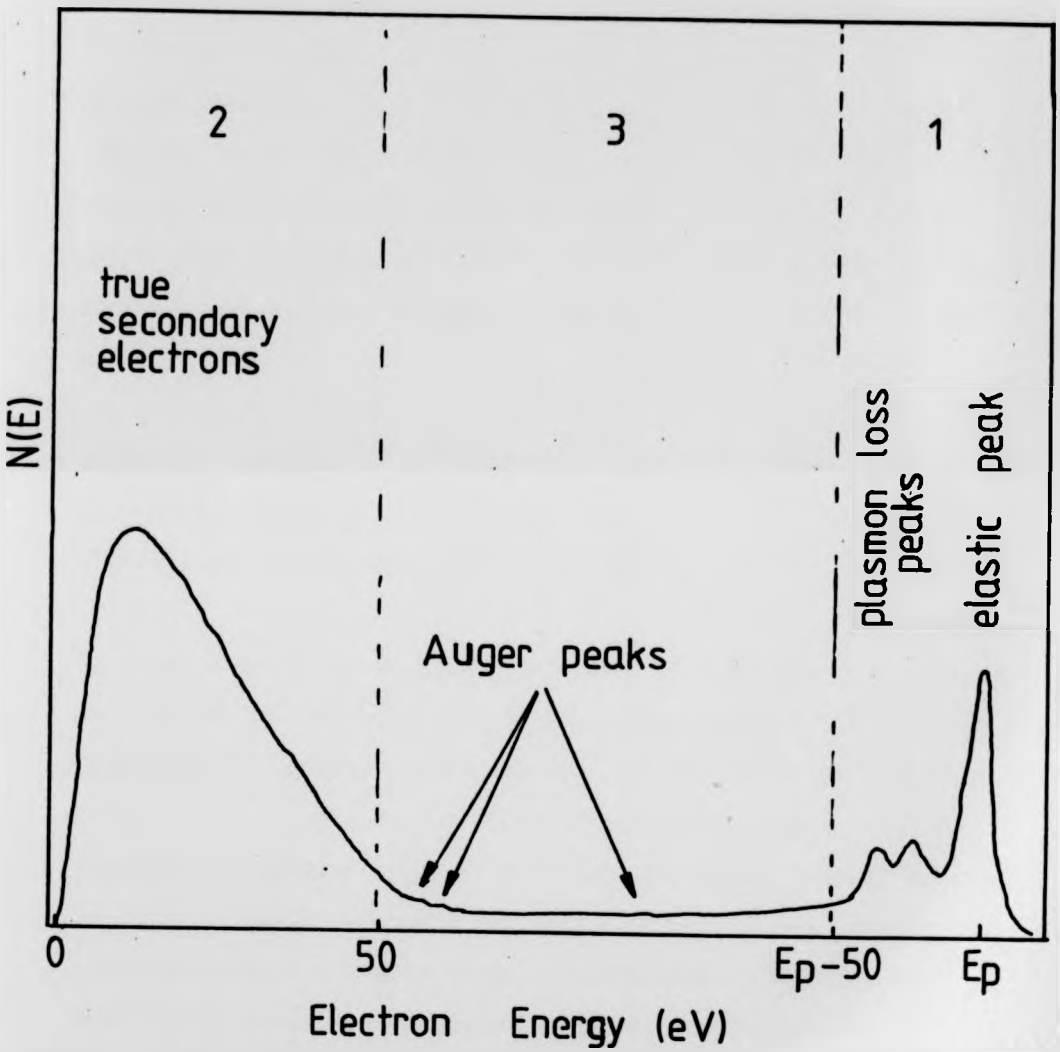

Fig. 5.1 Energy distribution of secondary electrons.

vacuum as a result of multiple inelastic scattering events, a so called **cascade process** involving the primaries and energetic secondaries, valence and core electrons. The shape of this part of the N(E) distribution is normally referred to as the slow secondary electron distribution curve (EDC). It is essentially independent of the direction and energy of the incident primaries and makes up the biggest contribution to the total yield. Fine structures observed on the EDC has been attributed to decay of plasmons into single electron excitations or Auger processes and band structure effects.

Region 3, consists of a relatively flat background of inelastically backscattered primaries and electrons due to ionisation processes. These electrons are particularly efficient at generating slow secondaries.

In this chapter, the result of the simple SEE theory and the assumptions implicit in its derivation will be given which qualitatively describes the experimentally observed yield curve. This will be followed by a brief presentation of results of a quantum mechanical theory of SEE which predicts the general shape of the cascade EDC curve. Finally, discussed briefly is the more recently developed quantum mechanical theory of SEE which includes, the plasmon decay mechanism of SEE excitation which gives rise to fine structure superimposed on to the smoothly varying EDC.

5.2 The Process of Secondary Electron Emission (SEE)

Due to the complexity of the situation the SEE process has been conveniently divided into three steps, illustrated schematically in Fig. 5.2. All theories of SEE would consider the three steps in isolation, or the last two in combination, with various simplifying assumptions to evolve a description of the process.

5.2.1 Basic Theory of SEE

The basic empirical theory of SEE was developed by Salow (1940), Baroody (1950), and Bruining (1954) and was based on the simplified three step process illustrated in Fig. 5.2. The general result for the secondary electron yield can be written as follows:

$$\sigma = \int_0^R \left(-1/\varepsilon \; E_p/R \right) B_1 \; B_2 \exp\left(- x/L\right) dx \qquad \ldots(5.1)$$

where the term $-E_p/\varepsilon R$ represents the production of the secondary electrons by a primary electron of energy E_p at a depth x, which has a range R inside the solid given by

$$R = K \; E_p^n \qquad \ldots(5.2)$$

and ε represents the average energy required to produce a secondary. The term $B_1B_2 \exp(-x/L)$ represents the transport and escape probability of the secondaries where B_1 is a coefficient which accounts for that fraction of the secondaries with upward momenta and B_2 is the probability that a secondary after diffusing to the surface, will escape across the surface barrier into the vacuum. And L is the effective escape depth or mean free path of the secondaries during diffusion to the surface. Expression 5.2 , is the range-energy relationship, where K is a constant depending on the density of the material and for n = 2 the range-energy relationship is that of Whiddington's power law. But Young (1956) and others have obtained experimental values for the power n to be = 1.35 from electron transmission experiments through self supporting Al_2O_3 films for E_p = 2.5 - 10 keV and gives better agreement between theory and experiment.

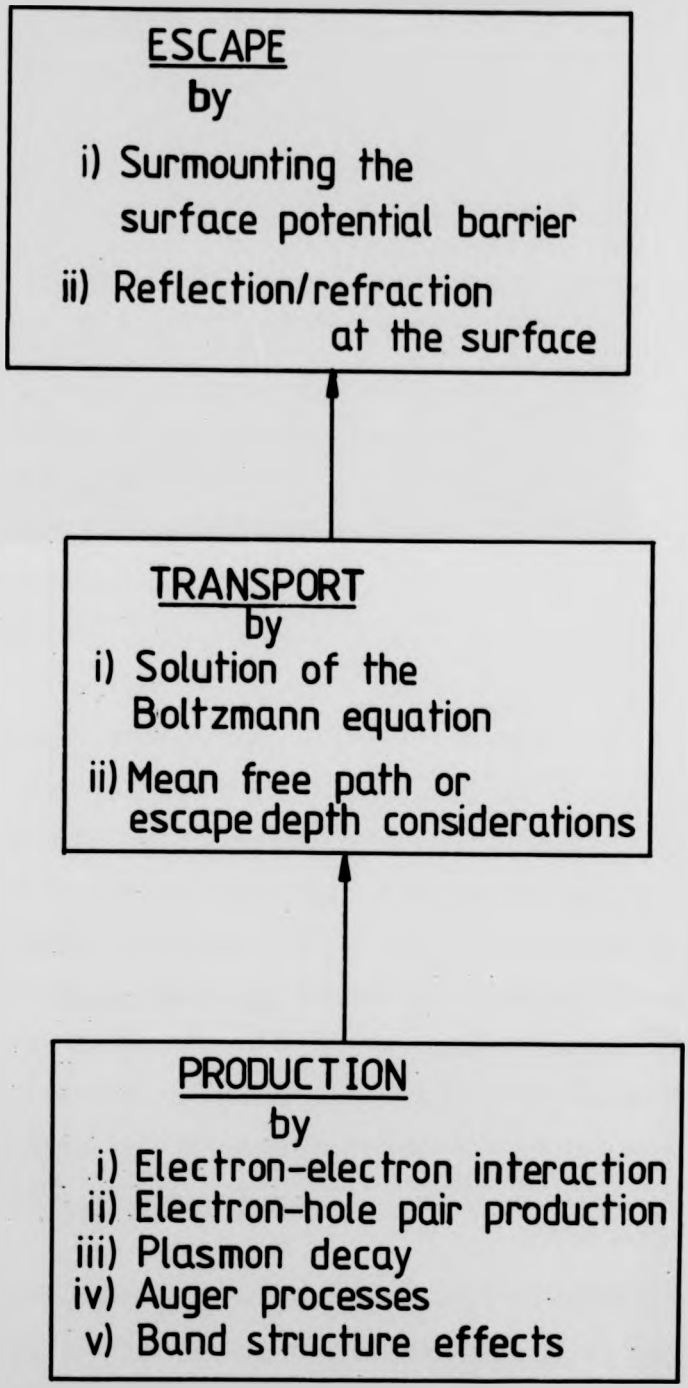

Fig. 5.2 Three step secondary electron emission process.

The work of Salow and Bruining has been reviewed by Dekker (1958) who also gave the implicit assumptions in the expression 5.1 and hence its shortcomings. Some of these are summarised below.

i) The three distinct stages of the SEE mechanism holds for metals and insulators. For metals and insulators this may not be true due to the nature of the cascade process.

ii) That the internal energy distribution of the secondaries may be ignored and just the total number considered.

iii) The escape mechanism is described by an exponential absorption law, without consideration of the true physical processes that may be occuring.

Due to the above simplifications, expression 5.1 cannot predict the true yield of a particular material or say anything about the energy distribution of the emitted secondary electrons. Though it gives the general form of the yield curve and more so of the universal reduced yield curve, first suggested by Baroody (1950). This is a normalised plot of the σ/σ_{max} against E_p/E_{pmax} where E_{pmax} is the primary electron energy at σ_{max} the maximum total yield. When Young's range-energy relationship is used, expression 5.1 also gives qualitative values for the mean escape depths for electrons from metals and insulators and correctly predicts a much higher L for insulators than for metals.

The basic theory also predicts increased yield, for off normal incidence of primary electrons with the sample, if x in expression 5.1 is replaced by x $\cos\theta$ as suggested by Jonker (1952). The yield expression 5.1, has been further modified by Kanaya and Kawakatsu (1972), and Dionne (1973, 1975) to give semi-empirical expressions in terms of surface and bulk parameters

with improved ability to predict quantitative yield results for metals and insulators.

A some what more successful semi-empirical formulation of the yield for insulators and metals has been given by Kanaya, Ono, and Ishigaki (1978), Kanaya and Ono (1978) and Ono and Kanaya (1979). Their semi empirical equations for the yield and its parameters also include the effect of the inelastically backscattered primaries and has been given in terms of the atomic number Z, first ionisation energy I, and the backscattering ratio (which depends on bulk density ρ) with several adjustable parameters to make more exact fits to the experimental data). For insulators, they have used the free-electron scattering theory with plasmon theory to explain the high yield exhibited by these materials, again in terms of Z, ρ, I and free electron density and atomic weight and adjustable parameters for probable multiple plasmon losses. A review of the above work has been given by Fadavi (1981).

In the next section, a quantum theory of the production of secondaries will be given in which the interaction between primary electrons and the individual lattice electrons are considered and the subsequent transport and escape of the Secondary electrons (SEs) are treated in terms of Wolff's cascade theory.

5.2.2 General Quantum Theory of SE Production

Quantum mechanical treatments of the production of secondary electrons by interacting primary electrons and the lattice electrons have been given by Frohlich (1932), Wooldridge (1939), and Dekker and van der Ziel (1952). The latter have given a most general formulation of the SEE production step, where the electron interaction between primary electrons, conduction

electrons and more strongly bound electrons are represented by Bloch functions.

Following Dekker and van der Ziel's procedure, consider a primary electron of energy $E_p = \hbar K_p^2/2m$ colliding with a bound lattice electron of wave vector K_c, and positional vector r and state ψ_{Kc}, after the collision the wave vectors will be K_p' and K_c'. The number of transitions per unit time, $P(K_p, K_c \rightarrow K_p', K_c')d\Omega'$ for which the primary electron is scattered into a solid angle $d\Omega'$ around the vector K_p' and the lattice electron is excited into a new state $\psi_{Kc'}(r)$ as given by time dependent perturbation theory is

$$P\left(K_p, K_c \rightarrow K_p', K_c'\right) d\Omega' = 4 m^2 e^4 K_p'/\epsilon^2 \hbar^4 q^4 K_p |I|^2 d\Omega' \qquad ...(5.3)$$

where $$I = \int e^{(iq.r)} \psi_{Kc}(r) \psi_{Kc'}(r)\, dr \qquad ...(5.4)$$

is the matrix element connecting the initial and final Bloch functions of the lattice electron states and where $q = K_p - K'_p$.

5.2.2.1 Secondary Electron Production in Metals

Equation 5.3 is a general statement of the production of secondary electrons as a result of simple coulomb interaction. In metals though due to a high density of conduction electrons, the field of the primary electron dies away very quickly over very short distances and this effect is allowed for by use of a screened coulomb potential of the type

$$V(r) \propto 1/r \exp(-k_s r) \qquad ...(5.5)$$

where k_s is the screening vector of the order of 1 A^{-1}. In expression 5.3, q^4 is then replaced by $(q^2 - k_s^2)^2$ so that

$$P(K_p, K_c \rightarrow K_p', K_c')\, d\Omega' =$$

$$4m^2 e^4 K_p'/\hbar^4 (q^2 - k_s^2)^2 K_p \, |I|^2 d\Omega' \qquad \ldots(5.6)$$

5.2.3 Transport and Escape of SEs: The Cascade Theory

After production, slow secondary electrons will diffuse through the interior of the solid, suffering multiple inelastic collisions with the conduction electrons, as a result multiplying in number. Some of these internal secondaries with sufficient energy will escape into the vacuum or fall back into the sea of conduction electrons.

This description of the cascade process is due to Wolff (1954) who has used the Boltzmann transport equation to describe the cascade process instead of the simpler exponential absorption and mean free path considerations used in the basic theory in section 5.2.1. The solution of the Boltzmann transport equation gives an external energy distribution of the secondary electrons in term of the internal incident secondaries at the surface and the refraction effect suffered by these due to the potential barrier, before emergence. The Boltzmann equation also gives the relationship between the external secondary electron emission current and the primary beam energy, the inelastic scattering cross-sections, multiple sources and the escape probability.

Wolff's analysis of the Boltzmann equation for secondary electron transport is as follows:

$$\partial N/\partial t\ (\mathbf{r},\Omega,E,t) + v.\text{grad}\ N(\mathbf{r},\Omega,E,t) =$$

$$- vN(\mathbf{r},\Omega,E,t)/\lambda_T(E) + S(\mathbf{r},\Omega,E,t)$$

$$+ \int dE' \int v'N'(\mathbf{r},\Omega',E',t)/\lambda(E')\ F(\Omega',E';\Omega,E)\ d\Omega' \qquad ...(5.7)$$

where $N(\mathbf{r},\Omega,E,t)$ represents the number of electrons as a function of the position vector $\mathbf{r}$, unit vector Ω along the direction of velocity v, the energy E and time t. Therefore the first term on the left of equation 5.7, represents the time rate of change of $N(\mathbf{r},\Omega, E, t)$ and the second, the rate of change due to the gradient of $N(\mathbf{r},\Omega,E,t)$. On the right hand side of equation 5.7, in the first term $\lambda_T(E)$ is the effective or total mean free path and the whole term represents the number of electrons removed by the elastic and inelastic scattering. The second term on the right, i.e. $S(\mathbf{r},\Omega,E,t)$ is a source function representing the density of internal secondaries produced by the primaries. In the final term $F(\Omega',E';\Omega,E)$ the probability that electrons scattered into lower energy states from Ω', E', to Ω, E and electrons scattered from the sea of conduction electrons to higher energy states Ω,E. This probability factor F is then normalised to 2, to account for the result of each cascade electron, that 2 electrons result after the scattering.

$$\int_0^{E'} dE \int F(\Omega',E';\Omega,E)\ d\Omega' = 2$$

Wolff simplified eq. 5.7 by assuming steady state conditions so that $\partial N/\partial t = 0$ and grad N = 0 for the case of normally incident primaries. N, S, and F have been expanded into spherical harmonics in terms of new variables z, θ, E and ϕ such that

$$N(z,\cos\theta,E) = \Sigma_l(2l+1/4\pi)N_l(z,E)P_l(\cos\theta)$$

$$S(z,\cos\theta,E) = \Sigma_l(2l+1/4\pi)S_l(z,E)P_l(\cos\theta)$$

$$F(\Omega',E';\Omega,E) = F(\cos\phi,E,E') = \Sigma_l(2l+1/4\pi)F_l(E',E)P_l(\cos\phi)$$

where z is the normal depth below the surface, θ angle of v with z, and ϕ the angle between Ω' and Ω. Further defining equation $\Psi_l = vN_l/\lambda_T(E)$ then the solution of 5.7 is given by

$$\Psi_l = \lambda_T(E)[(l/2l+1)\partial\Psi_{l-1}/\partial z + (l+1/2l+1)\partial\Psi_{l+1}/\partial z]$$

$$+ \int_E^{\infty} dE' F_l(E',E)\Psi_l(z,E') + S_l(z,E) \qquad \ldots(5.8)$$

In seeking a solution to equation 5.8 Wolff assumed the following

i) secondaries lose energy by scattering with the conduction electrons.

ii) Losses by electron-phonon scattering is negligible.

iii) The electron-electron interaction is described by a screened Coulomb potential (see equation 5.5) and is s-wave in character i.e., $l = 0$.

iv) The scattering is spherically symmetric in the c-mass system up to 100 eV.

v) The conduction electrons are effectively free, so that the result is particularly applicable to metals.

vi) For $E_s > 100$ eV scattering is Rutherford type.

vii) That Ψ_1 is independent of z i.e. no surface effects.

Equation 5.8 was solved by Wolff to give the number of internal secondaries isotropically produced by an incident primary of energy E_p to be

$$N(E_s) = A\,[E_p/E_s+E_I]^X \qquad \ldots(5.9)$$

where A is approximately a constant and E_s is the external kinetic energy of the secondary electron and E_I is the inner potential of the metal and x is $\simeq 2$.

Streitwolf (1959) who also developed a cascade theory, gives an external secondary electron spectrum of the form

$$N(E_s) \propto 1/(E_s + \Phi)^2 \qquad \ldots(5.10)$$

where Φ is the metal work function. If equations 5.9 and 5.10 are multiplied by the surface escape probability $Q(E_s)$, each gives the externally observed SE energy distribution. Thus equation 5.9 of Wolff becomes

$$N(E_s) = A\,Q(E)\,[E_p/E_p+E_I]^X \qquad \ldots(5.11)$$

and

$$Q(E_s) = 1 - [E_I/E_s+E_I]^{1/2}$$

$$N(E_S) = A[1-(E_I/E_S+E_I)^{1/2}]\ [E_p/E_S+E_I] \qquad ...(5.12)$$

which is the total secondary electron distribution collected by an analyser of collection angle of 2π radians. Assuming that no reflection of the secondaries occur. For electron energy analysers of small solid angle of acceptance and angle of emission, the probability of escape has been rewritten by Seah (1969) from refraction index and conservation of momentum considerations and can be shown to be

$$Q(E_S) = [E_S/E_S+E_I]^{1/2}\ 1/[E_S\cos^2\theta_o + E_I]^{1/2}$$

$$\times\ E_S^{1/2}\cos\theta_o \qquad ...(5.13)$$

where θ_o and θ_i have meanings as depicted in Fig. 5.3

Thus the external SE distribution becomes

$$N(E_S) = A[1-(E_I/E_S+E_I)^{1/2}][E_p/E_S+E_I]^X$$

$$\times\ [E_S/E_S+E_I]^{1/2}\ [E_S\cos^2\theta_o+E_I]^{1/2}$$

$$\times\ E_S^{1/2}\cos\theta_o \qquad ...(5.14)$$

From measurements of the secondary EDC from Ag and Cu samples, for SEs emitted in the normal direction, Seah showed that,

$$N(E_S) \propto [1/(E_S+\phi)^X]\ [E_S/E_S+0.35] \qquad ...(5.15)$$

where x was found to be 2.0 for Ag and 1.6 for Cu and ϕ which is the work function of the metal. Seah also suggested that Wolff's cascade equation

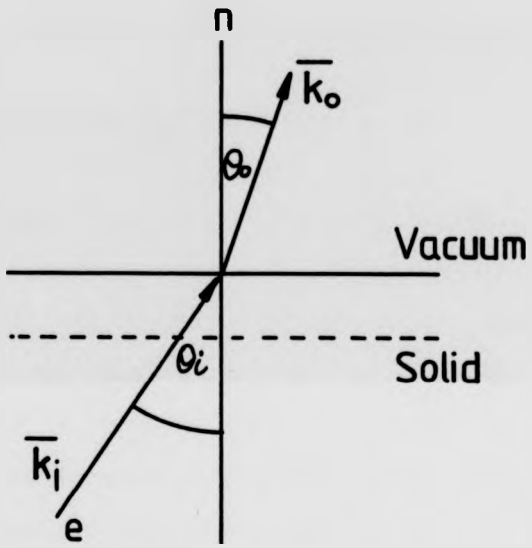

Fig. 5.3 Refraction of escaping secondary electrons at a metal surface due to the inner potential.

gave better agreement with experimentally observed EDC, if the energy of the emitted secondary electrons are referred to the Fermi level rather than bottom of the conduction band. This became apparent when trying to compare the $N(E_s)$ maximum with the experimentally observed maximum.

5.2.3.1 SE Angular Distribution

In the derivation of the Cascade theory of Wolff, one of the assumptions was about the isotropic distribution of the cascade electrons inside the material. This was confirmed by the experimental work of Jonker (1951) who showed that for SEs in the energy range 1.5 - 100 eV, the angular intensity distribution of the secondary electron current at a specific E_s, varied as the cosine of the angle between the surface normal and direction of emergence as predicted by equation 5.14.

5.2.3.2 True (δ) and Total (σ) Secondary Electron Yield

In addition to the energy and angular distribution of the secondary electrons, predictions about the true and total yields of metals can be made using expression 5.12 as well as its variation with the work function. By integration of equation 5.12 between appropriate limits, gives an expression for the true secondary yield δ. Wolff has shown that by differentiation of this yield integral, an expression for change in δ with work function is given by

$$\partial(\ln\delta)/\partial\phi = 1-x/(E_F+\phi) \qquad \ldots(5.16)$$

Therefore equation 5.16 predicts the variation of the true yield with the work function fairly accurately.

Wolff has also given estimates of the total yield by solving the transport equation with a source function that takes account of the finite depth of penetration of the primaries into the metal by assuming a Whiddington power law i.e. penetration depth $z \propto E_p^2$. His expression for σ is as follows

$$\sigma = J_s/J_o = [\pi n_o e^4/2n_c\sigma_{eff}]\ [1/E_p(\phi+E_F)]$$

$$x\ [1 - 40\lambda_o/3\pi z_o]\ [\ \ln(E_p/\phi+E_F) - 1] \qquad ...(5.17)$$

where J_s is the secondary electron current density, J_p is the primary electron current density, n_o is the number of loosely bound electrons contributing to SEE per cm^3, n_c density of conduction electrons. σ_{eff} effective electron-electron scattering cross-section, λ_o is a constant mean free path and z_o is the maximum penetration depth of the primaries.

Equation 5.17 was maximised to estimate the total maximum yield as given below

$$\sigma_{max} = 4/3(\pi a^2/\sigma_{eff})\ (n_o/n_c)\ [R_y/(\phi+E_F)E_{pmax}]$$

$$x\ [\ \ln(E_{pmax}/\phi+E_F) - 1\ ] \qquad ...(5.18)$$

where a_o is the Bohr radius and R_y the Rydberg constant $(me^4/8\epsilon^2h^3c)$.

Wolff obtained some good estimates of σ_{max} for various metals, by using experimental values of E_{pmax} and substituting approximations on values of n_o its variation with E_p.

So far in the quantum theory of the production of secondaries, interaction between the primary electrons and the individual electrons was allowed.

Also in the treatment of the transport and escape of the secondaries by the Wolff's cascade theory, the result is an externally observed smooth secondary electron distribution curve. However recently observed fine structure on this smooth EDC have been strongly linked to the plasmon loss peaks accompanying the elastically scattered primaries and excitation of plasma oscillations in aluminium.

In the next section, theories of SEE will be given which also include SE production due to the interaction of the primary electrons and collective system of conduction electrons leading to excitation of surface and bulk plasmons and their contribution to SE production as they decay into single electron excitations.

5.2.4 SEE Theories: Contribution by Plasmon Decay to the Yield

An important source of slow secondary electrons from nearly free electron NFE, metals may arise through interband transitions of the decay of surface and bulk plasmons excited by energetic primary electrons. For aluminium this mechanism of secondary electron excitation is very important and in this section quantitative theories of SEE (in which the above effect is included) developed by Chung and Everhart (1977), Ganachaud and Cailler (1979), Bindi, Lanteri and Rostaing (1980), and Rosler and Brauer (1981a,b) will be briefly presented and results of their calculations as applied to aluminium will also be given. These calculations include, the energy distribution, angular distribution, and the true and total yields.

In the theories of SEE given by the above authors the SEE process has been described by the simplified three-step process illustrated in Fig. 5.2. In the production term, excitation by direct electron-electron interactions and by decay of plasmons have been included, in direct contrast with Dekker

and van der Ziel, and Wolff's treatment of the SEE process described in the last section.

The transport and escape of the secondaries has been tackled either by solving the Boltzmann transport equation (Bindi et al, and Rosler and Brauer) or by simple mean free path considerations (Ganachaud and Cailler, and Chung and Everhart).

5.2.4.1 Production of Secondary Electrons

Excitation of the secondary electrons, by the direct interaction of the primary electrons with the lattice electrons via electron-electron scattering and SE excitation by decay of plasmons created by the primaries can be included in one equation as given by Chung and Everhart

$$P(K_p,K_v \rightarrow K_f,K_c) = 2\pi/\hbar \sum_q [4\pi e^2/q^2\Delta]^2$$

$$\times [1/|\epsilon(q,\omega)|^2] \; |\langle K_f|e^{iq\cdot r}|K_p\rangle|^2$$

$$\times |\langle K_c|e^{-iq\cdot r}|K_v\rangle|^2 \; \delta(E_p+E_v-E_f-E_c) \qquad \ldots(5.19)$$

where the term on the left hand side of equation 5.19 represents the probability per second for a primary electron in state E_p, K_p to be scattered into a conduction state E_f,K_f by losing energy $h\omega$ due to excitation of a valence electron from state E_v,K_v to conduction state E_c,K_c or by excitation of plasmons, as depicted in Fig 5.4. Δ is the volume of the solid, $\epsilon(q,\omega)$ is the frequency and momentum dependent complex dielectric function equal to $\epsilon_1(q,\omega) + i\epsilon_2(q,\omega)$ where $q = K_p - K_f$ and δ is the Dirac delta function which ensures conservation of energy and momentum.

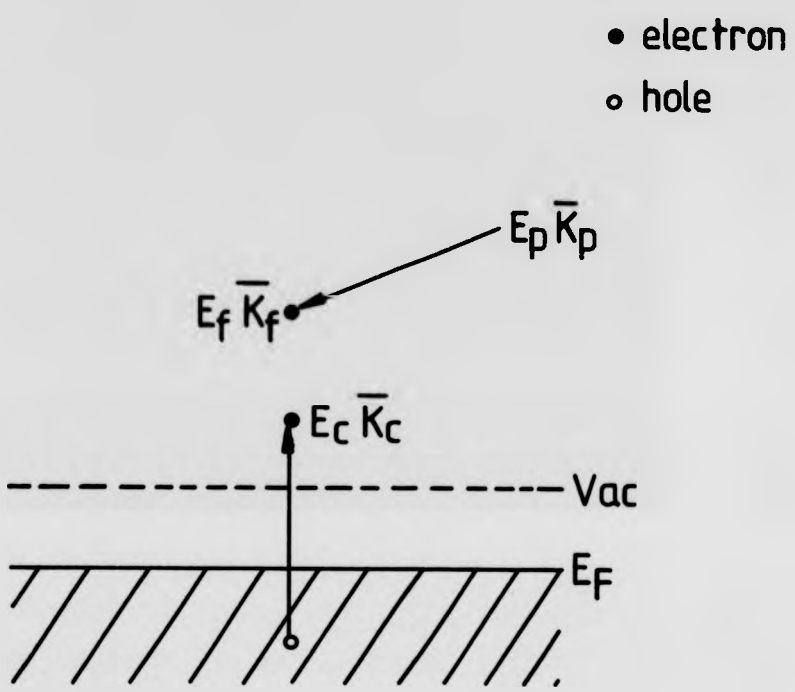

Fig. 5.4 The secondary electron excitation process.

Chung and Everhart have made several approximations to the dielectric function in equation 5.19 in order to separate the contribution to the probability of excitations from electron-electron scattering and plasmon decay. For very small momentum transfers, the $1/q^4$ term will dominate equation 5.19.

5.2.4.1.1 Excitations by Screened Electron-Electron Scattering

Chung and Everhart have used the static form of the Lindhard dielectric function in order to describe the direct electron-electron scattering between the incident primaries and lattice electrons which are themselves represented by the free electron gas model. The Lindhard dielectric function is given by $\lim_{q\to 0} \varepsilon_L(q,0) = 1 + q_{FT}^2/q^2$ where q_{FT} is the Thomas-Fermi screening vector and its appropriate for excitation of very low energy SEs. With further assumptions that

$\langle K_p \, | e^{iq\cdot r} | \, K_f \rangle = \delta K_f, K_p+q$, indicates the primary electrons before and after scattering are described by plane waves and since for q very small $e^{iq\cdot r} \to 1$, and that the crystal electrons are described by plane waves, then equation 5.19 is rewritten to give the SE contribution due to electron-electron scattering as

$$P(K_p,K_\nu \to K_f,K_c) = 2\pi/\hbar \left[4\pi e^2/\Delta \right]^2$$

$$\times \Sigma_q \, f_0(E_\nu)(1-f_0(E_c))\delta K_f,K_p+q$$

$$\delta(E_p+E_\nu-E_f-E_c)/(q^2+q_{FT}^2)^2 \qquad \ldots(5.20)$$

where f_0 is the Fermi-Dirac distribution function.

Rosler and Brauer however have used dynamical screening approximations to the Lindhard dielectric function. For the case of SEs of energy E > 100 eV they showed that the use of an unscreened excitation function was sufficient approximation. At lower energies this approximation was no longer sufficient and over estimated the excitation rate. Thomas-Fermi approximation on the other hand under estimated the excitation rate throughout the relevant energy range. Rosler and Brauer also included a contribution by the excitation of core electrons but this was found to be too small.

5.2.4.1.2 Excitation by Decay of Plasmons

This mechanism, manifests itself, by the appearence of fine structure on the external secondary EDC. Plasmons excited by the fast primaries, decay via single particle excitations from the valence band. The energy positions of the fine structure on the EDC, correspond to $\hbar\omega_p - \Phi$, with reference to the vacuum level.

5.2.4.1.2.1 Excitation by Decay of Volume Plasmons

The volume plasmon decay contribution to the excitation of SEs, was quantitatively determined by Chung and Everhart who have evaluated the plasmon pole contribution to the dielectric function in equation 5.19 i.e. $|1/\varepsilon(q,\omega)|^2$. The wave vector and frequency dependent dielectric function $\varepsilon(q,\omega)$ has been evaluated for small q and ω near ω_p. For aluminium, ε_1 is very small in the vicinity of q = 0 plasmon frequency and consequently $|1/\varepsilon|$ has a large resonance for small ε_2. Chung and Everhart arrived at the following rate expression for plasmon decay contribution to the SEs

$$\lim_{q\to 0} P(K_v \to K_c) = [4\pi e^2 \omega_p/\hbar q^2 \Delta]^2$$

$$\times [\Gamma/2(\hbar\omega-\hbar\omega_p)^2+(\Gamma/2)^2]\ F(E,\hbar\omega) \qquad \ldots(5.21)$$

where A of equation 5.21 is the transition rate for generating long wavelength plasmons and $F(E,\hbar\omega)$ is the electron energy distribution due to plasmon decay via vertical interband transitions and Γ is the damping constant for $\lim_{q\to 0} \hbar\omega_p \epsilon_2(q,\omega_p)$, and $F(E,\hbar\omega_{\bar{p}})$ is also the optical energy distribution of the joint density of states JDOS. Equation 5.21 therefore describes the creation of plasmons with q = 0 which subsequently decay via vertical interband transitions, producing secondary electrons.

5.2.4.1.2.2 Excitation by Decay of Surface Plasmons

As for decay by volume plasmons, Chung and Everhart have also calculated the contribution to SEs by decay of surface plasmons created by incident primaries. Their expression for differential probability per unit distance and energy of SE excitation is

$$P\ (\ K_n \to K_c)/dE = 2\ Q\ e^{-2Qz} F(E,\hbar\omega_s) \qquad \ldots(5.22)$$

where Q is the two dimensional wave vector of the surface plasmon field, z is the vertical depth below the surface and $F(E,\hbar\omega_s)$ is the normalised energy distribution of surface plasmon decay via single electron excitation, $2Q\ e^{-2Qz}$ is the probability per unit distance of exciting SEs inside the solid by the exponentially decaying plasmon field into the solid.

5.2.4.2 Transport and Escape

In the treatment of the transport and escape of the SEs due to electron-electron collisions and volume plasmon decay, Chung and Everhart assumed that these suffer no scattering on their way to the surface. In addition, SEs excited in the above way suffer a once only scattering before escaping into vacuum across the potential barrier. In the case of single particle excitations due to surface plasmon decay, these are assumed to escape after creation without subsequent scattering, due to their proximity to the surface. Chung and Everhart have considered inelastic MFP, mean escape depth and refraction effects at the surface to relate the external angular and energy distribution to the internal distribution. Rosler and Brauer have solved the Boltzmann transport equation in which they also took into consideration elastic scattering of the internal secondaries. Bindi et al have used a similar approach.

5.2.4.3 Applications to Aluminium

The above theoretical analysis of SEE has been applied to aluminium by Chung and Everhart, and Rosler and Brauer for primary electrons of energy, E_p = 1 - 2 keV, incident normal to the surface. In summary, interesting variables calculated include the external energy and angular distributions of the true secondary electrons and the true and total yields δ and σ. The total SE current is expressed as a sum of each individual contributing process and the integration of the externally observed SE current over all angles of a hemisphere gives the energy distribution

$$J(E) = \int J(E,\Omega)\, d\Omega \qquad \ldots(5.23)$$

The angular distribution of the true SEs was obtained by integration over the conventional energy range

$$J(\Omega) = \int_0^{50} J(E,\Omega)\, dE \qquad \ldots(5.24)$$

and the total yield σ is given by

$$\sigma = \int_0^{E_p} J(E)\, dE = \int_0^{50} J(E)\, dE + \int_{50}^{E_p} J(E)\, dE = \delta + \eta \qquad \ldots(5.25)$$

True SE generated by the incident and backscattered primaries are also given by $\delta = \delta_p + \eta\delta_b$ and coefficient $\beta = \delta_b/\delta_p > 1$ defines the empirical production efficiency of backscattered primaries for SEs.

The results of Chung and Everhart for the external secondary EDC and its derivative are shown in Figs. 5.5(a) and 5.5(b). The following parameters were used E_F = 11.6 eV, ϕ = 4.0 eV, E_p = 1 and 2 keV, and Γ_S and Γ_B of 1 eV and 2 eV (Γ_S and Γ_B are the plasmon damping parameters, which determine the plasmon peak FWHM width, which in turn depends on the nature of the sample surface, whether single crystal or polycrystalline surface and grain sizes).

The above theoretical results for the external EDC show the contributions by volume plasmon decay, electron-electron scattering and surface plasmon decay. The dominant contribution is due to volume plasmon decay. Also predicted, are two broad humps on the EDC at $\hbar\omega_S - \phi_{AL}$ and $\hbar\omega_B - \phi_{AL}$ which correspond to 6.0 and 10.5 eV above the vacuum level. Good overall agreement exists between theoretical and experimentally obtained EDCs and their differentials (see section 6.2.3). Also the calculated cascade peak width are in good agreement with experimental values.

Fig.5.6(a) shows the angular distribution of SEs for E_s = 2 eV as calculated by Rosler and Brauer. As can be seen the distribution is pure cosine like, confirming Jonker's experimental results, and contributions by

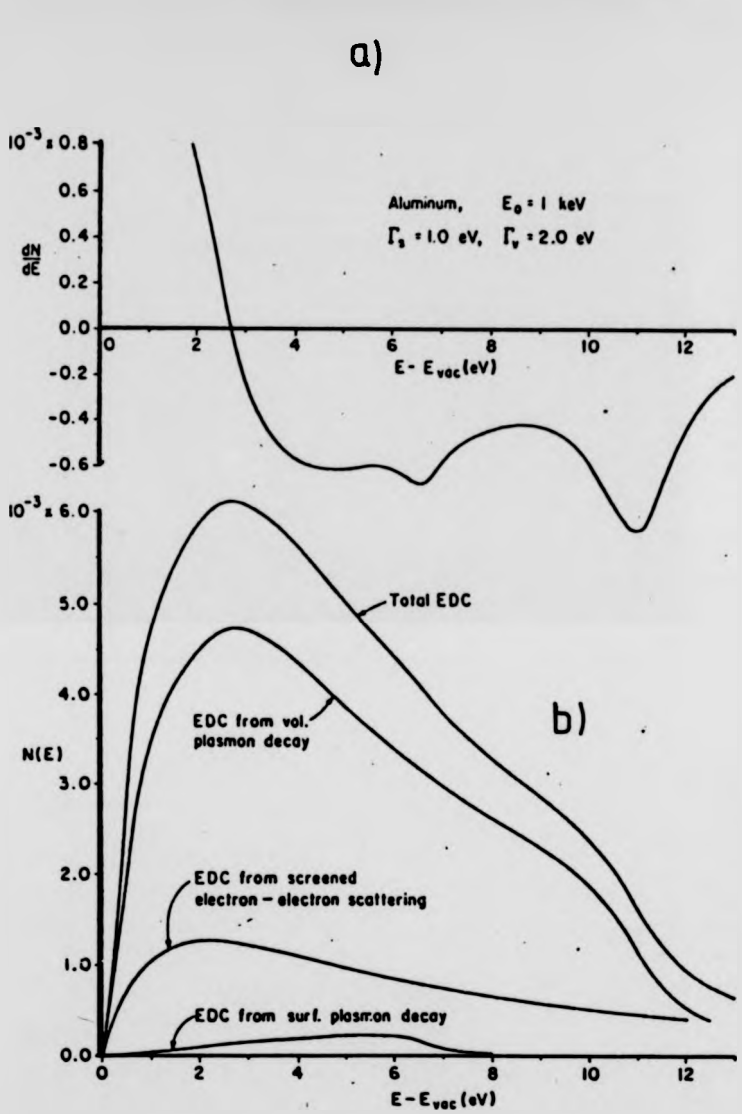

Fig. 5.5 (a) Calculated secondary electron distribution curve (EDC), differentiated. (b) EDC, N(E) and contribution to it by surface and bulk plasmon decay and screened electron-electron scattering (reproduced from Chung and Everhart 1977).

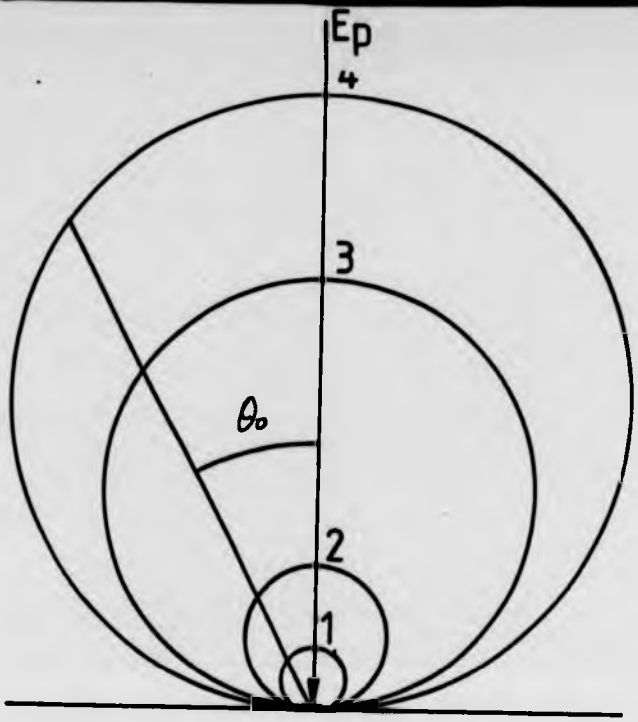

a)

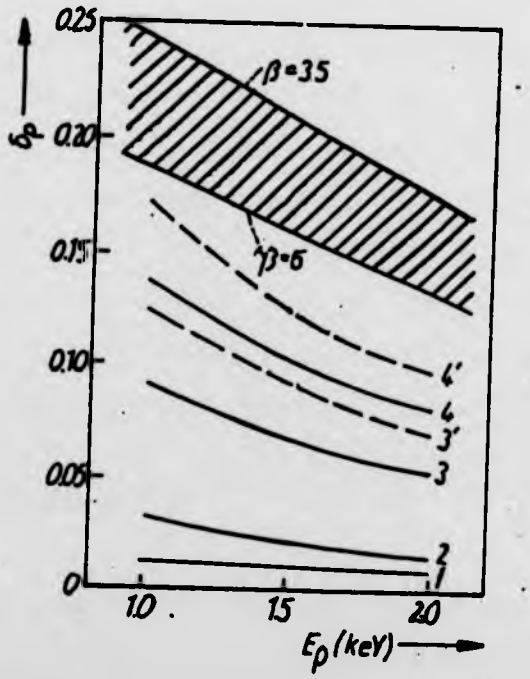

b)

Fig. 5.6 (a) Angular distribution of secondary electrons and contributions by core-excitation (1), electron-electron scattering (2), plasmon decay (3) and total contribution to the angular distribution (4)

(b) Energy dependence of the true yield and contributions to it by same mechanisms as above (reproduced from Rosler and Brauer 1981b)

electron-electron scattering (2), core electrons (1), volume plasmon decay (3), and total distribution (4) for E_p = 2 keV are also illustrated.

The secondary electron yield calculations of Rosler and Brauer also give good agreement with experiment. Fig. 5.6(b) shows the contribution of core-electron, electron-electron scattering volume plasmon decay to the true secondary yield δ_p as a function of primary electron energy E_p from 1 to 2 keV.

In table 5.1 numerical values of SE yield δ_p for E_p = 2 keV have been summarised. These calculated values of δ_p by Rosler and Brauer are a factor of two, less than the experimentally observed values.

Bindi et al and Ganachaud and Cailler have also obtained results of theoretical calculations of the secondary yield δ and its dependence on E_p in the range 0.4 - 2 keV. Their results also show good agreement with experiment. The discrepancies with experimental values can be attributed to various simplifying assumptions stated at the beginning of the chapter. Also contributions to the true yield, due to Auger and ionisation processes and diffraction effects where enhancement of emission can occur at particular external angles to the normal have not been considered and this effect will be prevalent for single crystals of aluminium.

5.2.4.4 Conclusions

In this chapter a semi-empirical basic theory of SEE has been given, followed by a description of results of a quantum mechanical treatment of the production of SEs. The cascade theory of SEE gave good qualitative results for the external energy distribution of SEs. In the second part of the chapter, the SEE theories dealing with plasmon decay mechanism was

Table 5.1 Summary of numerical calculated values of secondary electron yield δ_p (due to the primary electrons) by Rosler and Brauer. and Chung and Everhart for E_p = 1 and 2 keV.

	Primary Energy E_p (keV)	δ_p	Contribution by c-e	e-e	VP
Rosler and Brauer	1	0.14	0.01	0.03	0.09
	2	0.10	0.01	0.02	0.07
Chung and Everhart	1	0.051			
	2	0.038			

considered. Contribution by these to the EDC and yield was shown to be dominant particularly for aluminium. Fine structure observed on the EDC was correctly predicted by this theory.

In the next chapter a review of the experimental SEE studies performed on aluminium and oxygen exposed aluminium surfaces will be reviewed.

CHAPTER SIX

REVIEW OF EXPERIMENTAL SECONDARY ELECTRON EMISSION YIELD STUDIES OF CLEAN AND OXYGEN COVERED ALUMINIUM SURFACES

6.1 Introduction

Clean and oxidised surfaces of aluminium have been extensively studied by use of secondary electron yield measurements. The primary aim of these studies had been to establish the suitability of Al_2O_3 in technological applications and to test various theories of SEE which had been developed in terms of experimentally measured yield parameters.

This chapter will review some of these studies, together with electron transmission and reflection characteristics of self supporting Al films bombarded by keV electrons. Particularly the contribution of the inelastically backscattered primary electrons to the total yield. Also in this chapter, a small number of recent experimental studies which have concentrated on measuring the evolution of the total yield with oxygen coverage in UHV environments on very clean aluminium sample surfaces will be reviewed. In particular those experiments which sought to examine the contribution of decaying plasmons to the slow secondary electron distribution and hence to the total yield.

Finally, the role of SEE in ESD and decomposition will also be reviewed, since this aspect plays a major role in the determination of desorption cross-sections with primary energy.

6.2 True, Total and Backscattering Coefficient Measurements from Aluminium Surfaces

Thomas and Pattinson (1970) have measured the total secondary electron yield σ, and the backscattering coefficient η, as a function of primary electron energy E_p in the range 75 - 2000 eV. They deposited in-situ thin films of aluminium of known thickness (25 - 750 Å) monitored by a quartz crystal micro-balance, on to substrates of Pt, Au and Ag which exhibit backscattering coefficients much higher than aluminium. They recorded σ and η plots, automatically within a matter of seconds by direct measurement of the ratio of the collected secondary current to the incident primary current. Such a typical set of σ, plots for aluminium films of thickness 25 - 650 Å, deposited onto a Pt substrate is shown in Fig. 6.1(a) and is reproduced from Thomas and Pattinson.

Curve J is characteristic of bulk aluminium and no contribution from the underlying substrate is apparent. Its shape is typical of total secondary electron yield curves for other materials. The initial smooth rapid rise in σ at low E_p is followed by a broad maximum at several hundred electron volts, after which it slowly decreases.

Thomas and Pattinson report a value of 0.96 for σ_{max}, which occured at an E_p of 350 eV. Kollath (1956) also determined the value of σ_{max} to be 0.95 but Dobretsov and Gomoyunova (1966) reported a value of 0.89. At an E_p of 2 keV, Dobretsov and Gomoyunova, and Bronshtein and Denisov (1967) quote yields of 0.51 and 0.49 respectively, compared with 0.66 of Thomas and Pattinson whose measurements were probably more accurate due to their measurement technique and UHV conditions.

It is apparent from Fig. 6.1(a) that at higher primary energies of 1 - 2 keV the contribution to the total yield of Al, by the underlying substrate is significant up to 650 Å thick layers. Fig. 6.1(b) which has also been reproduced from Thomas and Pattinson shows the variation of η as a function

a)

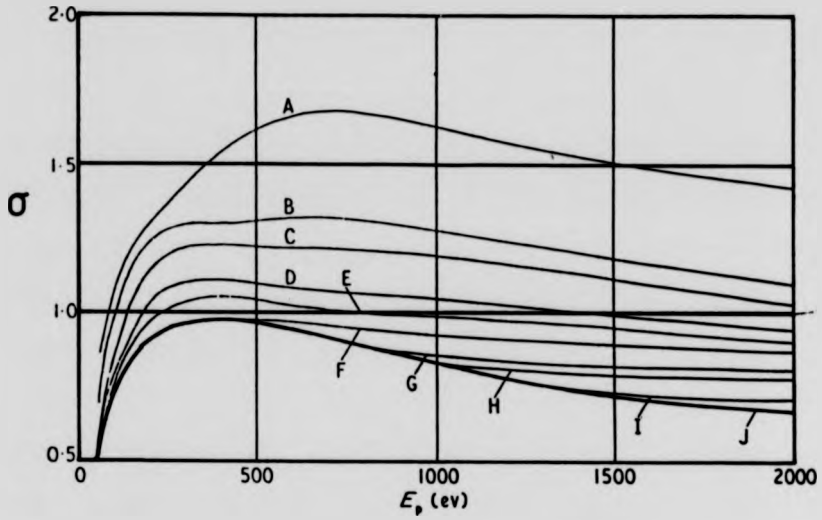

b)

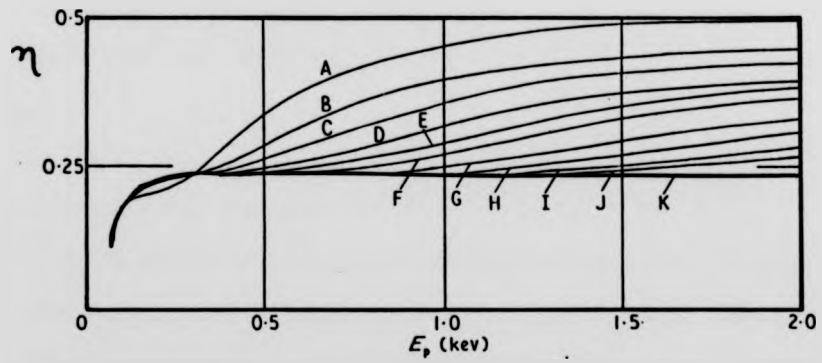

Fig. 6.1(a) σ characteristics of thin films of Al on Pt substrate. Curves A, Pt; B, 50; C, 75; D, 100; E, 150; F, 200; G, 350; H, 450; I, 650 A; J thick Al film.

(b) η versus E_p characteristic of thin films of Al thicknesses as in (a) (reproduced from Thomas and Pattinson 1970).

of E_p. For a thick Al film (> 1000 A) η increases steeply at first, reaching a value of .23 at around 250 eV. There after it remains constant up to 2 keV. A backscattering coefficient of 0.23, implies that 23% of the incident primaries, after under going inelastic and elastic collisions with the sample atoms, escape as secondaries. Of course there is no way one can distinguish these from true secondaries except by an arbitrary energy cut off limit of 50 eV above which all the electrons are supposed to be backscattered primaries.

Bronshtein and Fraiman (1961) have quoted a value of 0.21 at 2 keV and 0.22 at 1.2 keV. However Sternglass (1954), Holliday and Sternglass (1957), and Kanter (1961) found a backscattering coefficient of 0.14 at 2 keV. But their samples had been evaporated in very poor vacuum conditions, on nitrocellulose backing film which were subsequently baked at atmosphere at room temperatures of 200°C to give self supporting films of various thickness.

Consequently the films developed thick oxide layers on the surface and more probable oxygen and carbonacious contamination throughout the bulk. These samples were subjected to bombardment by keV electrons to determine the reflection and transmission coefficients of the materials and estimate the rate of energy loss i.e., the stopping power, and determine the range of the primary electrons as a function of primary energy.

At the time it was assumed that, since only the back scattered electrons were collected, this represented a property of the bulk and the contaminated surface did not influence the final result, since the true secondary electrons were not collected. (these emerge from the top few atomic layers of the surface and are very strongly dependent on the topography, physical and chemical nature of the surface.)

Thomas and Pattinson were also able to obtain estimates of the primary electron range R, from development of σ and η plots as a function of primary energy for progressively thicker Al films (25 - 1000 A). At certain primary energies, breaks in the σ plot, correspond to that film thickness for which, the primary electron has sufficient energy to penetrate the Al film, interact with the substrate and return through the Al film and just escape as a backscattered electron. This distance corresponds to twice the film thickness which was shown by the transmission and reflection experiments of Lane and Zaffarano (1954), Young (1956), Holliday and Sternglass (1957) and Cosslet and Thomas (1964).

Fig. 6.2 is reproduced from Thomas and Pattinson and shows the primary electron range R(A) against primary electron energy which extended down to 200 eV. This so called **energy-range** relationship is of the form $R = K E_p^n$ where the exponent n was measured to be 1.3 for Al (n is normally assumed to be 2 i.e., the Thomas-Whiddington law) and K is a property of the bulk and hence different for different materials. The range-energy relationship is quite an important parameter in deriving SEE theories because it can be used to make estimates of the number of secondary electrons generated by the penetrating electrons as they slow down (see also section 5.2.1).

Thomas and Pattinson were also able to obtain an estimate of the escape depth X_s, of the true secondaries (E_s = 0 - 50 eV) from plots of $\delta = (\sigma - \eta)$ versus film thickness d for various values of primary electron energy. δ decreases with increasing film thickness. The value of X_s was determined by extrapolation and varied between 50 - 80 A $\pm$10 A.

The importance of the contribution of the backscattered primaries to the slow secondaries was demonstrated by Bronshtein and Segal, and Kanter. On their way to the surface, backscattered electrons lose energy via

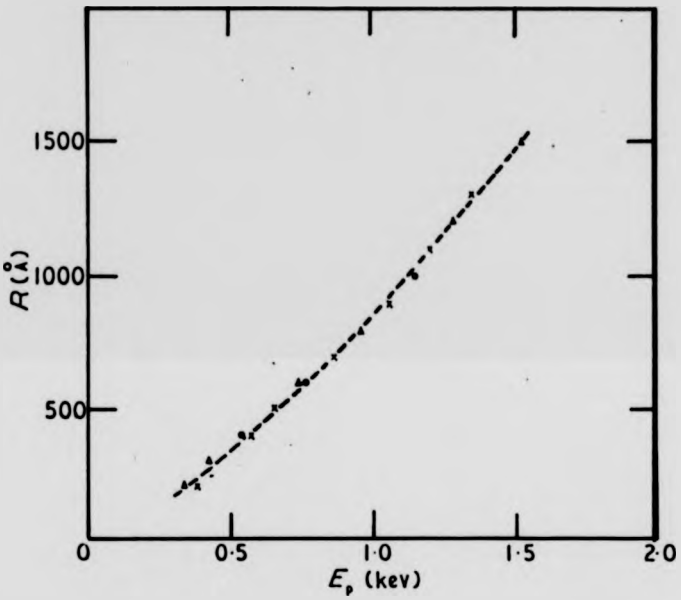

Fig. 6.2 Maximum range against primary energy as obtained from Al on Pt (x) Au (▼) and Ag (●) substrates (reproduced from Thomas and Pattinson 1970).

collisions and liberate more secondary electrons due to the cascade process. Kanter (1961) measured the fractional backscattering ratio η/η_{bulk} and fractional true yield δ/δ_{bulk} from various film thickness of Al and bulk aluminium. He plotted these fractional terms as a function of primary energy in the range 1 - 10 keV. By extrapolation to zero fractional backscattering ratio, the fractional true yield, was determined to be 0.60. Thus Kanter had shown that the backscattered primaries generated 40% of the true secondaries even though the ratio to the incident beam was only 0.14. (cf Thomas and Pattinson's 0.22).

An efficiency parameter β had been defined to estimate the effectiveness of the backscattered electrons in generating slow secondaries and Thomas and Pattinson estimated the values of β to lie in the range 5.8 to 3.2 for E_p = 1 - 2 keV. Bronshtein and Segal, and Kanter had obtained very similar figures.

Secondary electron yield parameter measurements on evaporated aluminium reported by Thomas and Pattinson would appear to be the more reliable because of the use of UHV. Even though at the time the surface could not be directly characterised by AES. More recent measurements would appear to confirm this.

Pillon and Ganachaud et al (1977) have used a four grid LEED/AES spectrometer with a coaxial electron gun to characterise a clean surface of single crystal of Al(421) by AES and ELS methods. The sample surface previously had been ion sputtered and annealed for several cycles. Total secondary electron yield σ as a function of primary electron energy up to 600 eV was measured for normal incidence. From their yield plot, σ_{max} has a value of 0.98 and occurs at a primary energy of 250 eV. This value of σ_{max} is in very good agreement with that of Thomas and Pattinson, but they

found their E_{pmax} to be at 350 eV. Bronshtein and Fraiman report an E_{pmax} at 400 eV which is much higher than the value quoted by Thomas and Pattinson.

Bindi, Lanteri and Rostaing (1980) who have used similar apparatus to Pillon and Ganachaud et al, report similar total yield, and true yield parameter measurements to Thomas and Pattinson for evaporated aluminium films. The differences in the results does appear to be due to the nature of the surfaces . Evaporated films displaying higher E_{pmax} than single crystals of Al.

Pillon and Ganachaud et al, and Bindi et al have also presented theoretical models of SEE based on Monte Carlo Simulation methods and three step models as discussed in section 5.2.3, and these have been tested by their experimental yield results which will further be discussed in section 6.2.3. Cailler, Ganachaud and Roptin (1981), also show the variation of the backscattering coefficient η, with primary energy up to 600 eV for a clean single crystal of Al. For a primary energy range of 100 - 230 eV, η increased and reached a maximum around 230 eV at $\eta = 0.22$, by 600 eV η had decreased to 0.20.

Fig. 6.3 shows the variation of σ and η as a function of E_p, as reported by the most recent workers. The most striking difference does appear to be the location of E_{pmax} which is much higher for evaporated polycrystalline samples than for single crystals of aluminium.

6.2.1 Total and True Yield of Fully Oxidised Al Surfaces

The total secondary electron emission yield σ of a clean metal surface is known to increase upon oxidation considerably. Consequently fully oxidised

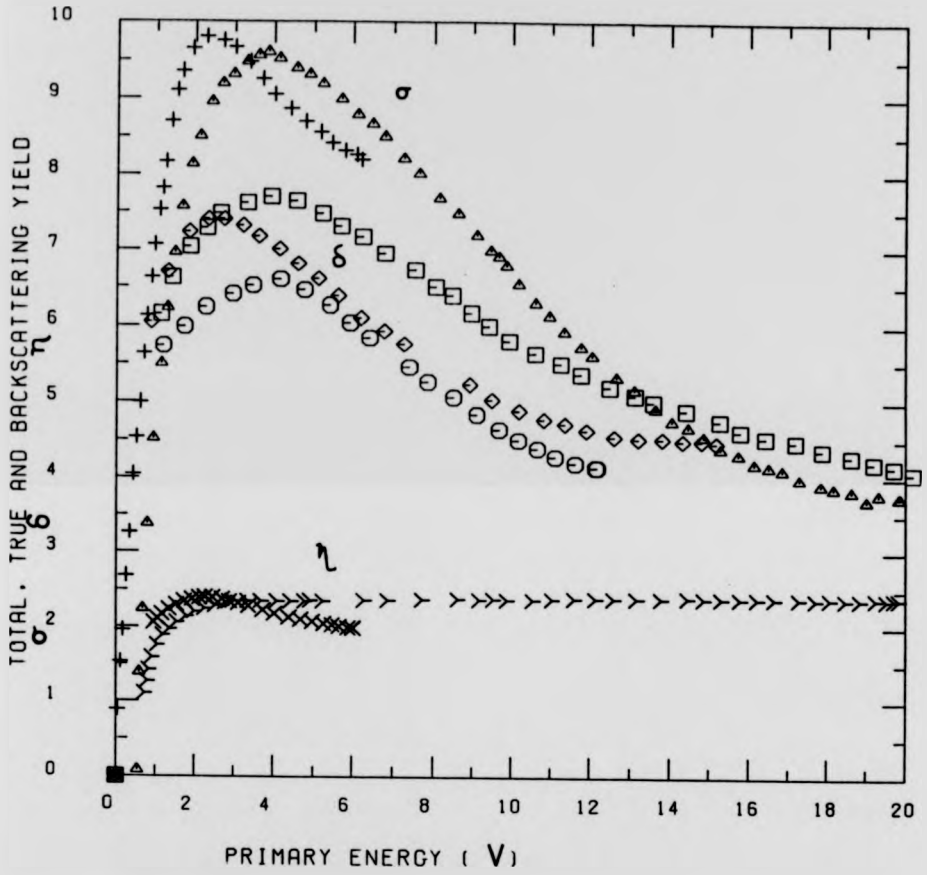

AUTO/PB/09 JUL 1985

Fig. 6.3 Variation of σ, δ and η as a function of E_p as reported by most recent workers (x, + and ◆ Roptin 1975; ➢, ▲ Thomas and Pattinson 1970; ◪ Bindi et al 1980; ⊖ Bronshtein and Fraiman 1961.

metal surfaces exhibit very large secondary electron yields. There are very serious practical problems associated with yield measurements of insulators, due to surface charging, and consequent electron beam induced effects (as discussed in chapter 3). The number of published data on Al_2O_3 is very small and these date back to the 1930's and 1960's. Bruining and de Boer (1938), Salow (1940) and Shulman and Makedonsky et al (1953), have reported σ measurements for Al_2O_3 films on conducting substrates using pulse techniques.

Values reported vary between 2 - 9 and some of these variations may be due to contaminated surfaces since the experiments were conducted in high vacuum conditions. The primary electron energy at maximum yield was reported to be around 700 eV. Dawson (1966) employing similar pulse methods and charge neutralisation techniques, reported true secondary electron yield δ, measurements for various commercial ceramics including sapphire. His measurements were carried out in UHV conditions, for normal incidence electron beams in the energy range 10 - 3000 eV.

For the unpolished, as received sapphire surface, the true yield maximum δ_{max} was reported to increase from 6.4 to 7.8 when the surface had been highly polished and ground. The corresponding primary energy occured at 650 eV. The increase in yield after polishing implied that the original surface was probably heavily contaminated with a carbonacious layer which inhibits secondary electron emission. Fig. 6.4 shows δ as a function of E_p for the unpolished and polished sapphire surfaces reproduced from Dawson (1966).

6.2.2 Variation of SEE Yield with Oxygen Exposure of Al Surfaces

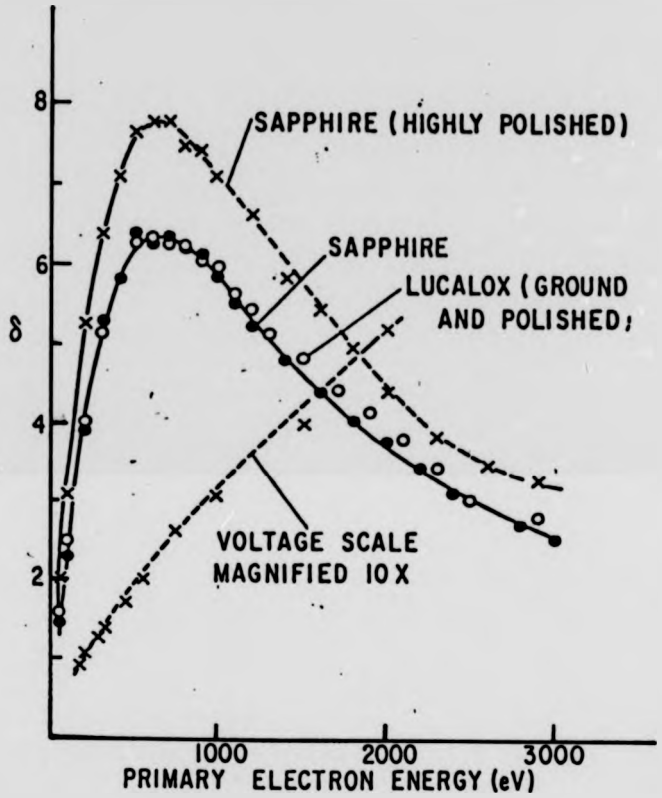

Fig. 6.4 True yield δ versus E_p for the unpolished and polished sapphire surfaces (reproduced from Dawson 1966).

In the preceding sections it was established that, 78% of the total maximum yield of a clean aluminium surface is entirely due to the true secondary electrons i.e. of energy 0 - 50 eV. Of these 40% were estimated to be directly generated by the energetic inelastically backscattered primary electrons, but a small percentage of the elastically scattered electrons also contribute to the total yield. The variation of σ and its components as a function of oxygen exposure has not been studied widely.

But its values are expected to lie in a range for that of clean Al and fully oxidised Al surface. One such study was carried out recently by Pellerin and Le Gressus (1980), who have investigated the contribution of the true secondary electrons, inelastically and elastically backscattered electrons to the total yield σ for a clean Al surface which was subsequently exposed to oxygen at various levels. The primary energies employed were in the range 30 - 400 eV.

The polycrystalline sample was subjected to various argon ion sputter and anneal cycles. The surface cleanliness was confirmed by AES and ELS employing a CMA with a coaxial electron gun. The clean surface was exposed to oxygen in the range 0 - 10^4 L and slow secondary electron spectra (0 - 30 eV), elastic peak spectra ($E_p \pm 2$ eV) and electron loss spectra (E_p-2) - 28 eV was recorded. They measured the total yield σ by monitoring the absorbed sample current and incident primary current such that $\sigma = (I_p - I_a)/I_p$. Since the spectra were acquired in the EN(E) mode, a correction was made to take into account the CMA resolution and converted to N(E). Pellerin and Le Gressus then integrated the spectra within appropriate limits to give areas corresponding to the slow secondary electron current α, the electron loss current β and the elastic peak current γ.

The results reproduced from Pellerin and Le Gressus are shown in Fig. 6.5 which shows the variation of σ, α, β and γ with oxygen exposure for a primary energy of 100 eV. From this figure it is clear that β decreases with oxygen exposure while σ, and α increased smoothly and γ showed a sudden increase around 10-15 L. Pellerin and Le Gressus also report that the general evolution of the parameters σ, α, β and γ with oxygen exposure were similar for other E_p (30, 50, 250, and 400 eV) with following observations, that for $E_p < 250$ eV γ, dominates the entire N(E) curve and provides the major contribution to σ. For $E_p > 250$ eV, α provided the major contribution to σ. The electronic processes, contributing to the slow secondary electron current and the shape of the experimental slow secondary electron yield curves of Al have been discussed in chapter 5 and will further be discussed in the next section. The value of σ_{100} for the clean Al surface as found from Fig. 6.5 to be 0.67 and after 10^4 L of oxygen exposure to 1.17.

From chapter 4, it is clear that the chemisorption stage (0 - 30 L) is followed by oxidation. This is known to enhance the number of escaping electrons due to an increased escape depth of secondary electrons and which results from a modification of the band structure and the effective work function (electron affinity χ + E_g band gap and this aspect has been discussed in section 4.2.3).

It seems that the conclusions reached by Pellerin and Le Gressus on the contribution of α to σ may have been under estimated largely due to the unreliability of the CMA when very low energy spectra are being recorded (see Appendix B). The CMA is known to distort the true secondary electron spectra (i.e. EDC) due to the erroneous transmission of the CMA . Therefore α is expected to dominate σ even down to 100 eV. This conclusion

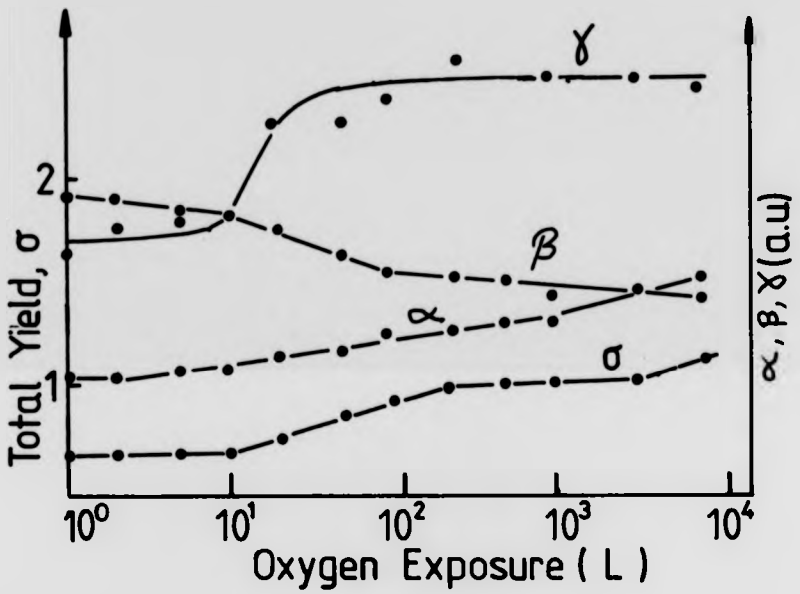

Fig. 6.5 Variation of total yield σ, elastic peak current γ plasmon loss current β and slow secondary electron current α with oxygen exposure. E_p = 100 eV and spectra obtained with a CMA (reproduced from Pellerin and Le Gressus et al 1980).

of Pellerin and Le Gressus will be further discussed in the results and discussion of chapter 8.

Pellerin and Le Gressus in an extention of their results, after examining the secondary EDC and the fine structure superimposed on it, as well as ELS spectra, reached the conclusion that the contribution to the EDC by plasmon relaxation was small compared with single electron excitations from the O_{2p} chemisorption resonance level and several final states above E_F. This aspect of this paper was further reviewed in section 4.2.3 and will further be discussed in the next section (6.2.3).

6.2.3 Plasmon Decay Contribution to SEE from Aluminium

The slow secondary electron distribution curve EDC, normally has a peak around 1-2 eV above the vacuum level, and FWHM of 8 eV and a smooth profile. This picture is true for most materials. But the assumption that the slow secondary EDC, carries no specific information about the material was shown to be wrong with the advent of high resolution electron spectrometers, which revealed fine structure superimposed on to the EDC, several eV's above the vacuum level. That these may be directly due to decaying plasmons excited by the impacting primary electrons was first suggested by Gornyi, Rakhovic and Skirko (1967) when they observed such structure on the EDC of evaporated films of Aluminium. Since then, a succession of research workers have shown the existence of such structure and these have been linked directly to the plasmon loss peaks accompanying the elastic peak.

Among those workers who have reported such structure are Jenkins and Chung (1971), Powell and Woodruff (1972), Wright and Pattinson (1972), and Henrich (1973). These authors have all used 3 or 4 grid retarding grid

analysers, and employed a variety of Al samples including single crystals. The sample surfaces were subjected to cycles of argon ion bombardment and annealing. N(E) and dN(E)/dE spectra of the slow EDC showed fine structure at 5.5 and 10.5 eV above the vacuum level. The 5.5 eV correlated with the appearence of the 10.5 eV surface plasmon loss peak and the 10.5 eV EDC peak with the 15.5 eV bulk plasmon loss peak. More recently Ozkok (1983), and Ozkok, Webber and Dobson (1983) reported very similar results utilising a photometer to measure angle-integrated and angle-resolved spectra from the LEED screen.

The retarding grids of the RFA were appropriately biassed so that spurious slow peaks associated with SEE from the grids were safely ruled out. The fine structure on the EDC were found to be very sensitive to surface contaminants, particularly the 5.5 eV peak. (Auger effects diffraction effects and band structure effects were ruled out).

Powell and Woodruff, suggested that the fine structure observed on the EDC is due to decay of plasmons which excite single electrons from top of the Fermi level across the surface barrier into vacuum. Aluminium has a work function of $\simeq$ 4.0 eV and the effective analyser work function is also $\simeq$ 4.5 eV. Hence the structure appear at $\hbar\omega_B - \Phi$ and $\hbar\omega_S - \Phi$ above the vacuum level.

Henrich on the other hand, proposed a different mechanism to account for the origin of these peaks. He suggested that the hot electrons inside the solid with energy $E_s > \hbar\omega_B + E_F$ have a high probability of exciting bulk plasmons $\hbar\omega_B$ and hence lose energy, thereby decreasing the density of electrons above $\hbar\omega_B + E_F$ hence this would result in a change of slope around $\hbar\omega_B - \Phi$ on the EDC. A similar argument would also apply to the surface plasmon linked peak.

In an attempt to discover the true origins of the observed structures on the true secondary EDC of clean and slightly oxidised Al, Everhart and Saeki et al (1976) using a similar experimental set up to Henrich but employing sample bias modulation techniques have recorded N(E) and dN(E)/dE spectra of EDC and ELS regions.

The results of Everhart and Saeki et al have been reproduced in Fig. 6.6 which shows low energy spectra obtained for various primary electron energies for the sputter cleaned polycrystalline sample. Essentially these results confirm the previous work already reviewed. In that for the slightly oxidised surface the EDC became narrower, structure associated with the surface plasmon disappeared and the bulk plasmon linked peak decreased substantially. From a consideration of the plasmon dispersion relation, Everhart and Saeki et al have concluded that plasmon decay into single electron excitation and energy loss through plasmon creation mechanisms could both be plausible but preferred the former because the discontinuities suggested by Henrich were not observed on the EDC.

Pillon, Roptin and Cailler (1976) have produced a more convincing experimental evidence towards the plasmon decay hypothesis. Using a single crystal (421) of aluminium Pillon et al recorded true secondary electron spectra and ELS from the oxidised and clean Al surfaces. They also noticed that the EDC corresponding to the clean surface had structures at 5.5 eV and 10.5 eV above the vacuum level and was rather broad. Where as for the slightly oxidised surface, the EDC was narrower with the 10.5 eV feature recognisable as a hump. Also for the clean surface, Pillon et al noticed that the intensity of the 10.5 eV surface plasmon loss peak diminished sharply, when E_p fell slightly below 30 eV. From these observations Pillon et al, dismissed Henrich's hypothesis since this had predicted structure on the EDC for the surface plasmon peak i.e. $E_S > \hbar\omega_S + E_F \simeq 20$ eV, was not

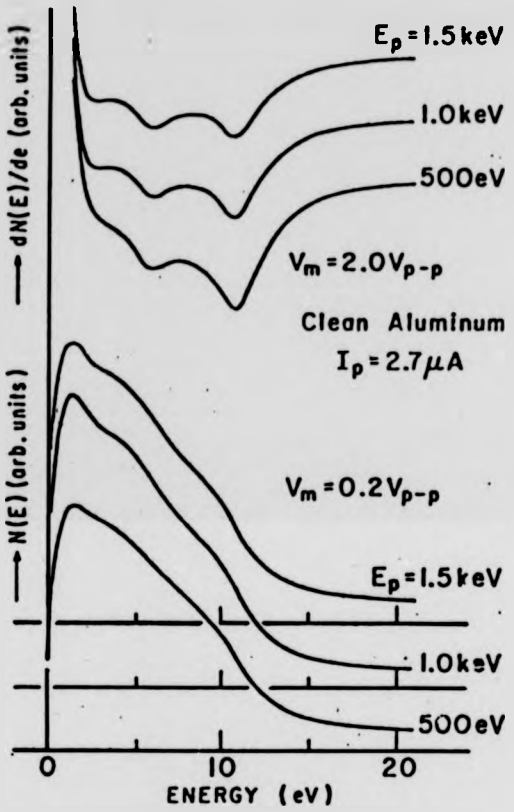

Fig. 6.6 Experimental slow secondary electron spectra N(E) and dN(E)/dE obtained at various E_p, for clean Al surfaces using an RFA (reproduced from Everhart et al 1976).

observed.

Further more, they produced a qualitative estimate of the contribution of the decaying plasmons to the SEE observed on the EDC. This they did by noting the increase in the area under the plasmon loss peaks upon cleaning of the sample surface and noting the resultant increase in the area under EDC. This procedure is shown in Fig. 6.7 which is reproduced from Pillon et al (1976).

Another observation which makes Henrich's hypothesis of SEE production through energy loss via plasmon creation unlikely, is the fact that discontinuities are to be expected at energies $\hbar\omega_B - \phi_{Al}$. Instead all experimental results point to structures in the form of humps.

The importance of the plasmon decay phenomenon to the secondary electron emission from Al, was realised by Chung and Everhart (1977), Pillon and Ganachaud et al, Bindi et al (1980) and more recently by Rosler and Brauer (1981) who have devised theoretical calculations and models, which show the plasmon decay contribution to SEE and hence yield to be very important. These theories have already been introduced in chapter 5. Chung and Everhart's theory successfully predicts the plasmon decay structure on the EDC.

6.3 Electron Beam Effects due to SEE

This aspect of secondary electron emission was already introduced in chapter 3. SEE, plays an important role in the studies of electron stimulated desorption and decomposition from gas adsorbed metal surfaces and insulators. Since for most of the ESD processes, threshold energies occur in the range 10 - 40 eV, the primary energy dependence of the

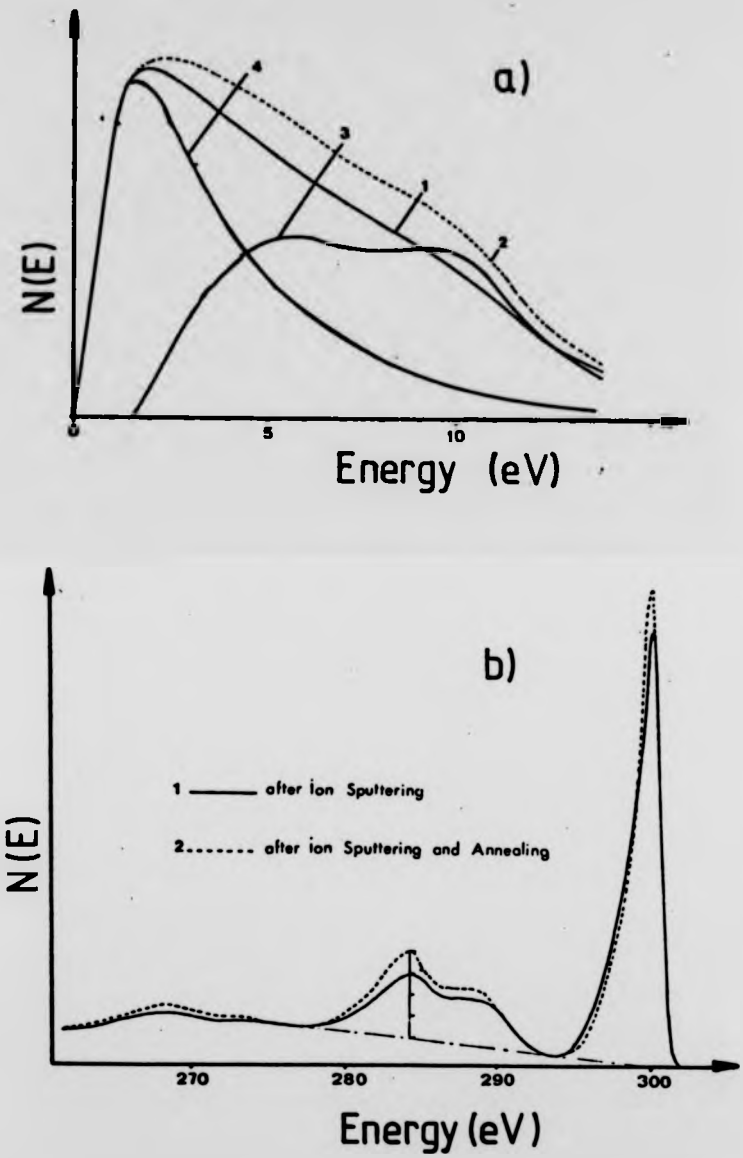

Fig. 6.7 Changes in the EDC due to variation in the relative intensity of the plasmon loss peaks (reproduced from Pillon et al 1976).

secondary electron yield becomes an important parameter to consider in such studies.

The primary electron energy dependence of the measured total desorption cross-sections, can be described in terms of the magnitude of the energy distribution of the secondary electrons, since the true secondary electrons dominate the total yield for primary electron energies in excess of 100 eV. For high primary energies (keVs) the total yield will be decreased and hence the contribution of the slow secondaries to electronic excitations will also be decreased as they diffuse through the surface layer. Therefore, for high kinetic energies, low energy secondaries effectively determine the total desorption cross-sections.

This aspect (i.e. the total desorption cross-sections) has not been widely investigated, and no literature, specifically on Al has been found. But Lambert and Comrie (1973) who have investigated desorption of CO from Pt(111) face using Auger techniques, showed that the measured total desorption cross-section due to the 1.5 keV primary beam was 10 times smaller than that due to the secondaries emerging through the adsorbed layer. (i.e. 2.5×10^{-19} compared with $2.5 \times 10^{-18} cm^2$). Johanssen, Spicer and Strausser (1976), have also demonstrated, a decreasing desorption cross-section with increasing primary energy (1-3 keV) from silicon dioxide surfaces, investigated by AES. This was directly linked to reduced secondary electron yield with primary energy.

Hence a knowledge of the secondary electron yield properties of surfaces can point to a sensible choice of E_p to use for AES studies for which beam effects can be minimised.

6.4 Summary and Conclusions

In this chapter previous experimental secondary electron yield measurements performed on clean and oxygen exposed aluminium surfaces has been reviewed. For the clean surface, the total yield was found to be approximately 1, but the location of the primary electron energy at maximum yield was found to depend on the nature of the sample. The oxidised surface exhibits very large total yields. The contribution of decaying plasmons to the yield had been deduced from ELS and slow secondary EDC spectra. In the next chapter, the experimental apparatus and procedures used in AES, beam effect and SEE measurements will be presented.

CHAPTER SEVEN

EXPERIMENTAL APPARATUS AND PROCEDURES

7.1 Introduction

The experimental apparatus, consists of an ultra high vacuum UHV, specimen treatment chamber STC, and specimen analysis chamber SAC, vacuum instrumentation and detection electronics for Auger electron spectroscopy AES, and secondary electron emission yield studies. In this chapter, the apparatus and the experimental procedures used in the two techniques have been described.

7.1.1 UHV Apparatus and Associated Instrumentation

The stainless steel experimental UHV chambers consist of a specimen treatment chamber STC, and a specimen analysis chamber SAC separated by a gate valve. All internal and external materials used in the construction of the apparatus are UHV compatible and before assembly all components were thoroughly cleaned as described in most standard texts on vacuum science and technology.

Fig. 7.1 shows a schematic diagram of the STC and the SAC. The SAC houses the retarding field analyser RFA, and the electron gun. This chamber was mainly pumped by a 140 L/s Ferranti getter ion pump. The chamber could also be independently roughed out by a single sorption pump and an 8 L/s ion getter pump, which helped to lower the pressure in the SAC sufficiently to enable the start of the bigger 140 L/s ion pump. The sorption pump was isolated from the SAC by an all metal bakeable valve.

Fig. 7.1 A schematic diagram of the sample treatment and analysis chambers (STC and SAC) and associated instrumentation.

The STC was pumped by a water cooled polyphenyl oil charged, diffusion pump (Edwards E02) backed by a rotary mechanical pump. A liquid nitrogen cold trap between the diffusion pump and the STC prevented oil backstreaming and a bakeable foreline trap was also installed between the diffusion pump and the rotary mechanical pump. The STC, housed a Bayard-Alpert ionisation gauge (VIG 17, with VG IGP3 controller) working pressure range 10^{-3}- 10^{-11} torr for measurement of argon and oxygen pressures and a quadrupole mass spectrometer (VG micro-mass Q4) mass range 2-60 a.m.u. for residual gas analysis, leak detection and general pressure measurement.

The STC also holds the saddle field ion source for sample sputtering and its argon gas admission system which are described in sections 7.1.3.1 and 7.1.3.2. The STC further incorporates the molecular oxygen dosing system for adsorption studies and this is described in section 7.1.4.2.

For achievement of UHV the experimental apparatus was baked for a period of 15 hours at a temperature of 250 °C as measured by a copper constantan thermocouple. During the bake out the gate-valve separating the two chambers was left open and the 140 L/s ion pump was baked into the diffusion pump. While the system was still hot i.e. 100 °C, all filaments were outgassed, this enabling a more rapid achievement of UHV. But prior to this, considerable difficulties were encountered with unreliable components. This took a long time and a lot of effort to correct.

7.1.2 Sample Mounting and Manipulation

The polycrystalline, 0.5 mm thick aluminium sample was supplied by Goodfellow Metals Ltd and was quoted to be of 99.999% (5N) purity. The sample was cut into a disc measuring 15mm in diameter. It was mechanically polished to a mirror finish ultimately using grade A (0.1 μm) diamond

paste. Pictures taken with an optical microscope indicated the surface to be relatively free from polishing scores.

The sample holder was made up of a stainless steel block with four faces. The aluminium sample was secured to one of the faces by use of spot welded tungsten wire. A 12 mm deep, 3 mm wide Faraday cup was drilled into one of the faces and coated with gold black, for measurement of electron beam currents. A fluorescent tablet, containing zinc-ortho-silicate (Zn_2SiO_4), was also mounted on to a free face for location of the electron beam and estimating its size.

The stainless steel sample holder was attached to the end of a stainless steel shaft by means of a chuck arrangement. The shaft was part of the sample transfer and manipulation device. This device designed and built within the department, consists of an edge welded bellows, a VG independent rotary drive.

The sample end of the shaft, can be extended along the axis of the edge welded bellows up to a distance of 375 mm by means of a rack and pinion drive. The sample holder could also be rotated by means of the rotary drive through 360°. Electrical connection to the sample holder was achieved by fish-spine bead insulated nickel wire, through the hollow centre of the transfer shaft. The wire is eventually taken outside vacuum via an electrical lead through on a standard sized vacuum flange. The transfer shaft was insulated at several places along its length by machinable alumina ceramic.

Apart from linear and rotational motion, the sample could be moved side to side or up and down (up to 10 mm) with reasonable reproduceability, by means of another bellows device which was attached to the linear transfer

device. The x-y-z movement on this final stage, was achieved by distorting the bellows by three adjustable screws. The linear transfer device and the x-y-z manipulator was attached to the STC via a 170 mm flange. Inside the STC the sample surface could be turned to face the argon ion source for sputter cleaning or the effusion source for adsorption experiments. At the end of either operation, the sample was transferred into the SAC and placed at the correct position with respect to the RFA for analysis.

7.1.3 Preparation of Clean Sample Surfaces

The polycrystalline aluminium surface could be cleaned in several ways. Either by electron bombardment or cycles of argon ion bombardment with or without annealing. In the first technique, the sample was heated by electron beam bombardment by employing high electron current densities at high energy and subsequent removal of contaminants by thermal desorption and by electron stimulated desorption. The source of the thermionic electrons was from a nude 1 kW projector filament in the vicinity of the sample. With this technique the surface was found to still contain traces of contaminants, mainly oxygen and carbon as established by AES spectra taken soon after heating.

The more satisfactory cleaning technique finally adopted was by argon ion bombardment using a saddle field argon ion source which is described next.

7.1.3.1 Saddle Field Ion Source

The ion gun used to generate energetic argon ions for sputtering the aluminium sample was a B21, wide beam saddle field ion source manufactured by Ion Tech. Ltd. The operation of this d.c. energised cold cathode source is based on the effect that electrons describe long oscillatory

paths in the presence of electrostatic saddle potential field between two cylindrical anodes (Franks 1979). Any gas present in the source is ionised and extracted through an aperature in the cathode which forms the outer casing. The emergent ion beam is divergent and contains a number of neutrals. The discharge can be maintained at a pressure of 10^{-3} - 10^{-4} torr.

The B21, has an overall length of 50 mm and was mounted on to a standard conflat flange. Electrical connections to the anode was established across a 15 kV, 15 A, extra high tension lead-through and argon gas, leaked in through to the source via a 5 mm bore stainless steel tube. The ion current monitor plate was internally shorted to ground.

Fig. 7.2 illustrates the pumping scheme for the STC and the high purity argon gas admission system to the ion source. The d.c. supplies to the ion source consisted of a 10 kV, 10 mA power supply unit which was designed and built within the department.

7.1.3.2 Argon Gas Supply System to the Ion Source

The admission system of high purity (99.999%) argon gas into the ion source is shown in Fig. 7.2. The argon gas was contained in a laboratory bench size cylinder. The pressure was eventually reduced via a series of control valves and finally leaked into the source via a VG MD6 all metal bakeable leak valve. The volume behind the leak valve to the argon bottle could be roughed out with another rotary mechanical pump fitted with a bakeable foreline trap. The stainless tubing behind the leak valve was coiled so that it could be immersed in a Dewar flask, containing liquid nitrogen or solid carbon dioxide for removal of water vapour from the bakeable gas line.

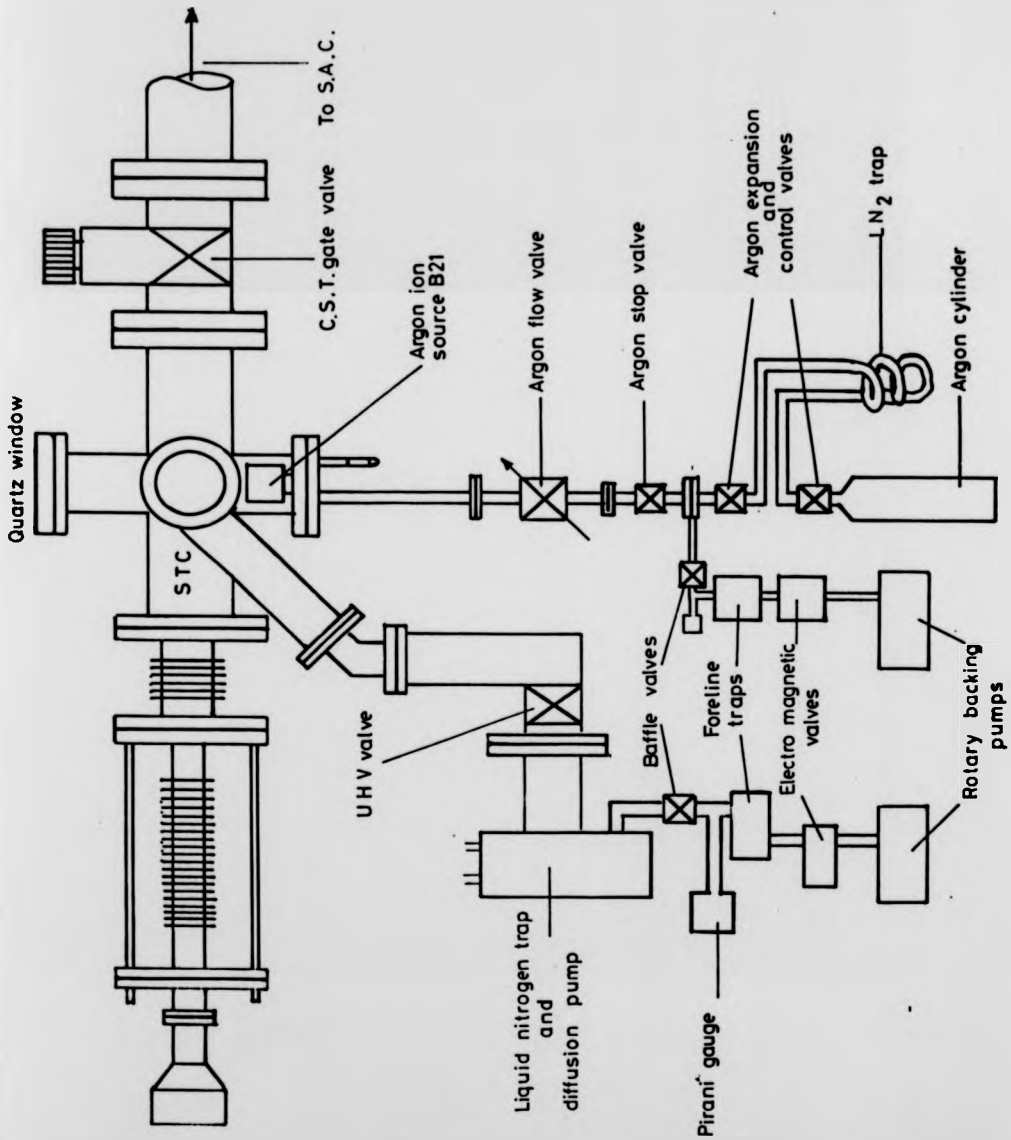

Fig. 7.2 Schematic diagram illustrating the pumping scheme for the STC and argon gas admission system to the ion source.

7.1.3.3. Operation of the Ion Source and Procedure for Sputtering of the Sample

Prior to any ion bombardment, the volume behind the leak valve was thoroughly flashed out with argon. The Dewar flask was then filled with LN_2, and once the stainless steel tube had cooled to LN_2 temperature, the volume behind the leak valve was flashed out with argon further couple of times. At this point the argon was ready for admission into the source via the MD6 valve.

Initially, if both chambers had been pumped by the ion pump, then the CST gate valve separating the two chambers was closed as shown in Figs. 7.1 and 7.2. Then the UHV all metal valve isolating the diffusion pump was opened. Argon was then leaked into the STC to a pressure of 10^{-3} torr as monitored on the Bayart and Alpert ionisation gauge. The leak valve was then closed and the chamber pressure allowed to recover. This argon flashing operation of the STC was repeated couple of times. The sample was rotated to face the ion source approximately at a distance of 5 cm

The voltage supply to the anode was switched on and set to 5 kV. Argon was then leaked into the ion source and at a pressure of 10^{-3} torr a purple discharge was observed through the zero length quartz widow. The ion beam landing at the sample surface was measured with a micro-ammeter with one terminal attached to the sample and the other grounded. The landing current was controlled by adjusting the argon pressure or anode voltage. This was kept between 10 and 15 μA. The surface was clean within 5 - 10 minutes of sputtering as monitored by AES.

At the end of the sputtering period the source was stopped either by closing off the leak valve or switching off the anode voltage. Within four

minutes of stopping the leaking of argon into the source the pressure inside the STC recovered to 10^{-9} torr. At this stage the sample was ready for adsorption of oxygen or transfer into the analysis chamber.

7.1.4 Oxygen exposure of the Sample Surface

Oxygen exposure of the sample surface was done by two methods. The first was by leaking of oxygen into the STC to a particular pressure and timing the duration of exposure. The second method was by the use of a very low conductivity porous plug attached to an effusion source several centimetres from the sample surface. The oxygen dosing system could deliver a molecular flux of 10^{12} molecules/cm^2/s. From initial experiments it was found that, the exposure times for low flux doses to adsorb monolayer coverage was too long. Consequently the dynamic method of oxygen exposure was found to be more satisfactory and was used for most of the adsorption work reported in this thesis. In the following sections the two methods will be described but with emphasis on the first.

7.1.4.1 Dynamic Exposure of Sample and Chamber to Oxygen

The oxygen admission line and the effusion source are shown in Fig. 7.3. Research grade oxygen (BOC) from a glass litre flask was expanded via a series of nupro valves to the effusion source or via a flow valve into the STC. The flushing out of the oxygen lines up to the valve V_1, was normally done before sputtering of the sample. This was done by first expanding oxygen into the volume between V_1 and V_2. And further expanding that into the volume between V_3 and V_4 which were then gently opened and oxygen leaked into the STC, pumped by the diffusion pump. The pressure never rising above 10^{-5} torr.

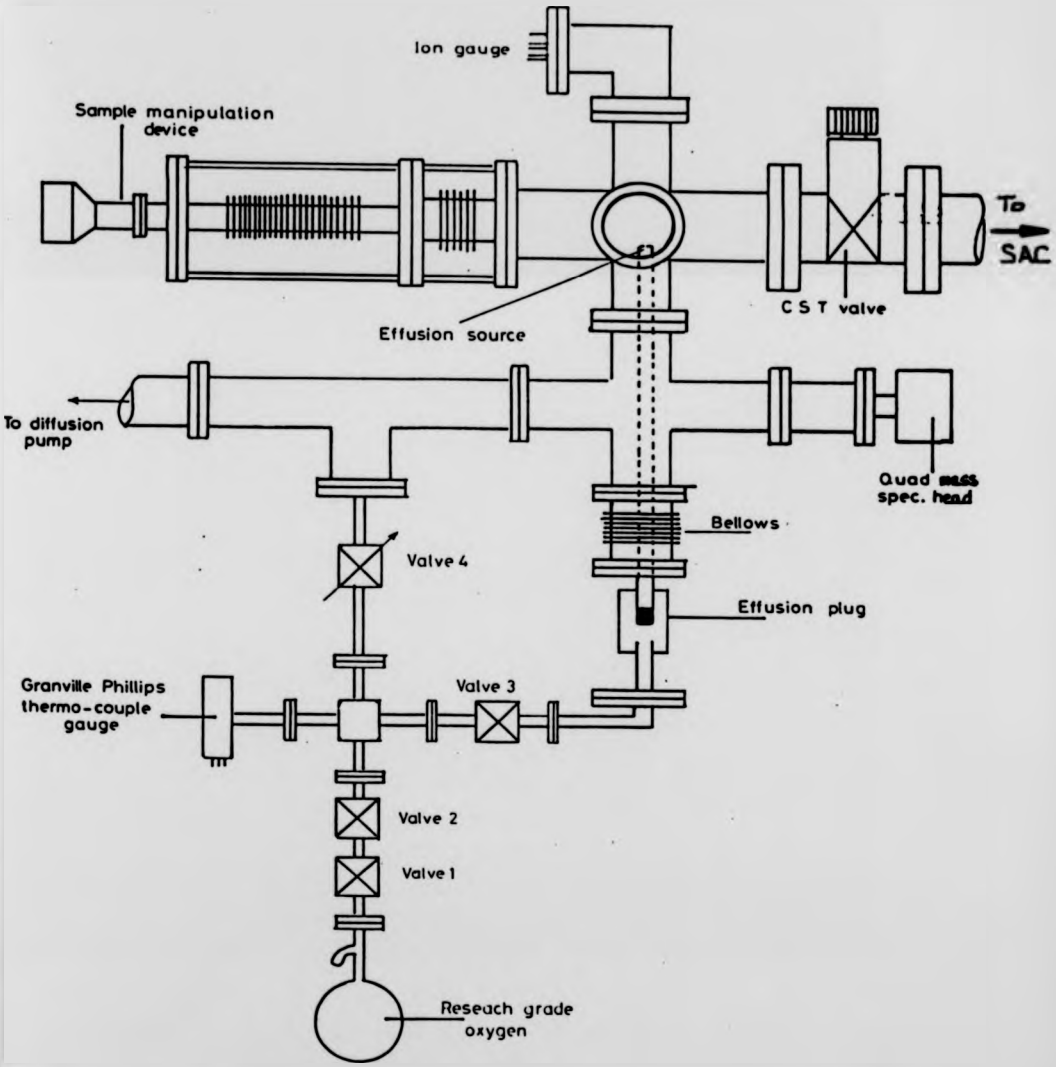

Fig. 7.3 The effusion source and oxygen admission line.

This operation was repeated couple of times. Then the volume between V_3 and V_4 was filled with oxygen to a pressure of 30 mbar, as measured on a Granville-Phillips thermocouple gauge. By means of leak valve V_4, oxygen was leaked into the STC until the adsorption pressure was reached. This pressure was measured with the Bayard-Alpert ionisation gauge, situated out of direct line of sight with the sample. Oxygen exposure was obtained by measuring the adsorption period and pressure and this gave the exposure directly in Langmuirs (exposure pressure torr/ 10^{-6} x time secs). At the end of a particular adsorption period, after closing the leak valve, the pressure in the STC recovered within minutes to 5 x 10^{-9} torr.

7.1.4.2 Molecular Effusion Source

The molecular effusion source was very similar to the one described by Madey (1972) but based on a modified version of Bellard (1980). The molecular effusion source consists of a silicon carbide porous plug sealed in a glass envelope (Christian and Leck 1966) of known conductance (2.3 x 10^{*6} L/s supplied by R. M. Williams of Liverpool University) and orifice of equal length with radius, out of which molecules effuse at a known rate of approximately 10^{12} molecules/cm^2/s. This was obtained from a calculated distribution of molecules leaving the orifice as a function of the effusion source to sample distance.

The operation of the molecular effusion source can be deduced from Fig. 7.3. And the flushing of the line with oxygen was as described in section 7.1.4.1. Research grade oxygen was expanded from the glass litre flask into the volume contained between V_2, V_3 and V_4. By gently opening V_3 oxygen was expanded into the high pressure side of the porous plug. The pressure was set to 0.2 torr by expelling some of the oxygen by use of V_4. A Granville-Phillips thermo couple gauge was used to measure the oxygen

pressure behind the plug.

The sample surface, after ion etching was rotated into the molecular stream for a given length of time. The effusion source to sample surface distance was set in two ways: either by using the x-y-z facility of the sample transfer device or by moving the effusion source up or down by adjusting the effusion source bellows. The distance was measured by use of a travelling microscope.

This dosing method, was found to be unsatisfactory after prelimenary experiments. Adsorption times were found to be too long, and the calibration of the flux rate to sample surface distance could not be experimentally confirmed by use of the quadrupole mass spectrometer, as no change in the background oxygen partial pressure could be detected when the sample was turned to face the source.

7.2 Electron Energy Analyser, Excitation Source, Electronics and Signal Detection

The electron energy analyser used for AES was a retarding field analyser RFA. And in the following sections construction, operation of the RFA, and Auger electron detection electronics will be described.

7.2.1 Retarding Field Analyser, RFA

This retarding field analyser is one of the simplest Auger electron spectrometers to build and operate. It consists of three spherical grids concentric with an outer solid spherical collector. The electron gun was mounted so that the sample was excited by a normally incident electron beam. The earthed shield housing the electron gun passes through a hole

across the collector-grid assembly.

The sample surface for analysis was placed at the centre of curvature of the spherical grids and collector so that emitted electrons travel along radial paths to the collector. The inner grid and the sample were held at earth potential and the retarding voltage was applied to the outer two electrically linked grids. Only electrons with sufficient kinetic energy surmount the retarding potential at the grids in order to reach the collector.

The energy distribution N(E) or the differential of the energy distribution dN(E)/dE (the normal mode in which Auger spectra are recorded) was obtained by a modulation technique. A small sinusoidal voltage was superimposed on to the retarding potential applied to the retarding grid. The differential of the energy distribution is proportional to the second harmonic of the current signal detected at the collector and the direct energy distribution N(E), to the fist harmonic.

This can most easily be demonstrated by showing the retarding voltage dependence of the detected secondary electron current in terms of a small sinusoidal modulation voltage, expanded in a Taylor series. If I is the detected secondary current reaching the collector, V the retarding voltage and $v_m \sin\omega t$ the modulation signal then

$$I(V + v_m \sin\omega t) = I(V) + I'(V) v_m \sin\omega t + I''(V)/2! \, v_m^2 \sin^2\omega t + I'''(V)/3! \, v_m^3 \sin^3\omega t + I''''(V)/4! \, v_m^4 \sin^4\omega t + \ldots\ldots\ldots\ldots \quad \ldots(7.1)$$

Algebraic and trigonometric re-arrangement gives

$$I(V + v_m \sin\omega t) = I(V) + [v_m^2 I''(V)/4 + v_m^4 I''''(V)] + [v_m I'(V) + v_m^3 I'''(V)/8 + ...] \sin\omega t - [v_m^2 I''(V) + v_m^4 I''''(V) + ...] \cos 2\omega t \quad ...(7.2)$$

Since N(E) is the derivative of the collected current and N'(E) the second derivative, the amplitude of the fundamental, $\sin\omega t$ is proportional to N(E) with proportionality factor v_m. The amplitude of the second harmonic, $\cos 2\omega t$ is proportional to N'(E) with a proportionality factor $-v_m^2/4$. The modulation amplitude v_m must be sufficiently small so that terms in v_m^3 and above can be neglected.

In order to extract the second harmonic of the detected current signal, from within the noise, a lock-in-amplifier was used. This contains an in built phase sensitive detector PSD, for comparing the signal phase with the reference modulation signal. The output of the lock-in-amplifier is a d.c. voltage proportional to the amplitude of the second harmonic of the detected electron current.

7.2.2 Experimental Arrangement of the RFA for AES

The retarding grid analyser assembly consists of a solid spherical collector and the three spherical concentrically arranged tungsten grids. The collector-grid assembly is situated beneath the top flange of the SAC as illustrated in Fig. 7.4. The spherical solid collector of diameter 125 mm was made of stainless steel and the three-grids had diameters of 106, 100, and 63 mm respectively. The whole of the assembly was electrically insulated from each other by use of alumina and fish spine bead ceramics. Electrical connections, external to the vacuum was made via special UHV BNC electrical lead-throughs attached to the top flange.

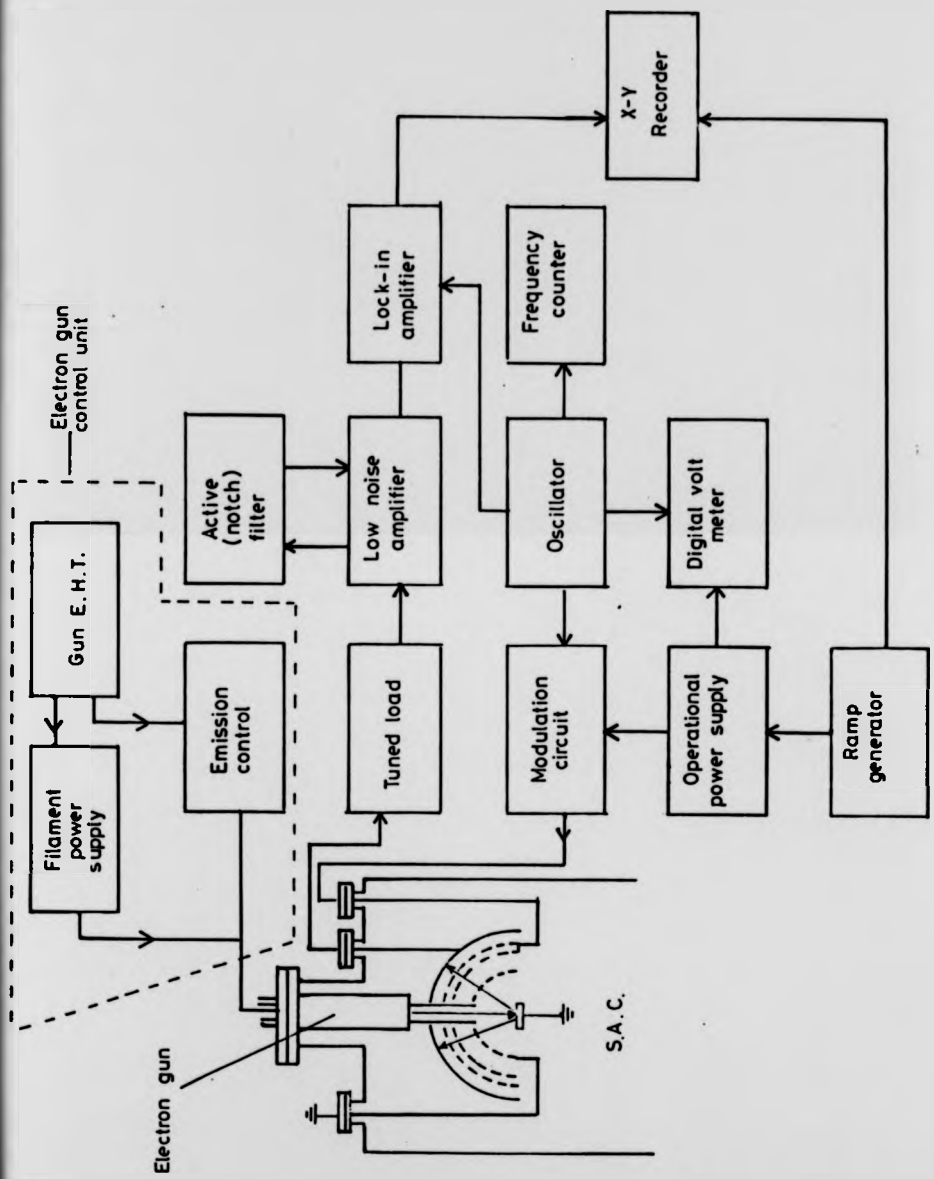

Fig. 7.4 Block diagram of the Auger electron detection system.

A hole 12 mm in diameter cut through the centre of the collector-grid assembly allows the grounded electron shield to protrude about a cm beyond the inner grid closest to the sample.

Palmbery and Rhodin (1968) and Weber and Peria (1967) were the first to adopt a LEED optics system for recording of Auger electron spectra by electronic differentiation based on the method of Leder and Simpson (1958). As described in section 7.2.1 electronic differentiation was brought about by superimposing a small sinusoidal modulation voltage on to the retarding voltage applied to the retarding grid. The amplitude of the collected secondary current was then proportional to the differential of the electron energy distribution.

In this system the two outer grids were used as the retarding grid and the inner grid was maintained at earth potential together with the sample. This arrangement helps to reduce capacitive coupling between the retarding grid and the collector and maintain a field free region between the inner-grid and the sample.

The main problems associated with the RFA which effects resolution and sensitivity arise from the mechanical misalignment of the grid-collector assembly, warping of the grids leading to distortion of field lines and further scattering of electrons by the grids can lead to spurious signals. The use of the double retarding grid as suggested by Palmberg (1968) improves the resolution from about 3% to 0.3%. But this tends to have a detrimental effect on the sensitivity. But since resolution also depends on the size of the electron beam and spread in the primary energy as well as the modulation amplitude and therefore the theoretical value is never attained. In this work a practical resolution value of 0.25% has been measured.

One of the major draw backs of the RFA is the high shot noise which tends to limit the signal to noise ratio. Since the RFA is a high pass filter at low retarding voltages almost all the secondary electrons surmount the potential barrier to reach the collector. This inevitably leads to a high electron background. Residual magnetic fields also tend to adversely effect the resolution of the RFA and to a large extent these have been eliminated by encircling the SAC with nectic-conectic mild magnetic screens.

7.2.2.1 The Static Electron Gun

The electrons for the excitation of the surface (normal incidence) were produced by an indirectly heated oxide coated cathode emitter (type KA809F and heater E7291) mounted on to a Superior Electronics electron gun type SE-3k/5U. The electron beam so produced could be focussed and positioned electrostatically. For location of the beam, a fluorescent material (zinc ortho-silicate) in the shape of a tablet was used. For the work in this thesis, primary electron beams of energy 600 - 1500 eV and currents of 4 - 15 μA have been used. The spot size was varied from 0.1 - 2 mm. The primary current was measured by collecting all the primary electrons in a Faraday cage coated with gold black.

The entire gun assembly was surrounded by a mu-metal shroud and its nozzle extended through the grid-collector assembly. The electron gun control unit consisted of three sub units; a highly stabilised d.c. filament power supply unit, a highly stabilised eht (0-3 keV) unit and a control unit of departmental design for focus, grid bias and deflection adjustments.

7.2.3 Electronics for Detection and Recording of Auger Electron Spectra

The retarding voltage was generated by a 0 - 1000 eV Kepco (OPS 1000) programmable operational power supply driven by a Kepco (FG100) linear ramp generator, with ramp speeds in the range 0.001-100 Vs^{-1}. The sinusoidal modulation voltage was generated by a low distortion oscillator (Brookdeal Ortec 5012F) with a variable modulation amplitude of 0 - 5 Vrms. This modulation voltage was superimposed on to the retarding voltage by a modulation circuit consisting of resistor-capacitor network, with its output feeding the double retarding grid of the analyser. Fig. 7.4 is a block diagram of the Auger electron detection system and Fig. 7.5 is a schematic of the electronics.

Electrons scattered from the surface by the action of the primary electron beam, emerge in a cone. The ones with sufficient kinetic energy overcome the retarding grid potential barrier and arrive at the collector.

The collector was positively biassed to 120 V by use of dry batteries in order to suppress creation of tertiary electrons by the impact of the secondaries at the collector and grids. A tuned load was connected to the collector and its resonant frequency chosen to be twice that of the modulation frequency so that the second harmonic of the detected secondary electron current was enhanced. The signal developed across the tuned load was then taken via an active notch filter (to further suppress the fundamental of the modulated signal), to the input of a Brookdeal 401A lock-in-amplifier.

The lock-in-amplifier contains an inbuilt phase sensitive detector and by use of an appropriate time constant and adjustment of the phase control dial, it produces a d.c voltage proportional to the amplitude of the second harmonic of the detected secondary electron current. The reference input of the LIA was connected to the oscillator for deriving the modulation

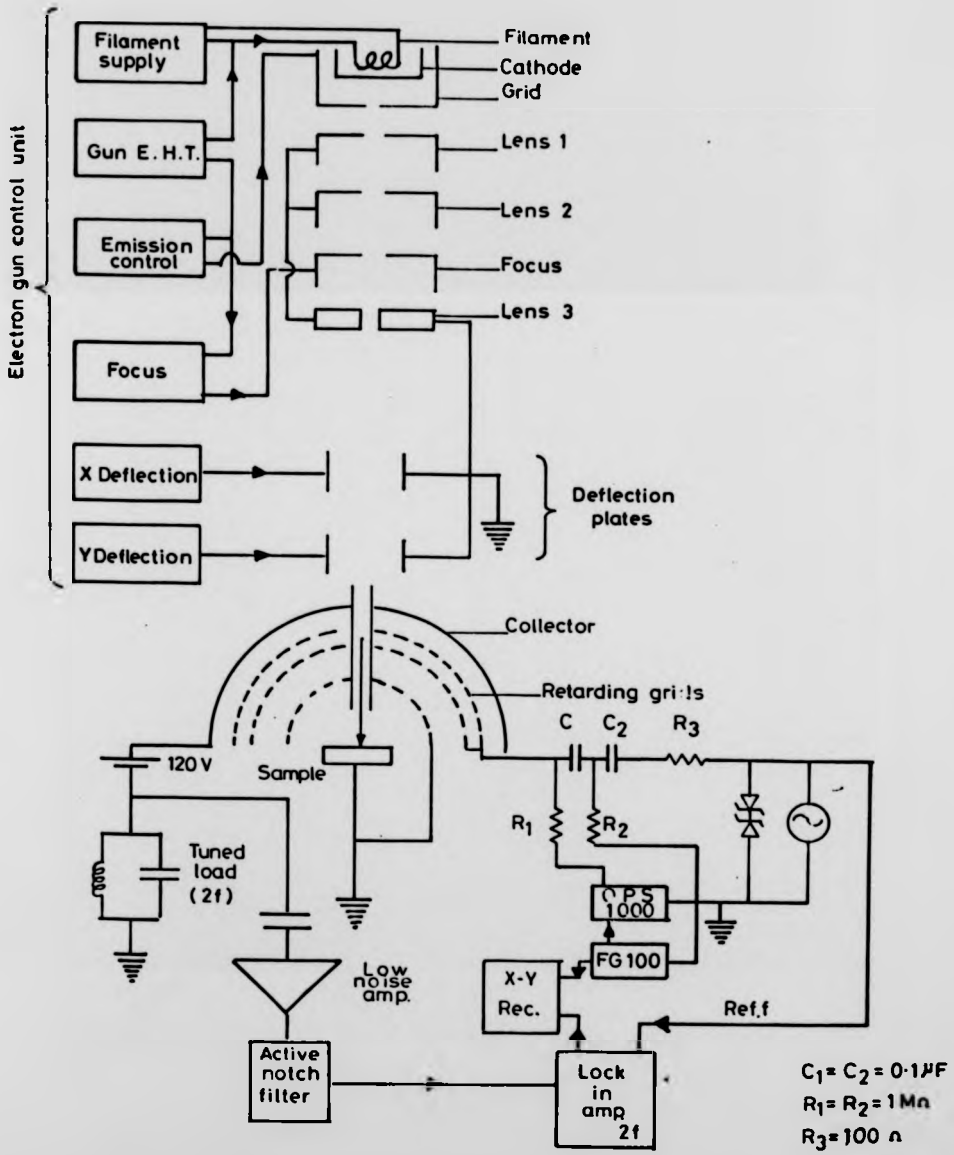

Fig. 7.5 A schematic of the electronics for detection of Auger electrons.

signal. The Y amplifier of the Bryans 26000A X-Y recorder was connected to the output of the LIA and the X input amplifier to the ramp generator.

7.2.3.1 Procedure for Recording of Auger Spectra and Measurement of Auger Electron Energies

First the resonant frequency of the tuned load was located by applying the modulation signal directly to the retarding grid and observing the output signal at the tuned load, output of which was connected to an oscilloscope. At resonance the peak-peak voltage was maximised and this frequency (2 kHz) was measured by a Philips PM 2521 automatic digital multimeter. The oscillator was then re-set to a modulation frequency half that of the resonant frequency i.e. 1 kHz. The active notch filter was then connected to the output of the tuned load and its output adjusted to null the fundamental signal.

The Auger electron detection circuitry was then reconnected as shown in Fig. 7.5 and the output of the LIA adjusted to maximise its output. This was done at the elastic peak energy E_p (or at the $L_{2,3}VV$ Auger peak of aluminium) of the secondary electron energy distribution by scanning and locating E_p and holding the retarding voltage at that point. The elastic peak was further maximised by adjusting the position of the sample with respect to the centre of curvature of the collector- grid assembly.

The above setting up procedure was carried out after all the electronics had been switched on and allowed to warm up for about 30 minutes in order to avoid any subsequent drift in the modulation amplitude and frequency and retarding voltage. At high retarding voltages, modulation amplitudes in the range 6 - 10 Vpp was used. For low retarding energies 50 - 200 eV 4 Vpp modulation amplitudes was used (Riviere 1970) in order to enhance

signal. The Y amplifier of the Bryans 26000A X-Y recorder was connected to the output of the LIA and the X input amplifier to the ramp generator.

7.2.3.1 Procedure for Recording of Auger Spectra and Measurement of Auger Electron Energies

First the resonant frequency of the tuned load was located by applying the modulation signal directly to the retarding grid and observing the output signal at the tuned load, output of which was connected to an oscilloscope. At resonance the peak-peak voltage was maximised and this frequency (2 kHz) was measured by a Philips PM 2521 automatic digital multimeter. The oscillator was then re-set to a modulation frequency half that of the resonant frequency i.e. 1 kHz. The active notch filter was then connected to the output of the tuned load and its output adjusted to null the fundamental signal.

The Auger electron detection circuitry was then reconnected as shown in Fig. 7.5 and the output of the LIA adjusted to maximise its output. This was done at the elastic peak energy E_p (or at the $L_{2,3}VV$ Auger peak of aluminium) of the secondary electron energy distribution by scanning and locating E_p and holding the retarding voltage at that point. The elastic peak was further maximised by adjusting the position of the sample with respect to the centre of curvature of the collector- grid assembly.

The above setting up procedure was carried out after all the electronics had been switched on and allowed to warm up for about 30 minutes in order to avoid any subsequent drift in the modulation amplitude and frequency and retarding voltage. At high retarding voltages, modulation amplitudes in the range 6 - 10 Vpp was used. For low retarding energies 50 - 200 eV 4 Vpp modulation amplitudes was used (Riviere 1970) in order to enhance

sensitivity without over distorting the Auger signals.

Actual measurement of Auger electron energies was done in two ways. First by directly measuring the energy of the minimum of the negative going differential peak by halting the retarding voltage at that minimum and noting the voltage on the digital voltmeter. Secondly by noting the start of the retard voltage and several other Auger peak energies and calibrating the horizontal axis of the X-Y recorder graph paper directly in volts/mm. In this work both techniques were used.

7.2.3.2 Reference of Measured Auger Electron Energies

The Auger electron energies as measured by the digital voltmeter, have been made with respect to the vacuum level of the analyser grids. These electron energies may be referenced to the Fermi level from a knowledge of the analyser work function Φ_W. The sample work function Φ_{Al}, does not enter, as can be seen from Figs. 7.6 (a,b) depicting instances when the sample and the analyser grids have been shorted, and when a retarding voltage V_R has been applied to the grids.

The measured kinetic energy of the electron E_k, just over the grids as referenced to the Fermi level is given by $V_R + \Phi_{Al} + (\Phi_W - \Phi_{Al})$ so that $E_k = V_R + \Phi_W$ (Φ_W= 4.5 eV, and Φ_{Al}= 4.2 eV).

7.2.3.3 Measurement of ELS Spectra

The instrumentation and procedures for recording of electron loss spectra, was identical to that of Auger electron spectra. The aluminium sample was excited by primary electrons of energy 600 and 900 eV. After location of the elastic peak E_p, the spectrum would be scanned from E_p-100 to E_p eV, to

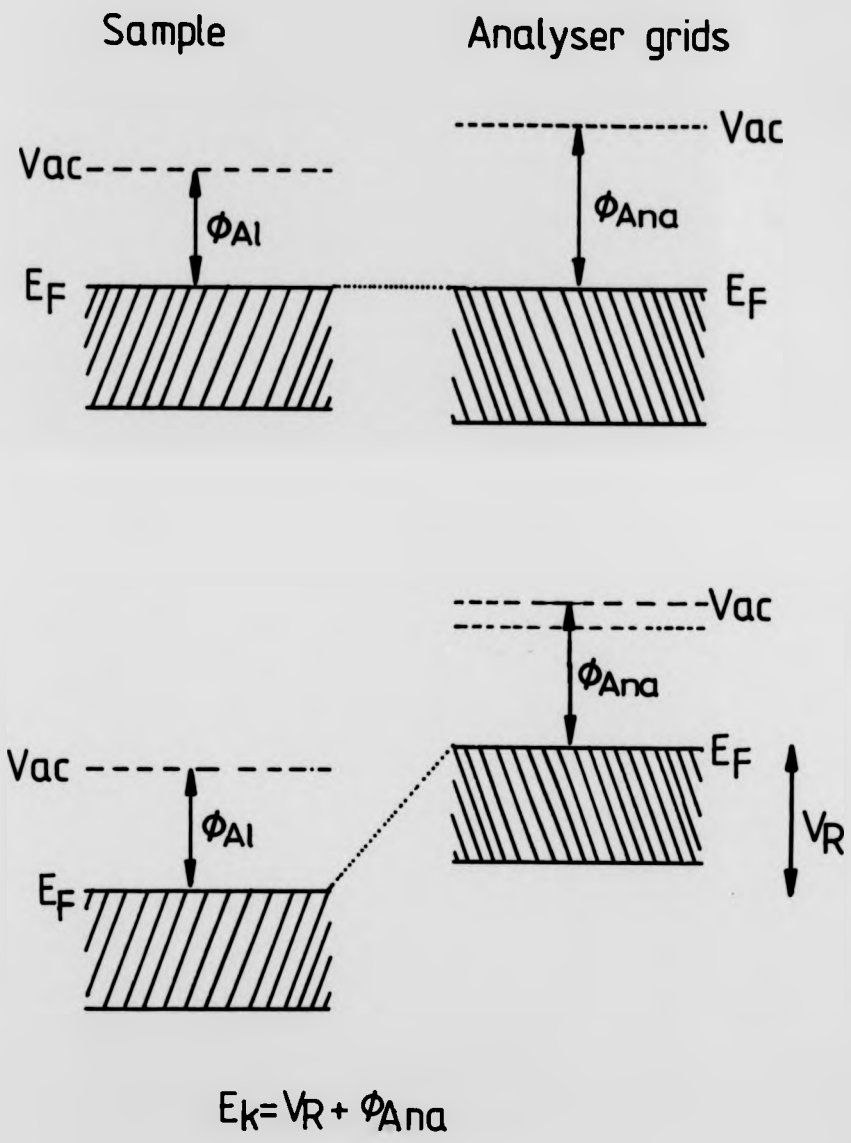

Fig. 7.6 Diagrams depicting instances when the sample and analyser grids have been shorted (a), and when a retarding voltage has been applied to the grids (b).

record the single and multiple plasmon loss peaks accompanying the elastic peak. These measurements were recorded for various signal modulation voltages and angles of incidence for clean and oxygen exposed aluminium surfaces.

7.2.3.4 Procedures for Electron Beam Effect Experiments

These experiments were performed on clean and oxygen exposed aluminium surfaces. The primary electron beam of known parameters would be incident on the sample, and Auger window spectra of O_{KLL}, C_{KLL}, Al $L_{2,3}VV$ and Al $L_{2,3}V_OV_O$ would be recorded as a function of time up to 90 minutes.

At the end of this irradiation period, the sample was slightly moved in the horizontal plane so that further Auger window spectra could be recorded from non-irradiated spots. These measurements were performed for various electron beam parameters and oxygen coverage levels. In chapter 8 this will be further described and discussed.

7.2.4 Experimental Arrangement of the RFA for Recording of Secondary Electron Emission Yield Curves

The retarding field analyser was readily adapted to record secondary electron emission yield curves. In the following sections, a fast and accurate yield measuring technique, and its electronics will be described as well as the procedure of yield measurement.

7.2.4.1 The Secondary Electron Yield

The secondary electron yield of a material is defined as the ratio of the secondary electron current to the primary electron current i.e.

$$\sigma = I_s/I_p \qquad \ldots(7.3)$$

Traditionally, the yield curves, σ versus E_p have been plotted manually point by point. E_p is increased in steps and the corresponding I_s and I_p measured. This method was rather tedious and time consuming.

The measured yield is the total yield because electrons of all energies which emerge in a solid angle of 2π are collected by the hemispherical collector. The true yield δ, or the backscattering coefficient η could be obtained by placing appropriate potentials to the grid and sample so that only secondary electrons within the defined energy bracket could reach the collector.

Automatic σ and η plotting systems have been devised, where I_s has been monitored directly as a function of E_p by maintaining constant I_p due to the feedback circuit in the electron gun grid bias, the method took a long time to complete and was also slightly inaccurate, since not all the secondary electrons could be collected. But for the first time it allowed the observation of fine structure on the smooth yield curve, mainly due to ionisation threshold events and elastic scattering processes particularly at low primary electron energies. These structures could further be enhanced by employing modulation and lock-in-detection techniques in obtaining derivative yield curves (Goto and Ishikawa 1972, Park 1981).

A static method of recording the variation in the yield at a specific E_p is by monitoring the changes in a I_a as a function of surface coverage or desorption while E_p and I_p are kept constant. This method was first suggested by Argile and Rhead (1982).

A slight modification of expression 7.3 led Henrich (1973), to suggest an alternative yield measuring technique. Here the total yield is monitored in terms of the absorbed sample current I_a, while the primary electron energy E_p and current I_p are kept constant. The variation in E_p is simulated by applying a retarding potential to the sample. This method is a lot faster and more accurate. In the following sections, this method is described in more detail.

Since $I_p = I_s + I_a$ where I_a is the absorbed sample current then expression 7.3 can be rewritten as

$$\sigma = (I_p - I_a)/I_p \qquad \ldots(7.4)$$

and further simplifying

$$\sigma = 1 - I_a/I_p \qquad \ldots(7.5)$$

If in expression 7.5 I_p is maintained constant, then the total yield will be given by the absorbed current I_a which is a function of the primary energy, E_p. In expression 7.5 a simple way of calibrating the yield curve is also seen if I_a is forced to equal I_p then, a value of 0 is obtained for σ. This is achieved by collecting all of the incident beam in a Faraday cage coated with a low yield gold black layer so that $I_a = I_p$.

The $\sigma = 1$, point on the vertical axis of the yield curve is obtained by making $I_a = 0$. This is done by applying a retarding potential greater than the kinetic energy E_p of the landing primary electron beam so that all the primary electrons are deflected away from the sample surface.

7.2.4.2 Electrical Re-connection of the RFA for Yield Measurements

The collector-grid assembly of the RFA was not altered but the external electrical connections were changed as shown in Fig. 7.7. The collector and the double retarding grids were electrically connected together and biased to +90 eV (to prevent creation of further secondary electrons by the ones arriving from the surface). The collected secondary electrons flowed to ground via a micro-ammeter.

The inner grid was connected to ground as in AES in order to provide a uniform equipotential field for the secondaries to travel along radial paths to the collector. The retarding potential was applied to the specimen and secondary electrons with insufficient energy were absorbed by the sample.

7.2.4.3 Electron Gun

The electron gun was operated in the same mode as used for recording of Auger electron spectra i.e. E_p and I_p were kept constant as the sample was ramped from 0 - E_p. The primary electrons were struck the surface at normal incidence and maximum primary energy employed was 1000 eV and current 3 - 7 μA.

7.2.4.4 Electronics for Recording of Secondary Electron Yield Plots

The electronic set up for recording of secondary electron yield curves using the RFA was based on the scheme first used by Henrich (1973). This was slightly modified and improved by Suleman and Pattinson (1980). A block diagram of the system is shown in Fig. 7.8 and an up to date circuit diagram of the yield circuit is shown in Fig. 7.9.

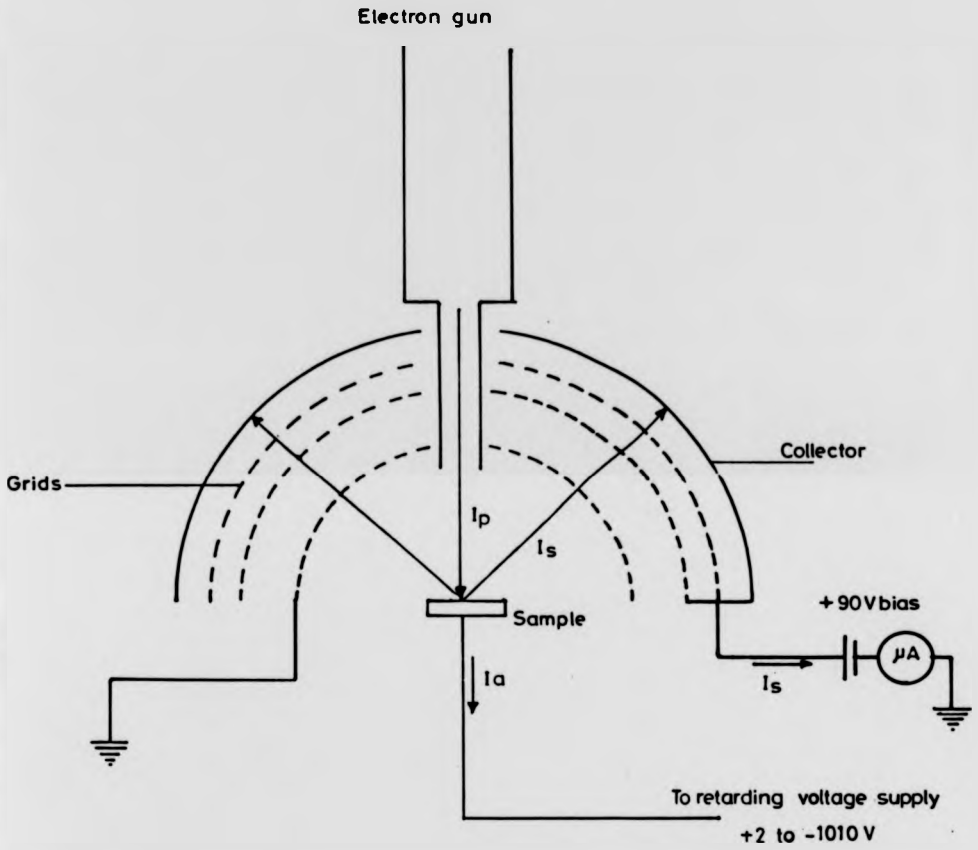

Fig. 7.7 Arrangement of the RFA for recording of SEE yield curves.

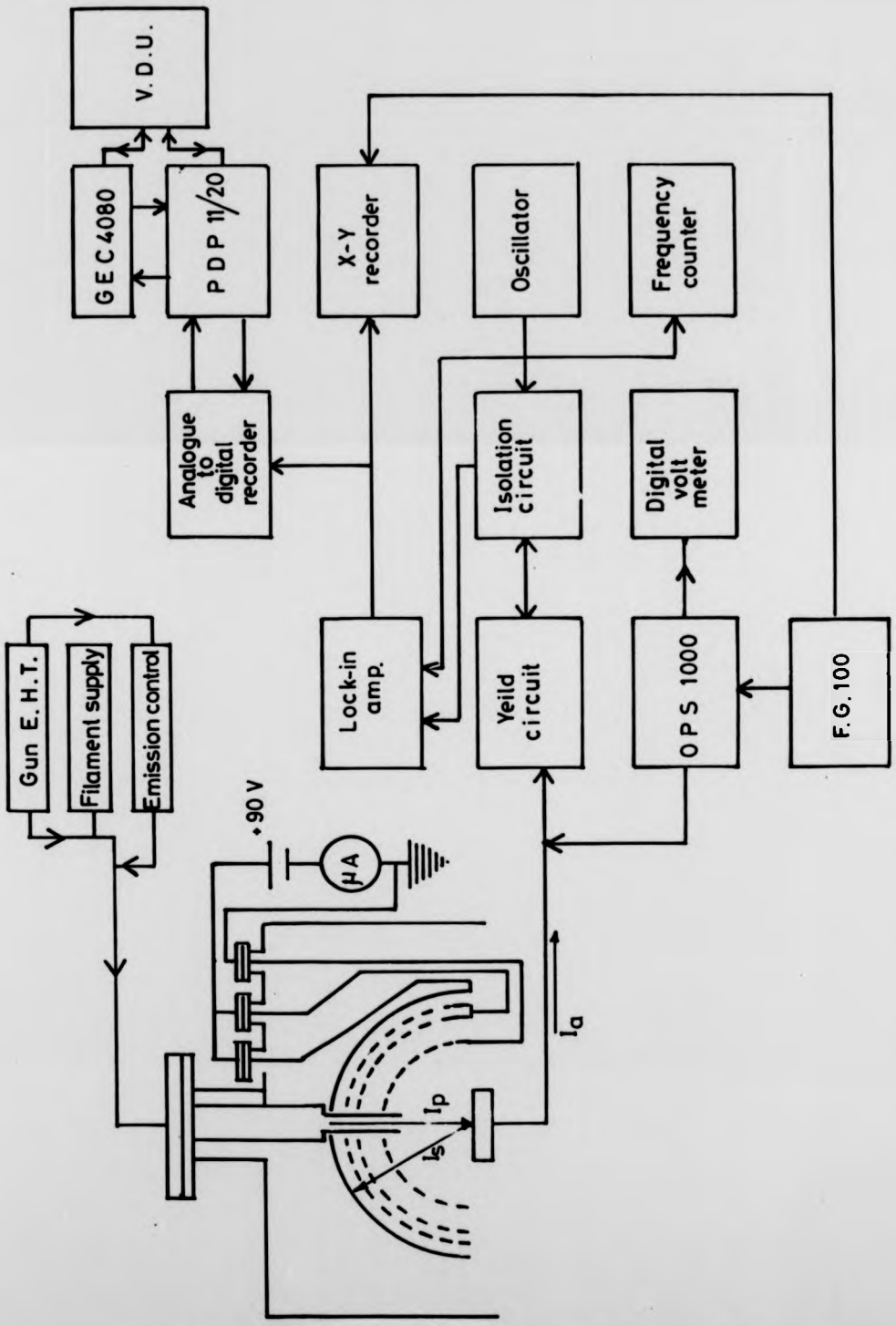

Fig. 7.8 A block diagram of the SEE yield detection system.

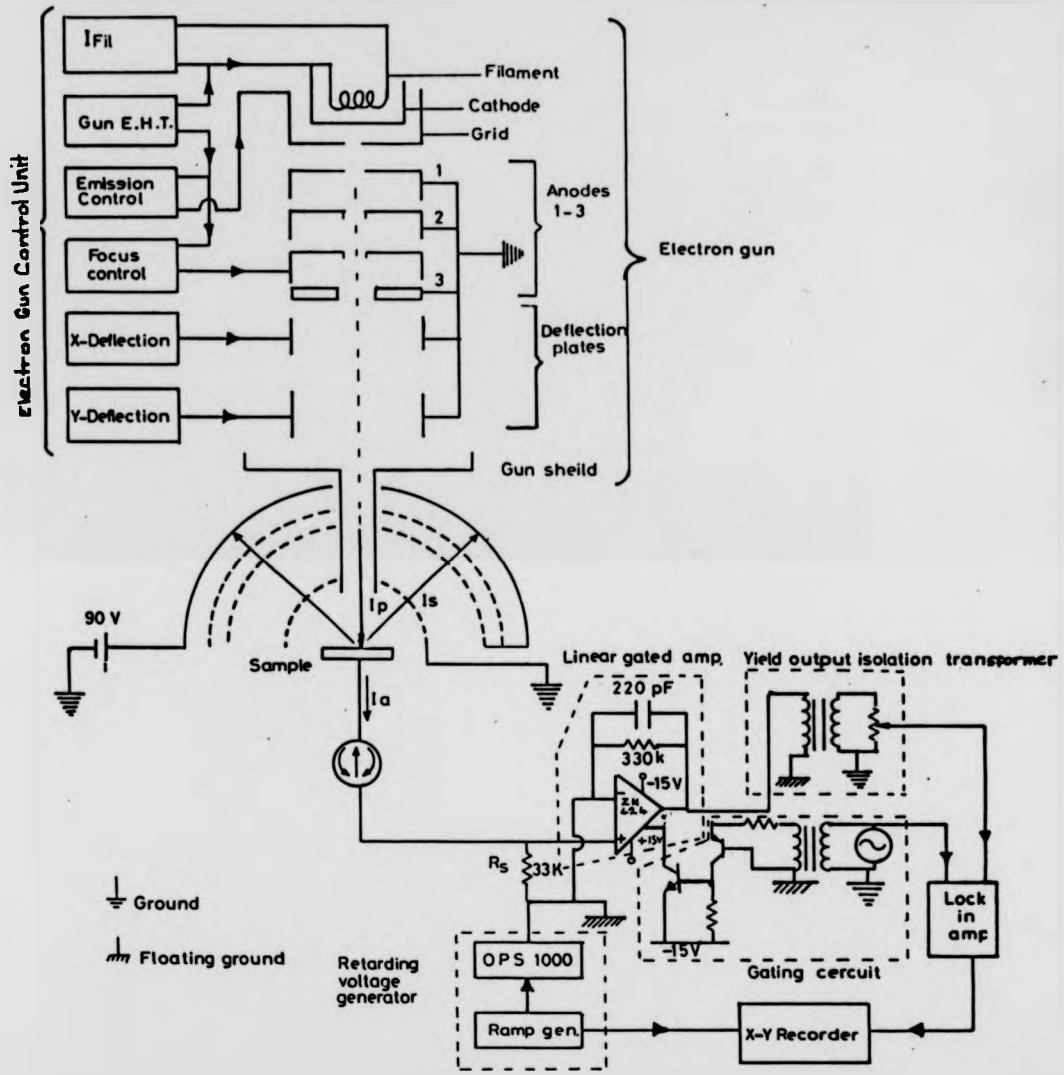

Fig. 7.9 Circuit diagram of the yield detection system.

The main advantage of this system was that the primary electron energy and current could be kept constant during the recording of an entire yield curve. The negative retarding potential applied to the specimen in order to simulate a change in the incident primary energy was obtained from a Kepco OPS1000 operational power supply driven by a Kepco FG100 linear ramp generator.

The current flowing into or out of the specimen was proportional to the yield σ as described in section 7.2.4.1. Since I_a becomes very small to measure, a gated linear amplifier, Ferranti ZN424 was used to amplify the voltage developed across the sensing resistor R_s shown in Fig. 7.9. Since I_a had to be measured in the presence of the negative retarding voltage down to -1000 eV, the entire amplifier circuit floats at the retarding voltage. The ±15 V d.c. power supply was derived from two dry 18 V batteries regulated to 15 V by use of zener diodes.

The gating sinusoidal signal was obtained from a Brookdeal 5012F low distortion oscillator and applied to the gate via an isolation transformer (1:1 turns ratio with a ferrite core) and gating npn transistor pair. The output of the gated linear amplifier is a product of the gating signal and the input voltage signal generated by the absorbed specimen current across the sensing resistor and consists of a trail of periodic pulses. The height of the pulses depends on the specimen current I_a and modulation signal ($\propto 3V_{pp}$, 10 kHz). The fundamental component of the gated linear amplifier output signal is proportional to I_a and was detected by a Brookdeal 401A lock-in-amplifier via an isolation transformer. The reference signal to the LIA was obtained from the oscillator.

The output of the LIA was taken to the Y input of a Bryans 26000A X-Y recorder and the output of the FG100 ramp generator (0-20 V) connected to

The main advantage of this system was that the primary electron energy and current could be kept constant during the recording of an entire yield curve. The negative retarding potential applied to the specimen in order to simulate a change in the incident primary energy was obtained from a Kepco OPS1000 operational power supply driven by a Kepco FG100 linear ramp generator.

The current flowing into or out of the specimen was proportional to the yield σ as described in section 7.2.4.1. Since I_a becomes very small to measure, a gated linear amplifier, Ferranti ZN424 was used to amplify the voltage developed across the sensing resistor R_s shown in Fig. 7.9. Since I_a had to be measured in the presence of the negative retarding voltage down to -1000 eV, the entire amplifier circuit floats at the retarding voltage. The ±15 V d.c. power supply was derived from two dry 18 V batteries regulated to 15 V by use of zener diodes.

The gating sinusoidal signal was obtained from a Brookdeal 5012F low distortion oscillator and applied to the gate via an isolation transformer (1:1 turns ratio with a ferrite core) and gating npn transistor pair. The output of the gated linear amplifier is a product of the gating signal and the input voltage signal generated by the absorbed specimen current across the sensing resistor and consists of a trail of periodic pulses. The height of the pulses depends on the specimen current I_a and modulation signal ($\simeq 3V_{pp}$, 10 kHz). The fundamental component of the gated linear amplifier output signal is proportional to I_a and was detected by a Brookdeal 401A lock-in-amplifier via an isolation transformer. The reference signal to the LIA was obtained from the oscillator.

The output of the LIA was taken to the Y input of a Bryans 26000A X-Y recorder and the output of the FG100 ramp generator (0-20 V) connected to

the X input of the recorder. An alternative yield data acquisition method is shown in Fig. 7.8. The output of the LIA was digitised by an analogue to digital converter under the control of a PDP11 microcomputer linked to the University GEC 4080 mainframe computer for data storage. The yield data could then be processed off-line. This system could not be fully used because of various system bugs.

7.2.4.5 Procedure for Measurement of the Secondary Electron Yield

The procedure for measurement of the secondary electron yield was rather straight forward. As a prelimenary linear operation of the yield circuit was checked by injecting a linear ramp of input current of 0-50 μA through the sensing resistor of the gated linear amplifier. The output of the LIA was also a linear ramp indicating correct operation of the yield circuit.

After having obtained a primary electron beam of energy E_p (900 eV and beam current of several μA as observed by the landing specimen current. The focus and beam size was checked on the fluorescent tablet and then the beam current measured by aiming it down the Faraday cup which was covered in a layer of gold black (Thomas and Pattinson 1970). The electron beam which arrives at grazing incidence into the side wall of the Faraday cup is fully absorbed and hence is accurately determined.

This current was normally set to a range between 3-7 μA and it was checked for every yield curve, and found to be very stable (1.5%). The specimen surface was then rotated into the beam and held at a horizontal plane with respect to the incident beam.

The retarding voltage applied to the specimen was held at 300 eV and the phase of the LIA adjusted to maximise the output signal. The calibration

of the yield curve was obtained as follows: the electron beam was again aimed into the Faraday cage with the retarding voltage driven slightly positive. Since all of the primary beam current is absorbed, $I_a = I_p$ and the resultant yield is 0 as given by expression 7.5. This gives the zero point on the vertical axis of the yield curve.

To determine $\sigma = 1$, the retarding voltage applied to the Faraday cage was slightly more negative then E_p, so that the beam was totally deflected and prevented from landing. For this case $I_a = 0$ and $\sigma = 1$. is obtained completing the scaling of the yield curve.

The specimen surface was next in the analysis position and it was ramped by the retarding voltage from +2 to -910 V, the resulting yield curve was permanently recorded on a Bryans 26000A X-Y recorder. Fig. 7.10 is a graph of the total secondary electron yield for a Faraday cup, indicating the calibration of the σ axis.

The aluminium sample surface was prepared in the same way as in AES experiments, In fact the growth of oxygen was monitored by AES by switching the RFA and electronics from one mode to the other so that the variation in the yield could be correlated to the level of oxygen coverage and oxide level on the surface.

7.2.4.6 Comments on the Yield Measurement Technique

This technique of measuring the secondary electron yield was accurate and fast. Accurate in that, σ is measured in terms of the absorbed specimen current I_a and not the secondary current I_s, which cannot be fully collected..

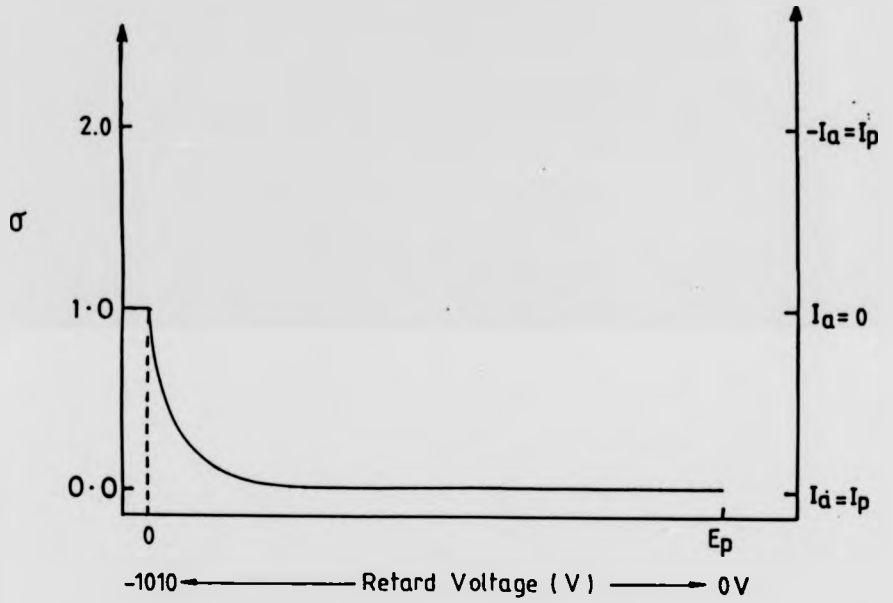

Fig. 7.10 Total secondary electron yield versus primary energy, for the Faraday cage for full absorption of primary current and indicating the calibration of the vertical axis.

Because the primary electron beam energy E_p and current I_p were kept constant during the recording of the yield, the measuring time was a lot faster and recording speeds were only limited by the time constants of the amplifier circuits.

A major drawback in the measurement method occurs at low retarding voltages. Severe defocussing of the electron beam results from distortion of the retarding electric field lines. This was caused by the field lines not being parallel to the primary electron momentum and by residual magnetic fields.

σ cannot be accurately measured for primary electron beams incident other than normal to the surface.

Secondary electrons produced at the inner grids may travel back on to the sample due to space charge effects. Several positive d.c. potentials were applied to the grids but no significant change in the quantitative value of σ was observed.

7.2.5 Conclusions

In this chapter, the experimental apparatus, instrumentation and procedures used in recording Auger electron spectra and secondary electron yield plots have been described. In addition, possible sources of error and limitations associated with each technique has been described. In the next chapter, results and discussion of AES and electron beam irradiation experiments performed on clean and oxygen exposed polycrystalline aluminium surfaces will be presented.

CHAPTER EIGHT

RESULTS AND DISCUSSION: OXYGEN ADSORPTION AND ELECTRON BEAM EFFECTS STUDIED BY AES

8.1 Introduction

In this chapter, the results of some preliminary experiments on setting up of the analyser are given. Then the results of AES measurements on the clean and oxygen covered polycrystalline aluminium surface, and electron beam effect experiments are also presented followed by a discussion of the results.

8.2 Preliminary Experiments, Observations and Surface Preparation

One of the first experiments performed on the AES system was to try and optimise the sample position with respect to the analyser. The sample height was adjusted in the axis of the electron gun and various elastic peak spectra recorded whose intensity (peak to peak height, PPH) and energy width measured and the position of the sample for each spectra noted (at this stage the aluminium surface was ion etched or heated).

Such a series of elastic peak spectra are shown in Fig. 8.1 together with the acquisition parameters. The spectra were acquired in the dN(E)/dE mode and since measurement of peak width for Auger peaks is rather ambiguous, the following method was used to determine this: the peak width ΔE was measured from the negative and positive going peaks and the energy E_p at which the derivative signal had crossed through zero. The measured resolution was 0.3 % obtained from $\rho = \Delta E/E \; |dN(E)/dE=0$ The theoretical resolution for the RFA is 0.1 % but a practical instrumental resolution of

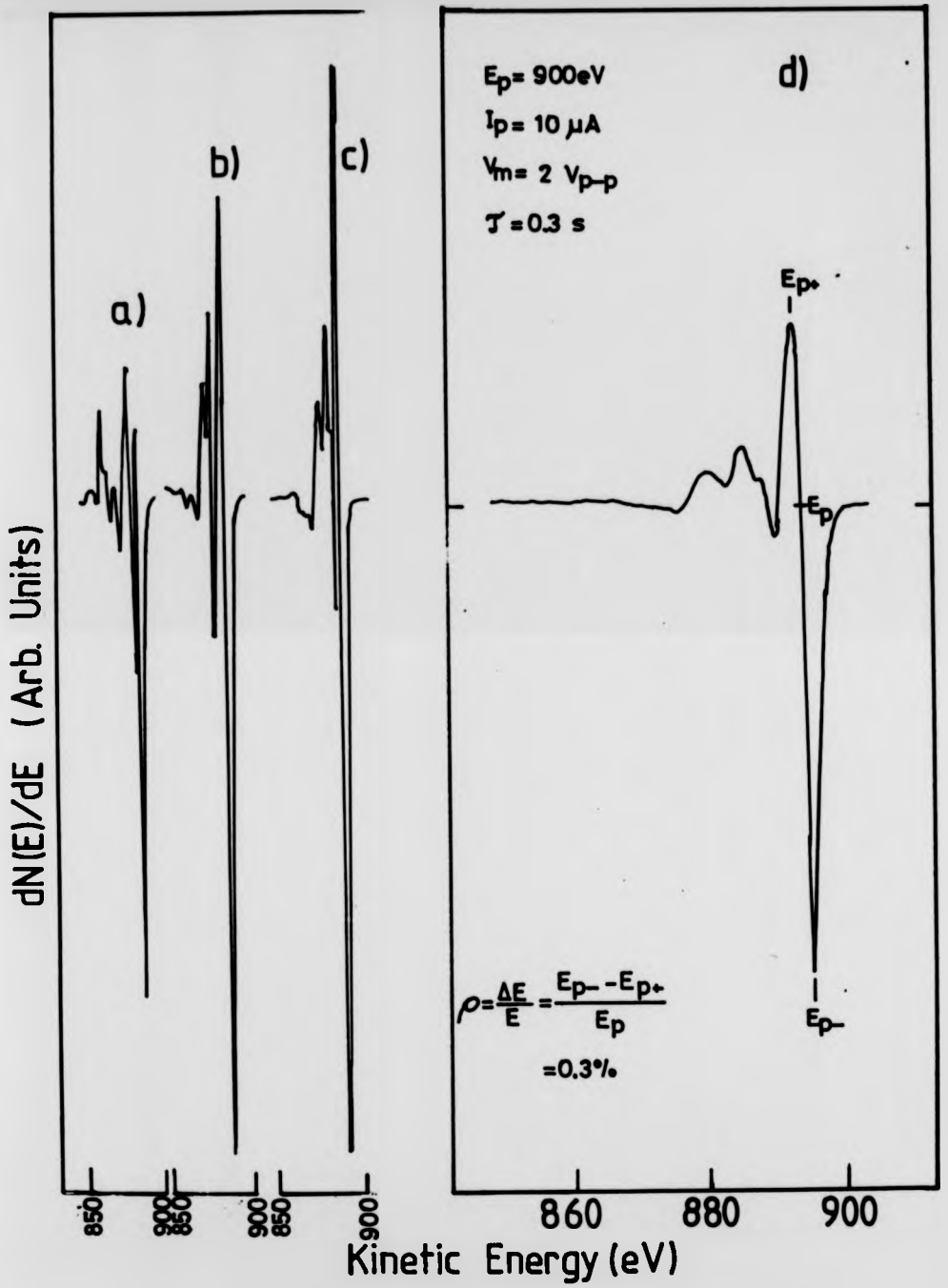

Fig. 8.1 Elastic peak spectra of contaminated Al surface for various sample positions in the up-down mode of the x-y-z manipulator (a, b, c). Spectrum c is at the ideal position, d is as c, with expanded energy scale to show measured resolution.

0.3 % with good sensitivity was found to be adequate for this work.

In order to check the reproducibility, instrumental drift and general stability of the AES system several elastic spectra were recorded at 45 minute intervals under the same acquisition conditions and parameters for spectra shown in Fig. 8.2. As can be seen the reproducibility is quite good. Fig. 8.3 is an Auger survey scan spectrum of the contaminated aluminium surface recorded at a base pressure of 3×10^{-10} torr after the STC and the SAC had been baked. The aluminium surface was heavily contaminated by a layer of carbon and oxygen. Some sulphur contamination was also detected. No elemental aluminium was identified, the Auger peak of energy 54 eV was identified to be due to aluminium oxide. All the above contaminants have been identified by reference to the Physical Electronics Industries handbook on Auger spectroscopy (1976). A more detailed analysis of the Auger transitions of the contaminants and metallic aluminium will be given in section 8.3.

Shown in Fig. 8.4 are a series of window spectra of oxygen O_{KLL} transition as a function of sample position with respect to the analyser centre of curvature. The fall off in signal intensity was appreciable when the sample was moved from the ideal. This position was relatively easily reproducible.

Several initial argon ion sputtering experiments were carried out in order to arrive at a suitable set of argon ion gun operating parameters for obtaining contaminant free surfaces as determined by AES. In Fig. 8.5 are shown a series of Auger window spectra for various etching periods. The survey spectrum was recorded after 10 minutes of argon ion bombardment resulting in total removal of the surface contaminants with the following operating parameters; anode voltage 5 keV, ion current at the sample 10 μA

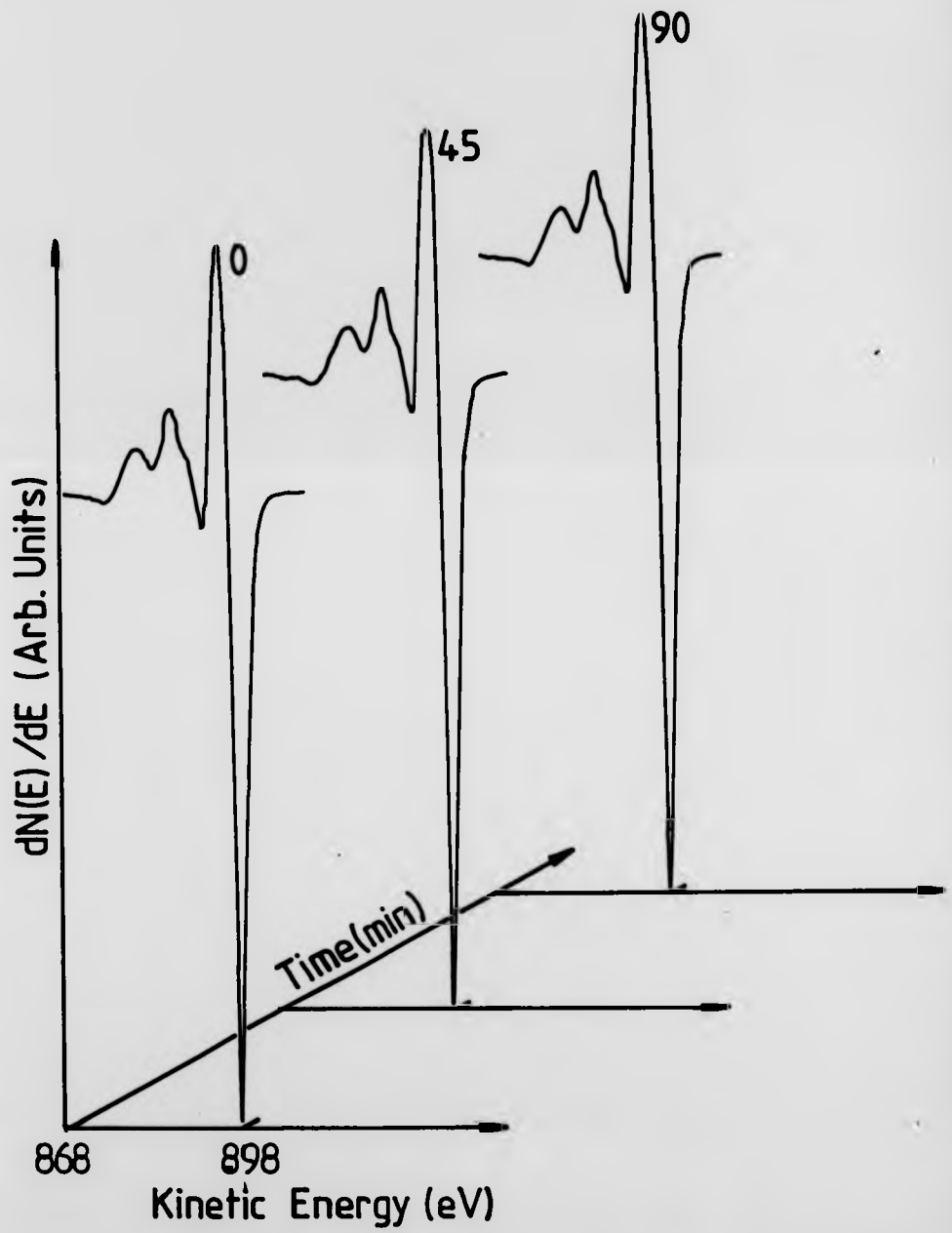

Fig. 8.2 Elastic peak spectra of the contaminated Al surface taken at 45 minute intervals (E_p = 900 eV, I_p = 10 μA, V_m = 2 V_{pp}).

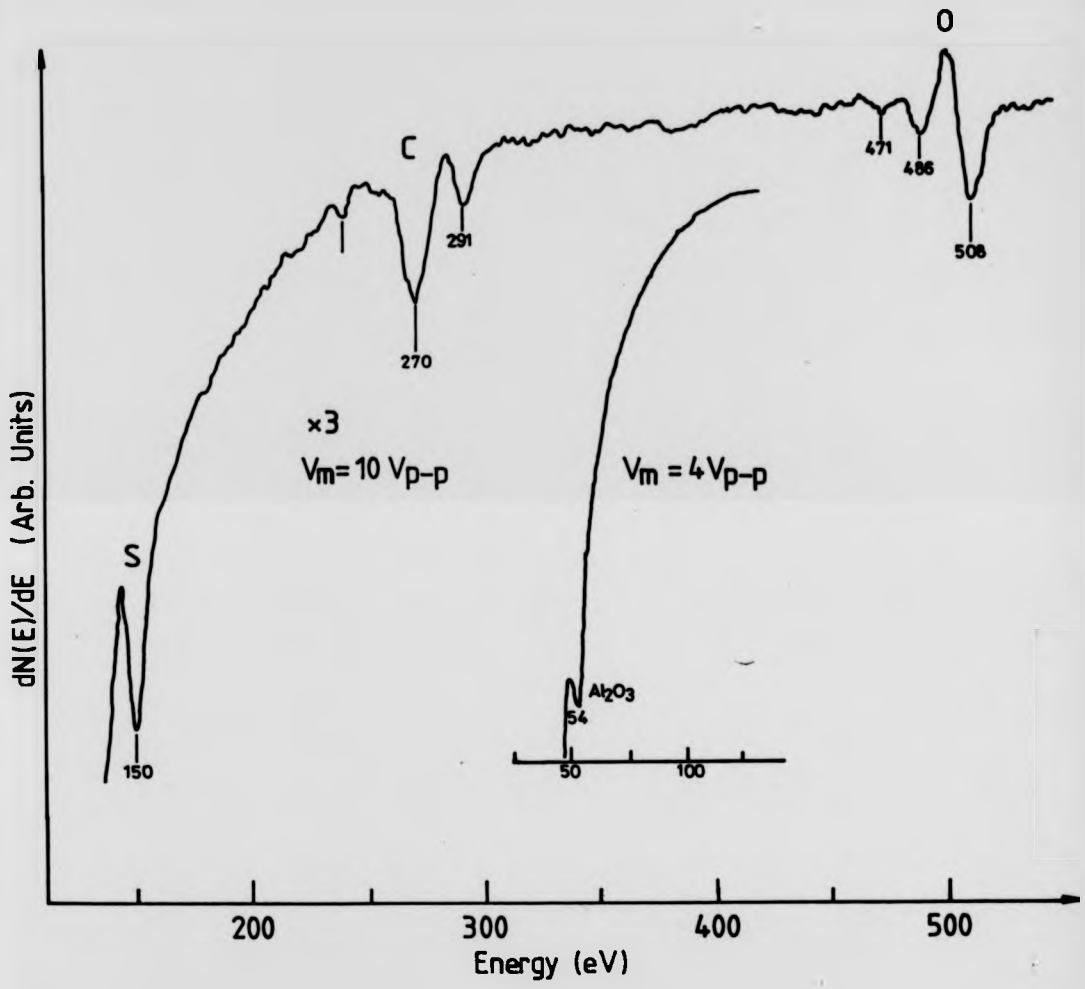

Fig. 8.3 Survey scan Auger electron spectrum of the contaminated Al surface after bakeout (E_p = 1500 eV, I_p = 10 μA).

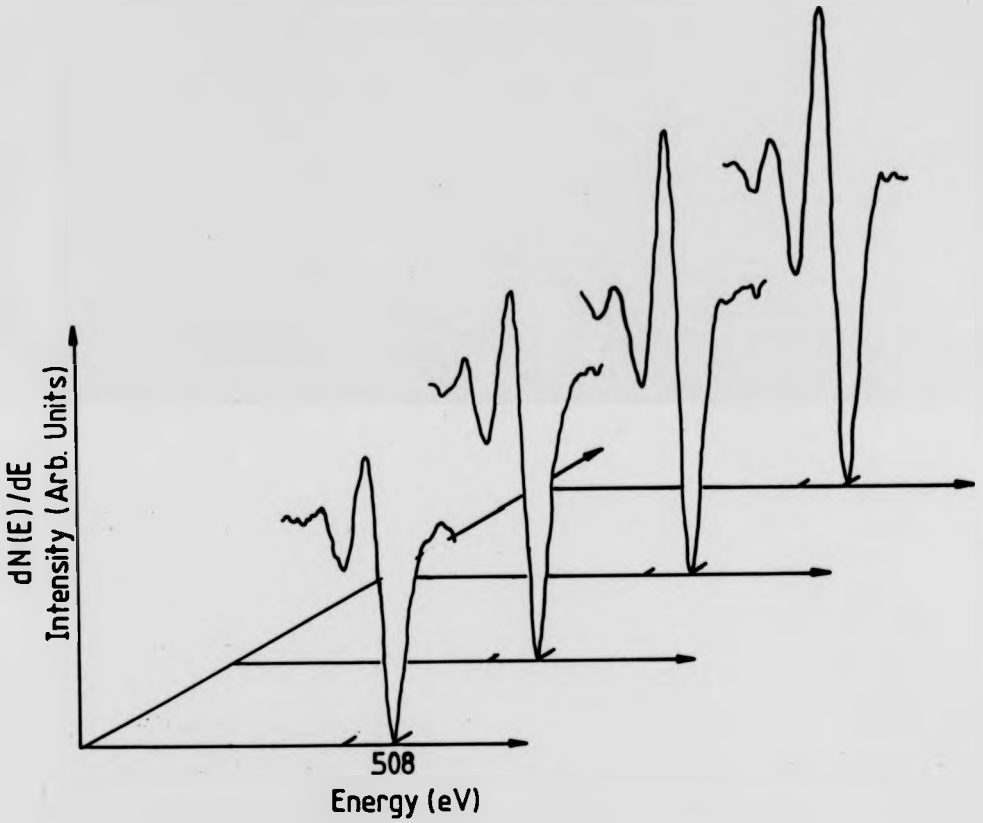

Fig. 8.4 Oxygen Auger window spectra showing fall off in PPH intensity with sample position (E_p = 1500 eV, I_p = 20 μA, V_m = 10 V_{pp}).

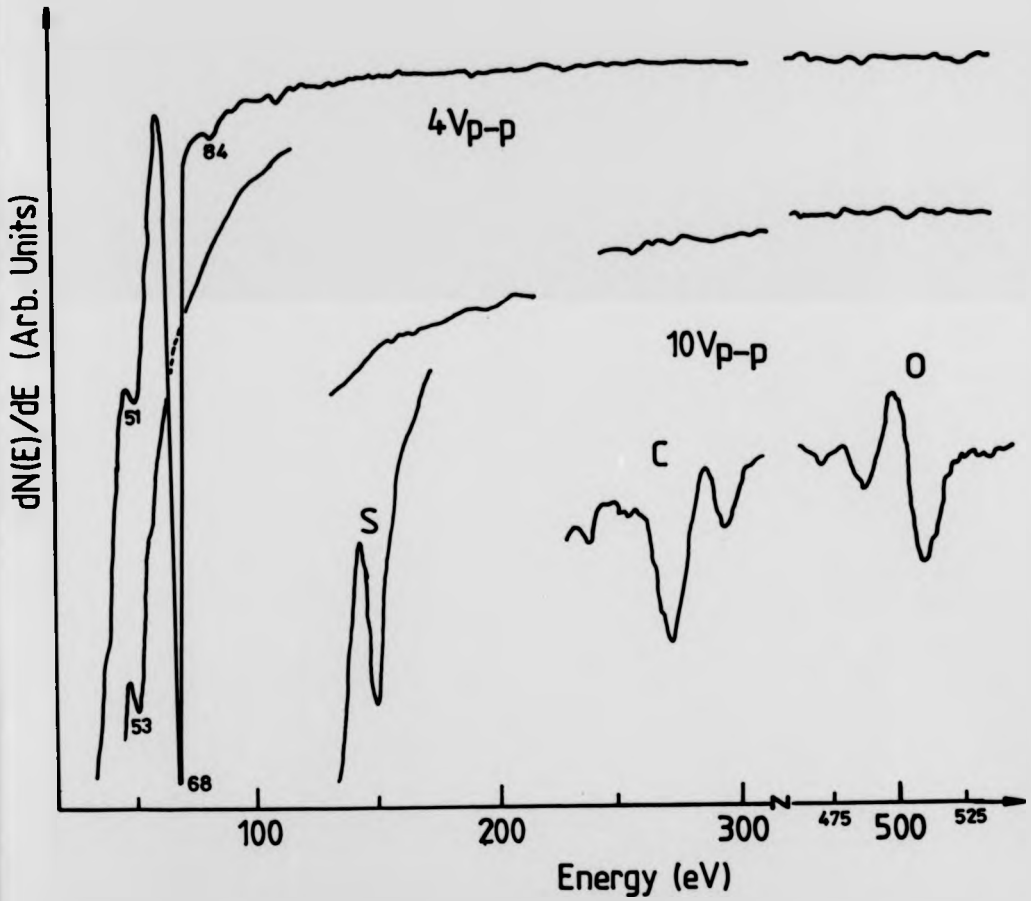

Fig. 8.5 Auger window spectra (E_p = 1500 eV and I_p = 20 μA) of the contaminated Al surface and argon ion etched surface (E_{A+} = 5 keV, I_{A+} = 15 μA, 10 minutes).

and sample to ion source distance approximately 5 cm.

8.3 Identification of Auger Electron Transitions observed on the Contaminated Clean and Oxygen Exposed Aluminium Surface

In Table 8.1, a summary is presented of all the Auger electron peaks observed for various states of the polycrystalline surface. Measured kinetic energies fall within ± 2 eV of published data. Clean aluminium surface exhibits an intense peak at 68 ± 1 eV which is attributed to an $L_{2,3}VV$ transition. Also accompanying this intense peak on the low and high energy shoulders are two smaller peaks occuring at 51 ± 1 eV and 84 ± 1 eV. The former is due to bulk plasmon loss processes, excited by the outgoing $L_{23}VV$ Auger electron, and the latter, more likely to be due to a double ionisation process. Quinto and Robertson (1971), Suleman and Pattinson (1971) and Dufour et al (1972) have already reported these transitions and discussed the origin and allocation of satellites.

The major Auger peaks observed on the contaminated sample surface were due to carbon KLL at 270 ± 1 eV and KLL transitions of oxygen, occuring at 508± 2 eV, 486 and 471 ± 2 eV. The sulphur LVV transition was measured at 150 ± 1 eV and this is quite a common contaminant found on metal surfaces that have been exposed to atmosphere.

On the low energy end of the Auger spectrum a small peak at 54 ± 1 eV was resolved after reducing the modulation voltage and increasing the sensitivity of the lock-in-amplifier. This was attributed to an inter atomic cross transition designated by $L_{2,3}V_0V_0$, and corresponds to bulk aluminium oxide (Al_2O_3).

Table 8.1 Measured Auger electron energies and their allocation, of various elements on the polycrystalline surface.

Contaminated Al Surface		Clean Al Surface		O_2 Exposed Surface	
Energy (eV)	Allocation	Energy (eV)	Allocation	Energy (eV)	Allocation
54±1	Al $L_{2,3}V_oV_o$	68±1	Al $L_{2,3}VV$	54±1	Al $L_{2,3}V_oV_o$
150±1	S L V V	40±1	Al $L_1L_{2,3}V$	68±1	Al $L_{2,3}VV$
240±1	Ca	51±1	$L_{2,3}VV-\hbar\omega_B$	48±1	
270±1	C KLL	84±1		84±1	
291±1	Ca			505±2	O $KL_{2,3}L_{2,3}$
471±2	O KL_1L_1			486±2	O $KL_1L_{2,3}$
486±2	O $KL_1L_{2,3}$			471±2	O KL_1L_1
508±2	O $KL_{2,3}L_{2,3}$				

Fig. 8.6 shows an Auger spectrum of oxygen adsorbed aluminium surface (10 minutes at 10^{-6} torr). The Al $L_{2,3}VV$ peak at 67 eV and the Al $L_{2,3}V_OV_O$ at 54 eV are both present and the oxygen KLL 505 eV peak clearly evident. This large apparent shift to lower kinetic energy by about 15 eV of the Al $L_{2,3}VV$ peak gives information about the chemical environment of the Al atoms. Both the 67 eV and the 54 eV peaks have been used in this work to monitor the surface adsorption of aluminium; in addition the O_{KLL} peak was also monitored. The high energy Auger peak of aluminium KLL at 1400 eV was not observed because the operational power supply could only generate a retarding potential of 1000 eV.

8.4 Effect of Residual Gases on the Clean Al Surface

Fig. 8.7 shows a mass spectrum of the UHV environment recorded with a quadrupole residual gas analyser after a bakeout. The major constituent of the residual atmosphere was argon (pp 5 x 10^{-9} torr) which was due to a slight leak from the MD6 leak valve. Carbon monoxide (1.2 x 10^{-10} torr) and water vapour (6.2 x 10^{-11} torr). The effect of the residual gases on the clean surface in the presence of the electron beam is shown in Fig. 8.8. Auger window spectra of the Al^{67}, carbon and oxygen peaks were monitored for three days. The Al^{67} had decreased significantly in intensity and both the carbon and oxygen peaks increased in proportion. At the end of this period the $Al\text{-}O^{54}$ peak associated with aluminium oxide did not appear. In fact the relative intensity of the carbon peak was higher than the oxygen peak.

The combined effect of the residual gases and electron beam irradiation on the the clean aluminium surface is shown in Fig. 8.9. Main constituents of the residual gases consisted of hydrogen, carbon monoxide and water vapour all in the 10^{-10} torr range. The intensity of the carbon and oxygen

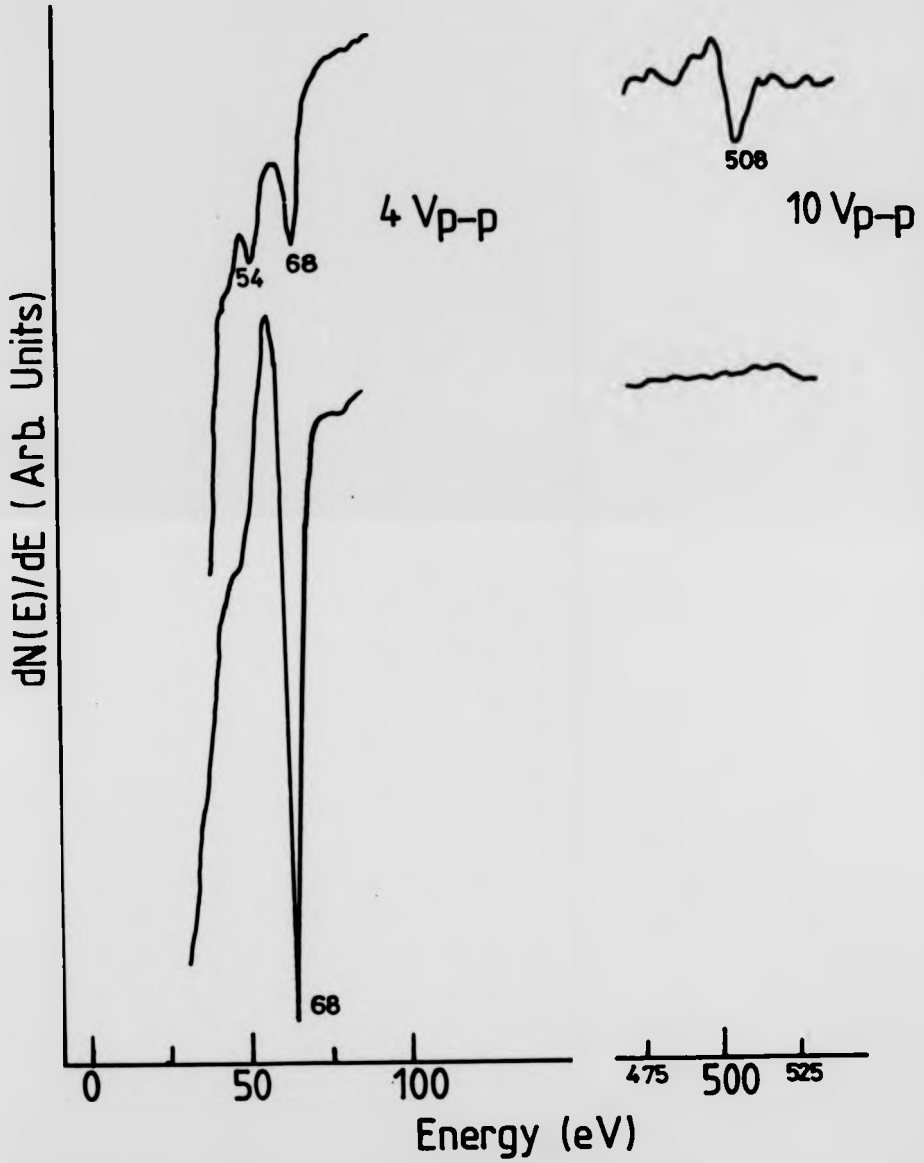

Fig. 8.6 Auger window spectra of clean Al surface (bottom), and oxygen exposed surface (top, 10^{-6} torr, 5 mins, E_p = 1500 eV and I_p = 15 μA).

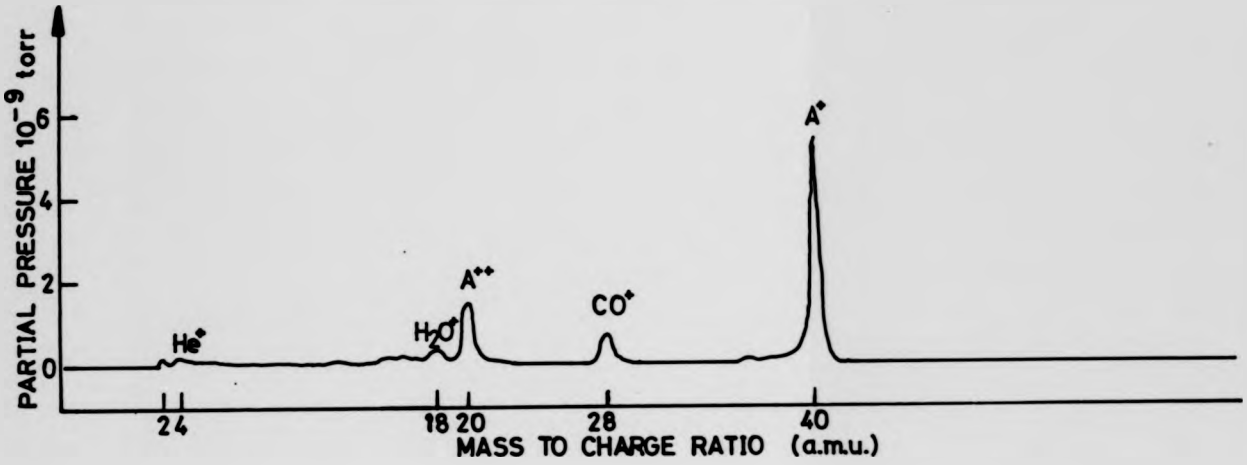

Fig. 8.7 Residual gas analysis of the UHV environment after ion etching for 10 minutes.

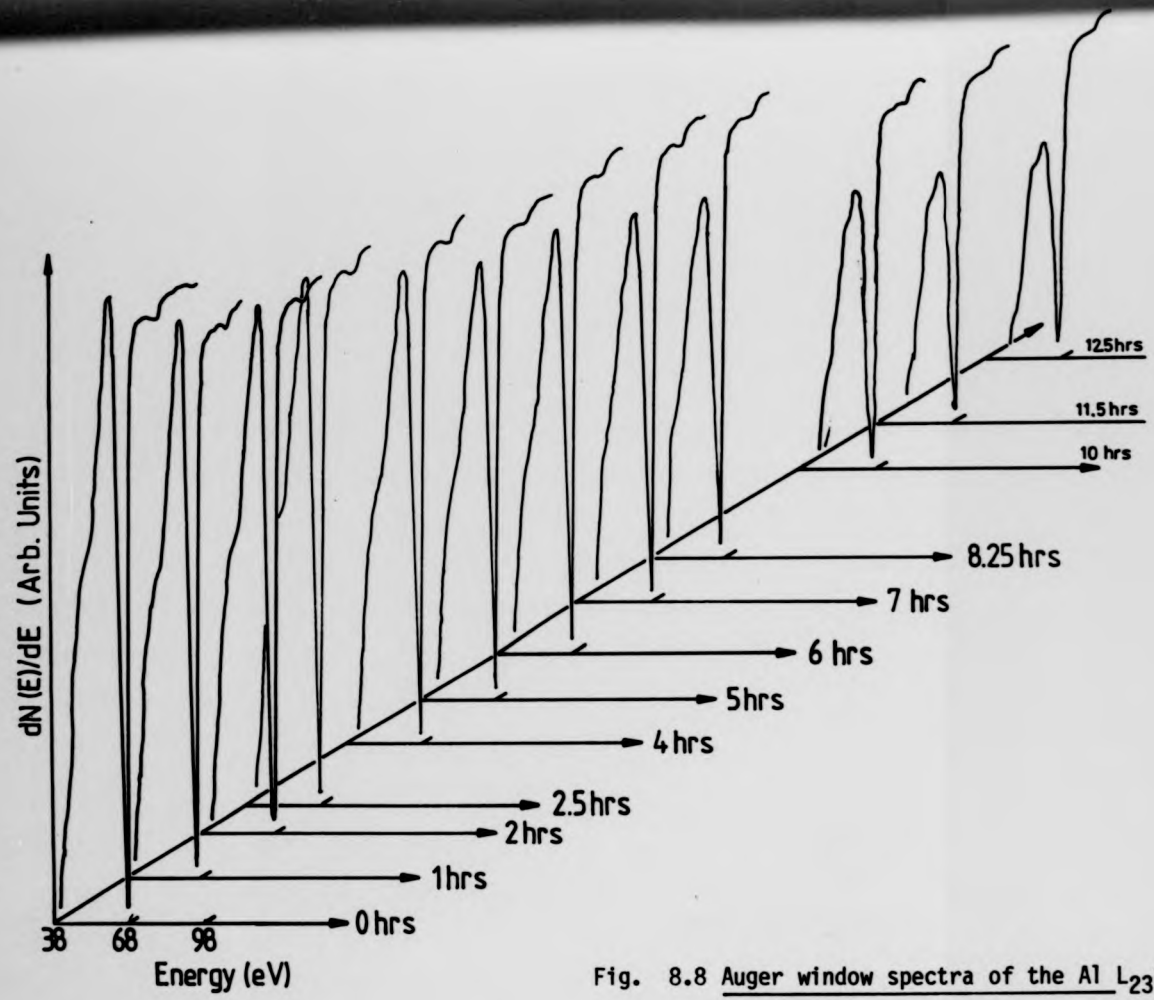

Fig. 8.8 Auger window spectra of the Al $L_{23}VV$ peak as a function of exposure time to the residual gases in the UHV environment and electron beam (E_p = 1500 eV, I_p = 20 μA, V_m = 4 V_{pp} at 10^{-10} torr).

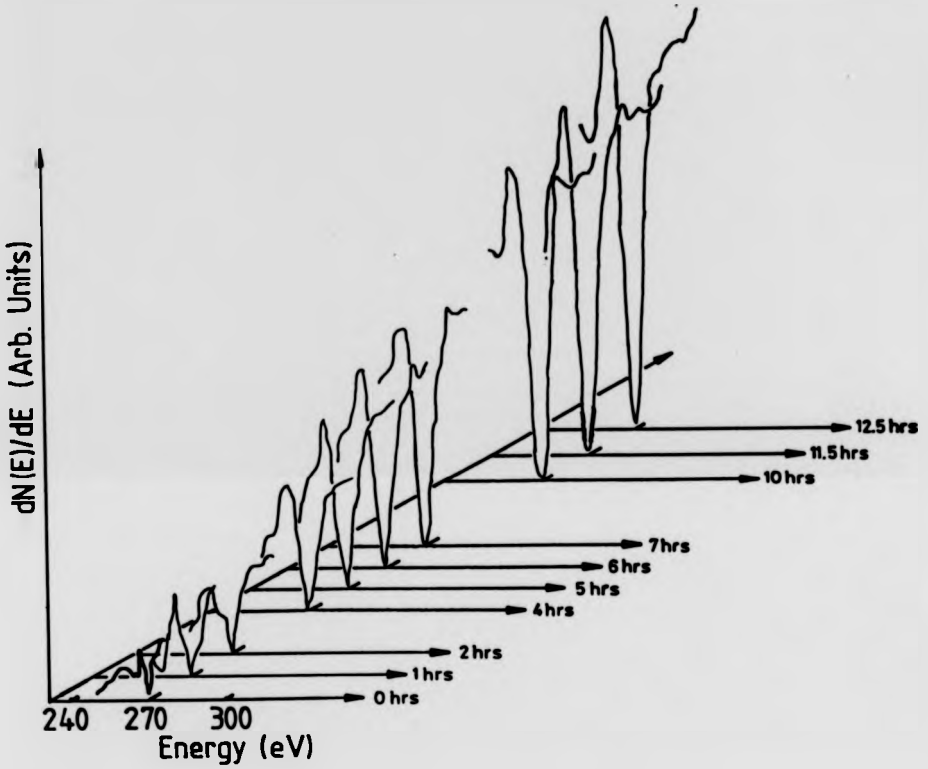

Fig. 8.9 C_{KLL} Auger window spectra as a function of exposure time to the residual gases in the UHV environment (E_p = 1500 eV, I_p = 20 μA and V_m = 10 V_{pp}).

Auger PPH only began to increase beyond the noise level after 4-5 hours of electron beam irradiation. The aluminium peak intensity on the other hand appeared to be stable at first, decaying at a faster rate after several hours of electron beam irradiation. Carbon appears to be incorporated on the surface by the electron beam, oxygen to a smaller extent as it is actively desorbed from the surface by mechanisms already discussed in chapter 3.

8.5 Oxygen Adsorption on Clean Aluminium Surface

8.5.1 Introduction

The evolution of oxygen on a clean polycrystalline aluminium surface was monitored by AES, by exposing the surface to oxygen at various pressures. The total exposure was calculated by multiplying the pressure with exposure time and converting the product into Langmuir units (1 L = 10^{-6} torr second).

The choice of electron beam energy and current density for these oxygen exposure experiments was chosen after some prelimenary trials to see at what value of current density, beam effects are observed i.e. desorption and adsorption phenomena. Shown on Fig. 8.10 is a typical plot of normalised Al^{67}, $Al\text{-}O^{54}$, and O^{505}, Auger PPH as a function of electron irradiation time for I_p= 20 μA.

A compromise value of 7.5 μA for the electron beam current was used to evolve the main oxygen adsorption profiles on aluminium. This value gave, minimum desorption effects and reasonable signal to noise ratio so that oxygen could be detected for very low levels of adsorption. The sample surface was only exposed to the electron beam for the duration of recording

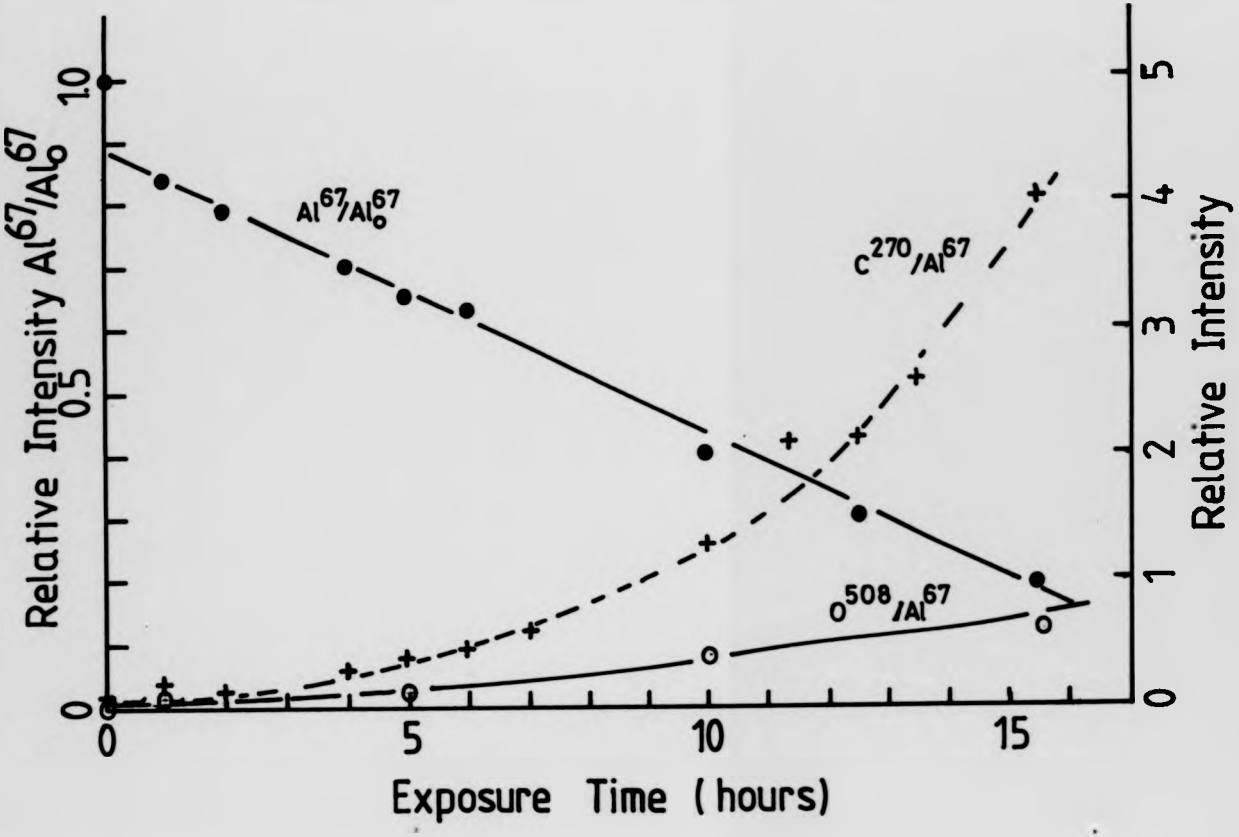

Fig. 8.10 Variation of relative Auger PPH intensities of Al^{67}, O^{505} and C^{270} peaks as a function of exposure time (E_p = 1500 eV, I_p = 20 μA, V_m = 4 and 10 V_{pp}).

of Auger window spectra. This varied from 2 to 5 minutes for each data point.

The adsorption profiles were formed for cumulative exposures of the surface. The general form of the adsorption curves was cross checked by discrete ion etch-adsorb experiment cycles. Fig. 8.11 shows that the two adsorption methods yield the same profile and hence the former was used throughout

8.5.2 Evolution of the Adsorption Profile 0 - 1000 L

In this section attention will be focussed on the evolution of the oxygen O_{KLL}, aluminium $L_{2,3}VV$ and aluminium oxide $L_{2,3}V_OV_O$ Auger peak intensities as a function of oxygen exposure in the range 0 to 1000 L. Fig 8.12 represents Auger window spectra of O^{505}, Al^{67} and $Al\text{-}O^{54}$ peaks for successive oxygen exposures up to 1000 L.

The Al^{67} elemental peak is very sensitive to the state of the surface and as oxygen exposure is gradually increased it diminished in intensity at a very fast rate. The O^{505} Auger peak increased slowly at first from the noise level and by 30 L a new peak appeared at 54 eV. This of course is the $Al\text{-}O^{54}$ inter atomic cross transition peak and marks the conversion of adsorbed oxygen into surface oxide. By this time the Al^{67} peak has diminished to 20 % of its initial value.

With increasing oxygen exposure the $Al\text{-}O^{54}$ and O^{505} Auger peaks increased in intensity while the Al^{67} decreased though at a smaller rate. After 240 L of oxygen exposure, the changes in the Auger PPH were only slight. In order to show the amount of oxygen that has been adsorbed on the surface the O^{505} Auger PPH has been plotted as a function of oxygen exposure as

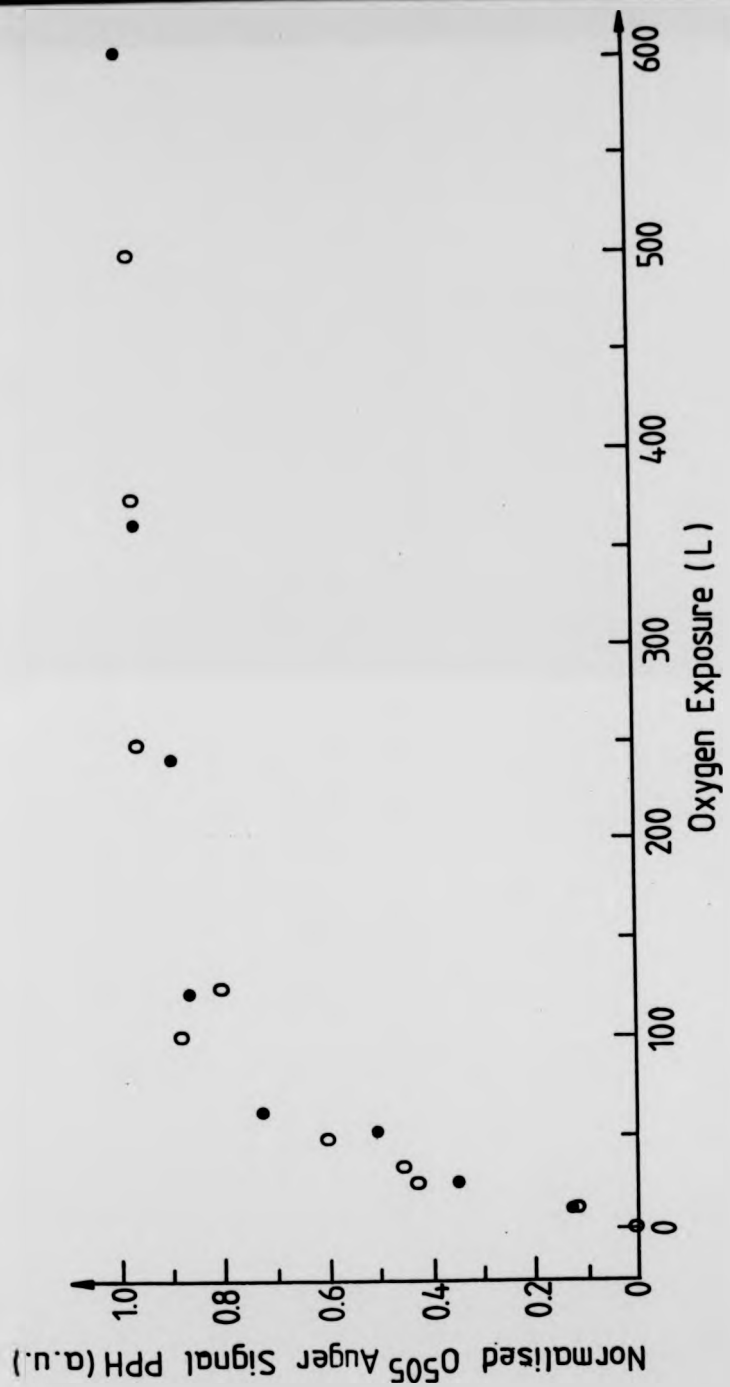

Fig. 8.11 Normalised O^{505} Auger signal PPH versus oxygen exposure. Adsorption of oxygen, by cumulative (•) and discreet etch-expose method (○).

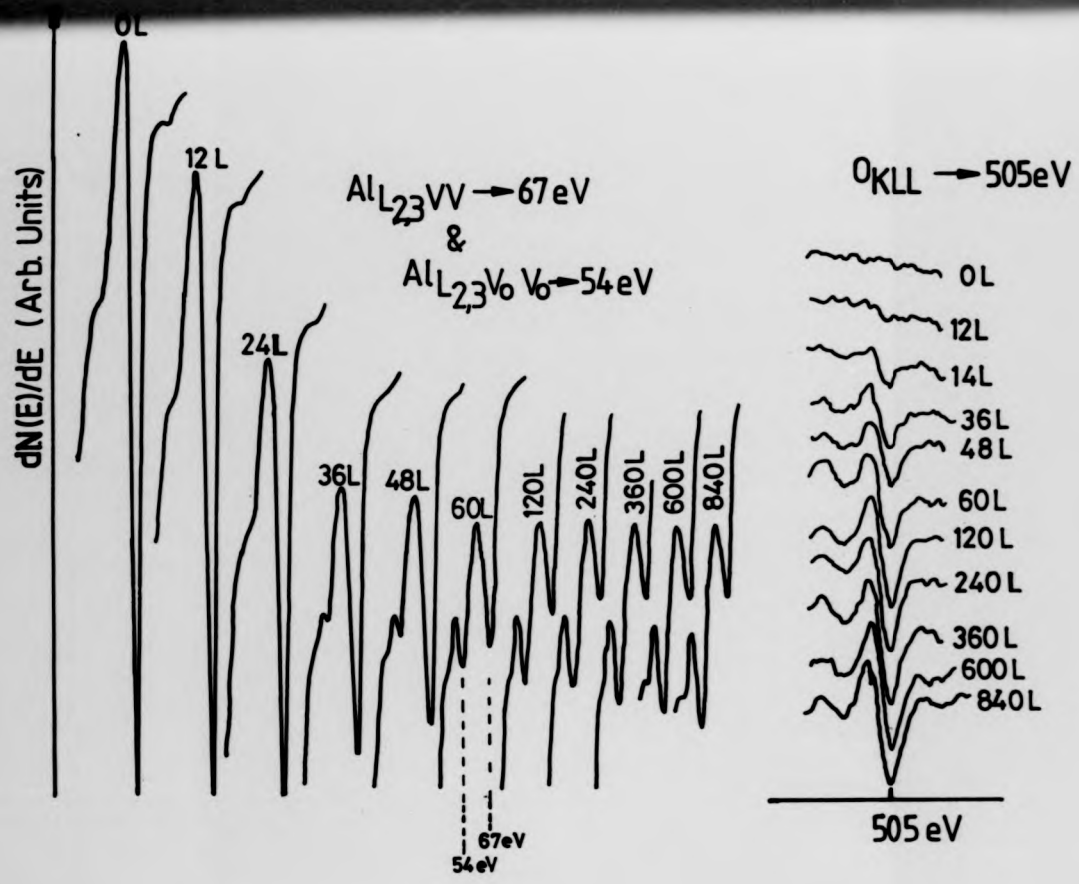

Fig. 8.12 AES window spectra of Al_{67}. Al-O^{54} and O^{505} peaks for various oxygen exposure levels up to 840 L (E_p = 1500 eV, I_p = 7.5 μA, V_m = 4 and 10 V_{pp}).

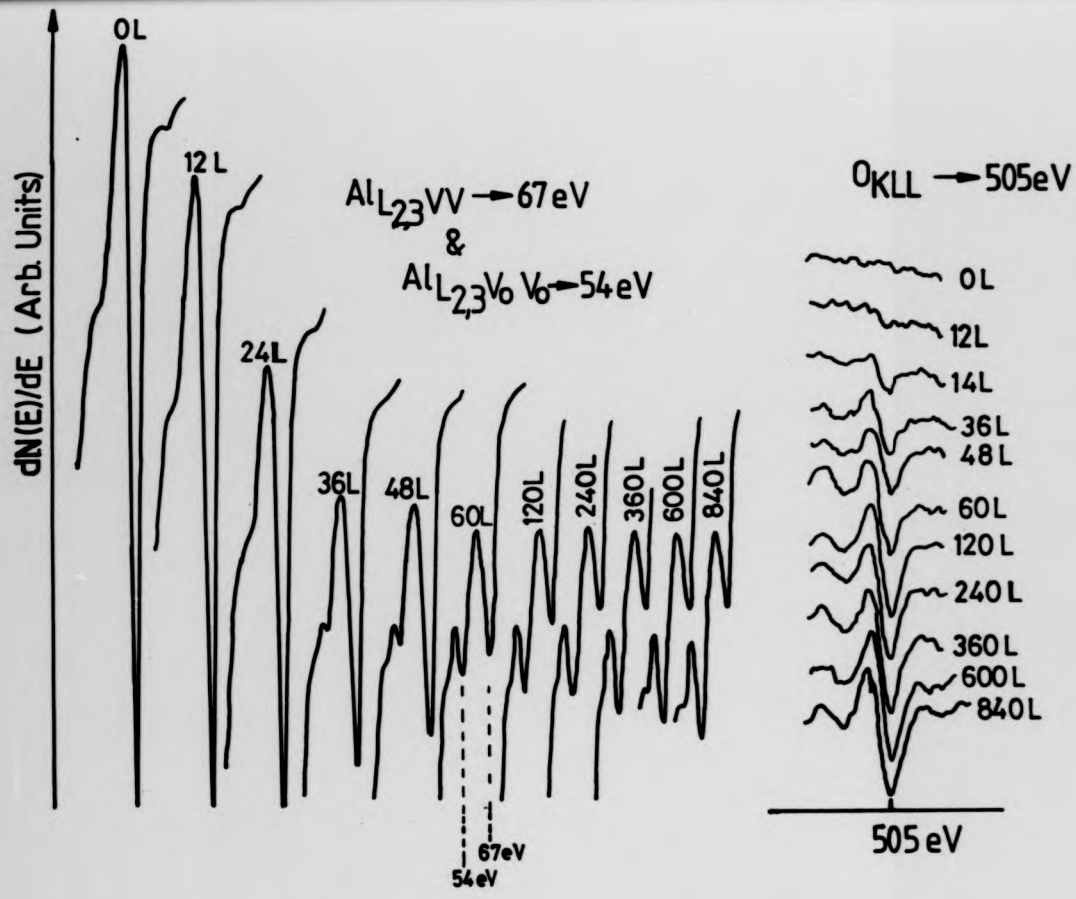

Fig. 8.12 AES window spectra of Al_{67}, $Al\text{-}O^{54}$ and O^{505} peaks for various oxygen exposure levels up to 840 L (E_p = 1500 eV, I_p = 7.5 μA, V_m = 4 and 10 V_{pp}).

shown in Fig. 8.13(a). The AES PPH is proportional to the elemental concentration on the surface. Also shown on this figure are the changes in the Al^{67} and $Al\text{-}O^{54}$ Auger peaks.

Fig. 8.13(a,b) represents Auger profiles from a single experiment and is typical of rest of the experiments. The scatter in the data points may be attributed to several factors (see section 8.7.1). One of the more obvious ones is due to sample repositioning problems with the sample manipulator and different degrees of surface roughness due to argon ion bombardment of the surface prior to each experiment. Also another source of error is due to the residual oxygen in the sample treatment chamber (STC) during pump down after a given exposure. This will tend to effect the low oxygen exposure levels and has not been taken into account.

In order to follow the adsorption kinetics of the O^{505} exposure, Fig. 8.13(a) has been replotted with the O^{505} AES PPH normalised at its saturation value corresponding to oxygen exposures in excess of 800 L. This plot is shown in Fig. 8.14 and from it an estimate of the initial sticking coefficient S_o can be made.

The estimated value of S_o will depend on the point at which, monolayer coverage is complete. Here it will be assumed that ML coverage occurs when the O_{KLL} PPH reaches 90% of its saturation value and this is reached after a total of 120 L of oxygen exposure. It is further assumed that the total number of adsorption sites per cm^2 on the polycrystalline surface will be an average of the adsorption sites available on Al(111), (110), and (100) faces, if these facets are randomly distributed throughout the surface.

The Al(111) face has the highest packing density and the Al(100) the least, as can be calculated from a knowledge of the lattice parameter and geometry

shown in Fig. 8.13(a). The AES PPH is proportional to the elemental concentration on the surface. Also shown on this figure are the changes in the Al^{67} and $Al\text{-}O^{54}$ Auger peaks.

Fig. 8.13(a,b) represents Auger profiles from a single experiment and is typical of rest of the experiments. The scatter in the data points may be attributed to several factors (see section 8.7.1). One of the more obvious ones is due to sample repositioning problems with the sample manipulator and different degrees of surface roughness due to argon ion bombardment of the surface prior to each experiment. Also another source of error is due to the residual oxygen in the sample treatment chamber (STC) during pump down after a given exposure. This will tend to effect the low oxygen exposure levels and has not been taken into account.

In order to follow the adsorption kinetics of the O^{505} exposure, Fig. 8.13(a) has been replotted with the O^{505} AES PPH normalised at its saturation value corresponding to oxygen exposures in excess of 800 L. This plot is shown in Fig. 8.14 and from it an estimate of the initial sticking coefficient S_o can be made.

The estimated value of S_o will depend on the point at which, monolayer coverage is complete. Here it will be assumed that ML coverage occurs when the O_{KLL} PPH reaches 90% of its saturation value and this is reached after a total of 120 L of oxygen exposure. It is further assumed that the total number of adsorption sites per cm^2 on the polycrystalline surface will be an average of the adsorption sites available on Al(111), (110), and (100) faces, if these facets are randomly distributed throughout the surface.

The Al(111) face has the highest packing density and the Al(100) the least, as can be calculated from a knowledge of the lattice parameter and geometry

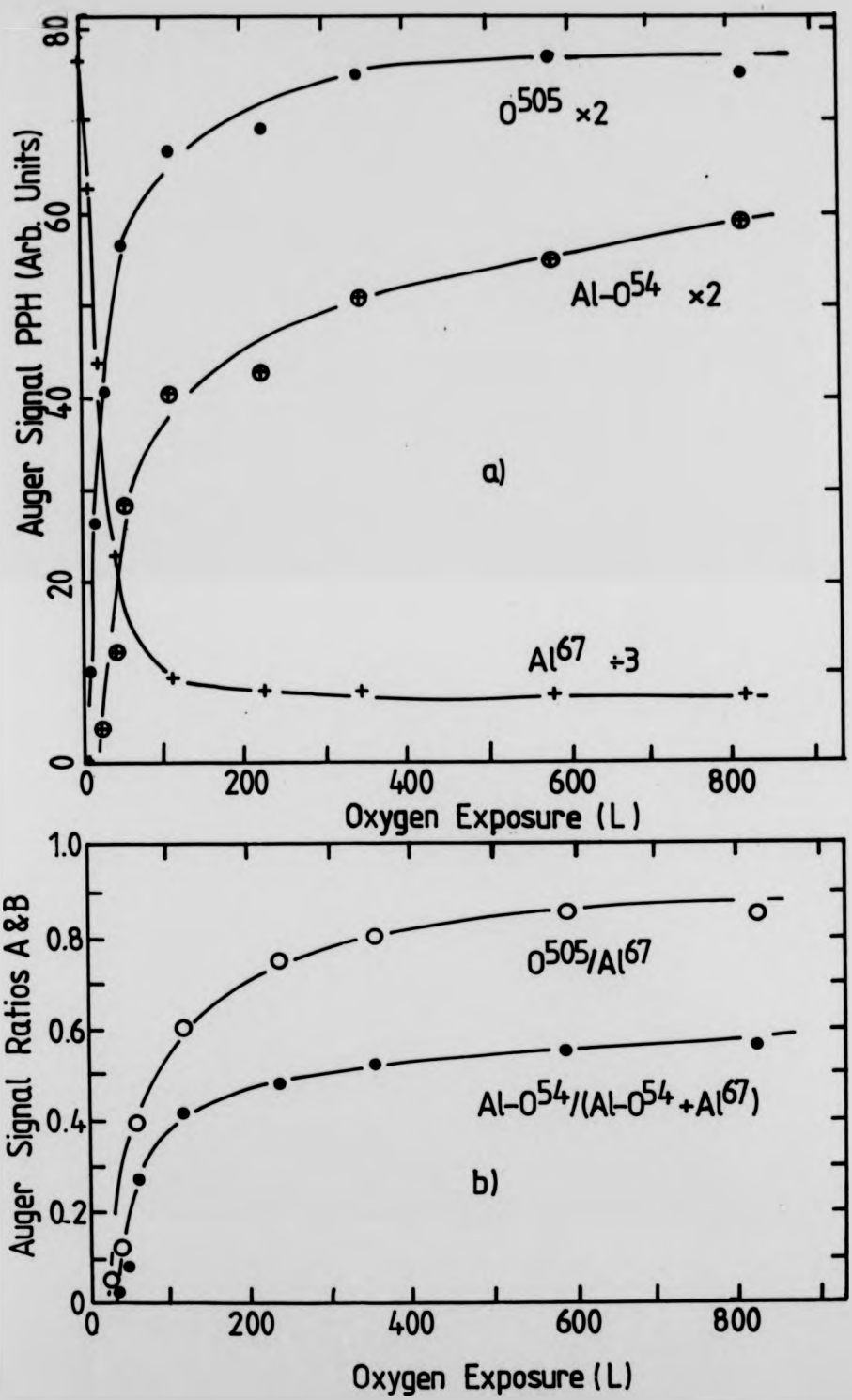

Fig. 8.13 (a) Al^{67}, Al-O^{54} and O^{505} Auger PPH as a function of oxygen exposure. (b) Auger PPH ratios A (O^{505}/Al^{67}) and B [Al-O^{54}/(Al-O^{54}+Al^{67})] versus oxygen exposure.

of the fcc unit cell. The average number of adsorption sites is then 1.0 x 10^{15} atoms/cm^2. Also assuming that 1 L is equal to an arrival rate of 3 x 10^{14} molecules/cm^2/s at room temperature at the surface and that oxygen adsorbs dissociatively, then the initial sticking coefficient S_o can be estimated by drawing a tangent to the initial rise in the O^{505} profile, where the extrapolated tangent intersects the line equivalent to coverage of 1 as indicated on Fig. 8.14. The gradient of this tangent multiplied by the number of adsorption sites will yield S_o of 0.03 ± .01. This value of the initial sticking coefficient is in good agreement with those reported by Martinson and Flodstrom for the Al(111) face and that of Gartland.

By use of a non-linear least squares fitting, computer program, a function of the form $f(L) = P_2[1 - \exp(P_1 L)]$ was fitted to the adsorption data points of Fig. 8.14. The program optimises the parameters P_1 and P_2 where P_1 is an effective sticking coefficient and P_2 is the normalised saturation value of the O_{KLL} PPH. Fig. 8.15(a) shows such a plot with the calculated line of best fit drawn through the data points. A good reproduction of the experimental data is observed, with an effective sticking coefficient of 0.02 which is in good agreement with the experimentally measured value.

From a similar consideration of the variation in the intensity of the Al^{67} Auger PPH was also calculated using the same non-linear least squares program to optimise the function $f(L) = P_2 \exp(-P_1 L) + P_3$ where P_2 is the maximum PPH corresponding to clean Al and P_3 is the equilibrium value. Again a good reproduction of the Al^{68} PPH variation with oxygen exposure was obtained as illustrated in Fig. 8.15(b) with a similar effective sticking coefficient.

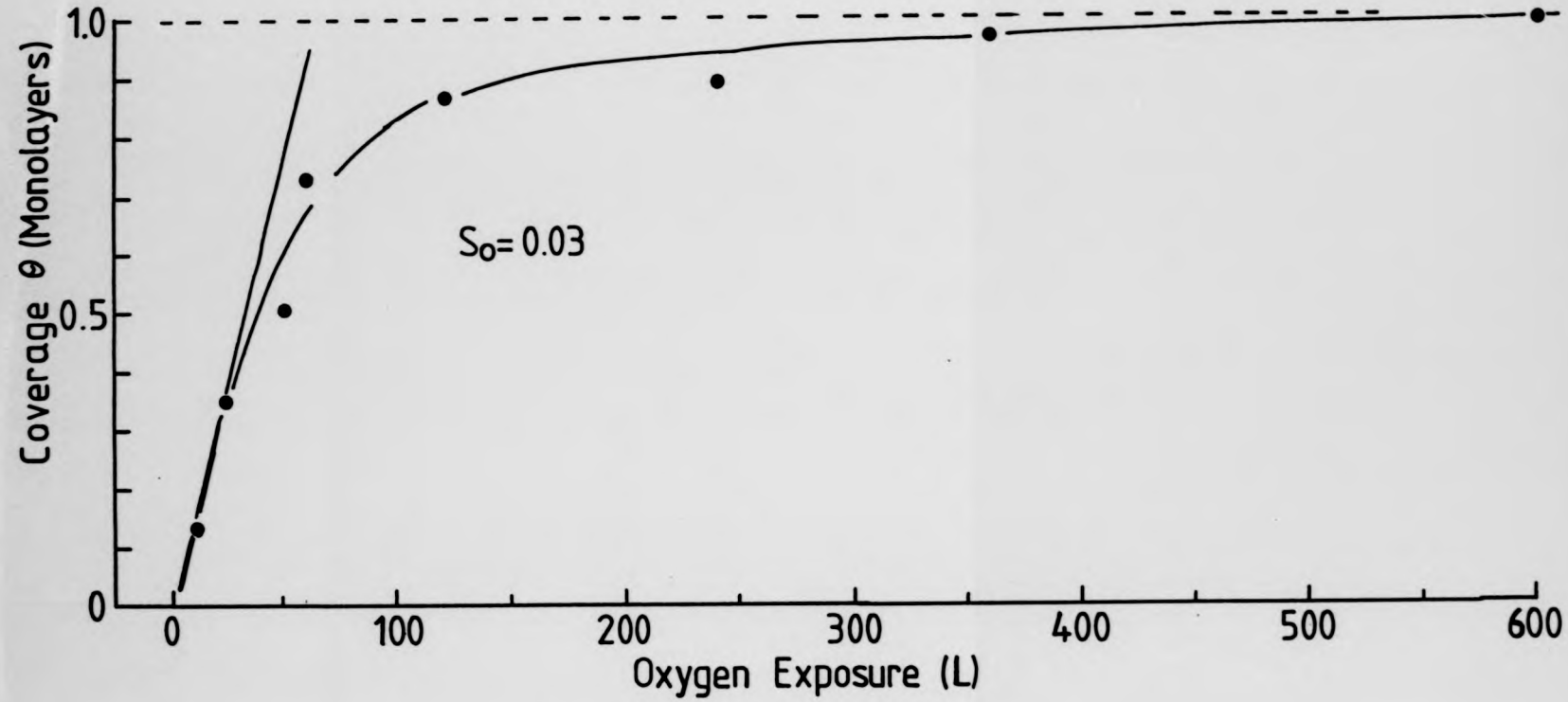

Fig. 8.14 Coverage versus oxygen exposure. The calibration of coverage scale is in monolayers and has been derived by normalisation of O^{505} versus exposure data of Fig. 8.13(a).

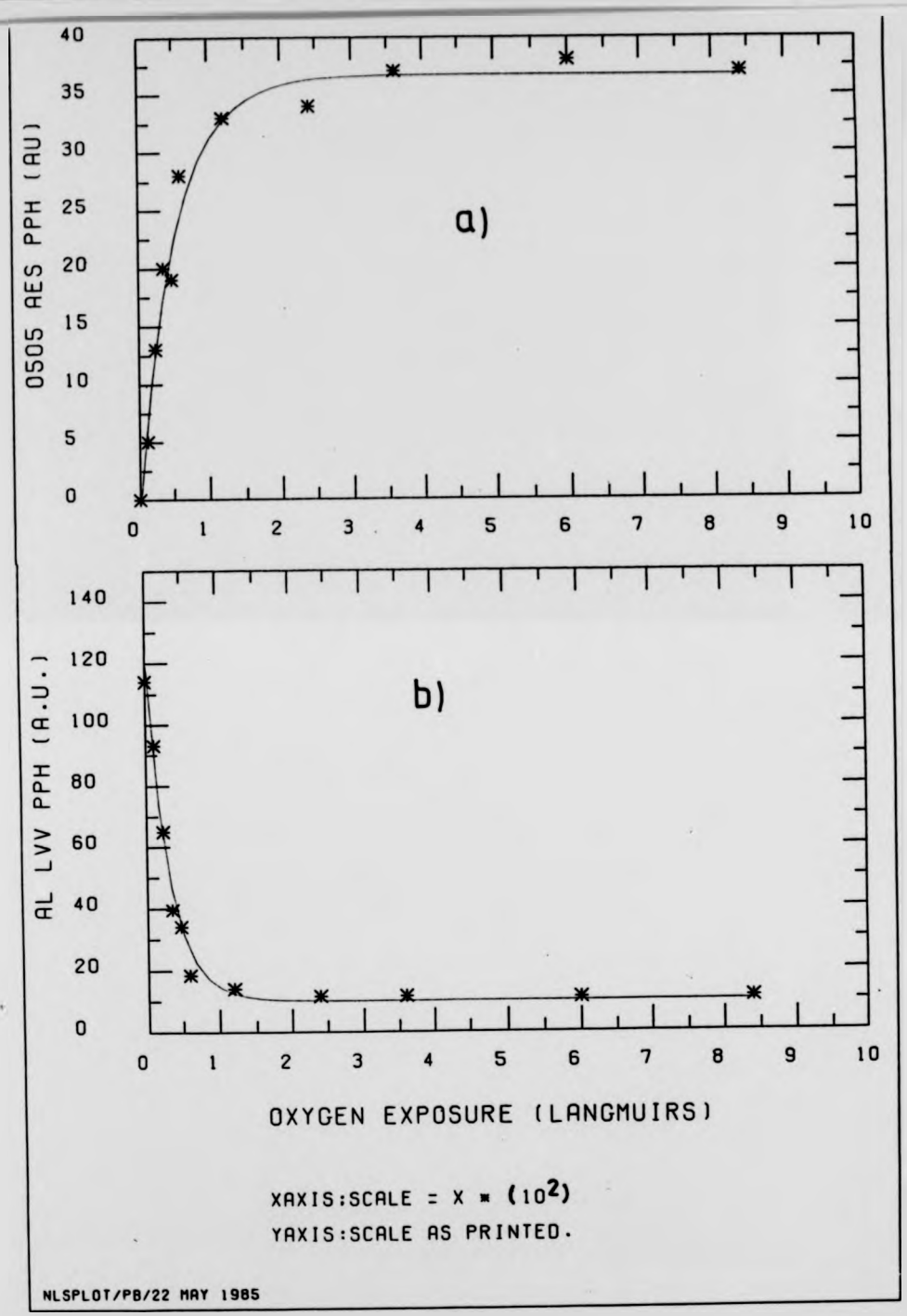

Fig. 8.15 (a) Adsorption of oxygen on Al. O^{505} AES PPH versus oxygen exposure, and solid line from computer fitted non-linear least squares calculation. (b) As above but for Al^{67} AES peak.

An alternative way of defining the onset of monolayer coverage, is the first appearance of oxidised aluminium as deduced by the Al-O^{54} Auger peak, marking the completion of a chemisorbed monolayer. This occurs in the oxygen exposure range of 20-50 L from which S_o of 0.01-.02 can be estimated. (In the XPS measurement of Martinson and Flodstrom, and Bradshaw et al, this point was marked by a 2.6 eV shift in the Al(2p) binding energy level to a higher one.)

The ratio O^{505}/Al^{67} plotted as a function of oxygen exposure as in Fig. 8.13(b) also yields a reliable adsorption profile from which a similar S_o was estimated.

8.5.3 Evolution of Adsorption Profiles for Oxygen Exposures of 0 - 50 L

The PPH of O^{505} and Al^{67} as well as Al^{54} has been plotted versus oxygen exposure in Fig. 8.16. In this range the oxygen PPH has not reached its saturation value nor the Al^{67} PPH decayed to its minimum value. The appearance of the Al-O^{54} oxidised aluminium peak was after 20 L of oxygen exposure in agreement with the previous experiment.

8.6 Electron Beam Irradiation Experiments on Clean and Oxygen Exposed Polycrystalline Aluminium Surface

8.6.1 Summary of Experimental Procedure

In this section, results of electron beam irradiation experiments on clean and oxygen exposed polycrystalline aluminium surfaces will be reported. In the majority of the experiments the sample prior to electron bombardment

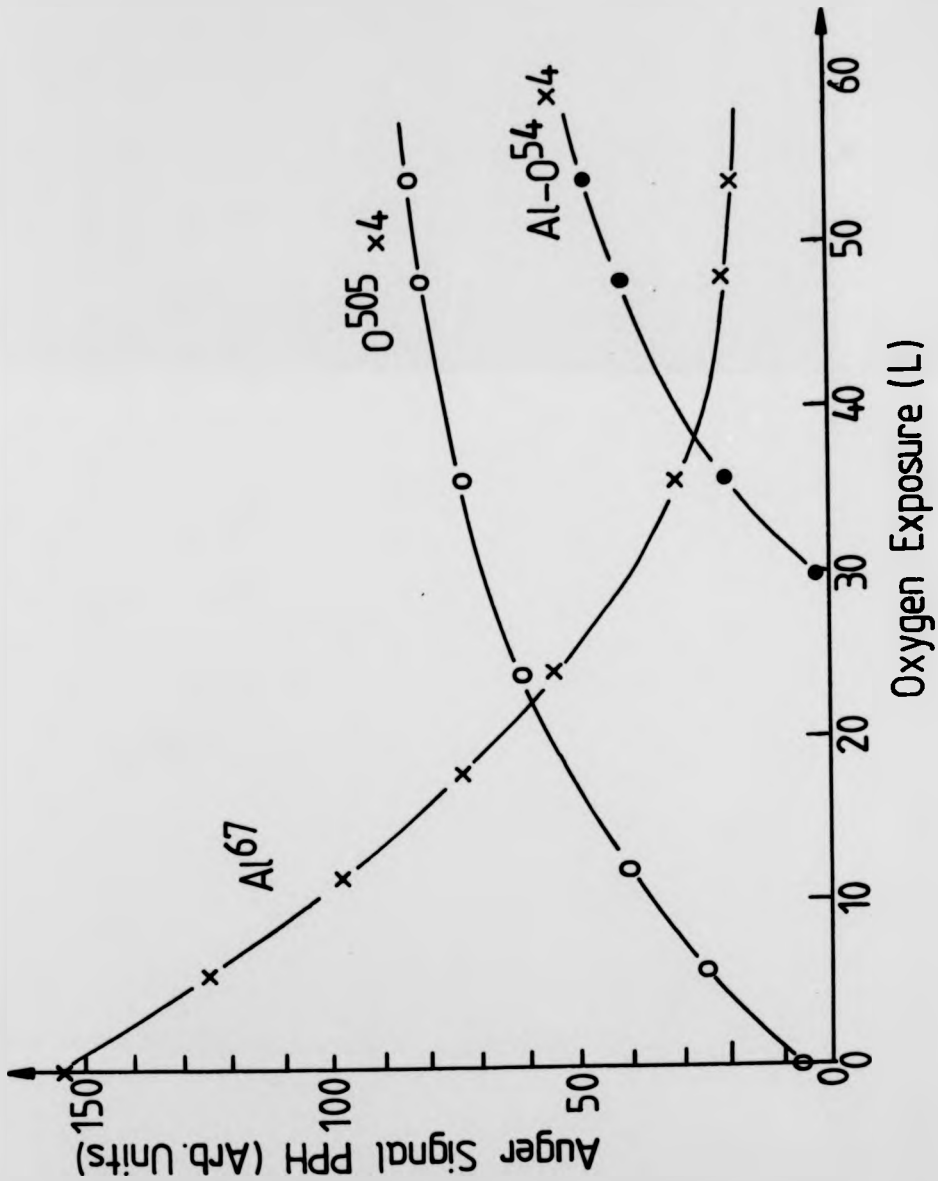

Fig. 8.16 Variation of Al^{67}, Al-O^{54} and O^{505} Auger PPH with oxygen exposure up to 50 L.

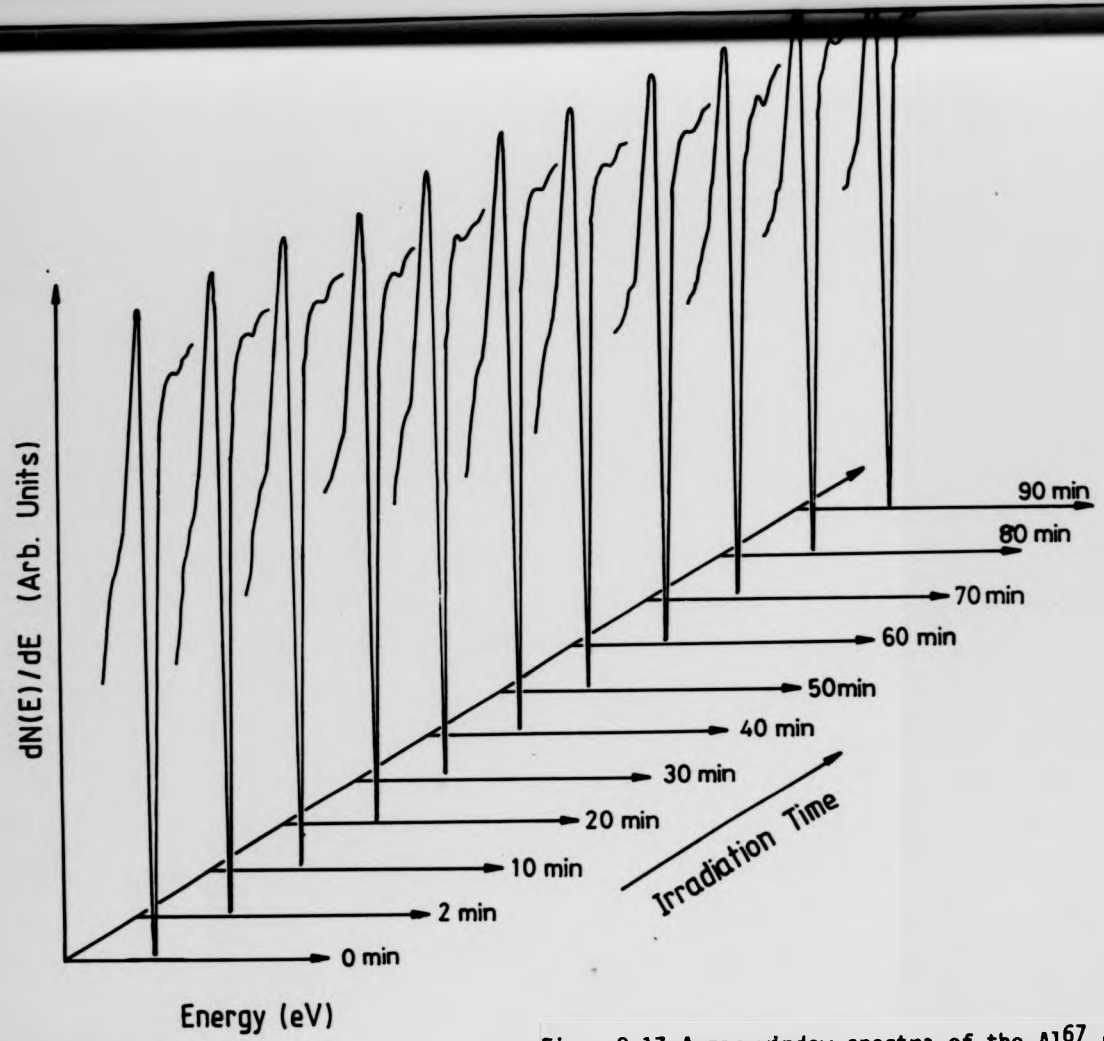

Fig. 8.17 Auger window spectra of the Al^{67} peak (clean surface) with irradiation time (E_p = 1500 eV and J = 9.5 x 10^{-4} A/cm^2).

was exposed to oxygen, in a range 50-1000 L. As demonstrated in the preceding section, in this range, the surface is assumed to have at least monolayer coverage.

The choice of electron current densities employed, was also determined by considerations of Auger signal sensitivity of the analyser and minimisation of thermal desorption effects and at the same time use of sufficiently high electron beam densities to cause measurable change in the AES PPH so that effective decomposition and desorption cross-sections could be measured with confidence. An electron beam current density of $J=9.5 \times 10^{-4}$ A/cm^2 corresponding to an $I_p = 7.5$ μA proved appropriate and majority of the electron beam irradiation experiments were conducted with this current density. The other current densities used were 1.9×10^{-3}, 5×10^{-4}, and 1.2×10^{-4} A/cm^2. All at a primary electron energy of 1.5 keV.

The oxygen exposure of the sample was as described in chapter 7. Auger window spectra (40 - 90 eV and 470 - 530 eV) of the electron irradiated spot was recorded every ten minutes for 90 minutes. At the end of this period the sample was moved slightly so that the beam was incident on a non-irradiated spot and the window Auger spectra of this spot was also recorded. The spectra were recorded in the dN(E)/dE mode and the scan speed was 1 eV/s and modulation voltages of 4.6 Vpp and 11 Vpp were used for the Al^{67} and O^{505} Auger peaks respectively. Initially the carbon 270 eV Auger peak was also monitored but did not increase beyond the noise level. All of the experiments were done at room temperature.

8.6.2 Electron Beam Exposure of the Clean Surface

The effect of the residual gases and the electron beam irradiation (current density $J = 9.5 \pm 0.5 \times 10^{-4}$ A/cm^2) on a clean polycrystalline surface was

investigated by following the changes in the Al^{67} and O^{505} Auger peaks over a 90 minute period. Fig. 8.17 represents a succession of O^{505} and Al^{67} Auger window spectra recorded every 10 minutes. It is apparent from this figure that no significant change in the Al^{67} PPH results. The O^{505} on the other hand does not increase beyond the noise level. Also no significant change in the signal shape as a function of irradiation time was noted.

A typical plot of the Al^{67} PPH versus irradiation time is shown in Fig. 8.18. After 90 minutes of electron beam exposure the Al^{67} PPH has dropped to 88 % of its original height. Point N on Fig. 8.20 represents a non-irradiated spot and the Al^{67} PPH from this had dropped to 94 % of its initial PPH. With reference to Fig. 8.13 the effect of the adsorption of residual gases and electron beam irradiation was equivalent to 10 L of direct oxygen exposure, while the effect of the background residual gas alone over the 90 minutes was approximately equivalent to 6 L of oxygen exposure. The oxygen and carbon Auger peaks always remained within the noise level throughout the 90 minute irradiation period. Also during this period no $Al\text{-}O^{54}$ Auger peak was detected.

It is worth while at this stage to estimate the probable temperature increase in the irradiated area of the sample, caused by the electron beam. The sample itself was securely attached to its holder and was in good thermal contact with it. Assuming a worst case of maximum current density, in the steady state, the temperature rise in the irradiated spot can be estimated from the relationship $\Delta T = 2E_pI_p / \pi Kd$, given by Knotek and Feibelman (1978), where E_p and I_p have their usual meanings, K is the thermal conductivity (2.37×10^2 W/m/K) and d is the irradiated spot diameter. In the steady state, a calculated temperature rise of 0.2 K is found for the irradiated spot. It is apparent that this is unlikely to be the cause of any thermal desorption phenomena.

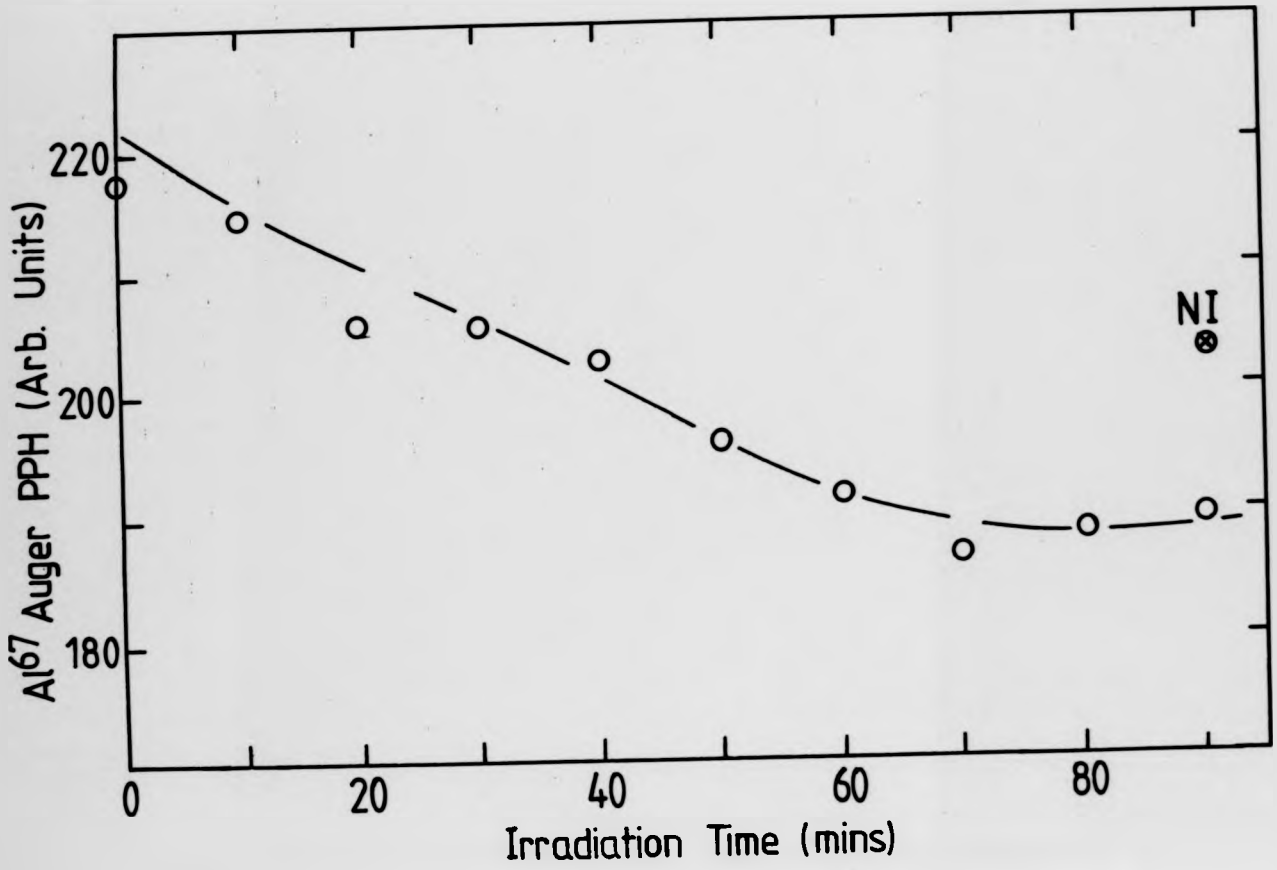

Fig. 8.18 Variation of the Al^{67} Auger signal PPH with electron beam irradiation time for the clean surface. NI is for non-irradiated spot (E_p = 1500 eV and J = 9.5 x 10^{-4} A/cm^2).

8.6.2.1 Simultaneous Oxygen Exposure and Electron Beam Irradiation of the Clean Surface

An experiment was attempted in which the response of the clean surface to simultaneous electron beam bombardment and oxygen exposure was investigated. At chamber pressures of $\gtrsim 10^{-8}$ torr it was found that the emission from the electron gun emitter cathode became unstable and severely attenuated and continuity in the recording of Auger spectra and constancy of the electron beam current density was lost. Therefore the attempt to pursue these experiments were abandoned.

8.6.3 Electron Beam Bombardment $J = 9.5 \times 10^{-4}$ A/cm^2 and $E_p = 1.5$ keV

8.6.3.1 Electron Beam Bombardment ($J=9.5 \times 10^{-4}$ A/cm^2) of the 1000 L Oxygen Exposed Surface

The effects of electron beam bombardment on the 1000 L oxygen exposed surface by 1.5 keV electrons of current density $J=9.5 \times 10^{-4}$ A/cm^2 is illustrated in Fig. 8.19(a) by the changes in the O_{KLL}, Al_{LVV} and Al_{LVoVo} PPH intensities versus irradiation time. The O^{505} and Al-O^{54} signals decreased considerably with dosage, where as the Al^{67} signal increased with dosage. At the end of the 90 minute irradiation period the sample was slightly moved and Auger spectra from this non-irradiated spot recorded. The PPH intensities from these spots have been marked as N on the figures.

A useful plot is the ratio O^{505}/Al^{67} (to be known as **ratio A**) versus irradiation time. Ratio A, gives an indication of surface oxygen coverage in any electronic environment. The **ratio B**, Al-O^{54}/Al-O^{54}+Al^{67}, on the other hand gives an indication of the concentration of the surface oxide since the Al-O^{54} Auger cross-transition only grows in intensity when

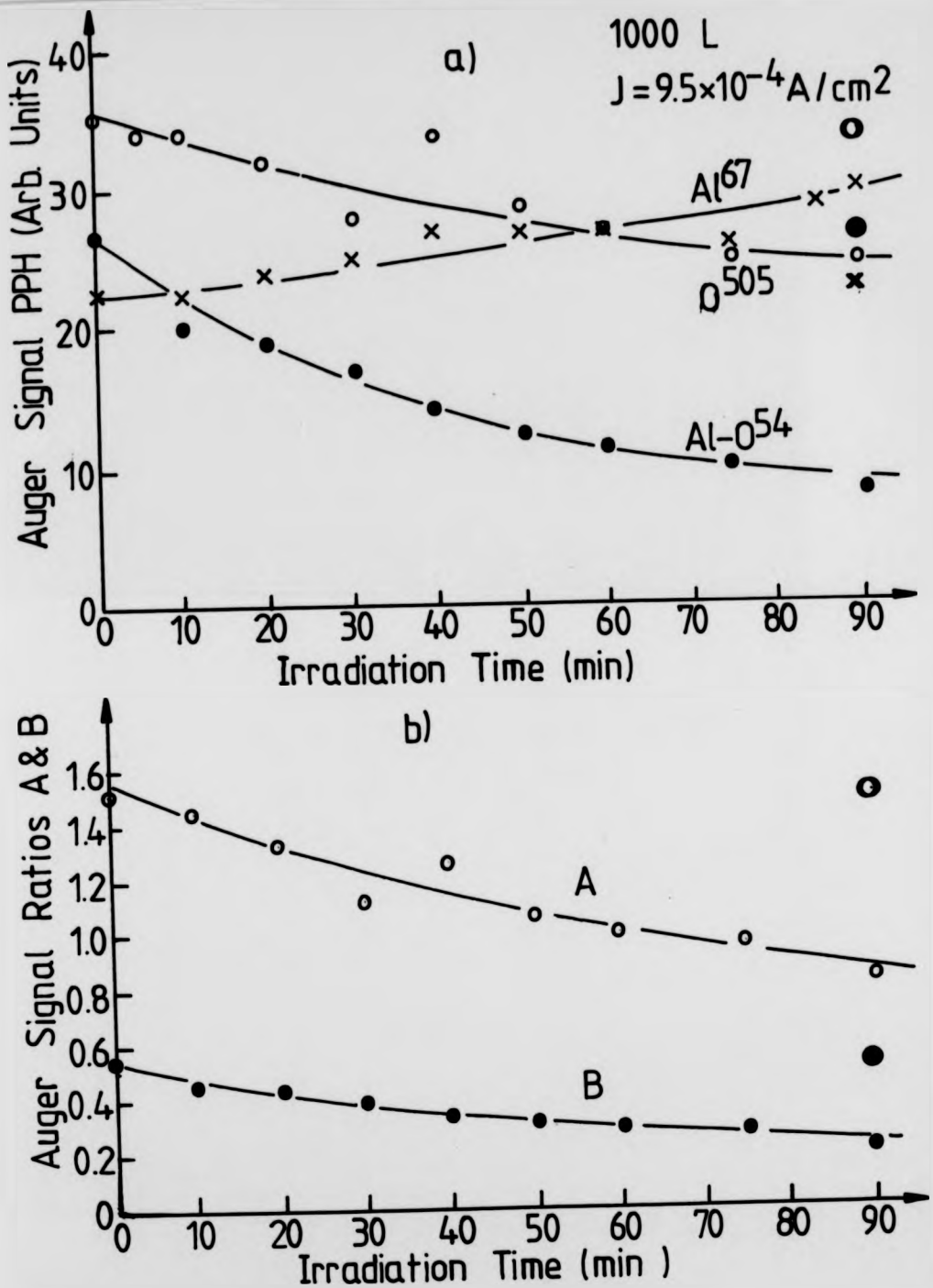

Fig. 8.19 (a) AES PPH variation of Al^{67}, O^{505} and Al-O^{54} peaks with electron beam irradiation time for the 1000 L exposed surface (J = 9.5 x 10^{-4} A/cm^2). (b) As above, but ratios A and B versus irradiation time.

chemisorbed oxygen becomes oxidic.

The ratios A and B have been plotted in Fig. 8.19(b) against irradiation time and points marked N correspond to non irradiated spots. Fig. 8.19(b) shows that the overall, rate of oxide reduction occurs at a faster rate than the decrease in the oxygen level. The reduction in ratio B and increase of elemental Al^{67} is being interpreted as decomposition of the aluminium oxide and possible desorption of oxygen under the direct action of the electron beam.

A qualitative feel for the changes in the PPH intensities can be made by noting these, after 50 minutes of continuous electron bombardment. The $Al\text{-}O^{54}$ and the O^{505} peaks decreased by 55 and 21 % respectively. Ratios A and B on the other hand decreased by 29 % and 44 %. The Al^{67} signal intensity increased by 17 %.

The signal PPH intensities from the non-irradiated spots compared with those at zero electron beam irradiation are consistent with the residual gases previously mentioned in section 8.6.2 and fall within the experimental error.

Effective total desorption cross-sections derived from the decrease in the AES PPH induced by the electron beam can be estimated if these are shown to obey first order rate expressions of the form, as given by eq. 3.7. Linear logarithmic least squares analysis has been performed on the $Al\text{-}O^{54}$, O^{505}, ratios A and B by use of a computer program, which showed the $Al\text{-}O^{54}$ and ratio B to decrease linearly with irradiation time, with regression coefficients of -0.98 or better.

Linear logarithmic least squares of the O^{505} signal PPH and Ratio A did not give a straight line fit through the data points indicating that the changes did not obey a first order rate expression. Ordinary linear least squares gave a similar result with wide scatter in the data.

Figs. 8.20(a,b) show normalised ln(Al-O^{54}) and ln(ratio B) to their initial values, as a function of irradiation time. The calculated error in the data has been drawn in as broken lines.

From the measured slope and knowledge of electron beam current density and electronic charge, the effective cross-section in the decrease of Al-O^{54} Auger signal PPH and ratio B induced by the electron beam, can be calculated. This has been done for a set of experiments, for the 1000 L oxygen exposed surface and an average effective cross-section of 3×10^{-20} cm^2 has been estimated. This value is in error by at least a factor of 2, since the electron current density can only be estimated to this accuracy in the present experimental set up.

By use of another computer program which can perform non-linear least squares fit of the first order rate expression of eq. 3.7, good estimates of the effective cross-section can be obtained. Eq. 3.7 has been re-written in the form

$$N(t) = N_\infty + (N_0 - N_\infty)\exp(-Q_T\, J/e\, t) \qquad \ldots(8.1)$$

where Q_T, J/e, N_0 and N_∞ are parameters to be optimised by an iterative procedure. After initial guesses for these have been made, the program gives a line of best fit through the experimental data points. In eq. 8.2 N(t) is the number of remaining atoms (proportional to the AES PPH) at time t, N_0 is the initial concentration of the atoms on the surface, N_∞ is the

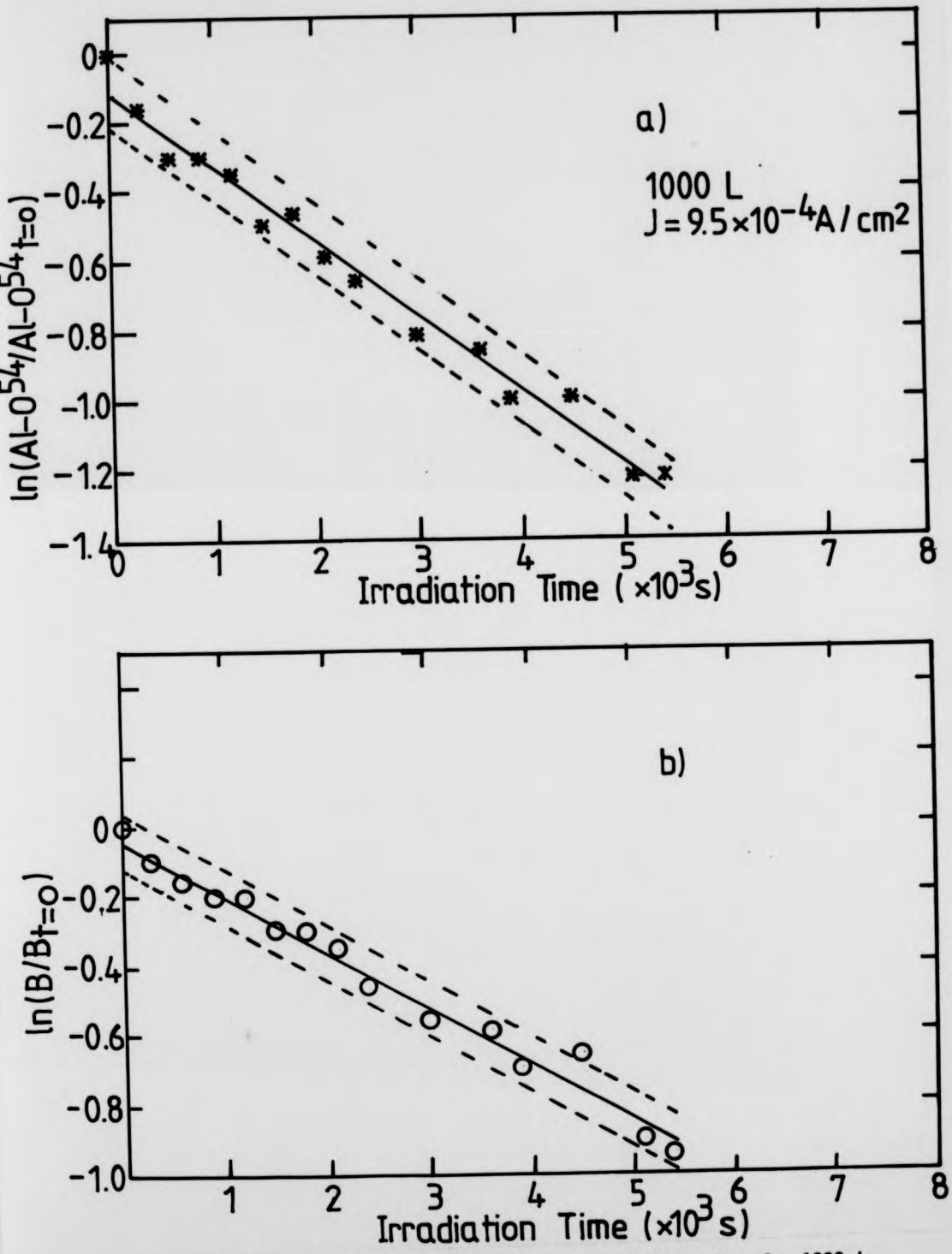

Fig. 8.20 (a) Natural log of Al-O^{54} versus irradiation time for 1000 L exposed surface ($J = 9.5 \times 10^{-4}$ A/cm^2 E_p = 1500 eV). (b) Natural logarithm of ratio B versus irradiation time.

equilibrium value after prolonged electron bombardment, Q_T is the effective total cross section in the decrease of the AES PPH of the atoms in question and J/e is the electron current density which is held fixed during the iteration procedure.

A non-linear least squares fit of eq. 8.2 (solid line) to the experimental data of ratio B is shown in Fig. 8.21 which is in very good agreement with the data. The calculated value of the effective cross-section was also 3 x 10^{-20} cm^2 and compares very well with the value obtained from the logarithmic linear least squares analysis.

8.6.3.2 Electron Beam Bombardment (J=9.5 x 10^{-4} A/cm^2 of the 750 L Oxygen Exposed Surface

The effects of electron beam irradiation on the 750 L oxygen exposed surface has also been investigated and similar analysis performed as for the 1000 L surface. The overall Auger signal PPH intensities recorded prior to electron irradiation were comparable to those from the 1000 L surface. Fig. 8.22(a) shows the variation of the O^{505}, $Al\text{-}O^{54}$ and Al^{67} PPH intensities with irradiation time. Shown in Fig. 8.22(b) are the variation of ratios A and B with irradiation time. After 50 minutes of irradiation time, the $Al\text{-}O^{54}$ and O^{505} PPH had decreased by 74% and 14% respectively and ratios B and A by 69% and 33% respectively. The Al^{67} peak on the other hand had increased by 33%.

A linear logarithmic least squares analysis of the $Al\text{=}O^{54}$ and ratio B data yielded an effective cross-section of 7 x 10^{-20} cm^2 and these plots are shown in Fig. 8.23(a,b). Non-linear least squares fit to the experimental data of ratio B is shown in Fig. 8.24 and from this an average effective cross-section of 5 x 10^{-20} cm^2 was calculated.

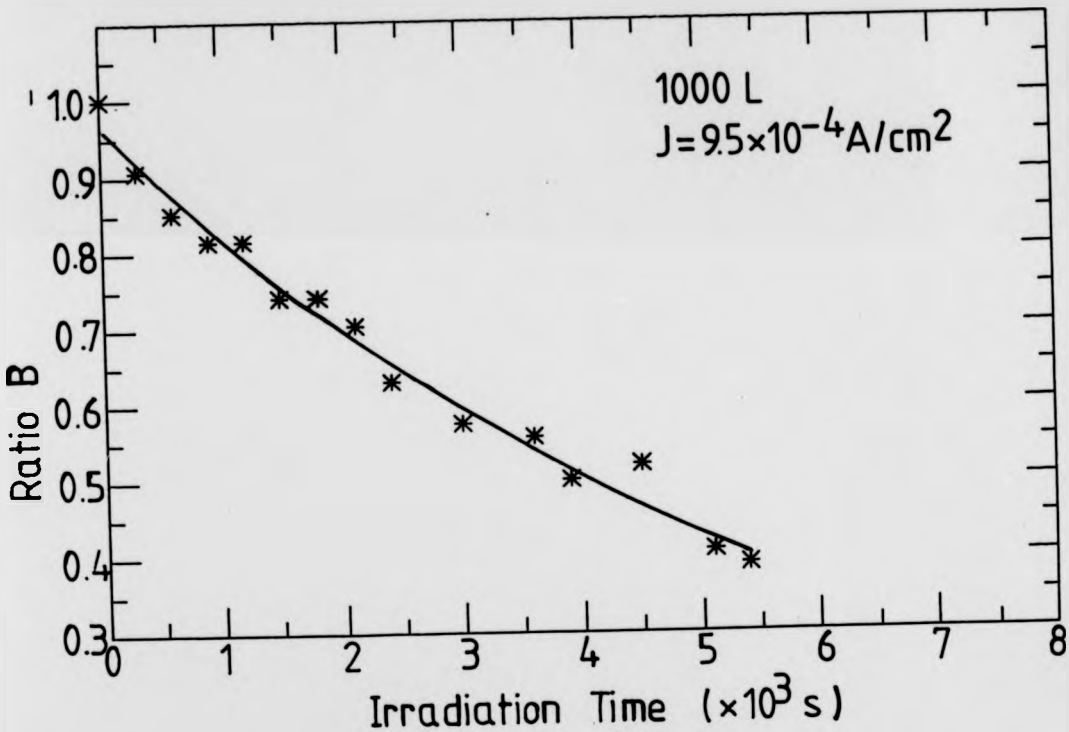

Fig. 8.21 Non-linear least squares fit (solid line) to the data of Fig. 8.20 (b), normalised ratio B versus irradiation time (E_p = 1500 eV, J = 9.5 x 10^{-4} A/cm^2, 1000 L).

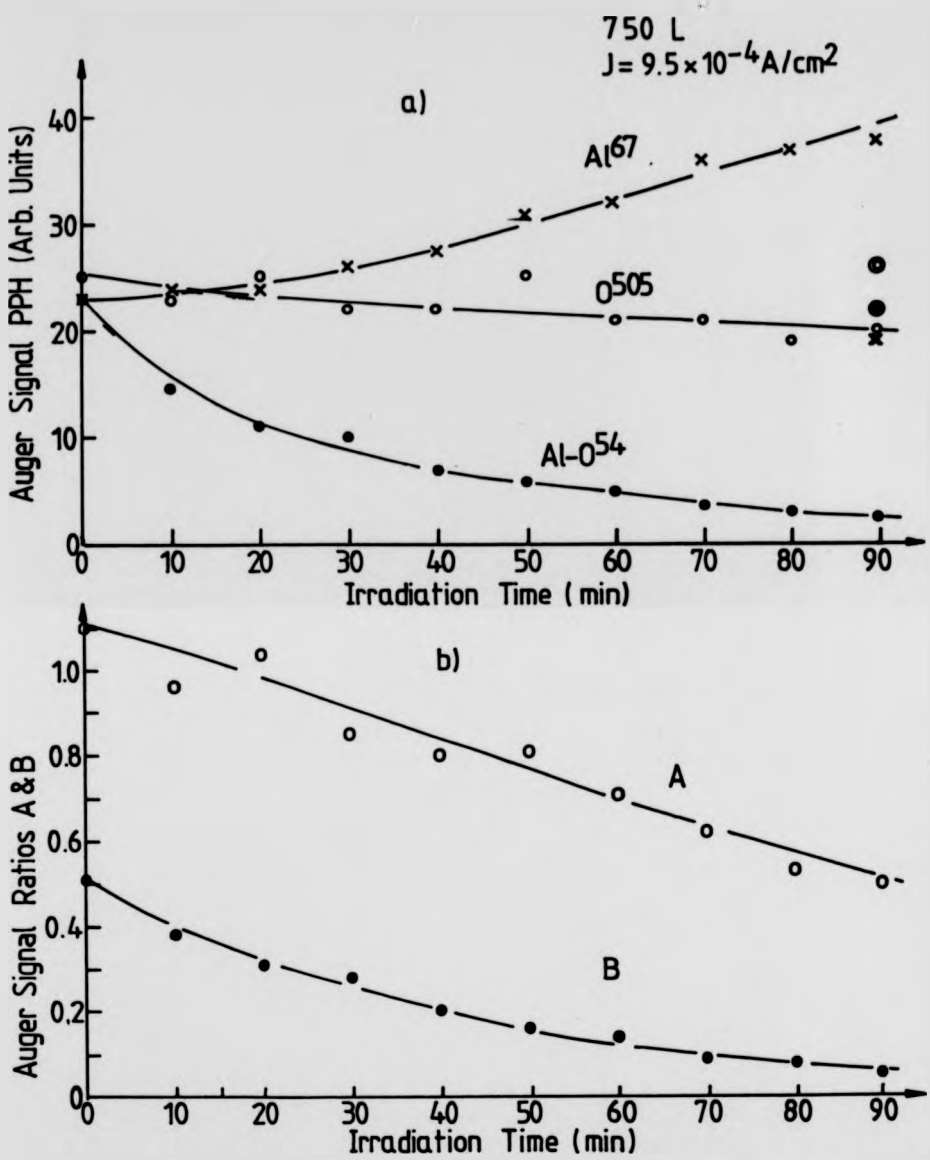

Fig. 8.22 (a) Variation of O^{505}, Al^{67} and $Al\text{-}O^{54}$ Auger PPH with irradiation time. (b) Variation of Auger ratios A and B with irradiation time (750 L. J = 9.5 x 10^{-4} A/cm^2, E_p = 1500 eV).

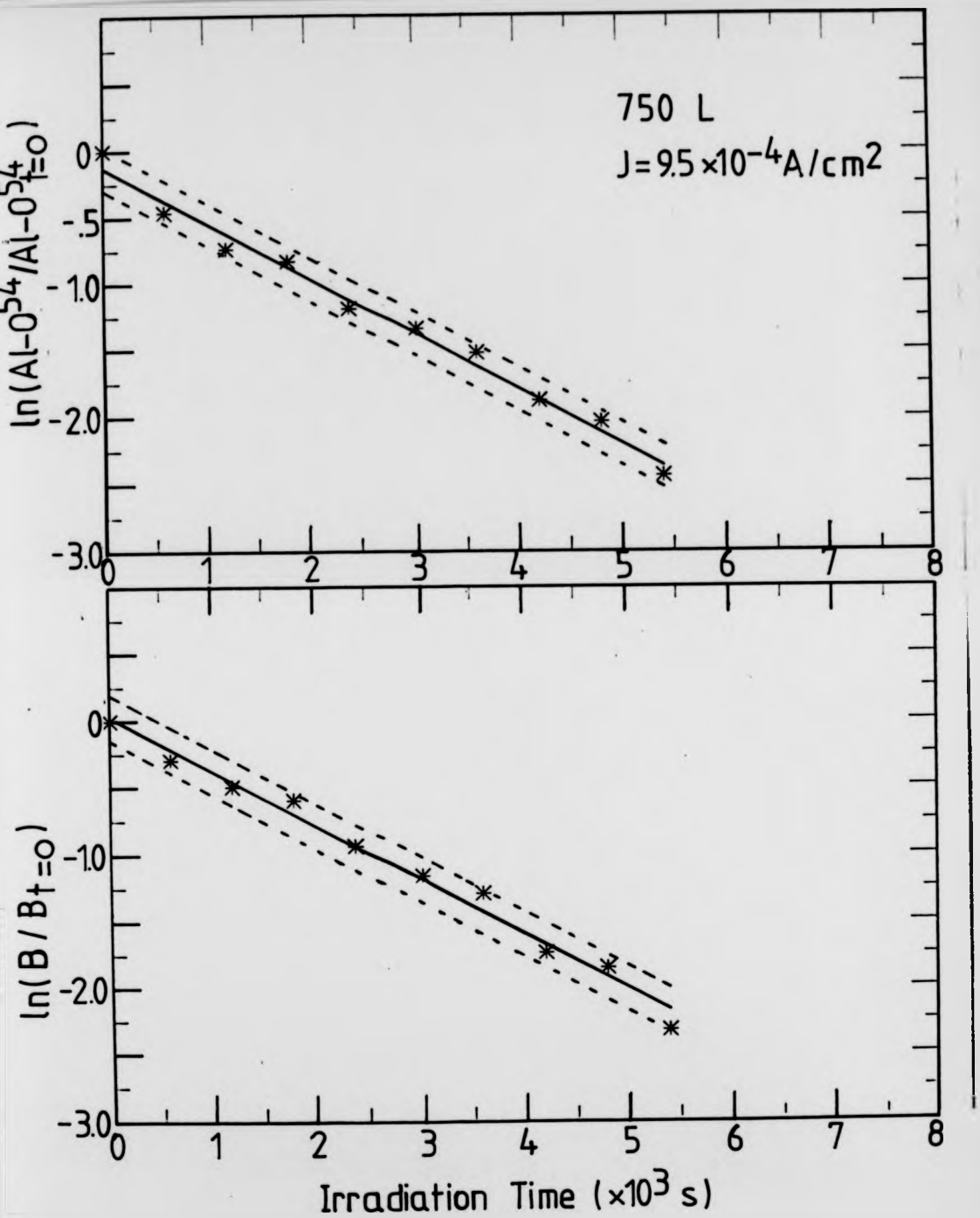

Fig. 8.23 (a) Natural log of Al-O^{54} and ratio B versus irradiation time for the 750 L oxygen exposed surface (J = 9.5 x 10^{-4} A/cm^2).

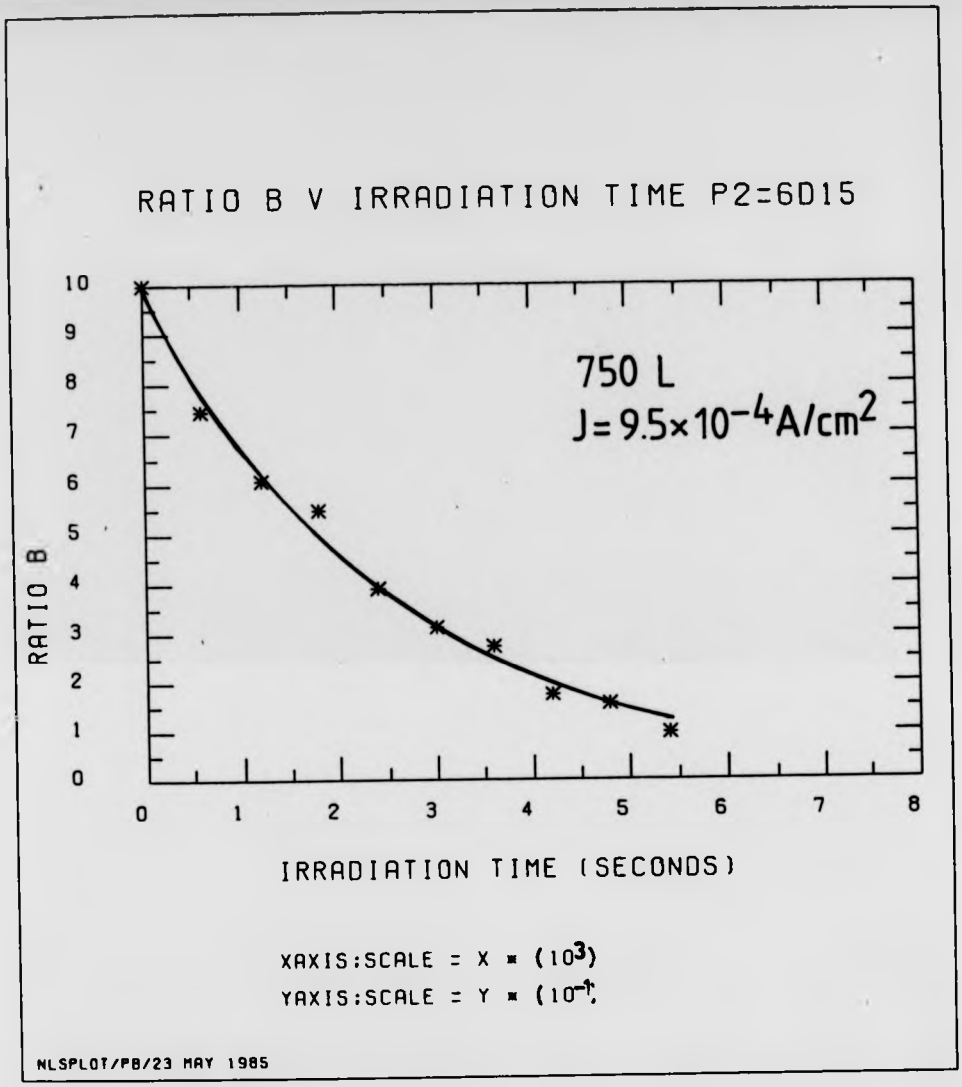

Fig. 8.24 Non-linear least squares fit to the data of Fig. 8.22(b), normalised ratio B versus irradiation time (750 L, J = 9.5 x 10^{-4} A/cm^2).

The decrease in the O^{505} PPH with irradiation was not exponential in nature could be approximated with a straight line drawn through the data points.

8.6.3.3 Electron Beam Irradiation ($J=9.5 \times 10^{-4}$ A/cm^2) of the 250 and 100 L Oxygen Exposed Surface

The response of the 250 and 100 L oxygen exposed surfaces to electron beam bombardment was quite similar and for this reason have been treated together. The initial PPH of the Al-O^{54} was slightly less intense, the Al^{67} slightly more and the O^{505} PPH of same intensity compared with the more heavily oxygen exposed surfaces.

The variation in the O^{505}, Al^{67} and Al-O^{54} Auger PPH intensities with irradiation time is shown in Fig. 8.25(a) and those of ratios A and B in Fig. 8.25(b) for the 250L exposed surface. The percentage decrease in the Al-O^{54} signal after 50 minutes of electron beam irradiation time was 82% and that of O^{505} only 10%. Ratio B had decreased by 72% and A by 25%. The Al^{67} signal PPH on the other hand had increased by 16%.

A linear logarithmic plot of the decay of ratio B with irradiation time for the 250L surface is shown in Fig. 8.26(a) and an effective cross-section of 7×10^{-20} cm^2 was estimated from its slope. And from the non-linear least squares fit to the experimental data, Q_T was calculated to be 5×10^{-20} cm^2. This plot is shown in Fig. 8.26(b).

Again the decrease in the O^{505} signal and ratio A was not exponential like and could be approximated by a straight line drawn through the data points.

8.6.3.4 Electron Beam Irradiation ($J=9.5 \times 10^{-4}$ A/cm^2) of the 50L Oxygen Exposed Surface

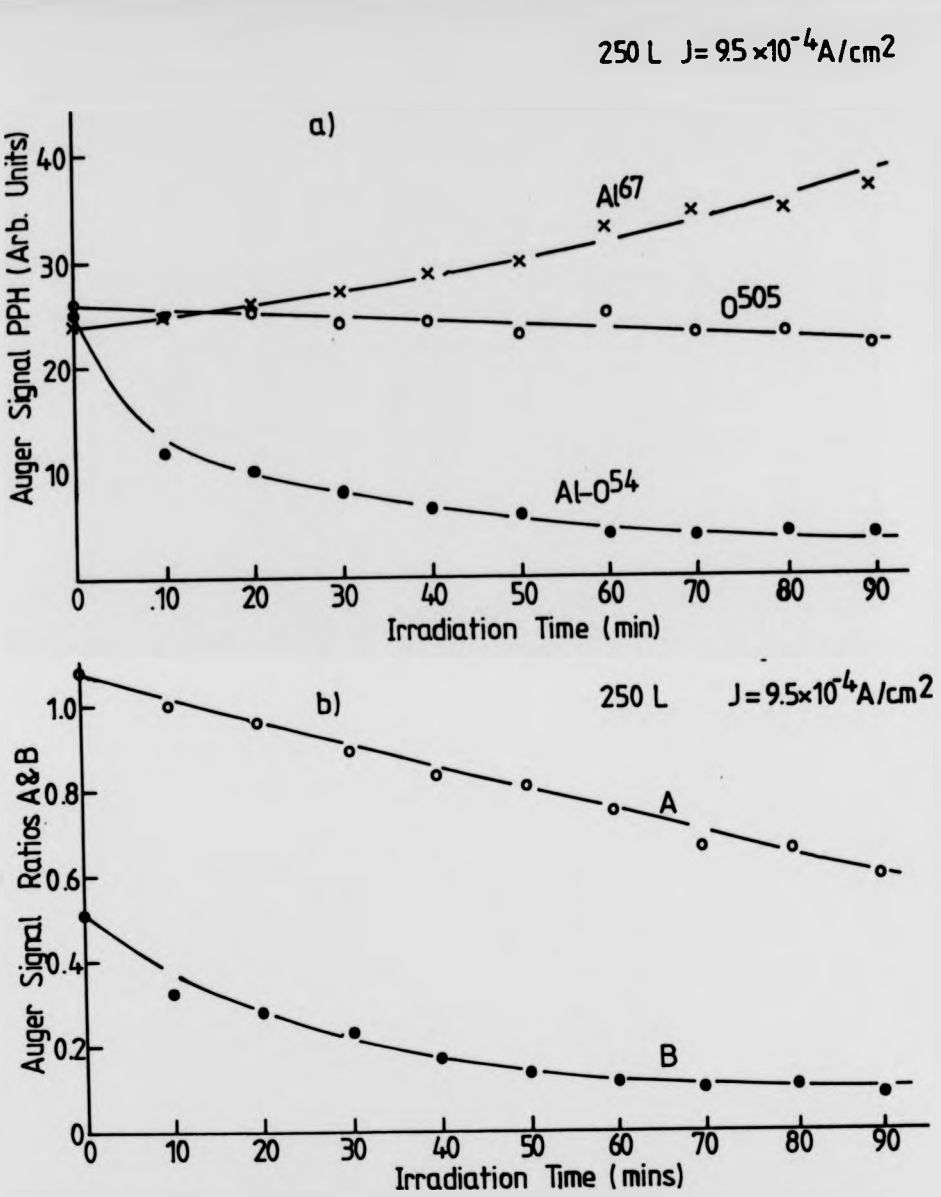

Fig. 8.25 (a) Auger signal PPH of Al^{67}, $Al\text{-}O^{54}$ and O^{505} versus irradiation time. (b) Ratios A and B versus irradiation time for the 250 L exposed surface ($J = 9.5 \times 10^{-4}$ A/cm^2).

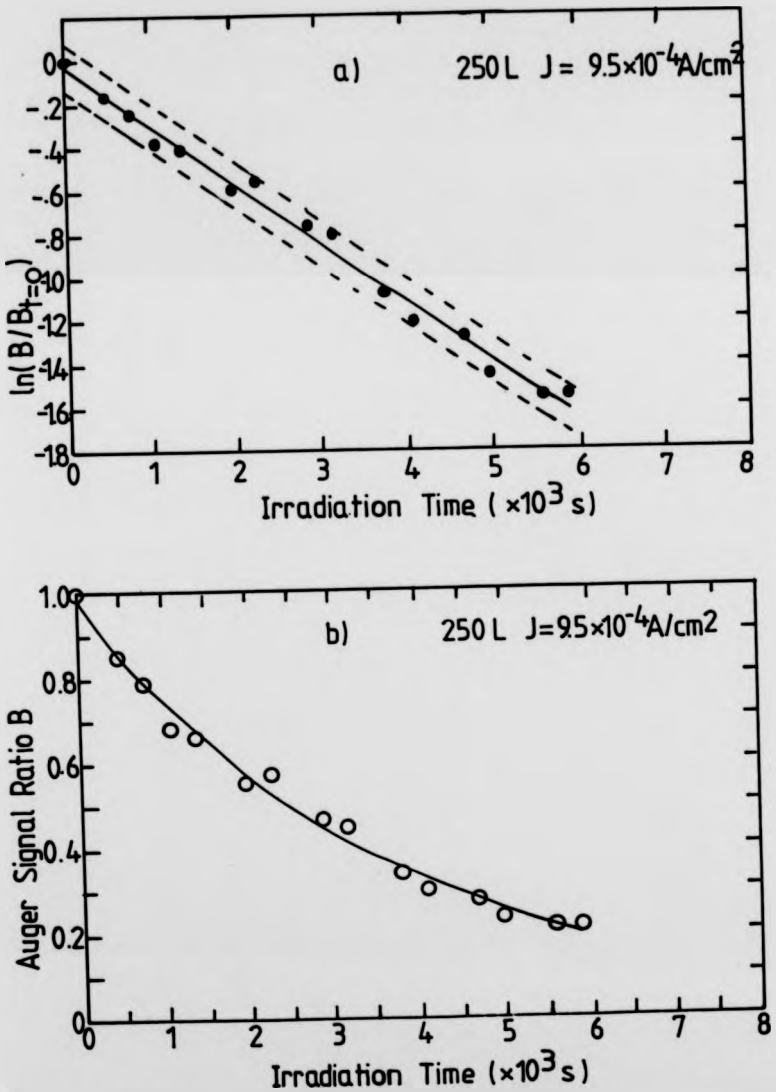

Fig. 8.26 (a) Linear logarithmic least squares plot of the decay of ratio B with irradiation time. (b) Non-linear least squares fit (solid line) to the data of Fig. 8.25(b) (250 L. J = 9.5 x 10^{-4} A/cm^2).

The behaviour of the 50L oxygen exposed surface to electron irradiation was quite similar to the more heavily oxygen exposed surfaces. But since 50L corresponds to an oxygen coverage well below the saturation level, the Al-O^{54} Auger signal PPH is very small compared with the Al^{67} signal.

Cross-section measurements from the decay of the Al-O^{54} PPH were not made because the values were considered to be less reliable. However a plot of Al^{67}, O^{505} Auger PPH and ratio A against irradiation time are shown in Fig. 8.27(a,b).

8.6.4 Electron Beam Irradiation (J=5 and 1.2 x 10^{-4} A/cm^2) of the 250 L Oxygen Exposed Surface

The response of the 250 L oxygen exposed surface to electron bombardment with reduced current densities of J = 5 x 10^{-4} and 1.2 x 10^{-4} A/cm^2 was also investigated. A reduction in the electron flux, inevitably resulted in less intense Auger signal intensities and hence reduction in the sensitivity of the analyser. This was particularly so for the latter electron current density.

The variation of the Al^{67}, Al-O^{54} and O^{505} Auger signals and ratios A and B against irradiation time are shown in Figs. 8.28(a,b) respectively. For J = 5 x 10^{-4} A/cm^2, the Al-O^{54} PPH decreased very much as before but in this case by only 50% in the first 50 minutes of irradiation time. The O^{505} PPH stayed virtually unchanged from its initial value and the Al^{67} PPH increased at a slower rate with an overall increase of 5%.

From the logarithmic linear least squares plot of the normalised ratio B versus irradiation time of Fig. 8.29(a), the effective cross-section in the reduction of ratio B was estimated to be 6 x 10^{-20} cm^2. The non-linear

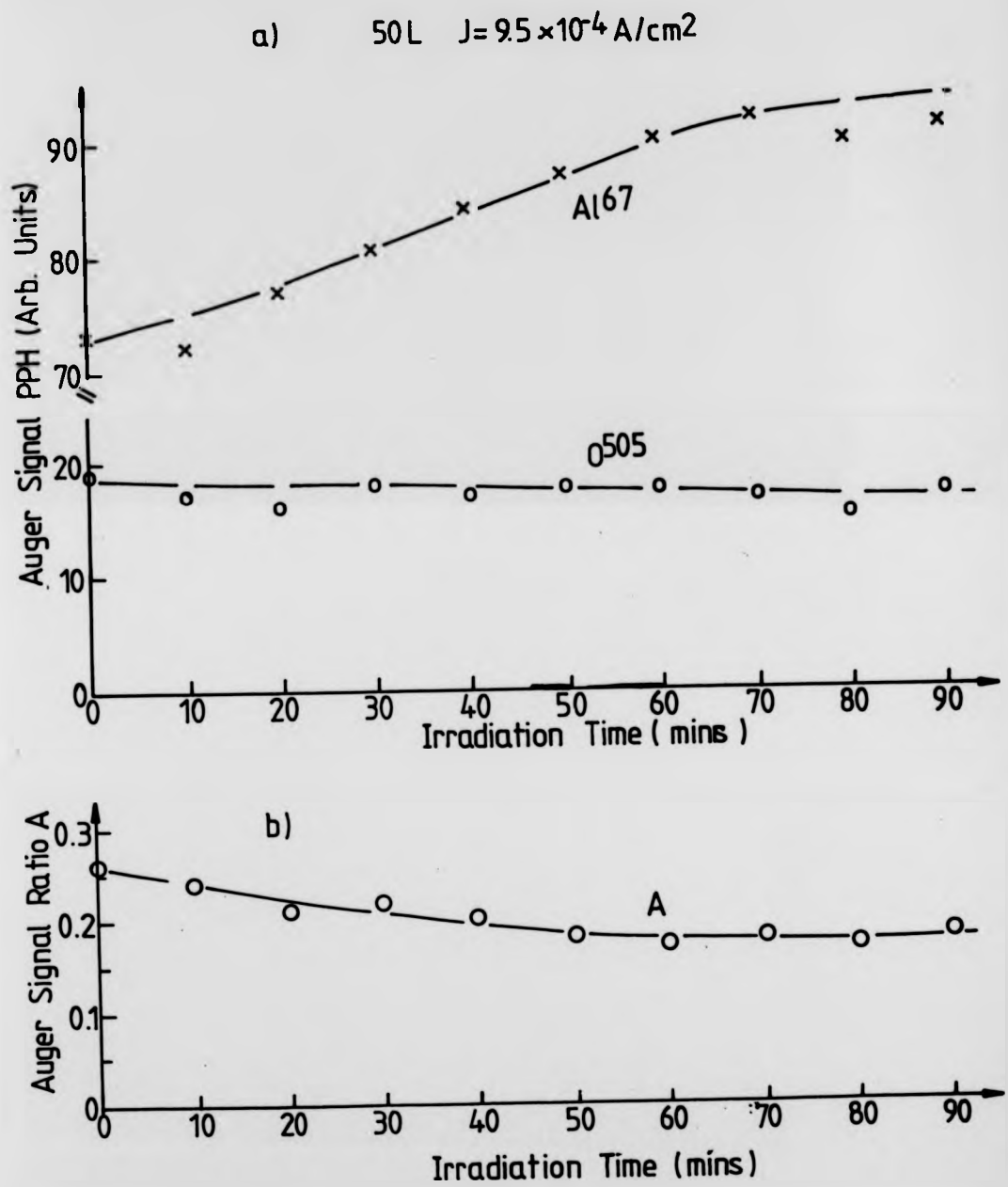

Fig. 8.27 (a) Variation of Al^{67} and O^{505} Auger signal PPH with irradiation time. (b) Variation of ratio A with irradiation time (E_p = 1500 eV, J = 9.5 x 10^{-4} A/cm^2, 50 L).

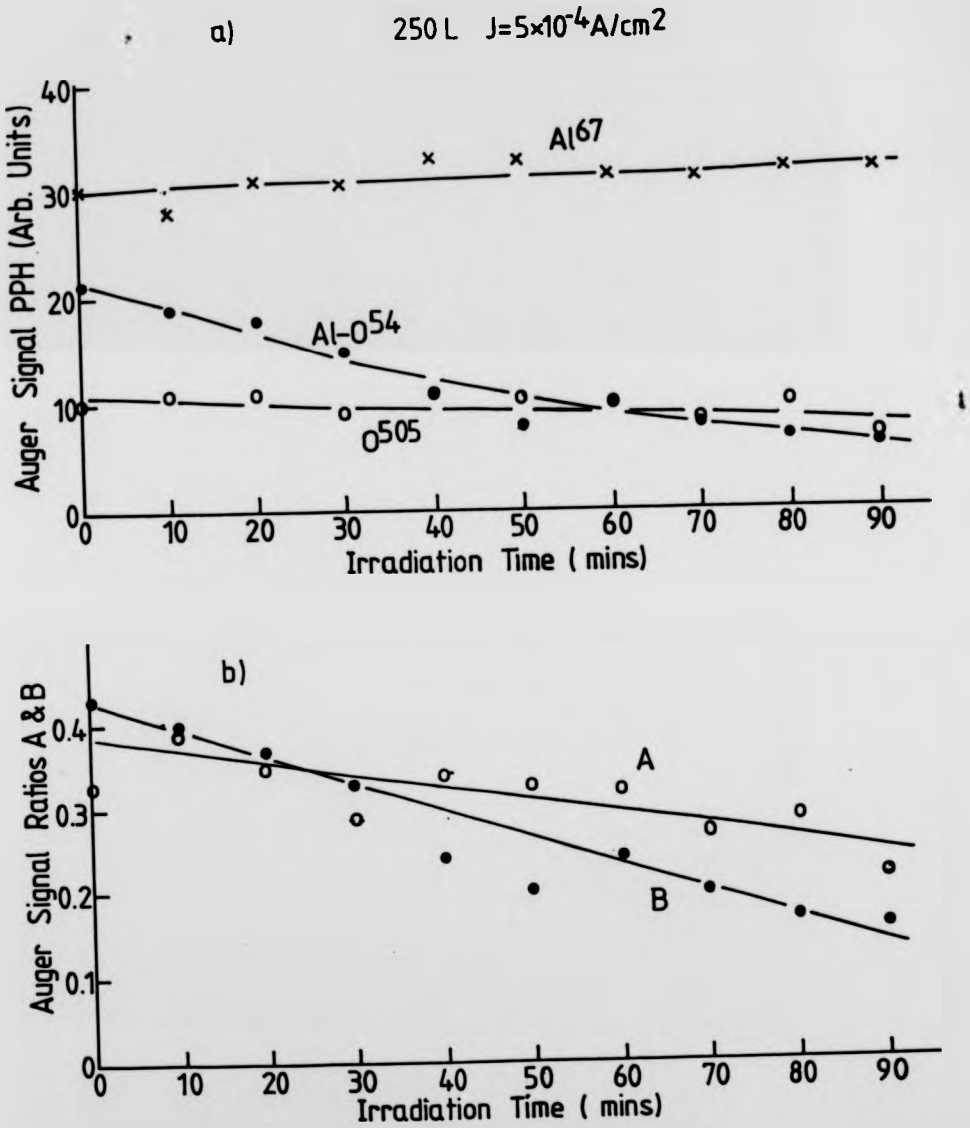

Fig. 8.28 (a) Variation of Al^{67}, O^{505} and $Al\text{-}O^{54}$ Auger PPH with irradiation time ($J = 5 \times 10^{-4}$ A/cm^2, 250 L exposed surface). (b) Variation of ratios A and B.

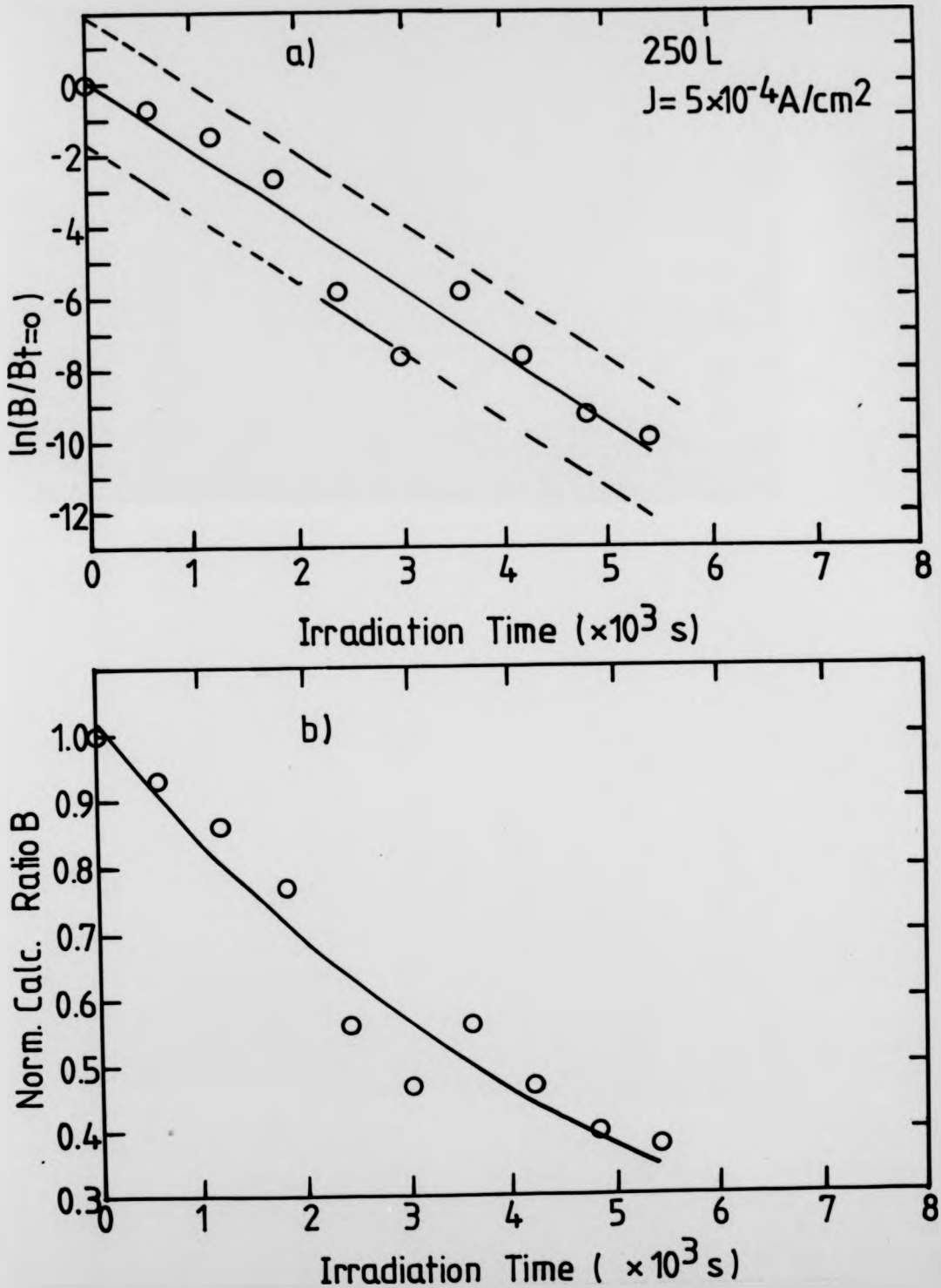

Fig. 8.29 (a) Linear natural logarithmic plot of ratio B versus irradiation time (b) Non-linear least squares fit (solid line) to the raw data of ratio B (50 L J = 5 x 10^{-4} A/cm^2, E_p = 1500 eV).

least squares fit to the data gave $Q_T = 5 \times 10^{-20}$ cm^2. This plot is shown in Fig. 8.29(b).

For the current density $J = 1.2 \times 10^{-4}$ A/cm^2 the signal to noise ratio was very poor and but in this case the PPH intensity of both the Al-O^{54} and Al^{67} signals actually decreased where as irradiation time with the O^{505} signal remained unchanged. No cross section estimates were made using this data.

8.6.5 Electron Beam Irradiation ($J = 1.9 \times 10^{-3}$ A/cm^2) of the 350 L Oxygen exposed Surface

In this experiment a 350L oxygen exposed surface was bombarded by an electron beam current density of 1.9×10^{-3} A/cm^2 for a period of 280 minutes. The response of this surface to irradiation at a higher electron flux was similar to previous irradiation experiments, except for the Al^{67} PPH which only decreased by only 5% during the first 50 minutes of bombardment. The variation of the Al^{67}, Al-O^{54} and O^{505} peaks with irradiation time is shown in Fig. 8.30(a) and those of ratios A and B in Fig. 8.30(b).

Logarithmic linear least squares analysis performed on the Al-O^{54}, O^{505}, ratios A and B all yielded straight line fits to the data. In addition the O^{505} data also gave a good fit when treated with ordinary linear least squares analysis. Estimate of the cross-section from this was considered less reliable. Fig. 8.31(a) illustrates the logarithmic linear least squares plot of ratio B with irradiation time and from its slope an effective cross-section of 1.3×10^{-20} cm^2 has been calculated. Non-linear least squares fit to the same data is shown in Fig. 8.31(b). From this an effective cross section of 1.6×10^{-20} cm^2 was calculated. Estimates of Q_T

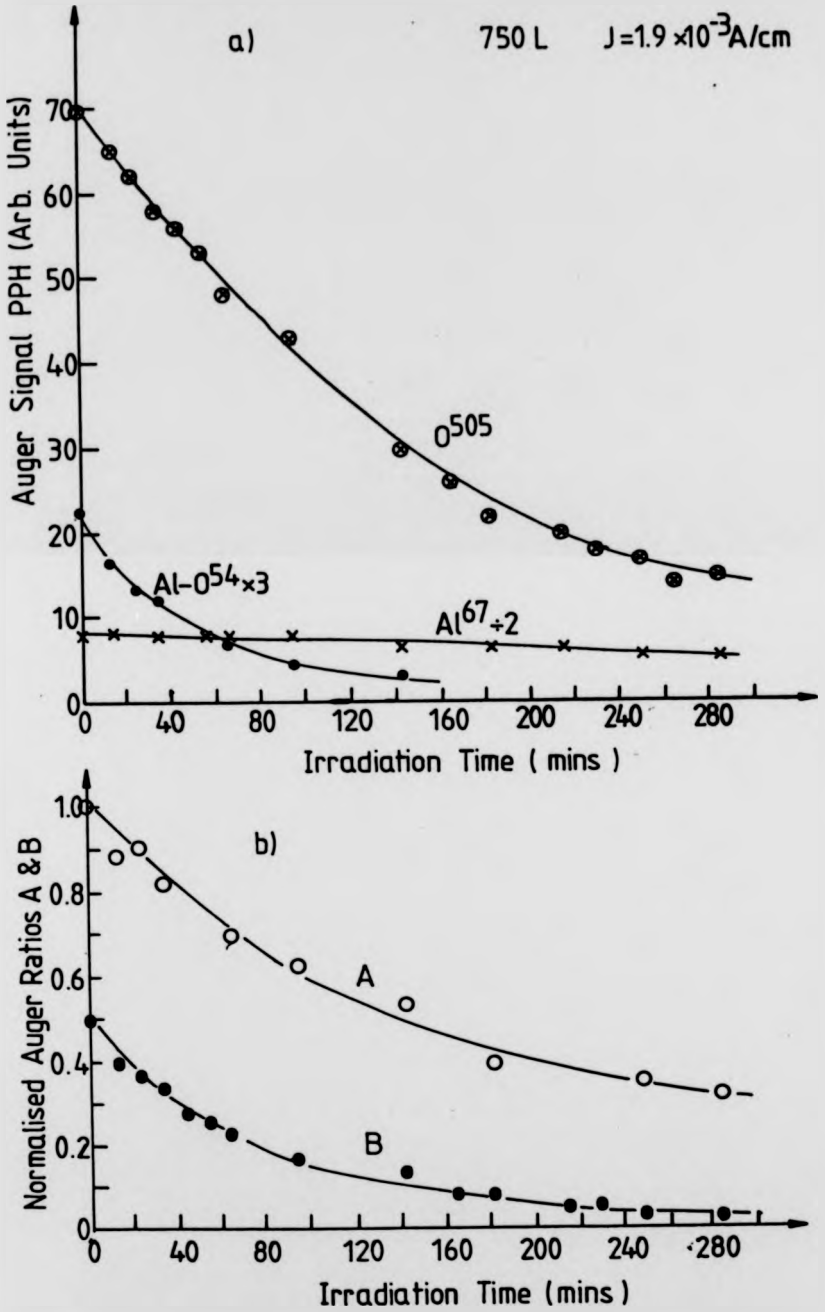

Fig. 8.30 (a) Variation of Al^{67}, $Al\text{-}O^{54}$ and O^{505} AES PPH intensities versus irradiation time (350 L, J = 1.9 x 10^{-3} A/cm^2, E_p = 1500 eV). (b) Normalised Auger ratios A and B versus irradiation time.

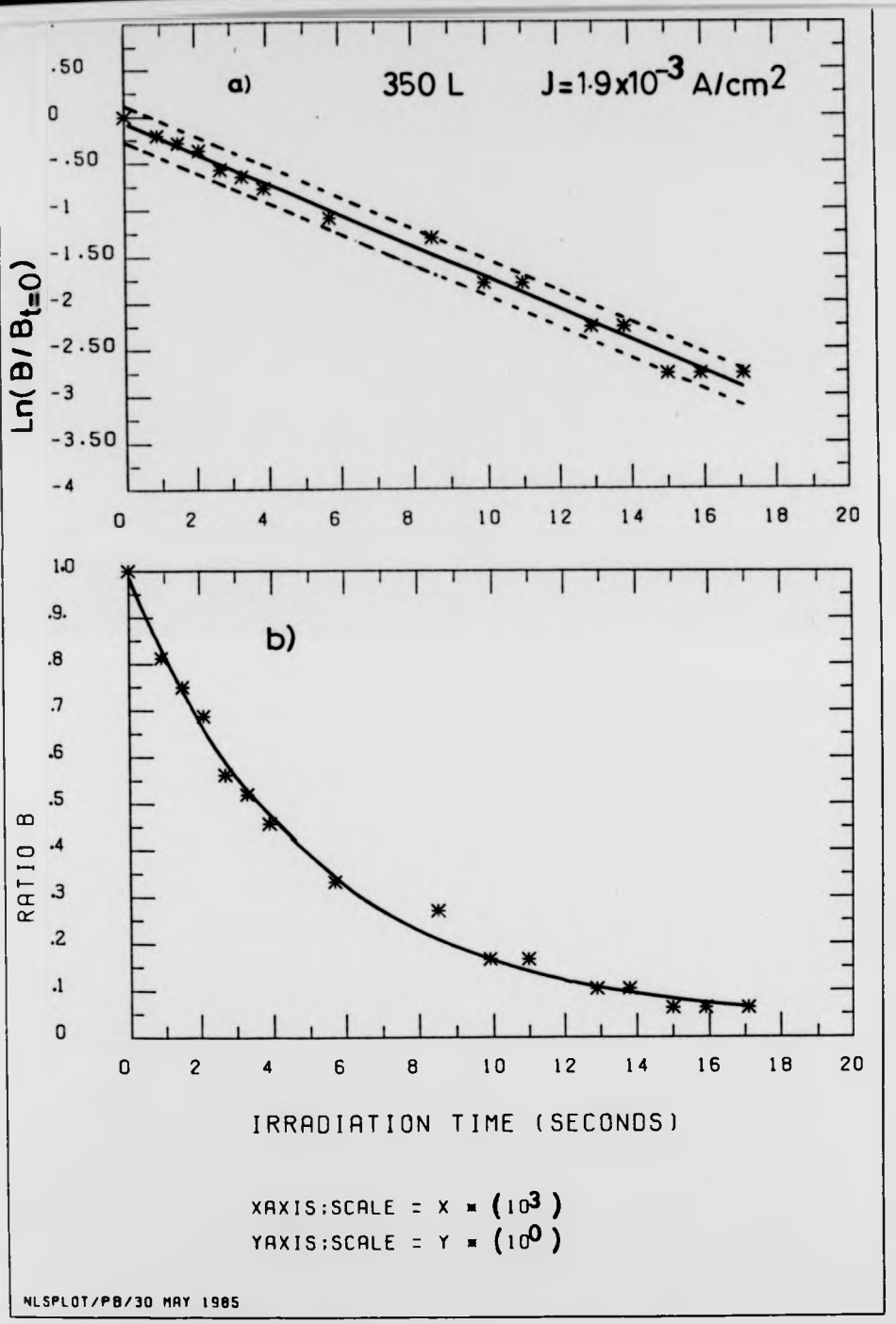

Fig. 8.31 (a) Natural log of ratio B versus irradiation time (b) Non-linear least squares fit (solid line) to the raw data of ratio B (350 L, J = 1.9 x 10^{-3} A/cm^2).

made from O^{505} and ratio A data were approximately 50% smaller.

Tables 8.2 and 8.3 provide a summary of the percentage changes in the PPH intensities of Al^{67}, O^{505}, $Al\text{-}O^{54}$ and ratios A and B after 50 minutes of electron bombardment for the 50, 100, 250, 350, 750 and 1000L oxygen exposed surfaces for electron current densities of 1.9×10^{-3}, 9.5×10^{-4} 5 $\times 10^{-4}$, and 1.2×10^{-4} A/cm^2. A summary of the estimated effective decomposition-desorption cross-sections from the decrease in the $Al\text{-}O^{54}$ and ratio B data for the same electron current densities mentioned above is shown in Table 8.4.

The results of the electron beam irradiation experiments will be discussed and interpreted in the next section.

8.7 Discussion of Results

8.7.1 Discussion of the Possible Sources of Error

The scatter associated with the adsorption and electron beam irradiation data can be attributed to the following possible sources of error.

1) Argon ion sputtering of the surface, will have resulted in roughness on the microscopic scale, in the form of kinks, steps and cones. Due to the broad nature of the ion beam these structural defects were probably distributed across the whole of the sample surface. Compared with a smooth surface the Auger signal intensities would be slightly attenuated.

2) Since exposure of the surface to oxygen was carried out in the STC, the sample had to be transported, backwards and forwards between this and the SAC. For the recording of the AES spectra the, sample was required to be

Table 8.2 Summary of percentage changes in the Al-O^{54}, Al^{67} and O^{505} Auger PPH of pre-oxygen exposed surfaces after 50 minutes of electron beam irradiation.

Current Density J (A/cm^2)	AES Peak	Level of Oxygen Exposure (Langmuirs) 0	50	100	250	350	750	1000
$(19 \pm .5) \times 10^{-3}$	Al-O^{54}	-	-	-	-	-67%	-	-
	Al^{67}	-	-	-	-	- 5%	-	-
	O^{505}	-	-	-	-	-23%		
$(9.5 \pm .5) \times 10^{-4}$	Al-O^{54}	-	-	-84%	-80%	-	-74%	-55%
	Al^{67}	-9%	+12%	+13%	+20%	-	+33%	+17%
	O^{505}	-	-16%	-10%	-12%	-	-14%	-21%
$(50 \pm .5) \times 10^{-4}$	Al-O^{54}	-	-	-	-50%	-	-	-
	Al^{67}	-	-	-	+5%	-	-	-
	O^{505}	-	-	-	±1%	-	-	-
$(12 \pm .5) \times 10^{-4}$	Al-O^{54}	-	-	-	-24%	-	-	-
	Al^{67}	-	-	-	-10%	-	-	-
	O^{505}	-	-	-	±1%	-	-	-

Table 8.3 Summary of percentage changes in the Auger ratios A (O^{505}/Al^{67}) and B [$Al\text{-}O^{54}/(Al\text{-}O^{54}+Al^{67})$] after 50 minutes of electron beam irradiation.

Current Density J (A/cm^2)	Ratios A & B	Level of Oxygen Exposure (Langmuirs)					
		50	100	250	350	750	1000
$(1.9\pm.5)\times10^{-3}$	A	-	-	-	-23%	-	-
	B	-	-	-	-50%	-	-
$(9.5\pm.5)\times10^{-4}$	A	-13%	-22%	-27%	-	-33%	-29%
	B	-	-72%	-72%	-	-69%	-44%
$(5.0\pm.5)\times10^{-4}$	A	-	-	-21%	-	-	-
	B	-	-	-18%	-	-	-
$(1.2\pm.5)\times10^{-4}$	A	-	-	-9%	-	-	-
	B	-	-	-5%	-	-	-

Level of Oxygen Exposure (L)	Cross-section Measurements Q_T (cm^2) for					
	$J=19\times10^{-3}A/cm^2$		$J=9.5\times10^{-4}A/cm^2$		$J=5\times10^{-4}A/cm^2$	$J=1.2\times10^{-4}A/cm^2$
	$Al\text{-}O^{54}$	B	$Al\text{-}O^{54}$	B	$Al\text{-}O^{54}$ B	$Al\text{-}O^{54}$ B
50			9×10^{-20}*; 10×10^{-20}*			
50						
100			7×10^{-20} ; 7×10^{-20}			
100**			; 4×10^{-20}			
250			7×10^{20} ; 6×10^{-20}		8×10^{-20}; 6×10^{-20}	10×10^{-20}*
250**			; 4×10^{-20}			
350	2×10^{-20} ; 1×10^{-20}					
350**	1.6×10^{20} ; 3×10^{-20}					
750			7×10^{-20} ; 7×10^{-20}			
750**			; 6×10^{-20}			
1000			3×10^{-20} ; 2×10^{-20}			
1000**			; 3×10^{20}			

Table 8.4 A summary of the estimated effective decomposition-desorption cross-sections from the decrease in the $Al\text{-}O^{54}$ and ratio B data at various electron current densities and oxygen exposure levels (* values unreliable due to poor $Al\text{-}O^{54}$ signal to noise ratio. ** cross-section values calculated by non-linear least squares fitting).

placed at the previously determined position for resolution and intensity reasons. A great deal of the observed scatter in the data may have been due to sample positioning problems.

3) Because the oxygen Auger KLL peak occurs at a higher energy than the aluminium LVV peak a higher energy modulation voltage was required to increase the sensitivity for detection of the oxygen signal. The modulation amplitudes were set normally within several percent of the pre determined values but sometimes not so.

4) A significant amount of vibration from the rotary backing pumps, will have led to the forced oscillations of the sample transfer rod which was quite long and susceptible to oscillations of amplitude 25 to 50% of the electron beam diameter are possible. For oscillations in the surface plane, the effective irradiated area is consequently larger.

5) The pump down time associated with the initial adsorption of the clean surface and in between adsorption cycles may have an effect on the overall exposure level in terms of determining the exposure scale.

6) Exposure of the surface with the ion gauge on may influence the reactivity of the oxygen atoms or molecules with the surface, since it is well known that ion gauges produce excited species. In this case the ion gauge was out of direct line of sight with the surface, and due to the low exposure pressures the excited molecules or atoms are likely to collide with the walls of the appendages before arriving at the sample surface due to the long mean free path and consequently any arriving will be in the ground state.

8.7.2 Adsorption of Oxygen on the Polycrystalline Surface

The general form of the adsorption profiles for oxygen on polycrystalline aluminium surface, obtained by AES, is very similar to those reported by Martinson and Flodstrom (1979) and others, whose work have already been reviewed in section 4.2.1.

From Figs. 8.13 -8.17 and consideration of adsorption results of previous authors who have used techniques other than AES, a two stage oxidation process for the polycrystalline surface is suggested: a chemisorption stage proceeded by an oxidation stage. i) Chemisorption stage: this stage is characterised by initial interaction of oxygen with the clean surface. As the available adsorption sites become occupied, the growth in the O^{505} Auger signal slows down and the Al^{67} Auger signal diminishes in intensity very rapidly. The completion of the chemisorption stage is marked by the first appearence of the $Al\text{-}O^{54}$ Auger inter -atomic cross transition due to formation of bulk-like aluminium oxide. This occurs at oxygen exposures of 20-50 L.

ii) Oxidation stage: with increasing exposure the O^{505} and $Al\text{-}O^{54}$ signals gradually reach saturation values. The surface characteristics is more like aluminium oxide like, with oxygen most probably penetrating the sub surface atomic layer. After 1000 L of oxygen exposure a tiny Al^{67} signal is still detectable.

The source of the elemental aluminium signal may be due to several reasons.

a) Contribution by the underlying bulk aluminium atoms is very likely. The inelastic mean free path (IMFP) of the 67 eV electrons is about 7 A as determined from the universal MFP versus kinetic energy curve of Fig. 2.4

of section 2.2.1.3. In addition, the information or escape depth corresponds to three times the MFP and is defined as the depth from which 95 % of the electrons are able to escape without under going inelastic collisions. The Al_2O_3 lattice distance is approximately 5.1 A. This distance could be approximated by at least two aluminium lattice and two aluminium oxide lattice distances from which Al^{67} electrons can escape without suffering energy losses.

b) A possible source, could be due to the active decomposition of the surface oxide by direct action of the electron beam. However contribution from this process is likely to be very small, due to the small overall dose delivered to the surface during acquisition of Auger spectra.

c) The surface may not be homogeneously oxidised, and may consist of areas of chemisorption and fully oxidised regions under the area of the incident beam.

The general shape of the adsorption profile and value of the initial sticking coefficient agreed very well with those obtained by Martinson and Flodstrom (1979) for the oxygen on Al(111) face. Hence it would appear therefore that the polycrystalline sample surface was probably composed of (111) facets.

8.7.3 Electron Beam Irradiation Experiments

The electron beam effects, observed at the oxygen exposed polycrystalline aluminium surfaces will be interpreted and discussed in terms of electronic excitation mechanisms that lead to the electron stimulated desorption (ESD) and electron beam induced decomposition (EBID) proposed by Redhead, Gomer and Menzel, and Knotek and Feibelman. Also in terms of electron stimulated

desorption (ESA).

Thermal effects, arising from direct power heating of the sample by the electron beam can safely be ruled out, due to use of relatively low electron current densities. In section 8.6.2 an estimate of the probable steady state temperature rise in the irradiated area was shown to be of the order of 0.2 K for the highest electron current density employed. This tiny rise above the room temperature is unlikely to cause any thermal desorption effects.

Charge accumulations, can also be confidently ruled out for two reasons:

1) No shift in the energy of the Al-O^{54}, Al^{67} or O^{505} Auger peaks was observed, during the course of the irradiation experiments. If the surface had acquired any charge then equal shifts in energy of the Auger peaks would have resulted.

2) Charge accumulations normally occur, and are a serious problem in insulators and in semiconductors. The most heavily oxygen exposed surface i.e. 1000 L, is unlikely to have developed more than a couple of monolayer coverages thick oxide layer.

Analysis of the electron beam irradiation experiments, show decisively, reduction with electron dose of Al-O^{54}, O^{505} Auger signal PPH intensities and ratios A and B for almost all levels of surface oxidation and electron current densities. The Al^{67} Auger signal on the other hand increased with electron dose.

Since Al-O^{54} and ratio B give an indication of the overall oxide content of the surface, a decrease in these , indicate that the aluminium oxide Al_2O_3,

desorption (ESA).

Thermal effects, arising from direct power heating of the sample by the electron beam can safely be ruled out, due to use of relatively low electron current densities. In section 8.6.2 an estimate of the probable steady state temperature rise in the irradiated area was shown to be of the order of 0.2 K for the highest electron current density employed. This tiny rise above the room temperature is unlikely to cause any thermal desorption effects.

Charge accumulations, can also be confidently ruled out for two reasons:

1) No shift in the energy of the Al-O^{54}, Al^{67} or O^{505} Auger peaks was observed, during the course of the irradiation experiments. If the surface had acquired any charge then equal shifts in energy of the Auger peaks would have resulted.

2) Charge accumulations normally occur, and are a serious problem in insulators and in semiconductors. The most heavily oxygen exposed surface i.e. 1000 L, is unlikely to have developed more than a couple of monolayer coverages thick oxide layer.

Analysis of the electron beam irradiation experiments, show decisively, reduction with electron dose of Al-O^{54}, O^{505} Auger signal PPH intensities and ratios A and B for almost all levels of surface oxidation and electron current densities. The Al^{67} Auger signal on the other hand increased with electron dose.

Since Al-O^{54} and ratio B give an indication of the overall oxide content of the surface, a decrease in these , indicate that the aluminium oxide Al_2O_3,

must be decomposing into elemental aluminium (as indicated by the growth of the Al^{67} signal) and oxygen in various excited states.

Observed reduction in the O^{505} AES PPH and ratio A (O^{505}/Al^{67}) further indicates that the overall concentration of oxygen in any electronic state is being depleted due to desorption from the surface. The source of the desorbed oxygen arises as product of the decomposition process and or from oxygen loosely associated with the surface substrate atoms. The desorption products are most probably in the ionic and neutral states.

The decomposition process is most favourably explained by the Knotek-Feibelman mechanism which is the dominant desorption mechanism in the maximal valence compounds, as explained in section 3.2.3 (aluminium oxide Al_2O_3 is one such compound). Electron excitation of the oxide creates a core hole on the cation, and subsequent electronic relaxation via interatomic Auger transitions lead to loss of electrons from the cation, leaving a two-hole final state Al^{+}--- O^{+} which exhibit strong Coulombic repulsion of sufficient force to cause decomposition, and **Coulomb explosion** desorption of O^{+} ions.

Such a process would then be expected to cause:

i) decomposition from those regions within the irradiated area where chemisorbed oxygen had become an oxide and formed $Al2^{O}3$ and therefore cause a decrease in the Al-O^{54} Auger signal ii) desorption of O^{+} ions and therefore a decrease in the O^{505} signal, though experimentally, the O^{+} ions could not be directly detected. iii) an increase in the Al^{67} Auger signal, due to depletion of the oxygen and uncovering of the underlying substrate aluminium bulk.

In the irradiation experiments with J=9.5 x 10^{-4} A/cm^2 this is exactly what has been observed and appears to be the dominant effect.

In addition to electron induced decomposition, reduction in the oxygen Auger signal could also result due to the Redhead-Gomer-Menzel mechanism whereby physisorbed or loosely bound oxygen atoms would be ejected from the surface via Franck-Condon transitions from their ground states to excited anti-bonding state. The major desorption product of this mechanism is known to be neutrals, though here these could not be directly monitored.

For the moment, referring to the results of irradiation experiments in which the electron current density was 9.5 x 10^{-4} A/cm^2, if the observed reduction in the Al-O^{54} and O^{505} Auger signals with electron bombardment was entirely due to the above electronic processes, then their decrease would be expected to obey exponential type decay curves from which total desorption-decomposition cross-sections could be deduced. The Al-O^{54} Auger signal and consequently ratio B was shown to obey such exponential decay curves by performing linear logarithmic least squares analysis and non-linear least squares fitting of the equation governing the exponential decay. Inspection of these figures for oxygen exposures of 100 - 1000 L reveals reasonable agreement but closer inspection, particularly of the logarithmic linear least squares plots indicate that the effective total cross-section in the decrease of Al-O^{54} Auger signal is changing during the course of the irradiation period. This indicates that in addition to the ESD and EBID other processes may be occuring.

Further evidence for this, is provided by the behaviour of the oxygen signal with irradiation. This signal does not decay exponentially and that the percentage decrease in the O^{505} signal was 7 times less than the decrease in the Al-O^{54} signal over the first 50 minutes irradiation period.

During the same period the Al^{67} signal showed a similar increase in intensity as the O^{505} . These observations can be interpreted in either or both of the two ways suggested below.

1) Decomposition of Al_2O_3 by the **Coulomb explosion** mechanism, may not result in total desorption and escape of the oxygen atoms and these are somehow re-captured by the surface. The new association with the surface need not lead to reoxidation. The probability of recapture is increased if the surface is not smooth but pitted or dominated by cones. In this case the desorption angles will not be well defined.

2) Electron stimulated adsorption of residual gases which can lead to adsorption of oxygen and deposition of carbon. This possibility is further favoured by the results of the irradiation experiments performed at clean aluminium surfaces and from which the decrease in the Al^{67} signal was faster from the irradiated than non-irradiated areas.

In addition, experiments performed at lower electron current densities, indicate a reduction in the rate of increase of the Al^{67} PPH and for $J=1.2 \times 10^{-4}$ A/cm^2 it actually decreased with electron dose. At the same time the O^{505} signal stayed more or less constant. Though this may partly be attributed to the reduction in the electron flux, requiring longer doses to record measurable changes in the Auger signal PPH intensities.

Therefore, dominant electron beam effects observed in these experiments will depend on various parameters, among which are, nature of the sample surface and extent of surface oxidation, level of residual gases, electron flux and possibly primary electron energy.

The predominant processes here, were electron induced decomposition and desorption which agree with the results of Smith (1976), and van Oostrom (1979) who, have observed decomposition and desorption from heavily oxidised aluminium surfaces. Their papers were reviewed in section 4.5.1.

The values of effective total cross-sections calculated from the decrease in the AES Al-O^{54} PPH and ratio B from this study (for the 1000 L oxygen exposed surface), and those calculated by the author from the works of Smith, and van Oostrom are in reasonable agreement.

The effective total cross-section values calculated for the 100, 250 and 750 L oxygen exposed surfaces were found to be approximately 2 times greater than the value calculated for the 1000 L surface. This result is not surprising, since more heavily exposed surfaces are likely to develop several monolayers which will modify the observed total cross-section. (see section 3.4.1)

From the measured effective total cross-sections, a critical dose D_c can be estimated. This is defined as the dose required to change the intensity of AES PPH by 10% so as to minimise the damage by irradiation during Auger analysis. For oxidised aluminium, by use of eq. 3.9, D_c was estimated to be 0.2 C/m^2 for a beam energy of 1.5 keV. Smith obtained a similar result, but van Oostrom found a D_c, 4 times greater.

Of major significance, are the reported results of electron beam irradiation experiments by Fontaine et al (1982), of oxygen exposed Al(111) and Al(100) surfaces. In fact their results and interpretations, would appear to be in variance with the results of this work. Fontaine et al, have observed enhancement of the Al-O^{54} and O^{505} Auger signal PPH

intensities with irradiation of the Al(111) surface, but observed no change on the Al(100) face.

The oxygen exposure levels prior to irradiation, and electron current densities and doses delivered to the surfaces were of the same magnitude as employed here, except for the energy of the primary electrons which was a lot higher at 5 keV.

The observed increases, were explained by a direct momentum transfer mechanism, whereby 5 keV electrons in near elastic collisions, cause transition of chemisorbed oxygen into oxide within the irradiated zone (it can be easily shown that the maximum possible momentum transfer to a heavy nucleus occurs during a head on collision and hence maximum kinetic energy gained by the nucleus is $4mE_k/M$). The growth in the oxide proceeds by another mechanism, whereby slow secondary electrons scattered from the walls of the analyser, cause chemisorbed oxygen atoms in the vicinity of the beam to diffuse into the irradiated area via Franck-Condon type energy gain mechanisms and become oxidised by the impact of the energetic primaries via the direct momentum transfer mechanism.

In contrast, the Al(100) face, on the other hand, no such enhancement of oxide was observed. This was explained by reference to the adsorption results of Martinson and Flodstrom who have reported that oxygen is incorporated directly on to the Al(100) face without the intermediate chemisorption phase. It would appear therefore, that the hypothesis of Fontaine et al requires the oxygen to be in a precursor state and energetic primary electrons of $E_p > 5$ keV for the enhanced oxidation in the irradiated area to be observed.

Fontaine et al claim that the source of the oxygen was not from the residual gases in the experimental chamber which mainly consisted of CO_2, CO and water vapour from the bulk. However, it is very surprising that even on the Al(100) face no desorption or decomposition effects were observed, this would imply an establishment of equilibrium between decomposition desorption and adsorption processes.

It would appear therefore, that in the experiments of Fontaine et al, enhanced adsorption by direct momentum transfer mechanism was dominant whereas in the experiments for this work desorption and decomposition phenomena dominated the outcome.

An interesting finding is that of Falconer et al and Pitts et al who have investigated simultaneous gas phase CO_2 and electron beam exposure of clean aluminium surfaces as reviewed in section 4.5.3. These authors found that a stable oxide layer within the irradiated area resulted only after removal of gas phase CO_2 and further bombardment by the electron beam. The carbon KLL signal was very small compared with the O_{KLL} signal, indicating dissociation of CO_2 into CO and O, with desorption of the CO and incorporation of the O on to the surface. An interesting observation here is that primary electron energies used for the irradiation ranged between 0.5 and 10 keV with electron current densities of 10^{-3} - 10^{1} A/cm^2.

These authors did not carry out further irradiation studies on the enhanced oxide layer (in the absence of gas phase CO_2) in order to see whether further oxidation or reduction of the oxide results. Since however adsorption and oxidation with 500 eV electrons are being observed this would rule out the Fontaine et al mechanism from occurring here.

It seems therefore that further experimental work is required to establish conclusively, the circumstances under which one or more of the electronic processes become dominant over the others. The nature of the sample surface and the experimental apparatus with its residual environment are probably the most important.

A possible explanation which would reconcile the experimental observations and interpretations of this work and those of Fontaine et al, is if the effect of secondary electrons are taken into consideration. These are expected to play a crucial role in the electronic processes that lead to the observed surface phenomena, as they emerge through the surface. This aspect of secondary electron emission was introduced in sections 5.2.4 and 6.3. and will further discussed in the next chapter.

The total number of secondary electrons generated by the incident primaries depend on the primary energy, angle of incidence with respect to the surface plane, nature of the surface. The total yield of a clean aluminium surface bombarded by 5 keV electrons at normal incidence, is approximately 0.3 and that of 1.5 keV electrons 0.6. For a fully oxidised aluminium surface, the total yield for 5 keV electrons is 2 and for 1.5 keV electrons 3.6 - 4. Therefore at higher energies the contribution by the slow secondaries to the electron flux is less than halved. In the case of the oxide, the intensity of the primary secondary electron current for E_p = 1.5 keV is 4 times that of the primary current. Hence the effective electron current density has to be modified to in order to take this into account.

This perhaps is the additional mechanism that contributes to the desorption processes. Since the secondary electrons are slow, these are expected to enhance desorption via the Redhead-Gomer-Menzel mechanism. Thus the observation of decomposition and desorption phenomena in this work and

those of Smith, and van Oostrom could be accounted by this effect. Where as in the work of Fontaine et al the secondary electron effect was not as influential. In the experiments of Smith, and van Oostrom 5 keV electrons were used to bombard the oxidised surface.

8.7.4 Conclusions

The initial steps of oxygen adsorption at a polycrystalline aluminium surface was analysed. This was shown to consist of two stages; initial chemisorption phase (up to 50 L of oxygen exposure) followed by monolayer coverage, and oxidation of the surface after a total of 120 - 150 L of oxygen exposure. The initial sticking coefficient S_0 was estimated to be 0.02.

Electron beam irradiation of the 50 - 1000 L oxygen exposed surfaces, resulted in the predominant decomposition of the oxide and desorption of oxygen by the **Coulomb explosion** and electron stimulated desorption mechanisms. Effective total cross-sections of the decrease in the Al-O^{54} AES PPH and ratio B, was estimated to be 6 ±.5 x 10^{-20} cm^2 for the 100 - 750 L exposed surface and (3 ±.5) x 10^{-20} cm^2 for the 1000 L surface. From these total cross-sections a critical dose D_c of 0.2 C/cm^2 at a beam energy of 1.5 keV was estimated to be necessary in order to limit surface damage to less than 10 %.

Further experimental work is necessary in order to establish the circumstances under which decomposition and desorption dominates adsorption and vica-versa. In the next chapter results and discussion of secondary electron emission yield measurements on the clean and oxygen exposed aluminium surfaces will be presented.

CHAPTER NINE

RESULTS AND DISCUSSION: SECONDARY ELECTRON EMISSION YIELD MEASUREMENTS CLEAN AND OXYGEN ADSORBED POLYCRYSTALLINE ALUMINIUM SURFACE

9.1 Introduction

In this chapter the results of total SEE yield measurements from clean and oxygen adsorbed polycrystalline aluminium surfaces will be presented. The evolution of the total yield with oxygen exposure, has been correlated to the variation of the Al^{67}, $Al\text{-}O^{54}$ and O^{505} Auger PPH intensities as established from the results of chapter 8. The total yield results will be discussed and interpreted in terms of the modern SEE theory presented in chapter 5.

9.2 Summary of the Experimental Procedure and Initial Yield Measurements of the Contaminated Aluminium Sample

A more detailed account of the experimental procedures has been described in section 7.2.4. The total yield σ, was measured in terms of the absorbed sample current I_a, which was detected by a gated linear amplifier employing modulation and lock-in detection. At the same time the sample was ramped with a retarding potential 0 to -1000 eV to simulate the variation in E_p. Of course E_p and I_p were kept constant throughout. The electron beam struck the surface at normal incidence.

The total secondary electron yield σ, versus E_p for the contaminated surface is shown in Fig. 9.1. The corresponding AES survey spectrum of this surface was shown in Fig. 8.3 in the last chapter but is reproduced here for convenience. This survey spectrum was taken after the system had

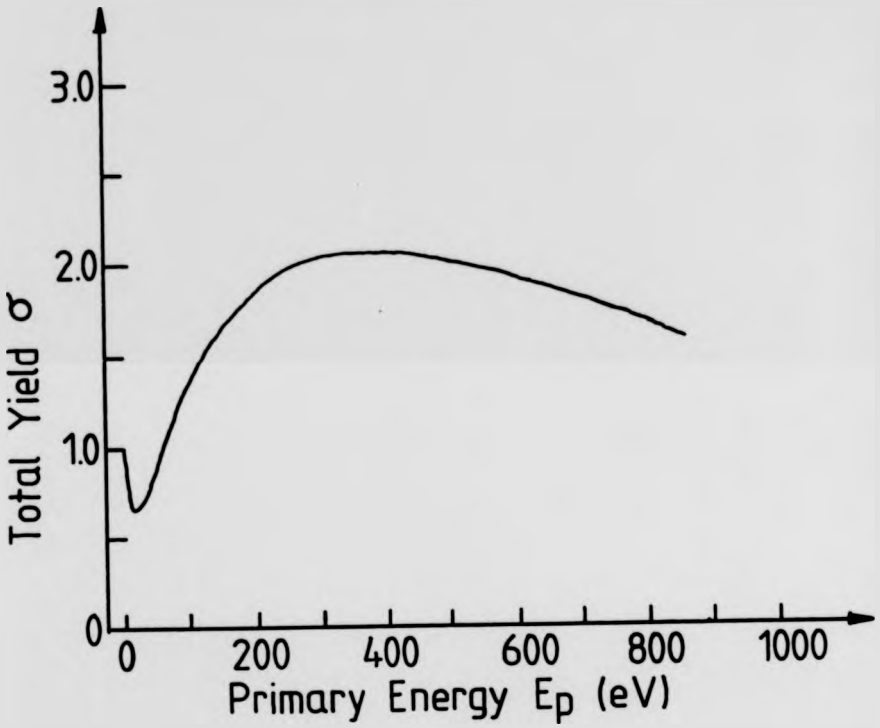

Fig. 9.1 Total secondary electron yield σ versus primary electron acceleration voltage for the contaminated surface, after the bakeout (E_p = 900 eV and I_p = 10 μA).

been baked to obtain STC and SAC base pressures of 10^{-9} and 10^{-10} torr. The AES survey spectrum of Fig. 9.2 indicates a heavily contaminated surface. The most intense Auger signals were due to carbon, oxygen and sulphur. The $Al \rightarrow O^{54}$ Auger peak due to aluminium oxide was barely detectable indicating that the carbon contamination masked the oxide signal. From Fig. 9.1 the value of the maximum total yield σ_{max} and corresponding primary energy E_{pmax} was measured to be 2.1 ±.02 and 379 ± 10 eV respectively. This value of σ_{max} is slightly lower than expected for a clean aluminium oxide surface. The uncertainty in the measurement of E_{pmax} is quite large due to the broad nature of the maximum yield. The yield curve of Fig. 9.1 was obtained with E_p = 900 eV and I_p = 10 μA.

The aluminium surface was cleaned by argon ion sputtering prior to each yield measuring experiment. Fig. 9.3 indicates σ versus E_p for the contaminated and sputter cleaned surfaces. Oxygen exposure of the sample surface was by the dynamic method as described in section 7.1.4.1. Oxygen was leaked into the STC to a particular pressure in the range (10^{-8}- 10^{-5} torr) and the duration of exposure timed. The pressure-time product was converted to Langmuirs i.e. 1 L = 10^{-6} torr second.

From a consideration of prelimenary electron beam effect results all subsequent yield measurements were made with E_p = 900 eV, I_p = 7.5 μA and defocussed beam diameter of 1.5 mm.

9.2.1 Digitisation of the Yield Curves

It was found necessary, to digitise most of the yield curves so that the yield could be deduced at specific primary energies. The yield curves were recorded permanently by use of an X-Y recorder. The actual digitisation process, consisted of using the **Ferranti Cetec** digitiser in conjunction

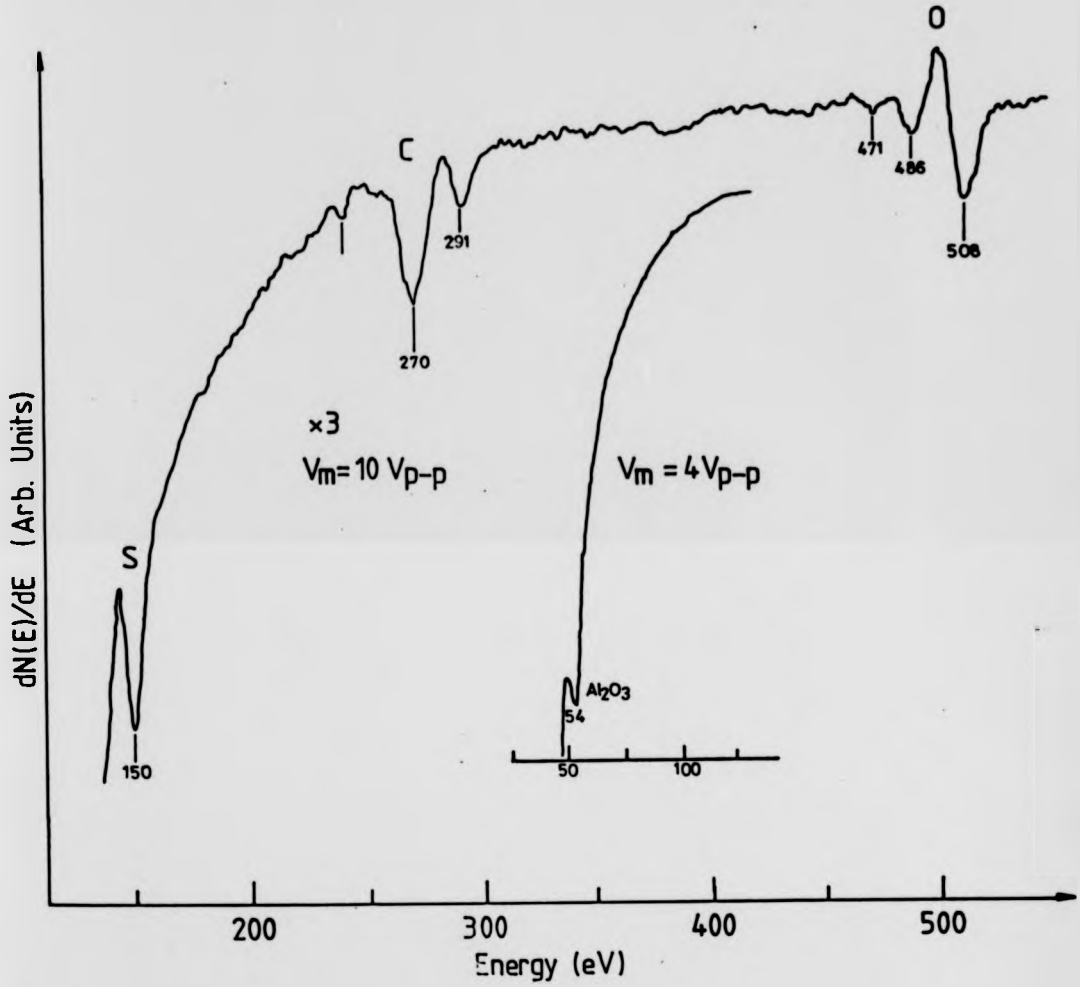

Fig. 9.2 AES survey spectrum of the contaminated Al surface after the bakeout (E_p = 1500 eV, I_p = 20 μA).

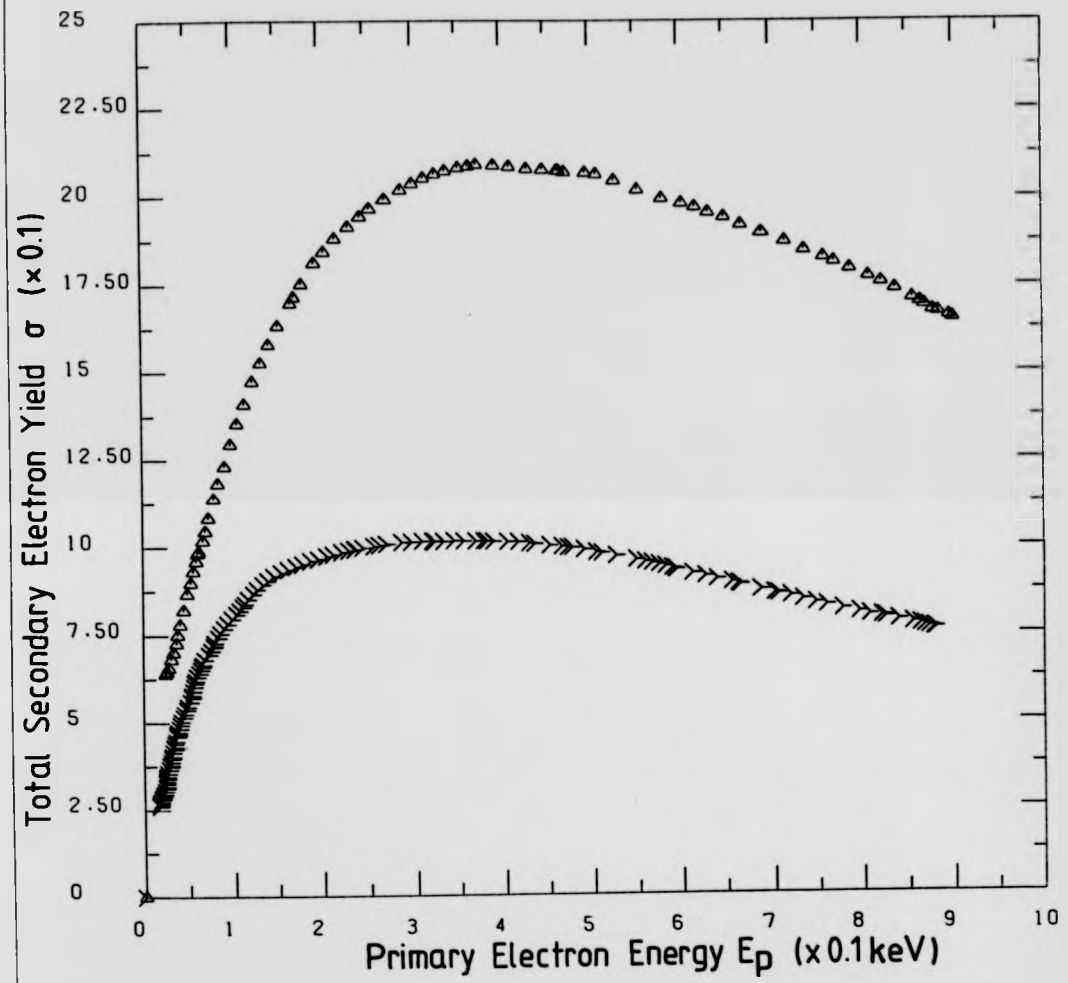

Fig. 9.3 Total secondary electron yield σ versus E_p for the contaminated Δ, surface and argon ion sputter cleaned surface (E_{A+} = 5 keV, I_{A+} = 15 μA for 10 minutes).

with the campus GEC 4080 main frame computer. The digitised raw data in the form of a series of X-Y coordinates given in mm, were processed by a library of Fortran subroutines, after which the Y coordinates were converted to absolute yield values and the X coordinates to primary acceleration voltage E_p from a knowledge of conversion factors.

The sampling rate during the digitisation process was quite high, and E_p could be located within ± 2 eV. N(E) spectra, was also digitised in the same way, and by use of simple Fortran programs, the digitised data was integrated to give areas under N(E) curves and hence the relative contributions of secondary electrons to the total yield.

9.2.2 Yield versus E_p Measurements for 0 - 10 000 L Oxygen Exposures

Fig. 9.4 shows a series of σ versus E_p curves at various oxygen exposure levels from 0 L corresponding to the clean aluminium surface, to 9600 L corresponding to several monolayers of oxygen adsorption. In this exposure range σ increased monotonically for all E_p. For the clean surface, σ_{max} was found to be 1.00 ± .03 at an E_{pmax} of 300 ± 10 eV and after 7200 L of oxygen exposure σ_{max} increased to 1.25 and E_{pmax} to 325 eV.

Fig. 9.5 shows the variation of σ_{max}, σ_{50}, σ_{100} and σ_{800} with oxygen exposure up to 9600 L. All four yield values increase with oxygen exposure but at slightly different rates. For σ_{50} and σ_{100} the overall increase was greater compared with yields at 310 eV and 800 eV.

Table 9.1 represents a summary of numerical changes in yield for E_p = 50, 100, 800 and E_{pmax} for various high oxygen exposure levels.

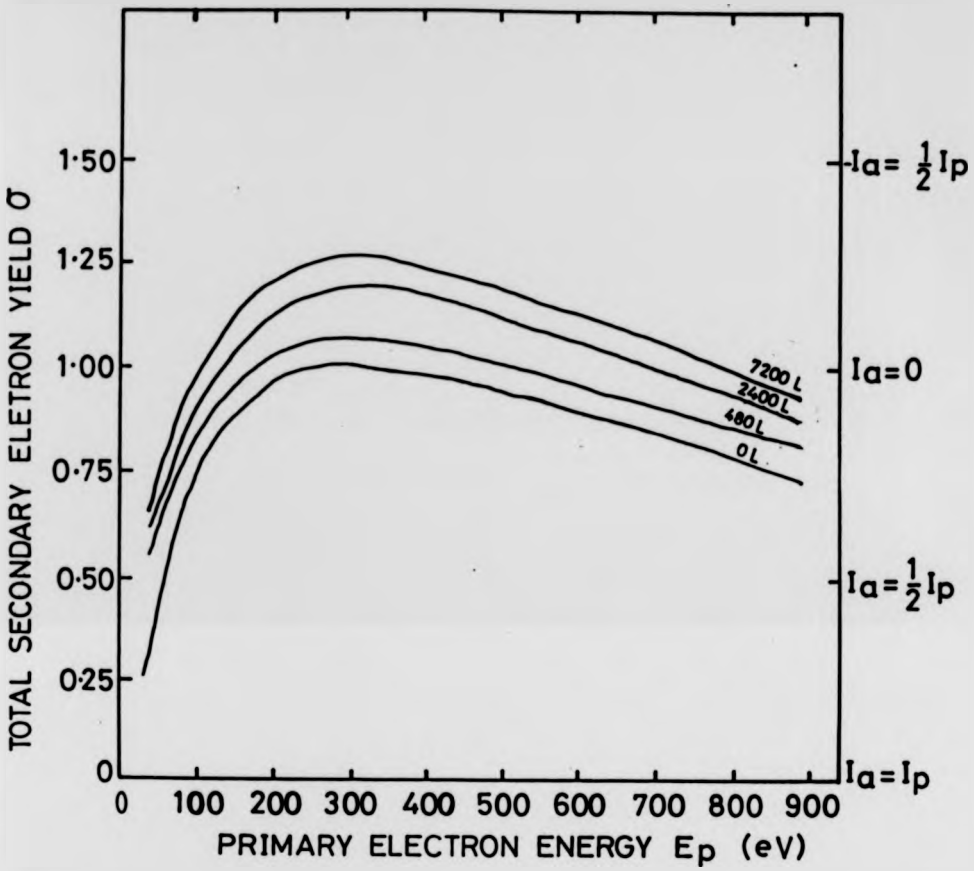

Fig. 9.4 Total yield curves (σ versus E_p) for various oxygen exposure levels 0, 480, 2400 and 7200 L.

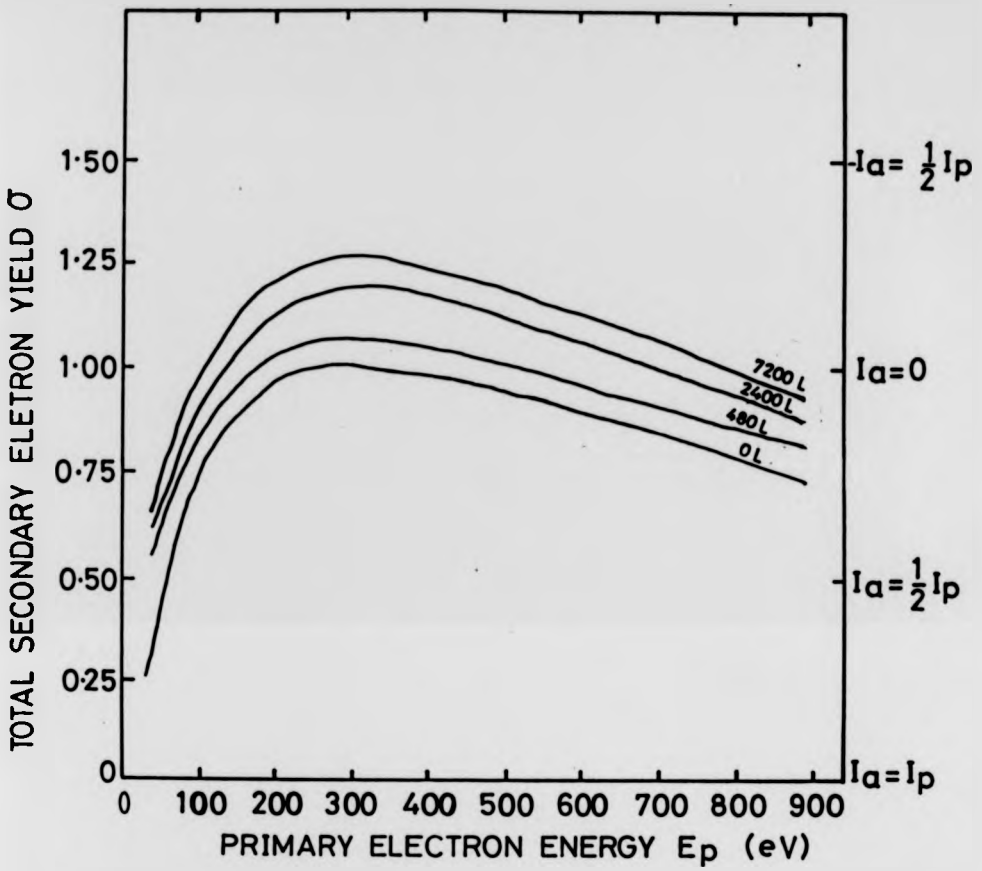

Fig. 9.4 Total yield curves (σ versus E_p) for various oxygen exposure levels 0, 480, 2400 and 7200 L.

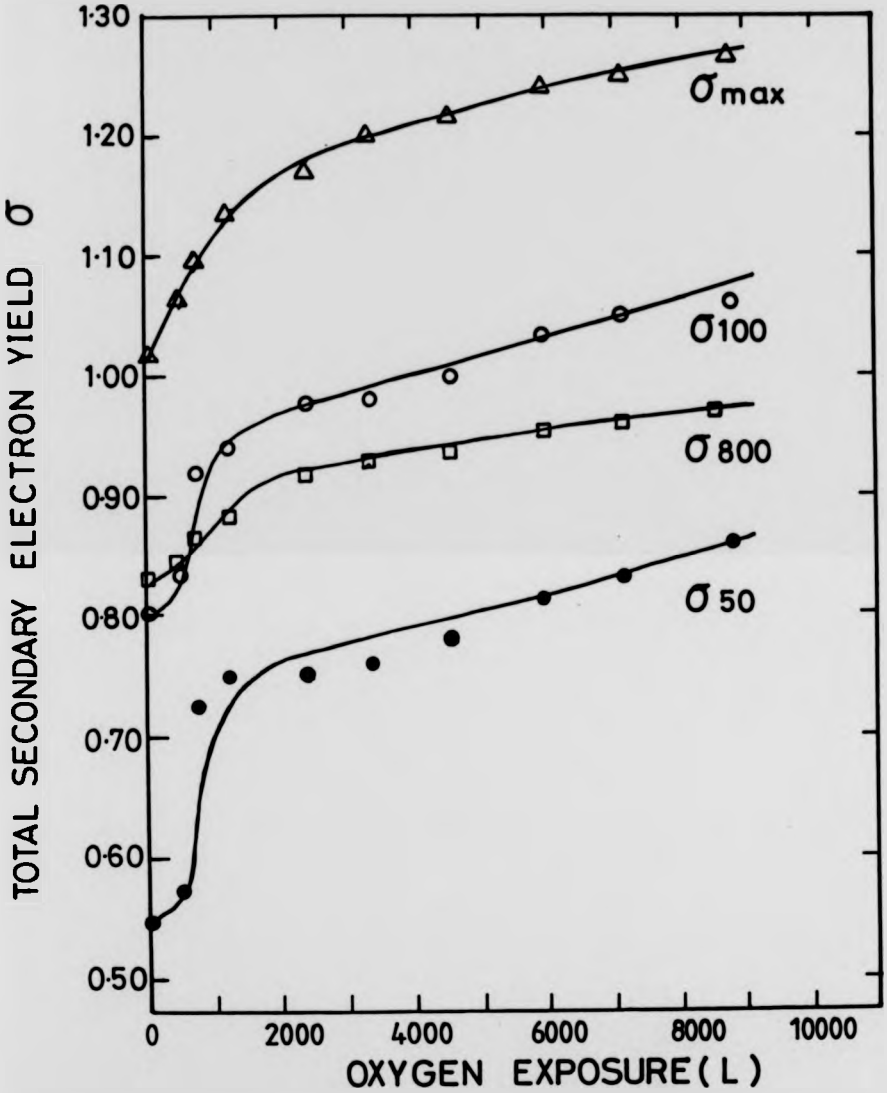

Fig. 9.5 Variation of σ_{max}, σ_{50}, σ_{100} and σ_{800} with oxygen exposure up to 10000 L.

Table 9.1 Typical numerical variation in the total yield σ for various primary energies at selected oxygen exposures up to 10000 L.

Oxygen exposure (L)	Total yield σ (±.02)			
	σ_{50}	σ_{100}	σ_{max}	σ_{800}
0	0.54	0.80	1.01	0.83
480	0.57	0.83	1.06	0.84
2400	0.75	0.98	1.18	0.92
4800	0.79	1.00	1.22	0.94
8880	0.86	1.07	1.27	0.97

9.2.3 Total yield Measurements for Oxygen Exposures of 0 - 1000 L

The changes in the yield, of the surface at early stages of oxidation, was investigated by reducing the oxygen partial pressure in the STC to between 10^{-8} and 10^{-7} torr, and exposing the clean surface to an equivalent time for 1000 L. In order to correlate the behaviour of the yield to the level of oxygen adsorption, AES window spectra of the Al_{LVV}, Al_{LVoVo} and O_{KLL} peaks were also recorded by the method already described in section 7.2.3.1 and illustrated in Fig. 9.6.

In the preceding chapter the ratios A and B were defined as follows: A is the ratio of the O^{505} Auger PPH intensity to Al^{67} Auger PPH. Its magnitude gives an indication of the overall oxygen content of the surface, irrespective of the chemical environment or state of the oxygen. B was defined to be the ratio $[Al\text{-}O^{54}/(Al\text{-}O^{54} + Al^{67})]$ and gives an indication of the overall oxide content of the surface. Since the $Al\text{-}O^{54}$ Auger signal is directly due to oxidised aluminium, it appears only after chemisorption of oxygen is complete.

The variation of the total maximum yield α_{max}, with oxygen exposure up to 1000 L, is shown in Fig. 9.7(a) together with the changes in the Al^{67}, $Al\text{-}O^{54}$ and O^{505} Auger PPH intensities. Variation of α_{max}, ratios A and B with oxygen exposure are shown in Fig. 9.7(b).

From the above figures it can be seen that, α_{max} increased in the same fashion with oxygen exposure as the O^{505} and $Al\text{-}O^{54}$ Auger signal PPH intensities and AES ratios A and B. One outstanding feature of the figures is the noticeable slight decrease in α_{max} for the very early stages of oxygen adsorpcion corresponding to 0-30 L of exposure. This decrease in α_{max} is not reflected by any corresponding change in the evolution of the

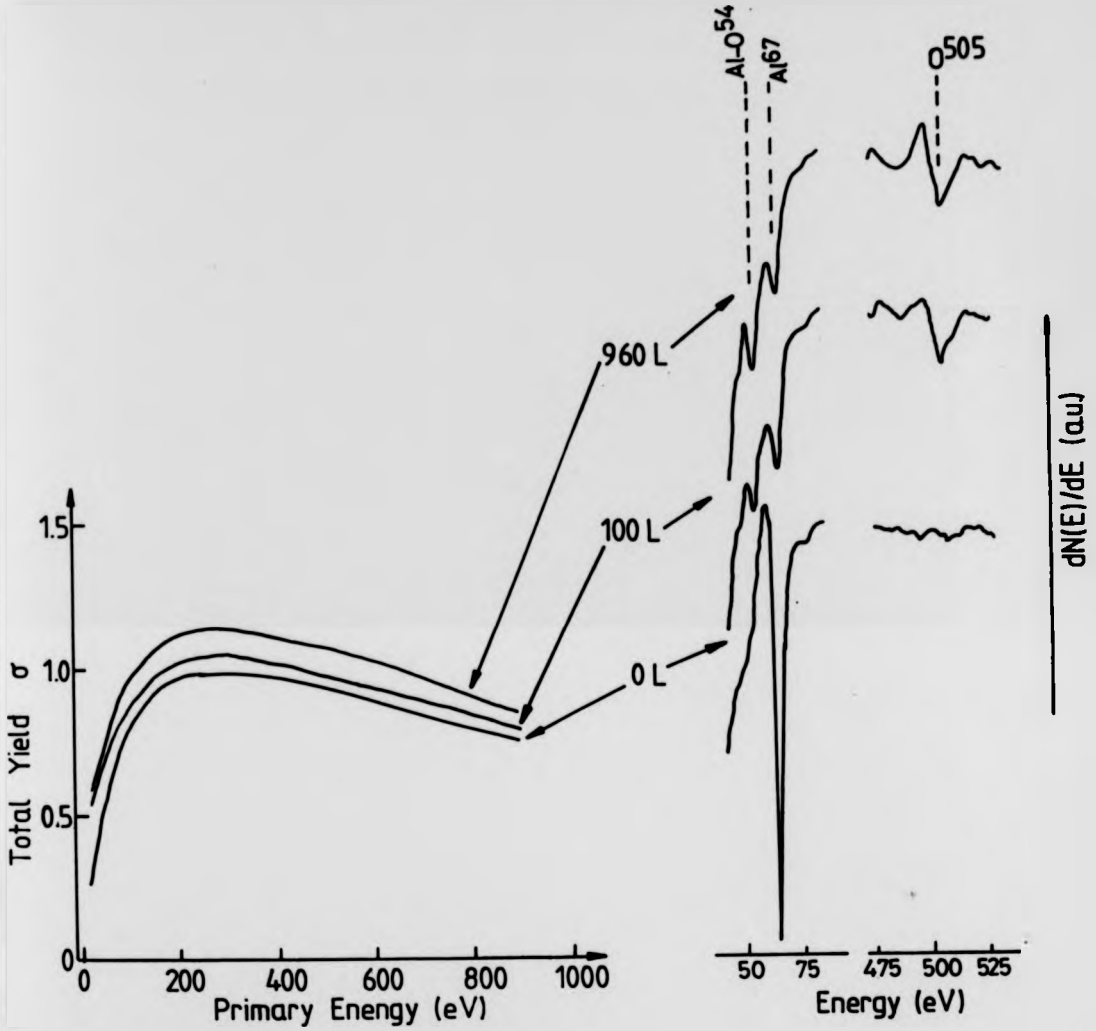

Fig. 9.6 Total yield σ versus E_p for three different oxygen exposure levels of 0, 100 and 1000 L and their corresponding Al^{67}, $Al\text{-}O^{54}$ and O^{505} Auger window spectra (E_p = 1500 eV, I_p = 7.5 μA, V_m = 4 and 10 V_{pp}).

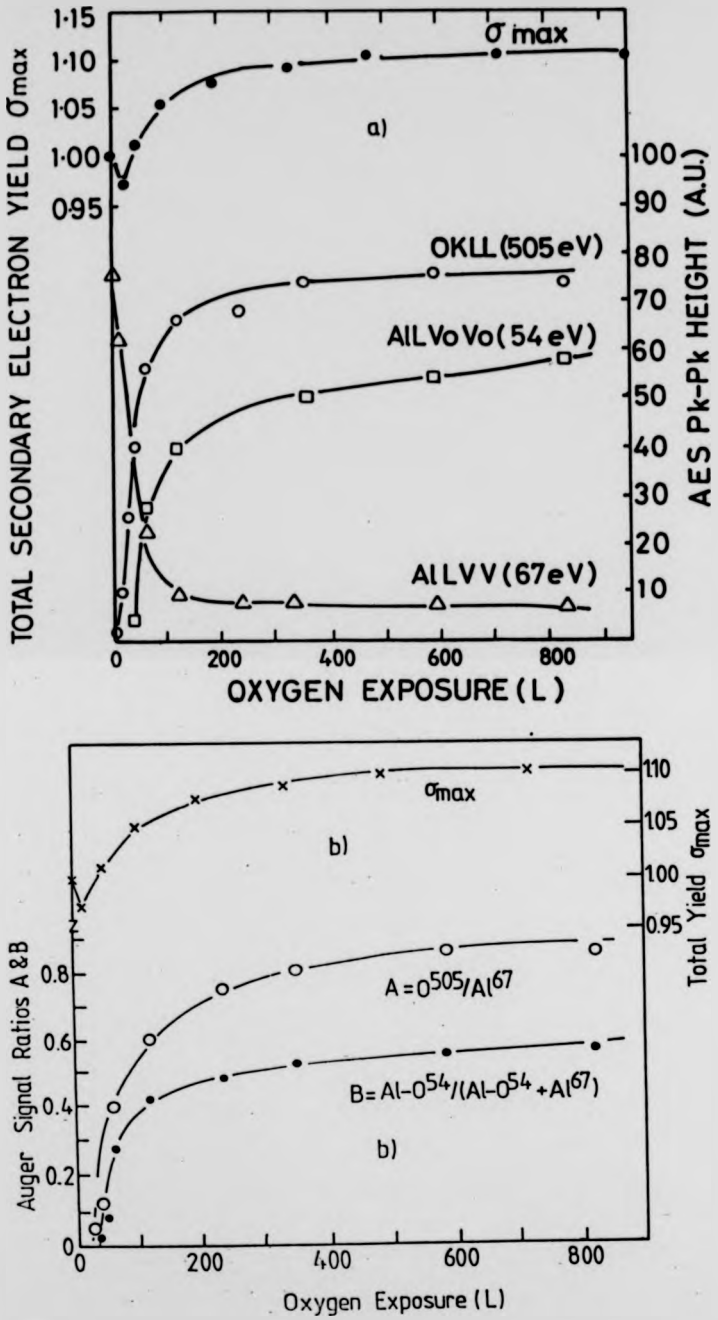

Fig. 9.7 (a) σ_{max}, Al^{67}, $Al\text{-}O^{54}$ and O^{505} AES PPH intensities versus oxygen exposure (0 to 1000 L). (b) σ_{max}, ratios A and B versus oxygen exposure.

O^{505} or Al-O^{54} Auger peaks. In fact, this slight decrease in σ_{max}, is observed well before the detection of the Al-O^{54} Auger signal.

The value of σ_{max} decreased from 1.02 to 0.97 for the first 10 L after which it began to increase in the same fashion as the O^{505} signal, reaching a value of 1.15 after 1000 L of oxygen exposure. The yields at other primary acceleration voltages for example 50, 100 and 800 eV, also increased in the same way as the O^{505}, Al-O^{54}, and ratios A and B as illustrated in Fig. 9.8. From these figures the initial slight drop in σ_{max} at the initial stages of chemisorption is also apparent.

For oxygen exposures greater 10 L and up to 1000 L the yields increased quite drastically, with large rate of increase occuring for the low primary electron acceleration voltages and corresponding to points on the exposure scale when monolayer coverage and chemisorption phase is complete. For example for E_p = 50 eV $\Delta\sigma$ = 0.20 and E_p = 800 eV $\Delta\sigma$ = 0.10.

Summarised in Table 9.2 are total yield values, for various primary acceleration voltages and at several oxygen exposure levels of up to 1000 L.

9.2.4 Total Yield Measurements for Oxygen Exposures of 0-50 L

In these set of experiments, changes in the yield for the very early stages of oxidation was investigated further. Adsorption pressure in the chamber was reduced to 10^{-8} torr and the clean surface exposed for a period equivalent to 0 - 50 L of oxygen. Evolution of σ_{max}, with oxygen exposure is shown in Fig. 9.9 together with the Al-O^{54}, Al^{67}, O^{505} Auger signal PPH intensities.

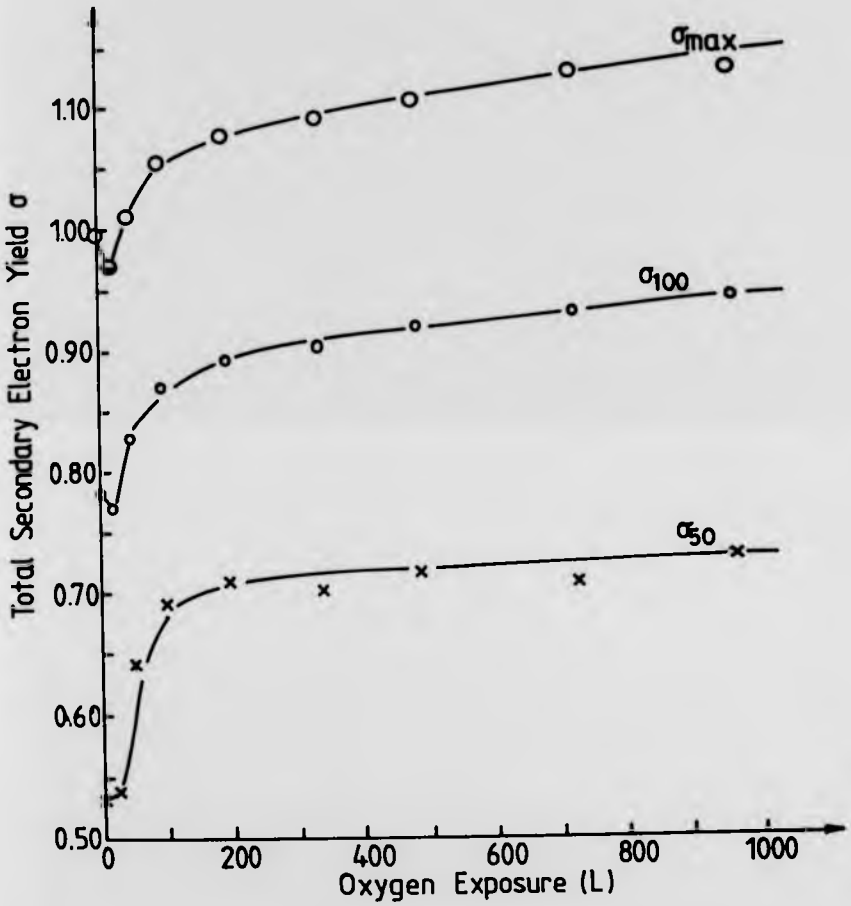

Fig. 9.8 σ_{max}, σ_{50}, σ_{100} and σ_{800} versus oxygen exposure (0 to 1000 L)

Table 9.2 Typical numerical variation of total yield σ at various primary electron energies for various oxygen exposure levels up to 1000 L.

Oxygen exposure (L)	Total yield σ (±.02)			
	σ_{50}	σ_{100}	σ_{max}	σ_{800}
0	0.53	0.78	1.00	0.82
48	0.60	0.83	1.01	0.85
192	0.71	0.89	1.08	0.90
480	0.72	0.92	1.10	0.90
960	0.73	0.94	1.14	0.94

Fig. 9.9 confirms the slight decrease in σ_{max}, observed in the experiments of section 9.2.3. The position of the minimum corresponds to 6-7 L along the oxygen exposure axis. By comparison, the Al-O^{54} Auger signal does not appear until after 24 L of oxygen exposure. The evolution of σ_{max} thereafter, follows that of the O^{505} Auger signal PPH increasing steadily. Because the O^{505} Auger signal has not quite reached saturation level the trend in σ_{max} is still upward.

In order to demonstrate the reproducibility of the observed minimum in σ_{max} the results of four different experimental runs have been shown in Fig. 9.10 together with σ for E_p = 130 eV (σ_{130}). Fig. 9.10 shows clearly a definite decrease in σ_{max} and σ_{130}.

The evolution of the yields at other primary acceleration voltages with oxygen exposure up to 50 L e.g. 50, 100, 800 eV, are shown in Fig. 9.11. The trend in the yields are upward particularly after the chemisorption phase of oxygen as marked by the appearence of the Al-O^{54} Auger signal. The biggest rate of increase in σ occured for low primary acceleration voltages. For E_p = 50 eV the resultant increase in σ was 0.18 and for σ_{100} 0.12. For E_p > 500 eV the overall change in σ was almost zero. Table 9.3 shows typical changes in the yield for various primary energies for the 0 to 50 L oxygen exposure regime.

Thus from the foregoing results, the following general statement can be made for the low oxygen exposure regime: for > 15 L, σ increased for all E_p; and that the overall increase in σ was greater for E_p < 100 eV than for E_p > 100 eV; and no minima in σ for E_p < 100 eV was observed.

The results of the yield measurements for clean and oxygen exposed aluminium surfaces will be interpreted in terms of the modern secondary

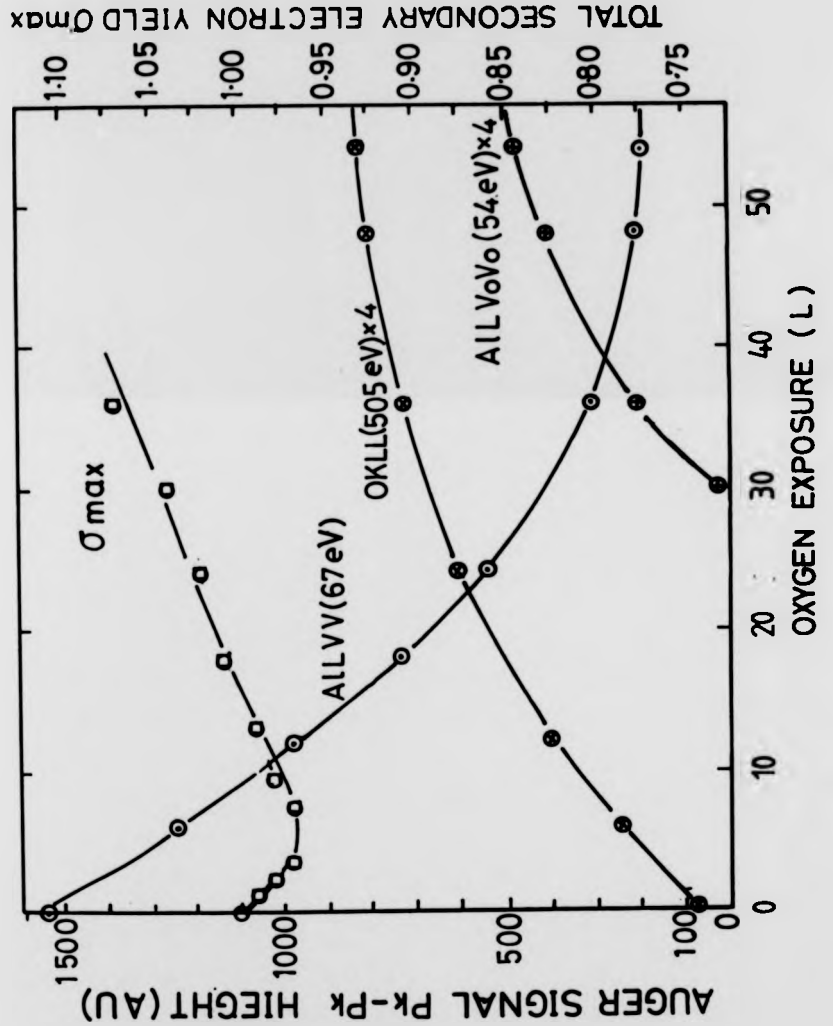

Fig. 9.9 Evolution of σ_{max} with very low oxygen exposure together with Al^{67}, $Al\text{-}O^{54}$ and O^{505} Auger signal PPH intensities.

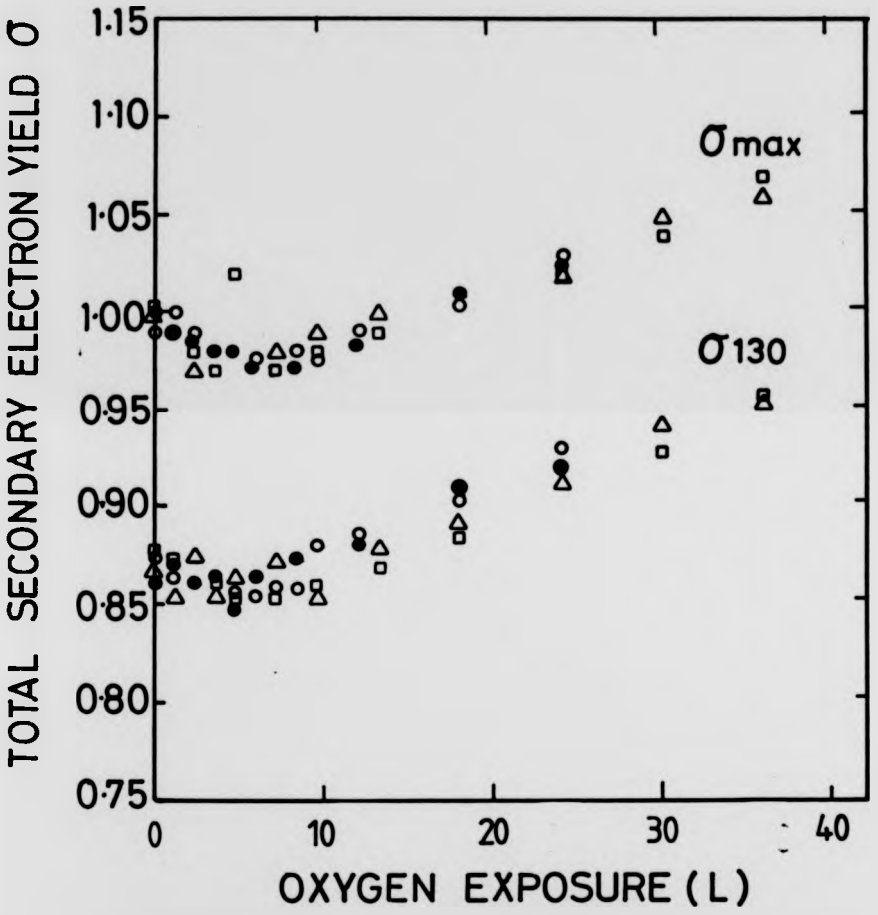

Fig. 9.10 Variation of σ_{max} and σ_{130} with oxygen exposure (0 to 50 L) displaying the results of four separate experimental runs.

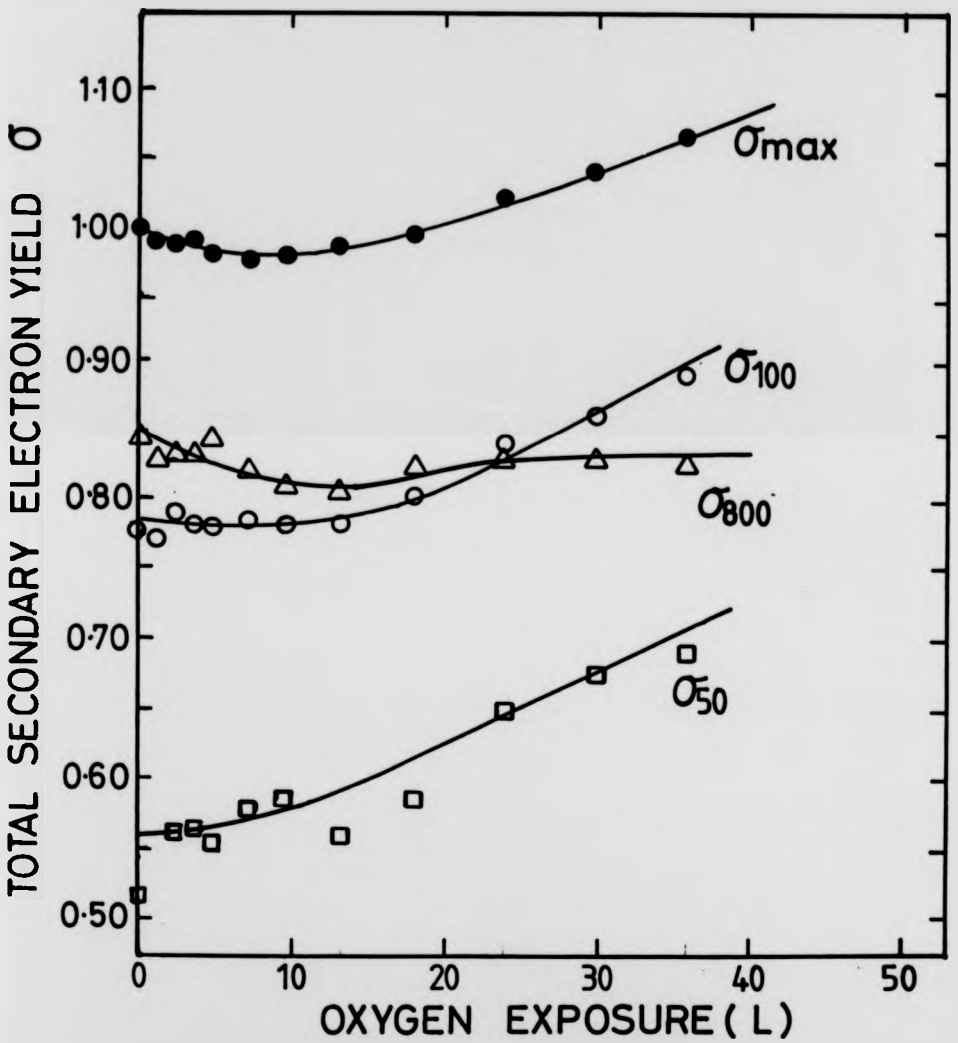

Fig. 9.11 Evolution of σ_{max}, σ_{50}, σ_{100} and σ_{800} with oxygen exposure (0 to 50 L).

Table 9.3 Typical numerical changes in yield σ at various primary energies for oxygen exposure levels up to 50 L.

Oxygen exposure (L)	Total yield σ (±.02)			
	σ_{50}	σ_{100}	σ_{max}	σ_{800}
0	0.52	0.78	1.00	0.84
2.5	0.55	0.78	0.98	0.83
10	0.58	0.78	0.97	0.81
24	0.65	0.82	1.02	0.83
36	0.70	0.90	1.06	0.83

electron emission theory for nearly free electron metals. The observation of the reduction in σ_{max} with initial oxidation which appears to be the first such experimental observation will be interpreted by the decrease of contribution of bulk and surface plasmon decay to SEE.

Enhancement of the yield with larger oxygen exposures will be described in more general terms by reference to SEE from insulators and their band structure.

9.3 Discussion of Results

From a consideration of results, the discussion section will be treated in three parts. In the first part, SEE yield measurements from the clean polycrystalline surface will be discussed, initially in general terms to describe the shape of the yield curve and then with reference to the more recent theories of SEE, which assigns an important role to the surface and bulk plasmons in SEE.

In the second part, the very early stages of oxygen adsorption and its effect on SEE will be discussed. The previously unreported, decrease in σ_{max} will be interpreted in terms of an attenuation of the contribution to SEE by bulk and surface plasmon decay, but other possible interpretations will also be considered, for example work function changes and backscattering ratio.

In the third part, the increased yield, and hence SEE, with oxidation will be discussed with reference to models of SEE from insulators.

9.3.1 Yield Measurements from the Clean Surface

The form of the secondary electron yield curve, for the clean surface polycrystalline aluminium surface is very similar to those from other metals. It consists of a smoothly rising yield for low primary electron energies, reaching a broad maximum at approximately 300 eV, and decreasing slowly for increasing primary electron energies. The maximum value of the yield, from 18 separate measurements was found to be 1.00 ± .02 where 0.02 is the standard deviation in the measurements.

A qualitative interpretation of the physical processes leading to the above form of the yield curve is as follows i) A loss of energy by the incident primary electrons in inelastic interactions with the lattice and core electrons of the metal can create secondary electrons mostly at the penetration depth. ii) The so created secondary electrons then diffuse towards the surface and are involved in further inelastic collisions with the lattice electrons creating further secondary electrons, in a so called **cascade process** with ever decreasing energy. Secondaries with kinetic energy less than $E_F + \Phi_{Al}$ incident normal to the surface do not escape and therefore make no contribution to the yield.

The concept of escape depth of secondaries is quite important and determines the magnitude of the yield. For low primary excitation energies, the penetration depth is small compared with the escape depth of the secondaries and these escape with ease leading to an increase of the yield with primary energy.

For higher primary excitation energies, electrons, penetrate deep inside the metal for which the penetration depth exceeds the secondary escape depth. Consequently a lower yield results. The observed maximum yield corresponds to the equality of the penetration depth of the primaries and escape depth of the secondaries.

The escape depth of the secondaries for Al has been estimated to be approximately 30 A and is typical for metals and is largely attributed to the high density of states in the conduction band in which the internal secondaries lose substantial amount of kinetic energy through inelastic collisions. The above processes satisfactorily describes the general form of the secondary electron emission yield curve.

In chapters 5 and 6 it was shown that the majority of the secondary electrons are slow (0 - 50 eV) and contribute up to nearly 80 % to the total yield for kinetic energies in excess of 200 eV. The remaining 20 % are made up of backscattered primaries which include the elastically reflected and inelastically scattered primaries which have lost discrete amounts of energy in creating surface and bulk plasmons within the electron sea.

There is now strong experimental evidence that these so generated plasmons, make an additional contribution to the slow secondary electrons by decaying via single electron excitations from the conduction band. Fine structure observed on the slow secondary electron distribution curve (EDC) correspond to energy positions $\hbar\omega_S$ and $\hbar\omega_B$ (10.5 and 15.5 eV) with respect to the Fermi level.

Though from these results direct quantitative estimate of the plasmon decay contribution to the slow secondaries cannot be made, the area under the plasmon loss peaks, can be correlated to the area under the EDC making up the slow secondary electrons.

9.3.2 Yield Results at very low Oxygen Coverages

The evolution of the total yield and in particular the total maximum yield σ_{max} can be divided into 2 stages. In the first stage, of the adsorption process i.e. 0 - 10 L, σ_{max} was observed to decrease and reach a broad minimum. From AES measurements it can be deduced that the chemisorption phase of oxygen is not complete and the surface retains its metallic character. In the second stage of the adsorption process i.e > 10 L, σ_{max} is observed to gradually increase but at an enhanced rate when the chemisorption phase of oxygen is completed and the surface has monolayer coverage. As the oxide level grows the yield also grows in proportion.

The observed decrease in σ_{max} has not been previously reported in literature and it can be accounted for by several qualitative interpretations.

i) Effect of work function changes on slow secondary electron emission with initial oxygen exposure.

ii) Direct reduction in the plasmon loss and elastic peak loss current and hence reduction in the backscattering ratio.

iii) As an indirect reduction in the contribution of decaying surface and bulk plasmons to slow secondary electron emission.

Changes in the work function is expected to influence the escape probability of hot secondary electrons. Experimental data, show little or no change in ϕ of Al with initial oxygen exposure. In the majority of the measurements reported in the literature which has been reviewed in section 4.2.4 a slight decrease is reported (0.05 eV) with the maximum decrease being 0.2 eV which occurs after 30 L of oxygen exposure. Assuming that all other secondary electron contributions to the yield remain constant this

decrease in the work function would lead to an enhancement of secondary electron emission which is of course opposite to that actually observed.

An estimate of the probable percentage increase in the number of slow secondary electrons emitted in the normal direction can be made by use of equation 5.15 (assuming a value of ϕ = 4.3 eV and maximum decrease in ϕ of 0.2 eV) which gives a percentage increase of 3 %. Hence changes in the work function are likely to oppose the decrease in the yield.

Another possible interpretation for the observed initial dip in the yield could be due to a direct reduction in the intensity of the surface and bulk plasmon loss peaks accompanying the elastic peak. This will lead to a reduction in the backscattering ratio and hence total yield.

Production of surface and bulk plasmons depend on the primary excitation energy of the exciting electrons, angle of incidence, nature of the surface, angle of emission and type of analyser. For the clean polycrystalline surface, at primary energies of 300 eV and normal incidence, the intensity of the surface and bulk plasmons are approximately equal. Slight exposure of the surface to oxygen, sees a sudden decrease in the surface plasmon intensity followed by a drop in the bulk plasmon peak intensity. Conduction electrons which were participating in the plasmon oscillations, are no longer available and are trapped by the adsorbed oxygen atoms.

Digitisation and integration of the ELS spectra from literature (see Appendix A), recorded as a function of oxygen exposure show a drop in the number of electrons contributing to the plasmon peaks and this would subtract from the total yield. So far, Pellerin and Le Gressus (1980) seem to have been the only workers to have investigated the evolution of the

total yield with oxygen exposure of polycrystalline Al surface and at the same time to have monitored the changes in the ELS, elastic peak and slow secondary EDC at primary electron energies of $30 < E_p < 400$ eV. The spectra were recorded in the EN(E) mode using a CMA.

Pellerin and Le Gressus reported no decrease in the total yield, with initial exposure. From measurements of areas under the resolution corrected spectra, they showed that the plasmon loss current and the total yield increased smoothly. The elastic peak current did not change until after 10-15 L after which it resulted in a sudden increase.

They also reported the following observations: that for $E_p < 250$ eV the elastic peak current dominated the entire N(E) curve and provided the major contribution to the total yield. For $E_p > 250$ eV, the slow secondary electron current, makes the largest contribution to the total yield for all levels of oxygen exposure.

In reaching the above observations and conclusions, Pellerin and Le Gressus did not take into account the transmission characteristics of the CMA at low kinetic energies. In fact they underestimated the contribution of the slow secondary electrons to the total yield, while over estimating that from the elastic peak (see Appendix B). Angle integrated N(E) spectra from three grid RFA apparatus show that the contribution to the total yield by the slow secondaries is dominant even down to primary electron energies of 70 eV. This has also led them to downplay the plasmon decay contribution to the slow secondary electron current.

The third possible interpretation for the observed decrease in the yield with initial oxygen exposure, can be attributed to conduction electrons, exhibiting plasmon oscillations induced by the primary electrons. Evidence

for the role of plasmons in the creation of slow secondary electrons was produced in the review chapter, section 6.2.3. Fine structure observed on the slow secondary electron distribution curve, at 5.5 and 10.5 eV above the vacuum level, have been attributed to decay of surface and bulk plasmons ($\hbar\omega_S$ = 10.5 and $\hbar\omega_B$ = 15.5 eV) into single particle excitations from the conduction and valence bands. Since the valence band structure of Al is nearly free electron like, the shape of the EDC, reflects that of the valence band and the energy position of the fine structure correspond to the edge of the Fermi level.

With slight oxygen adsorption, the intensity of the plasmon loss peaks, particularly the surface plasmons are drastically reduced, which in turn will lead to a reduction in the emission of electrons due to plasmon decay. This mechanism is expected to be dominant in aluminium and other metals which have nearly free electron like band structures and exhibit intense plasmon loss coupling with the primary electrons. Theories of SEE, reviewed in chapter 5, have taken this into account, and predict fine structure on the EDC, and qualitative estimates indicate a substantial contribution to the true yield and hence the total yield.

9.3.3 Yield at high Oxygen Exposures

With increasing oxygen exposure levels, the trend in the yield is upward for all primary electron energies. This trend occurs at around 25 L and corresponds to the beginning of the completion of the oxygen chemisorption monolayer and formation of aluminium oxide. The secondary electron emission properties of a clean metal surface is drastically changed by the presence of oxygen atoms and subsequent formation of an oxygen layer as deduced from AES measurements of chapter 8. It is an experimentally well established fact that insulators, in particular metal oxides have much

higher total electron yields than do pure metal surfaces. (see section 6.2.1)

The basic mechanism of SEE from insulators is similar to that from metals and it can be understood in terms of the modified electronic band structure of the metal due to formation of an oxide. Changes in the band structure are evident from the modification of the ELS peaks and slow secondary EDC. Substantial reduction in the bulk plasmon loss peak intensity indicate that the density of the electrons in the conduction band is in turn reduced and their presence can be totally ignored.

Interaction of the primaries now, is with the electrons in the totally occupied valence band. The escape and transport of the secondaries is governed by the effective potential barrier and since in insulators the Fermi level is not absolutely defined, the electron affinity χ is used instead. χ is defined as the energy from the empty conduction band and the vacuum level and is of the order of several electron volts. Thus secondary electrons are able to over come the electron affinity without significant loss of energy due to lack of conduction electron interactions. The only significant loss of energy is via collisions with the lattice atoms (0.1 eV). This is then manifested as an increase in the mean escape depth estimated to be 200 A, approximately 5-6 times that for pure metal.

Fully oxidised aluminium surfaces with fairly thick oxide layers will exhibit σ_{max} in the range 2-9 and a vast majority of the secondaries will be contributed by the true yield δ. Since in the results of this work, σ_{max} had increased to 1.15 after 1000 L of oxygen exposure and followed by 1.25 after 10 000 L, indicates that the surface oxide layer may not be thicker than couple of monolayers and that the substrate still influences the overall yield to some extent.

Table 9.4 A summary of the experimental yield values for the clean and oxygen exposed surface from this work and other workers.

Nature of sample	Adsorbate level	σ_{max}	Epmax eV	σ_{100}	σ_{800}	Author
Evap. thick film	clean	0.95				Kollath (1956)
"	"	0.88	400			Bronshtein and Fraiman (1961)
"	"	0.96	350	0.74	0.86	Thomas and Pattinson (1970)
Al(421)	"	0.98	250	0.70		Pillon et al (1977)
Polycryst. Al	"			0.67		Pellerin and Le Gressus (1980)
" "	10 L O_2 10000L O_2			0.67 1.17		" "
" " "	clean 10L O_2 8000L O_2	1.01 0.97 1.27	300 300 327	0.80 0.78 1.07	0.82 0.81 0.97	This work " " " "

A summary of the experimental yield values for the clean and oxygen exposed surface from this work and other workers is presented in Table 9.4.

9.4 Conclusions

In this chapter the results of SEE yield measurements from clean and oxygen exposed polycrystalline surfaces has been presented. For the clean surface the total maximum yield σ_{max}, was found to be 1.00 ± .02 and this occured at a primary energy of 300 ± 10 eV.

With slight oxygen exposure < 10 L, a small decrease in σ_{max} was observed. This has been interpreted as due to a fast decrease in the surface and bulk plasmon loss intensity, leading to a decrease in the plasmon decay contribution to the secondary electron yield and hence total yield. This conclusion, supports the more recent theories of SEE where the plasmon decay contribution is taken into account.

With increased oxygen exposure, the total yield increased for all primary electron energies, for σ_{max} had increased to 1.25 after 10 000 L, and this corresponded to a primary energy of 325 eV. The enhanced secondary emission was attributed to the formation of a several monolayer thick aluminium oxide as determined from the AES results.

In the next chapter, conclusions to the work presented in this thesis will be given together with suggestions for further work.

CHAPTER 10

Conclusions and Recommendations for Future Work

10.1 Conclusions

A summary of the conclusions of the the study of polycrystalline aluminium surfaces are presented below.

1. Adsorption of oxygen consists of two stages. In the first stage a chemisorption phase is formed after ~ 50 L of oxygen exposure. This is followed by the oxidation phase. Saturation coverage was reached after a total of 150 L of oxygen exposure. The interaction of oxygen with the surface is with an estimated initial sticking coefficient S_0 of 0.02.

2. Irradiation of the 50 L and 1000 L oxygen exposed surfaces with electron beam current densities of 10^{-3} - 10^{-4} A/cm^2, resulted in predominant decomposition of the oxide with subsequent desorption of oxygen as deduced from the AES measurements of Al $L_{23}VV$ (67 eV), Al $L_{23}V_OV_O$ (54 eV) and O KLL (505 eV) transitions. The mechanisms of electron stimulated desorption, and decomposition by **Coulomb repulsion** appeared to play a major role.

3. The decrease in the Al-O^{54} cross-transition AES PPH with electron irradiation time obeyed a first order law and similarly with the ratio B [Al-O^{54}/(Al-O^{54}+Al^{67})]. From these, an effective total desorption cross-section Q_T of 5 x 10^{-20} cm^2 has been estimated. For the 100 to 750 L exposed surface Q_T was found to be 6 x 10^{-20} and for the 1000 L oxygen exposed surface 3 x 10^{-20} cm^2.

4. From these cross-section values a critical dose D_c of 0.02 C/cm^2 at a beam beam energy of 1.5 keV was estimated to be necessary in order to limit surface damage to less than 10 %.

5. From SEE yield measurements, the total maximum yield σ_{max}, for the clean polycrystalline surface was found to be 1.00 ±.02 at a primary energy E_{pmax} of 300 ±10 eV. The yield at 100 eV was 0.80 and at 800 eV 0.83.

6. With slight oxygen exposure < 10 L a previously unreported small decrease in σ_{max} ~ 3 % was observed. This has been interpreted as due to a fast decrease in the surface and bulk plasmon loss intensities, leading to a decrease in the plasmon decay contribution to the slow secondary electron yield and hence to the total yield. A slight drop in yield at other primary energies is also observed.

7. With increasing oxygen exposure > 10 L σ_{max} increased for all primary electron energies. Low primary energies giving a faster increase in the yield compared with higher energies. The evolution of σ_{max} was very similar to the growth in the O KLL Auger PPH on the same oxygen exposure scale. The increase in σ coincides with the completion of the chemisorption phase and formation of Al_2O_3 like oxide as confirmed by AES. After 10000 L of oxygen exposure σ_{max} increased to 1.25 ±.02 at an E_{pmax} of 325 ±10 eV.

8. Secondary electron emission from oxidised surfaces, is enhanced due to increasing escape depth of secondary electrons in the solid as the conduction bands become virtually empty of electrons. Effective escape depth is 5 times that for a pure metal surface e.g. ~ 200 A.

10.2 Recommendations for further work

Further electron beam irradiation experiments should be undertaken in order to reconcile some of the differences between this work and those of the other authors in particular that of Fontaine et al (1982). The beam effect experiments should be repeated using a variety of oxygen exposed aluminium samples for example evaporated thin films, polycrystalline sheets, and single crystals at electron beam energies of 50 to 10 000 eV and at various current densities. Use of such a wide energy range would help to identify various desorption and adsorption mechanisms. It would also be very useful to investigate the response of annealed and non-annealed oxygen exposed surfaces to electron irradiation. The results of such investigations could help to make inter-lab comparison of results more meaningful.

In order for the above experiments to be done on the present apparatus it would be necessary to carry out some modifications. The sample holder would have to be re-designed to hold at least 3 samples. There should be a capability of direct resistive heating of the samples via the sample manipulator, and with a thermo-couple in good thermal contact with the sample to give accurate monitoring of temperature. Presently the sample can only be heated via electron beam bombardment with the electrons being provided by a projection filament. This method has various disadvantages one of the most serious being coating of the insulating fish spine beads with tungsten and substrate atoms that produce conducting paths between the collector and retarding grids.

In order to identify the desorption products directly, the quadrupole mass spectrometer should be transferred from the STC on to an appropriate port on the SAC. Also the effusion source should be transferred on to the SAC so that the sample would not have to be shunted backwards and forwards

between the STC and SAC so many times.

Presently the acquisition of secondary electron spectra with the existing electronics is in the dN(E)/dE mode so that Auger features can be amplified. The electronics should be modified so that N(E) spectra can be directly recorded. This could be quite useful in determining the contribution of each part of the N(E) distribution to the total yield, since the RFA has a near 100 % collection efficiency. The versatility of the RFA would further be increased by cutting slots in the collector so that angular resolved SEE work can be carried out. The present system is angle integrated, in that secondary electrons emitted in all directions are collected.

As a separate project automatic acquisition of data by a minicomputer would be very valuable. N(E) spectra can be acquired directly even without a lock-in-amplifier, and if necessary dN(E)/dE spectra produced by numerical differentiation of the N(E) data.

REFERENCES

Adams D.L. and Germer L.H., Surf. Sci., **27** (1971) 21.

Argile C. and Rhead G.E., J. Phys. C. : Sol. State Phys., **15** (1982) L193.

Auger P., J. Phys. Radium **6** (1925) 205.

Austin L. and Starke H., Ann. Phys., Leipzig, 9 (1902) 271.

Bachrach R.Z., Chadi D.J. and Bianconi A., Solid State Communications, **25** (1978) 489.

Balzerotti A. and Bianconi A., Phys. Status Solidi **(b)76** (1976) 689.

Bargeron C.B. and Nall B.H., Surf. Sci., **119** (1982) L319.

Baroody E.M., Phys. Rev., **78** (1950) 780.

Bearden J.A. and Burr A.F., Rev. Mod. Phys., **39** (1967) 125.

Bedair S.M., Hofmann F. and Smith H.P., J. of Appl. Physics, **39** (1968) 4026.

Bedair S.M. and Smith H.P., J. Appl. Physics, **42** (1971) 3616.

Bellard S.W., Ph. D. Thesis, University of Liverpool, (1980).

Benndorf C., Keller G., Seidel H. and Thieme F., Surf. Sci., **67** (1977) 589.

Benninghoven A. and Loebach E., Rev. Sci. Instrum., **42** (1971) 49.

Bishop H.E. and Riviere J.C., J. Appl. Phys., **40** (1969) 1740.

Blakely J.M., " Introduction to the Properties of Crystal Surfaces ", Pergamon Press, 1973.

Bianconi A., Appn. Surf. Sci., 6 (1980) 392.

Bindi R., Lanteri N. and Rostaing P., J. Phys., D., **13**(1980) 267.

Bohm D. and Pines D., Phys. Rev., **92** (1953) 609.

Bradshaw A.M., Hofmann P. and Wyrobisch W., Surf. Sci., **68** (1977) 269.

Brenig W., Z. Physik, **B23** (1976) 361.

Bruining H., " Physics and Applications of Secondary Electron Emission ". McGraw Hill, New York, 1954.

Bruining H. and De Boer J. H., Physica **5** (1938) 17.

Bronshtein I.M. and Denisov S.S., Sov. Phys. Sol. St., 7 (1965) 1484.

Bronshtein I.M. and Fraiman B.S., Sov. Phys. Sol. St., 3 (1961) 1188.

Buck T.M., in:"Methods of Surface Analysis" ed:A.W. Czanderna, Elsevier 1975.

Bujor M., Larson L.A. and Poppa H., J. Vac. Sci. Technol., **20(3)** (1982) 392.

Burhop E.H.S., " The Auger Effect and Other Radiationless Transitions " Oxford University Press, England 1952.

Cailler M., Ganachaud J.P. and Roptin D., Le Vide Les Couches Minces, **36** (1981) 279.

Christian R.G. and Leck J.H., J. Sci. Instrum., **43** (1966) 229.

Chung M.F. and Jenkins L.H., Surf. Sci., **22** (1970) 479.
Chung M.S. and Everhart T.E., Phys. Rev., **B15** (1977) 4699.
Coad J.P. and Riviere J.C., Surf. Sci., **25** (1971) 609.
Coghlan W.A. and Clausing R.E., Atomic Data, **5** (1973) 317.
Cosslet V.E. and Thomas R.N., Brit. J. Appl. Phys., **15** (1964) 883.
Cosslet V.E. and Thomas R.N., Brit. J. Appl. Phys., **15** (1964) 1283.
Davis L.E., McDonald N.C., Palmberg P.W., Riach G.E. and Weber G.E., " Handbook of Auger Electron Spectroscopy", 2nd Edn. (Physical Electronics Ind., Eden Prairie, Minnesota, 1976).
Davisson C.J. and Germer L.H., Phys. Rev., **30** (1927) 705.
Dawson P.H., J. Appl. Phys., **37** (1966) 3644.
Dekker A.J., in: " Solid State Physics; Advances in Research and Applications ". Eds. F. Seitz and D. Turnbull, Vol. 6., Academic Press, New York 1958.
Dekker A.J. and van der Ziel A., Phys. Rev., **86** (1952) 755.
Dionne G.F., J. Appl. Phys., **44** (1973) 5261.
Dionne G.F., J. Appl. Phys., **44** (1975) 3347.
Dobretsov L.N. and Gomoyunova M.V., "Emissionoya Elektronika", Nauka Moscow, 1966.
Dorey G., Surf. Sci., **27** (1971) 311.
Drinkwine M.J. and Lichtman D., Prog. in Surf. Sci., **8** (1977) 123.
Dufour, Guennou and Bonnelle, Surf. Sci., **32** (1972) 731.
Duraud J.P. and Le Gressus C., Le Vide, **36** (1981) 1.
Eberhardt W. and Kunz C., Surf. Sci., **75** (1978) 709.
Everhart T.E., Saeki N., Shimuzu R. and Koshikava T., J. Appl. Phys. **47** (1976) 2941.
Fadavi M., Ph. D. Theses, University of Keele, 1981.
Falconer J.L., Bischke S.D. and Hanna G.J., Surf. Sci., **131** (1983) 455.
Fehlner F.P. and Mott N.F., Oxidation of Metals, **2** (1970) 59.
Ferrel R.A., Phys. Rev., **107** (1957) 450.
Flodstrom S.A., Bachrach R.Z., Bauer R.S. and Hagstrom S.B.M., in: Proc. 7th Int. Vac. Congr. and Proc. 3rd Int. Conf. on Solid Surfaces Vienna, (1977) 869., Eds. R. Dobrozemsky et al., Berger, Vienna 1977.
Flodstrom S.A., Martinsson C.W.B., Bachrach R.Z., Hagstrom S.B.M. and Bauer R.S., Phys. Rev. Lett., **40** (1978) 907.
Flodstrom S.A., Petersson L.C. and Hagstrom S.B.H., J. Vac. Sci. Technol. **13** (1976) 280.
Fontaine J.M., Lee-Deacon O., Duraud J.P., Ichumara S. and LeGressus C., Surf. Sci., **122** (1982) 40.
Franks J., J. Vac. Sci. Technol., **16** (1979) 181.

Frohlich H., Ann. Physik, **13** (1932) 229.
Gallon T.E., in: Electron and Ion Spectroscopy of Solids ", Eds. L. Fiermans, J. Vennik and W. Dekeyner, Plenum London (1978) 230.
Ganachaud J.P. and Cailler M., Surf. Sci., **83** (1979) 519.
Gartland P.O., Surf. Sci., **62** (1977) 183.
Gornyi N.B., Rakhovitch L.M. and Skirko S.F., Sov. Phys. J., **10** (1967) 15.
Goto K. and Ishikawa K., J. Appl. Phys., **43** (1972) 1559.
Haas T.W., Grant J.T. and Dooley G.J., J. Appl. Phys., **43** (1972) 1853.
Habraken F.H., Kieffer E.P. and Bootsma G.A., Proc. 7th Int. Congr. and 3rd Int. Conf. Solid Surfaces, Vienna (1977) 877.
Hayden B., Hachicha S. and Bradshaw A.M., Proc. of 4th Int. Congr. on Surf. Sci., Vol. II. (1980) 1125.
Henrich V.E., Phys. Rev. **B37** (1973) 3512.
Henrich V.E., Rev. of Sci. Instrum., **44** (1973) 456.
Holliday J.E. and Sternglass E.J., J. Appl. Phys., **28** (1957) 1189.
Holloway P.H., Surf. Sci., **54** (1976) 506.
Huber E.E. and Kirk C.T., Surf. Sci., **5** (1966) 447.
Huber E.E. and Kirk C.T., Surf. Sci., **9** (1968) 217.
Ibach H. and Rowe J.E., Phys. Rev., **B9** (1974) 1951.
Ibach H. and Rowe J.E., Phys. Rev., **B10** (1974) 710.
Jenkins L.H. and Chung M.F., Surf. Sci., **28** (1971) 409.
Johanssen J.S., Spicer W.E. and Strausser Y.E., J. Appl. Phys. **47** (1976) 3028.
Johansson L.I. and Stöhr J., Phys. Rev. Lett., **43** (1979) 1882.
Jona F., J. Phys. Chem. of Solids, **28** (1967) 2155.
Jonker J.L.H., Philips Research Repts., 7 (1952) 1.
Jonker J.L.H., Philips Research Repts., 6 (1951) 372.
Kanaya K. and Kawakatsu H., J. Phys. D. : Appl. Phys., **5** (1972) 1727.
Kanaya K., Ono S. and Ishigaki F., J. Phys. D. : Appl. Phys., **11** (1978) 2425.
Kanaya K. and Ono S., J. Phys. D. : Appl. Phys., **11** (1978) 1495.
Kanter H., Phys. Rev., **121** (1961) 681.
Katayama Y., Kobayashi K.L.I. and Shiraki Y., Surf. Sci., **86** (1979) 549.
Khonde K., Darville J. and Gilles J.M., Vacuum **31** (1981) 449.
Khonde K., Darville J. and Gilles J.M., J. Vac. Sci. Technol., **20(3)** (1982) 834.
Kirby R.E. and Lichtman D., Surf. Sci., **41** (1974) 447.
Knotek M.L. and Feibelman P.J., Phys. Rev. Letters **40** (1978) 964.
Knotek M.L. and Feibelman P.J., Phys. Rev. **B18** (1978) 6531.

Knotek M.L., Phys. Today, **37** (1984) 24.
Kobayashi K.L.I., Shiraki Y. and Katayama Y., Surf. Sci., **77** (1978) 449.
Kollath R., Hanb. Phys., **21** (1956) 232.
Kruger Wm.H. and Pollack S.R., Surf. Sci., **30** (1972) 263.
Lambert R.M. and Comrie C.M., Prog. in Surf. Sci., **38** (1973) 197.
Lander J.J., Phys. Rev., **91** (1953) 1382.
Lane R.O. and Zaffarano D.J., Phys. Rev., **94** (1954) 960.
Lang N.D. and Williams A.R., Phys. Rev. Lett. **34** (1975) 531.
Lang N.D. and Williams A.R., Phys. Rev. **B18** (1978) 616.
Leder L.B. and Simpson J.A., Rev. Sci. Instrum., **29** (1958) 571.
Le Gressus C., Mogami A., Ichinokawa T.I., Pellerin F. and Massignon D., Le Vide Couches Minces, **36** (1981) 73.
Madey T.E., Surf. Sci., **33** (1972) 355.
Madey T.E., Yates J.T., King D.A. and Uhlaner C.J., J. Chem. Phys., **52** (1970) 5215.
Margoninski Y., Appl. Surf. Sci., **11** (1982) 784.
Martinson C.W.B., Petersson L.G., Flodstrom S.A. and Hagstrom S.B.M., " Proc. of Int. Photoemission Symposium ", Noordwijk, ESA Sp 118 (1976) 177.
Martinson C.W.B. and Flodstrom S.A., Surf. Sci., **80** (1979) 306.
Menzel D., In: " Interactions on Metal Surfaces ", ed: R. Gomer, Topics in Applied Physics Vol. 4 Springer-Verlag 1975.
Menzel D. and Gomer R., J. Chem. Phys., **41** (1964) 3311.
Menzel D. and Gomer R., J. Chem. Phys., **41** (1964) 3329.
McGuire and Seah M.P., (1979)...
McHugh J.A., in:" Methods of Surface Analysis ", Ch.6 SIMS, 223 ed. A.W. Czanderna, Elsevier 1975.
Muskett R.G., Surf. Sci., **21** (1970) 440.
Nall B.H., Jette A.N. and Bargeron C.B., Surf. Sci., **110** (1981) L606.
Norman D., Brennan S., Jaeger R. and Stohr J., Surf. Sci., **105** (1981) L297.
Ono S. and Kanaya K., J. Phys. D. : Appl. Phys., **12** (1979) 619.
Ozkok A.A., Ph. D. Thesis, University of London, (1983).
Ozkok A.A., Webber P.R. and Dobson P.J., Sol. Stat. Comm., **46** (1983) 109.
Palmberg P.W. and Rhodin T.N., J. Appl. Phys., **39** (1968) 2425.
Pantano C.G. and Madey T.E., Appl. of Surf. Sci., **7** (1981) 115.
Park R.L., Microbeam Anal., **16** (1981) 65.
Pattinson E.B. and Harris J., J. Electron Spectrosc. **1** (1972/73) 500.
Payling R. and Ramsey J.A., J. Phys. C (Solid State Phys.) **13** (1980) 505.
Pellerin F., Le Gressus C. and Massignon D., Surf. Sci., **103** (1981) 510.
Pellerin F., Le Gressus C. and Massignon D., Surf. Sci., **111** (1981) L705.

Pellerin F. and Le Gressus C., in: Proc. 4th Int. Conf. Sol. Surf. and 3rd ECOSS (Cannes 1980) 1400.

Pillon J., Ganachaud J.P., Roptin D., Mignot H., Dejardin-Horgues C. and Cailler A., in: Proc. 7th Int. Vac. Congr. and 3rd Int. Conf. on Solid Surfaces, Vienna (1977) 473.

Pillon J., Roptin D. and Cailler M., Surf. Sci., 50 (1976) 741.

Pines D., in: " Elementary Excitations in Solids ". Ed. W. A. Benjamin. New York, Amsterdam, 1963.

Pireaux J.J., Ghijsen J., McGowan J.W., Verbist J. and Caudano R., Surf. Sci., 80 (1979) 488.

Pitts J.R., Bischke S.D., Falconer J.L. and Czanderna A.W., J. Vac. Sci. Technol., A2(2) (1984) 1000.

Powell C.J. and Swan J.B., Phys. Rev., 115 (1959) 869.

Powell C.J. and Swan J.B., Phys. Rev., 118 (1960) 640.

Powell D.D. and Woodruff D.P., Surf. Sci., 33 (1972) 437.

Prutton M., "Surface Physics", Clarendon Press, Oxford 1975.

Quinto D.T. and Robertson W.D., Surf. Sci., 27 (1971) 645.

Raether H., " Plasmons and Inter-band Transitions ". Springer Tracts in Modern Physics, 38 1965.

Raether H., " Plasmons and Inter-band Transitions ", Springer Tracts in Modern Physics, 88 1980.

Redhead P.A., Canad. J. Phys., 42 (1964) 886.

Ritchie R.H., Phys. Rev., 106 (1957) 874.

Riviere C.J., in:" Practical Surface Analysis by Auger and x-ray Photoelectron Spectroscopy ", eds. D. Briggs and M.P. Seah,. John Wiley and Sons, 1983.

Roberts M.W. and Wells B.R., Surf. Sci., 15 (1969) 325.

Roptin D., Thèse d'Etat, University of Nantes, 1975.

Rosler M. and Brauer W., Phys. Stat. Sol. (b), 104 (1981) 161.

Rosler M. and Brauer W., Phys. Stat. Sol. (b), 104 (1981) 575.

Rudberg R.E., Phys. Rev., 50 (1963) 138.

Salahub D.R., Roche M. and Messner R.P., Phys. Rev., B18 (1978) 6495.

Salow H., Z. tech. Physik, 21 (1940) 8.

Seah M.P. and Dench W.A., Surf. Interface Anal., 1 (1979) 1.

Seah M.P. and Briggs D., " Practical Surface Analysis by Auger and x-ray Photoelectron Spectroscopy " . John Wiley and Sons, 1983.

Seah M.P., Surf. Sci., 17 (1969) 132.

Seigbahn K., Nordling C., Fahlman A., et al., " Atomic, Molecular and Solid State Structure Studied by means of Electron Spectroscopy ", Almquist and Wiksell Boktryckeri A.B., Uppsala 1967.

Shiraki Y., Kobayashi K.L.I. and Katayama Y., Surf. Sci., 77 (1978) 458.
Shulman A.R., Yaroshetsky J.D. and Makedonsky W.L., Zh. Tekhn. Fiz., 23 (1953) 1152.
Smith T., Surf. Sci., 55 (1976) 601.
Smith (1971)
Somorjai G.A., " Principles of Surface Chemistry ", Prentice Hall, Englewood Cliffs, New Jersey 1972.
Soria F., Martinez V., Munoz M.C. and Sacedon J.L., Phys. Rev. B24 (1981) 6926.
Sternglass E.J., Phys. Rev., 95 (1954) 345.
Stohr J., Johansson L.I., Brennan S., Hecht M. and Miller J.N., Phys. Rev. B22 (1980) 4052.
Stohr J., Johansson L.I., Lindau I. and Pianetta P., Phys. Rev., B20 (1979) 664.
Streitwolf V.H.M., Ann. Physik 3 (1959) 183.
Suleman M. and Pattinson E.B.P., J. Phys. F. 1 (1971) L21.
Suleman M. and Pattinson E.B., J. Phys. D., Appl. Phys., 13 (1980) 693.
Thomas S. and Pattinson E.B., J. Phys. D: Appl. Phys., 3 (1970) 349.
Thomas S. and Pattinson E.B., J. Phys. D: Appl. Phys., 3 (1970) 1469.
van Oostrom A., Surf. Sci., 89 (1979) 615.
Vrakking J.J. and Meyer F., Surf. Sci., 18 (1971) 226.
Wagner C.D., in:" Practical Surface Analysis by Auger and x-ray Photo-electron Spectroscopy ", eds. D. Briggs and M.P.Seah, John Wiley and Sons Ltd., 1983.
Wang D., Freeman A.J. and Krakuer H., Phys. Rev., B24 (1981) 3092.
Watanabe H., J. Phys. Soc. Japan, 16 (1962) 912.
Weber R.E. and Peria W.T., J. Appl. Phys., 38 (1967) 4355.
Wollf P.A., Phys. Rev. 95 (1954) 56.
Wooldridge D.A., Phys. Rev., 56 (1939) 562.
Wright B., Ph. D. Theses, University of Keele, 1974.
Wright B. and Pattinson E.B.P., (1974)
Young J.R., J. Appl. Phys., 27 (1956) 1.
Yu H.L., Munoz M.C. and Soria F., Surf. Sci., 94 (1980) L104.
Yue K.Y., Miller J.N., Chye P., Spicer W.E., Lang N.D. and Williams A.R. Phys. Rev. B14 (1976) 1446.

APPENDIX A

The changes resulting in the relative surface and bulk plasmon loss peak intensities as a function of oxygen exposure (0, 1, 10 and 30 L) is illustrated in Fig. A. as obtained by Bujor et al (1982) from Al films. The ELS spectra were recorded in EN(E) mode with E_p 250 eV.

The above loss spectra have been digitised using the Ferranti Cetec digitiser in conjunction with the GEC 4080 mainframe computer. The loss spectra were then numerically integrated within the energy limits of 220 and 250 eV and the background removed by linear subtraction. The relative contribution of the surface and bulk plasmon loss peaks to the loss current as a function of oxygen exposure have been summarised in Table A. The areas have been normalised to the plasmon loss peak area corresponding to the clean surface.

Table A. also illustrates the result of synthetic peak fitting to the surface and bulk plasmon loss peaks using Gaussians. It is clear that the overall contribution to the plasmon loss current by the surface and bulk plasmons diminish quite rapidly.

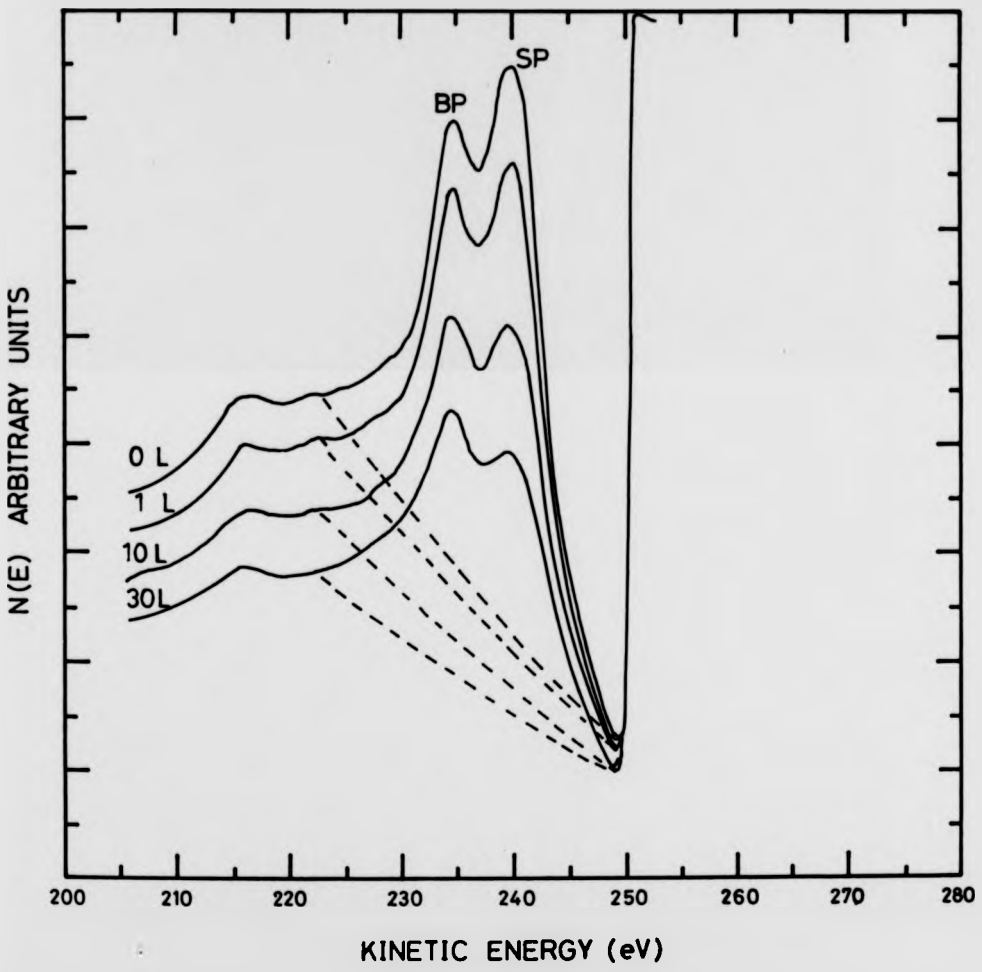

Fig. A. Evolution of the surface and bulk plasmon loss peaks with oxygen exposure (0, 1, 10, 30 L). (from Bujor et al 1982).

Table A. Relative numerical changes in the areas of the surface and bulk plasmon loss peaks with oxygen exposure. The areas have been normalised to the sum of the SP and BP for the 0 L exposed surface. (* areas calculated by numerical trapezoidal rule integration. ** denotes areas computed by fitting of synthetic Gaussians.)

Oxygen exposure (L)	Total area under* Surface and Bulk plasmons	Area under** Surface and Bulk plasmons	
	SP + BP	SP	BP
0	1.00	0.53	0.47
1	0.92	0.47	0.43
10	0.78	0.36	0.35
30	0.60	0.30	0.27

APPENDIX B

In order to establish the contribution of various parts of the secondary electron distribution to the total yield, it is necessary to demonstrate how energy analysers distort the N(E) curve.

At low kinetic energies, the CMA due to its transmission characteristic under estimates the intensity of the slow secondary electron distribution curve (EDC). Here EN(E) spectra taken from literature (Duraud and Le Gressus 1981) and N(E) spectra (Rudberg 1963) have been digitised and the areas under the spectra determined by simple trapezoidal rule within the following limits: the slow secondary electron current α ($\propto \int_{0}^{50} N(E)\ dE$), plasmon loss current β ($\propto \int_{E_p-35}^{E_p-5} N(E)\ dE$), and the elastic peak current γ ($\propto \int_{E_p-5}^{E_p+5} N(E)\ dE$). The overall area under the distribution θ ($\propto \int_{0}^{E_p+5} N(E)\ dE$) has been normalised to 1.

Fig. B.(a) illustrates an EN(E) spectra recorded using a CMA and Fig. B.(b) shows an N(E) SEE distribution recorded using a three grid RFA from a copper sample. The result of the integration is shown in Table B., which gives the relative contribution of α, β and γ to the overall distribution (normalised to 1.0).

It is quite clear from Table B. that the contribution to the overall secondary electron emission, by the slow secondary electron current α is under estimated by at least a factor of three.

This is a general illustration only and a proper comparison must take into account the incident primary energy, angle of incidence ature of the sample, angle of exit of electrons, analyser acceptance angle, and analyser resolution. The CMA because of its transmission characteristic suppresses

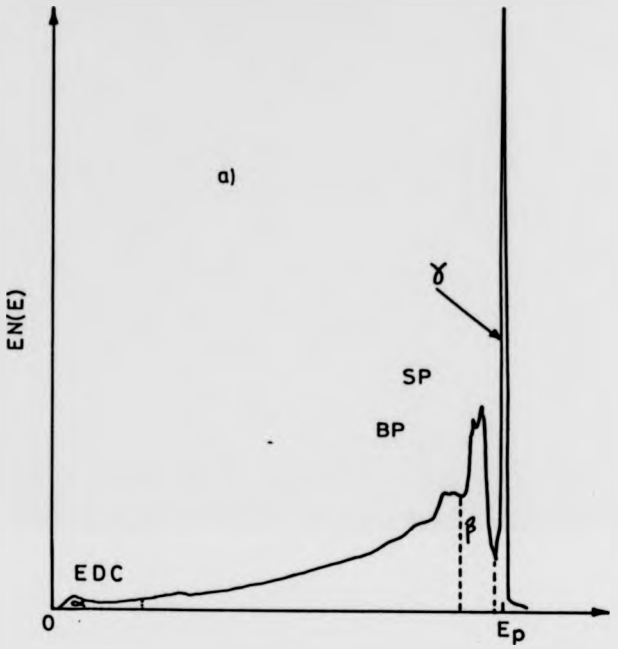

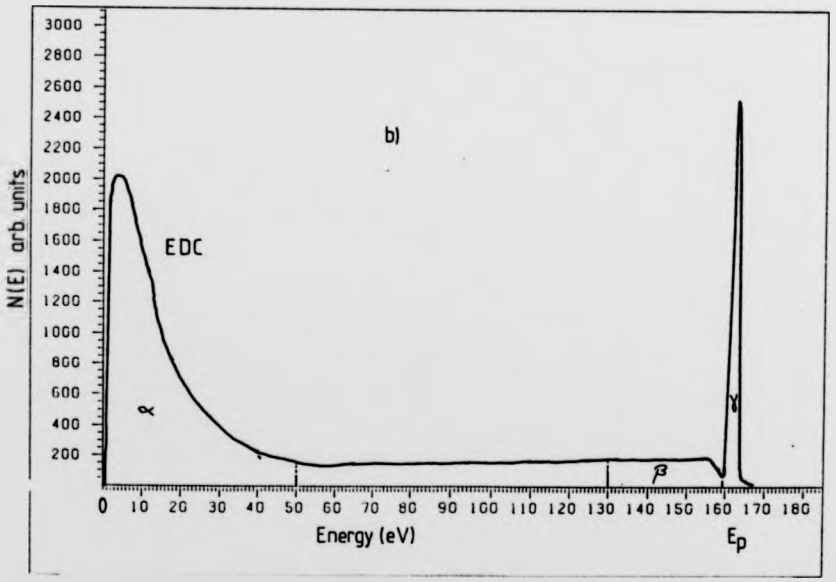

Fig. B.(a). EN(E) distribution of secondary electrons from a clean polycrystalline aluminium sample recorded with a CMA and at an E_p = 250 eV (Duraud et al 1981).
(b) N(E) distribution of secondary electrons from a clean polycrystalline copper sample using a 3-grid RFA at an E_p of 160 eV. (Rudberg 1963).

the slow secondary electrons.

Table B. Relative contributions of α, β and γ to the SEE distribution as recorded by a CMA and three-grid RFA. The total area has been normalised to 1.0.

	CMA	3-grid RFA
α	0.23	0.61
β	0.17	0.08
γ	0.10	0.09
θ	1.00	1.00

Surface Science 151(1984) 1-12

North-Holland, Amsterdam

excluded at the request of the university